

Recombination and Trapping in Multicrystalline Silicon Solar Cells

Daniel Harold Macdonald

May 2001

A thesis submitted for the degree of
Doctor of Philosophy
of The Australian National University

Declaration

I certify that this thesis does not incorporate without acknowledgement any material previously submitted for a degree or diploma in any university, and that, to the best of my knowledge, it does not contain any material previously published or written by another person except where due reference is made in the text. The work in this thesis is my own, except for the contributions made by others as described in the Acknowledgements.

Daniel Macdonald

Acknowledgements

I would like to thank my supervisor, Dr. Andres Cuevas, for his advice and encouragement, for always making himself available for discussions, and especially for his positive and enthusiastic approach to research. I am also grateful to Prof. Andrew Blakers for forming part of my supervisory panel and for providing much useful advice. Dr. Jenny Wong-Leung and Prof. C. Jagadish of EME at RSPHysSE, were also members of the supervisory panel, for which I am grateful. Jenny kindly helped with ion-implantation and Rutherford Backscattering experiments, while Jagadish was a source of great knowledge and assistance regarding DLTS, and kindly allowed access to the PECVD system.

I am also grateful to my fellow student Mark Kerr, who helped with many useful discussions and contributions. In particular, his knowledge of and assistance with PECVD SiN depositions was of great benefit. Also, he generously allowed me to use his improved lifetime analysis spreadsheet, which includes the Auger parameterisation and generalised analysis described in Chapter 1. I would also like to mention helpful discussions with Ron Sinton of Sinton Consulting, who was kind enough to devote time and effort to helping me with numerous issues, particularly the bias-light correction work in Chapter 3.

Chris Samundsett was of immeasurable assistance in the CSES laboratories. I am especially thankful for his patient tutelage in the intricacies of cleanroom work, for producing the mc-Si PERL cells of Chapter 4 and for assisting with many of the gettering experiments in Chapter 2. I would also like to thank the other members of the CSES and the Engineering Dept. for providing a friendly and enjoyable environment to work in.

Some other members of the group provided specific assistance for which I am grateful. Will Keogh kindly helped with the long-duration light source in Chapter 3, and Klaus Weber provided helpful advice on defect etching. Chris Jones designed and built the LED array used for steady-state measurements, while Anthony Sloan performed many of the gettering experiments on BPSolar material in Chapter 3. Kallista Stewart produced the Cu-implanted sample in Chapter 5.

I am also grateful to Mladen Petravic of EME for his cheerful assistance with SIMS measurements, and Sally Stowe of the Electron Microscopy Unit at RSBS for help with taking electron micrographs. Jim Williams of EME and Atsushi Kinomura of the Osaka National Research Institute, Japan, arranged and performed the NAA measurements. Jan Schmidt also contributed many helpful discussions during his visit to our group. Francesca Ferrazza kindly supplied the Eurosolare mc-Si material. The assistance of Saul Winderbaum and Tony Leo of BPSolar, Sydney, is also gratefully acknowledged. Mark Rosenblum of ASE Americas provided the EFG mc-Si samples.

Finally, I would like to express my deepest thanks to my wife Cath for her unfailing support and encouragement, for her proof-reading help, and for putting up with me over the last few months.

Abstract

In broad terms, this thesis is concerned with the measurement and interpretation of carrier lifetimes in multicrystalline silicon. An understanding of these lifetimes in turn leads to a clearer picture of the limiting mechanisms in solar cells made with this promising material, and points to possible paths for improvement. The work falls into three broad categories: gettering, trapping and recombination. A further section discusses a powerful new technique for characterising impurities in semiconductors in general, and provides an example of its application.

Gettering of recombination centres in multicrystalline silicon wafers improves the bulk lifetime, often considerably. Although not employed deliberately in most commercial cell processes, gettering nevertheless occurs to some extent during emitter formation, and so may have an important impact on cell performance. However, the response of different wafers to gettering is quite variable, and in some cases is non-existent. Work in this thesis shows that the response to gettering is best when the dislocation density is low and the density of mobile impurities is high. For Eurosolare material these conditions prevail at the bottom and to a lesser extent in the middle of an ingot. However, these conclusions can not always be applied to multicrystalline silicon produced by other manufacturers. Low resistivity multicrystalline silicon suffers from a concurrent thermally induced degradation of the lifetime. This had previously been attributed to the dissolution of precipitated metals, although we note that the crystallographic quality also appears to deteriorate. The thermal degradation effect results in an optimum gettering time for low resistivity material. Edge-defined Film-fed Growth (EFG) ribbon silicon was also found to respond to gettering, and even more so to bulk hydrogenation. Evidence for Cu contamination in the as-grown EFG wafers is presented.

Multicrystalline silicon is often plagued by trapping effects, which can make lifetime measurement in the injection-level range of interest very difficult, and sometimes impossible. An old model based on centres that trap and release minority carriers, but do not interact with majority carriers, was found to provide a good explanation for these effects. These trapping states were linked with the presence of dislocations and also with boron-impurity complexes. Their annealing behaviour and lack of impact on device parameters can be explained in terms of the models developed. The trapping model allowed a recently proposed method for correcting trap-affected data to be tested using typical values of the trapping parameters. The correction method was found to extend the range of useable data to approximately an order of magnitude lower in terms of carrier density than would be available otherwise, an improvement that could prove useful in many practical cases.

High efficiency PERL and PERC cells made on gettered multicrystalline silicon resulted in devices with open circuit voltages in the 640mV range that were almost entirely limited by

bulk recombination. Furthermore, the injection-level dependence of the bulk lifetime resulted in decreased fill factors. Modelling showed that these effects are even more pronounced for cells dominated by interstitial iron recombination centres. Analysis of a commercial multicrystalline cell fabrication process revealed that recombination in the emitter created the most stringent limit on the open circuit voltage, followed by the bulk and the rear surface. The fill factors of these commercial cells were mostly affected by series resistance, although some reduction due to injection-level dependent lifetimes seems likely also. Secondary Ion Mass Spectroscopy on gettered layers of multicrystalline silicon revealed the presence of Cr and Fe in considerable quantities. Further evidence strongly implied that they resided almost exclusively as precipitates.

More generally, injection-level dependent lifetime measurements offer the prospect of powerful contamination-monitoring tools, provided that the impurities are well characterised in terms of their energy levels and capture cross-sections. Conversely, lifetime measurements can assist with this process of characterising impurities, since they are extremely sensitive to their presence. This possibility is explored in this thesis, and a new technique, dubbed Injection-level Dependent Lifetime Spectroscopy (IDLS) is developed. To test its potential, the method was applied to the well-known case of FeB pairs in boron-doped silicon. The results indicate that the technique can offer much greater accuracy than more conventional DLTS methods, and may find applications in microelectronics as well as photovoltaics.

Table of Contents

INTRODUCTION	1
LOSS MECHANISMS IN CRYSTALLINE SILICON SOLAR CELLS	2
THESIS OUTLINE	6
CHAPTER 1: CARRIER LIFETIMES IN CRYSTALLINE SILICON	9
1.1 CARRIER RECOMBINATION MECHANISMS	11
1.1.1 Radiative recombination	11
1.1.2 Auger recombination.....	13
1.1.3 Recombination through defects.....	14
1.1.4 Surface recombination	17
1.1.5 Emitter recombination.....	19
1.2 THE EFFECTIVE LIFETIME.....	20
1.3 IMPACT OF LIFETIME ON SOLAR CELL PARAMETERS.....	21
1.3.1 Open circuit voltage	21
1.3.2 Short circuit current.....	22
1.3.3 Ideality factor and fill factor	23
1.4 LIFETIME MEASUREMENT TECHNIQUES	25
1.4.1 Transient photoconductance decay (PCD).....	26
1.4.2 Quasi-steady-state photoconductance (QSSPC)	28
1.4.3 Other techniques.....	30
1.5 SURFACE PASSIVATION TECHNIQUES.....	31
1.6 SUMMARY	33
CHAPTER 2: GETTERING AND THERMAL DEGRADATION IN MULTICRYSTALLINE SILICON.....	35
2.1 INTRODUCTION	35
2.2 GETTERING TECHNIQUES FOR SILICON DEVICES.....	37
2.3 PHOSPHORUS GETTERING OF EUROSOLARE MULTICRYSTALLINE SILICON INGOTS	40
2.3.1 Experimental Methods	41
2.3.2 Results and Discussion.....	43
2.3.2.1 Dislocation density distribution.....	43
2.3.2.2 Mobile impurity distribution (cross-contamination)	44
2.3.2.3 Gettering results.....	46
2.4 GETTERING AND THERMAL DEGRADATION OF LOW RESISTIVITY MULTICRYSTALLINE SILICON	49
2.4.1 Evidence of thermal degradation.....	51
2.4.1.1 Process monitoring of mixed resistivity high-efficiency cells.....	51
2.4.1.2 High temperature oxidation of mc-Si	54
2.4.2 Optimum gettering times for low resistivity mc-Si.....	56
2.4.2.1 Experimental methods	56
2.4.2.2 Results and discussion.....	56
2.4.3 Physical origin of thermal degradation	58
2.4.3.1 Precipitate dissolution model.....	58
2.4.3.2 Generation of crystallographic defects	61
2.5 GETTERING OF BPSOLAR MULTICRYSTALLINE SILICON INGOTS	62
2.6 GETTERING OF A ‘BLACKED-OUT’ MULTICRYSTALLINE SILICON INGOT	65
2.7 GETTERING OF EDGE-DEFINED FILM-FED GROWTH (EFG) MULTICRYSTALLINE SILICON	68
2.7.1 Results and discussion.....	69
2.7.2 SIMS analysis of gettering layer of EFG material	72

2.8 SUMMARY	74
CHAPTER 3: MINORITY CARRIER TRAPPING IN MULTICRYSTALLINE SILICON.....	77
3.1 INTRODUCTION	77
3.2 ANOMALOUS QSSPC AND PCD LIFETIMES AT LOW EXCESS CARRIER CONCENTRATIONS	79
3.2.1 Quasi-steady-state V_{oc} measurements.....	81
3.2.2 Long flash lifetime measurements	82
3.2.3 True steady-state lifetime measurements using staircase LED illumination	83
3.3 HORNBECK-HAYNES TRAPPING MODEL	85
3.3.1 Trapping statistics	86
3.3.1.1 Energy level of trapping states	91
3.3.2 Comparison with experimental data	92
3.3.2.1 QSSPC lifetime curves.....	92
3.3.2.2 Effect of traps on open circuit voltage	94
3.4 PHYSICAL ORIGIN OF TRAPPING CENTRES	95
3.4.1 Correlation with dislocation density in gettered material	96
3.4.2 Correlation with dopant density in non-gettered material	97
3.4.2.1 Cross-contamination experiments	98
3.4.2.3 Light-soaking and thermal annealing behaviour of traps	103
3.5 A METHOD FOR CORRECTING TRAP-AFFECTED LIFETIME DATA	104
3.5.1 The bias-light correction method.....	105
3.5.1.1 Case I: constant recombination lifetime.....	108
3.5.1.2 Case II: decreasing lifetime with increasing excess carrier density	109
3.5.1.3 Case III: increasing lifetime with increasing excess carrier density	112
3.5.2 General guidelines for applying the bias-light correction.....	113
3.5.3 Example of corrected measurements on 0.4 Ω cm mc-Si.....	114
3.6 OTHER EXPLANATIONS FOR ANOMALOUS PHOTOCONDUCTANCE EFFECTS	116
3.6.1 Release of carriers from a space-charge region	116
3.6.2 Single-level recombination in defect-compensated semiconductors	117
3.7 SUMMARY	118
CHAPTER 4: RECOMBINATION IN MULTICRYSTALLINE SILICON SOLAR CELLS	121
4.1 INTRODUCTION	121
4.2 INJECTION-LEVEL DEPENDENT BULK LIFETIMES IN MULTICRYSTALLINE SILICON PERL CELLS	122
4.2.1 Experimental Methods.....	123
4.2.2 Analytic Modelling Techniques.....	124
4.2.3 Results and Discussion	127
4.2.3.1 Junction recombination as an alternative explanation of non-ideal behaviour ..	132
4.2.3.2 Validity of assumptions in the modelling	136
4.2.3.3 Conclusions	136
4.3 IMPACT OF INTERSTITIAL IRON ON C-SI CELLS	137
4.4 RECOMBINATION MECHANISMS IN COMMERCIAL MULTICRYSTALLINE SILICON CELLS..	142
4.4.1 Bulk lifetime limitation.....	142
4.4.2 Limitation due to emitter recombination	143
4.4.3 Limitation due to Al BSF.....	143
4.4.4 Fill factor effects	145
4.4.5 Conclusions.....	146
4.5 ANALYSIS OF POSSIBLE BULK RECOMBINATION CENTRES IN MULTICRYSTALLINE SILICON	146
4.5.1 SIMS profiles of multicrystalline silicon	147

4.5.2 Modelling multicrystalline silicon lifetime data with chromium- and iron-related centres	150
4.6 MULTICRYSTALLINE SILICON PERC CELLS.....	153
4.6.1 Fabrication process.....	154
4.6.2 Results and discussion.....	155
4.7 SUMMARY	158
CHAPTER 5: INJECTION-LEVEL DEPENDENT LIFETIME SPECTROSCOPY (IDLS) OF FeB PAIRS IN SILICON	159
5.1 INTRODUCTION	159
5.2 THEORETICAL BASIS OF INJECTION-LEVEL DEPENDENT LIFETIME SPECTROSCOPY	162
5.3 IDLS STUDIES OF INTERSTITIAL Fe AND FeB PAIRS IN SILICON	166
5.3.1 Overview of Fe and FeB pairs in silicon.....	166
5.3.2 Experimental methods.....	170
5.3.2.1 Sample preparation	170
5.3.2.2 Lifetime measurements.....	172
5.3.3 Modelling procedure.....	173
5.3.4 Results and discussion.....	176
5.3.5 DLTS measurements	181
5.3.6 Ratio and difference of diffusion lengths	183
5.4 OTHER POTENTIAL APPLICATIONS OF IDLS	186
CONCLUSIONS AND FURTHER WORK	189
Gettering and thermal degradation	190
Trapping in mc-Si.....	191
Recombination in mc-Si	192
Injection-level dependent lifetime spectroscopy (IDLS).....	193
LIST OF PUBLICATIONS	195
BIBLIOGRAPHY	199

Introduction

Crystalline silicon remains the material of choice for large-scale commercial production of photovoltaic modules. It has the natural advantages of being an abundant element with a well-suited band-gap for photovoltaic conversion, and is non-toxic. Also, due to its dominance in the microelectronics industries, it has become by far the most studied of all the semiconductors, and many specialised processes involving its use have been developed and refined over several decades. Some of these processes and much of the accumulated knowledge have been directly transferred to photovoltaic applications with great benefit.

However, crystalline silicon is not guaranteed to maintain its dominant position in photovoltaics in the medium to long term, at least not in the form of wafers sawn from bulk ingots. Reduced processing costs and improved cell fabrication techniques will ultimately lead to the underlying cost of the wafers themselves placing a limit on how cheaply such cells can be produced[1]. The need for further cost reductions is expected to lead eventually to the dominance of thin-film technologies, possibly still based on crystalline silicon. However, it is fair to say that thin-film cells, sometimes referred to as second generation photovoltaics, have been slower to oust bulk silicon from market dominance than many observers originally expected. It seems unlikely that any current thin-film technique will be in a position to do this within the next few years at least.

Taking an even longer-term view, such thin-film technologies as they are being developed today may still not represent full maturity of the photovoltaic industry. The underlying material costs of these devices are anticipated to continue to impose a significant lower limit on final product price, though much reduced compared to bulk silicon. The best path to further reductions then is to dramatically improve efficiency without a corresponding price increase. Such improvements can only be achieved by employing completely new device structures that avoid the fundamental efficiency limits of current single band-gap structures. These technologies are only now beginning to be seriously considered, and are collectively termed third generation photovoltaics[1]. It is expected to be many years, perhaps twenty, before such novel devices are in a position to dominate the marketplace.

As such there will very likely be a fairly long period in which bulk silicon still plays a major role in the photovoltaics industry. This is reflected by the fact that in the year 2000, bulk silicon accounted for 86.4% of world production, up from 84.4% in 1999[2]. The work presented in this thesis is firmly rooted in such first generation technology, and is devoted to exploring ways of improving the performance of silicon solar cells manufactured using widely

available techniques. In particular, it focuses on the use of cast multicrystalline silicon (mc-Si), a material that has become increasingly important in the commercial sphere. This material is somewhat cheaper to produce than single-crystal Czochralski-grown (Cz) wafers, but also results in less efficient cells, although this gap is narrowing. This trade-off between cost and efficiency had resulted in mc-Si and single-crystal Cz cells being approximately comparable in price per watt terms. However, it seems that this balance has recently shifted in favour of mc-Si, which accounted for 48.1% of world production in 2000 compared with 42% in 1999[2]. Over the same period, the market share of single-crystal silicon cells dropped from 42% to 37.3%. Judging from planned capacity expansions over the next few years it appears that this gap will widen further. It seems then that mc-Si will enjoy at least several years of market dominance, and, depending on the success of thin-film development, possibly many more.

In broad terms, this thesis is intended to contribute to the existing body of knowledge concerning mc-Si cells and how their performance may be improved. To provide a context for the work, a brief overview of the main efficiency loss mechanisms in silicon cells in general is presented next. In particular, a comparison between high-efficiency single-crystal Float Zone (FZ) cells and standard commercially produced mc-Si cells, reveals the important points which provide the motivation for the ensuing work.

Loss mechanisms in crystalline silicon solar cells

For a single band-gap solar cell, there are a number of fundamental and hence unavoidable loss mechanisms. Two of the most important of these are illustrated in Figure 1. Photons with energy higher than the band-gap are easily absorbed, producing an electron-hole pair in the process. However, the extra energy of the photon causes the photogenerated carriers to be excited into states of higher energy than the band-edges. These ‘hot’ carriers then rapidly lose energy until they reach the band-edges, a process called thermalisation. This energy loss occurs through successive emission of phonons, and is generally complete within a nanosecond, making it effectively instantaneous in comparison to other important carrier processes such as diffusion and recombination. By using AM1.5G spectrum data[3,4] and assuming a silicon band-gap of 1.124eV and no reflection, these thermalisation losses alone result in a loss of approximately 28% of the available incident energy. This type of loss can be reduced by tandem cell approaches, and possibly also by ‘hot carrier’ cells which extract carriers before they can thermalise. For standard single-junction devices such as mc-Si cells, however, this loss is unavoidable.

Photons of energy less than the band-gap represent another loss, as they are not absorbed by silicon, as shown again in Figure 1. This transmission of infrared light represents an

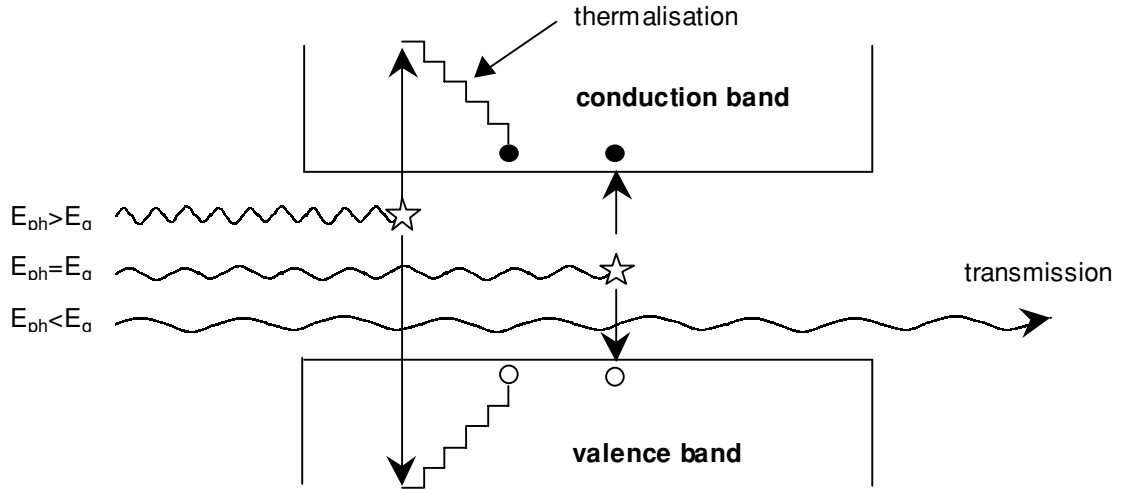


Figure 1. Thermalisation and transmission loss mechanisms in a single band-gap solar cell.

approximate loss of another 27% under AM1.5G conditions, assuming there is no sub-band-gap absorption due to phonon-assisted processes. Together, these fundamental mechanisms of thermalisation and infrared transmission reduce the maximum achievable efficiency for single-junction silicon cells to around 45%.

There are, however, additional fundamental processes that further reduce this figure. For a 1-sun cell (i.e. no concentration), radiative recombination brings this limit down to 31.7% when using the measured optical absorption spectrum of silicon, with the effects of free carrier absorption included[5]. Auger recombination causes a further reduction in the limit to around 29.8%[5,6]. Slightly higher values can be produced by including phonon- or impurity-assisted sub-band-gap generation, or by multiple electron-hole pair creation by very high energy photons[3,7]. However, the limits mentioned above are sufficient for our current purposes. All of these calculations still assume perfect light trapping and no external reflection, idealisations that are in practice unachievable. Other loss mechanisms that must be present to some extent in any real cell are recombination through defects in the bulk and at the surfaces, and resistive effects.

The best 1-sun single-crystal FZ silicon cell made to date was a 24.7% efficient Passivated Emitter and Rear Locally diffused (PERL) device[8], which, considering the potential for other losses, is remarkably close to the Auger limit above. To illustrate their relative importance, the impact of these other avoidable loss mechanisms in a typical high-efficiency PERL cell are shown in Figure 2. The values in the chart are based on those published by Aberle *et al.*[7] for a PERL cell with a slightly lower efficiency of 22.9%. The fundamental mechanisms of Auger, radiative, thermalisation and infrared loss discussed above have been excluded to allow better presentation of those that can be reduced through improved

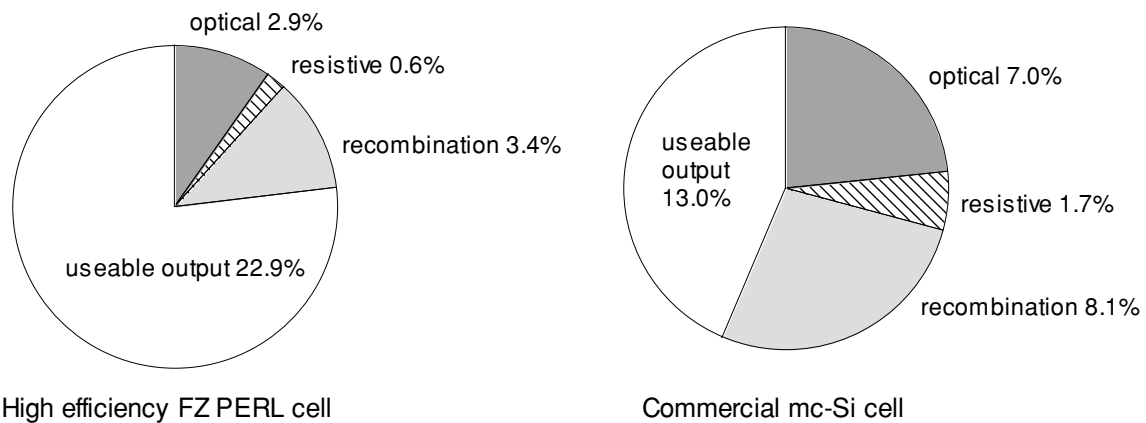


Figure 2. Relative impact of optical, resistive and recombination losses in high-efficiency PERL cells and standard commercial mc-Si cells at maximum power. In both cases only avoidable losses are depicted, hence the sum of the percentages in each chart is only 29.8%, the Auger efficiency limit.

processing and design. Therefore, the entire pie chart only represents 29.8% of the incident energy, consistent with the Auger limit quoted above.

The losses in the chart are broken into three broad categories, namely optical, resistive and recombination losses. In principle, these losses can be reduced indefinitely. Note that the optical section includes front surface reflection (from metal fingers and the anti-reflection coating (ARC)), absorption by the ARC and the rear reflecting surface, and escape of long wavelength light through the front surface (imperfect light-trapping). The resistive component includes bulk, emitter, contact and metal resistive losses. Finally, the recombination section also has a number of contributors, the significant ones being recombination in the bulk, the emitter, and at the front and rear surfaces. The results show that for this PERL cell resistive losses are minimal, while recombination and optical losses have approximately equal impact. No attempt has been made here to break these three major components into their respective parts, although that was partially done by Aberle *et al.* They showed that, at maximum power, approximately half of the recombination losses occurred in the base. The other recombination losses were split between the rear and front surfaces, with the rear probably having the greater impact of the two. Recombination in the emitter region was negligible in this cell. The chart for the PERL cell in Figure 2 serves as a useful ‘baseline’ for comparison with less efficient devices.

Figure 2 also shows a corresponding chart for a standard mc-Si cell produced commercially using screen-printed contacts on a heavily doped, homogeneous emitter with a TiO_x ARC and aluminium back-surface-field (BSF). The values are based on measurements of BPSolar cells, which are described in more detail in Chapter 4. The efficiency of 13% is typical for such cells[9]. Essentially, the optical losses can be easily modelled in PC-1D[10] using the known ARC properties and metal finger dimensions. The resistive losses are estimated from the

typical fill factor values, and the recombination losses assumed to make up the difference. As such the results are not exact, but they do serve as a useful comparison with the PERL cell. Also, it should be noted that it is not possible to simply state that by removing optical losses, the mc-Si cell efficiency would improve by 7% absolute, since the recombination and resistive dynamics would be altered also. Similarly, altering the recombination properties will induce changes in the resistive losses.

The results indicate that all three broad categories have increased their relative impact in the mc-Si cell in comparison to the PERL cell. The high optical losses are mostly a reflection of the fact that texturing is difficult to achieve on these substrates due to their random grain orientations. It is not surprising then that texturing of mc-Si has become a major focus of many researchers, with diverse approaches such as mechanical grooving[11], wet acidic etching[12,13], and reactive ion etching[14,15] currently being explored. The optical losses are further increased by absorption of long wavelength light at the rear Al-BSF, and by reflection from the screen-printed metal fingers, which typically cover about 10% of the front surface. By contrast, the PERL cell has inverted pyramid texturing on the front, better rear reflection, and a much lower front metal coverage due to the photolithographically defined and electroplated fingers. The relatively poor electrical performance of the screen-printed contacts also results in greater resistive losses in the mc-Si cells.

However, the major source of loss in these mc-Si cells is recombination, which produces a slightly more severe restriction on performance than optical losses. In fact, by completely eliminating recombination in such cells, the efficiency would improve to near 20%, although, as mentioned, resistive losses would then have more impact. Of course, it is impossible to achieve *zero* recombination in practice, especially considering that it may occur in many parts of the cell such as the bulk, at the surfaces, or within the heavily-doped emitter. Also, to maintain low costs it is necessary to use simple processes, which often lead to greater recombination. Nevertheless, it is clear from the chart that a better understanding of these recombination losses would be of great benefit in developing strategies to reduce their impact while maintaining process simplicity. It is in fact this analysis of recombination in mc-Si cells that forms the basic motivation and unifying theme for the work in this thesis. Optical and resistive losses are not considered in detail in this work, although, as mentioned, they are also important.

In a more general sense, this thesis also aims to develop and demonstrate techniques for studying recombination in semiconductors that can be applied to other types of solar cell, and even more broadly in microelectronics. Since the most relevant parameter for characterising recombination is the carrier lifetime, it is natural that such lifetime measurements and their interpretation play a central role in this thesis. Specifically, the Quasi-Steady-State Photoconductance (QSSPC) technique, a relatively recent and very versatile method for lifetime measurement, is used extensively. This technique is described in detail in Chapter 1, along with

other important concepts and tools that are heavily relied upon. Chapters 2 to 4 contain the core of the work regarding mc-Si, dealing with the areas of gettering, trapping and recombination respectively. Chapter 5 is more broadly focused in that it presents a new technique for characterising recombination centres in semiconductors, a development which arose out of the extensive use of lifetime measurements in the preceding chapters. The following section provides a brief outline of each of the five chapters.

Thesis outline

Chapter 1 is concerned with introducing the key techniques and concepts that are used in many places in the following chapters. In particular, the various recombination mechanisms that may be important in silicon solar cells are discussed from a physical point of view, including Auger, radiative and recombination through defects. Expressions for the injection-level dependence of the carrier lifetimes produced by each of these processes are introduced. These expressions are critical in later analysis of measured lifetimes. There are a number of ways in which these fundamental recombination mechanisms may be manifest in a cell, and these are discussed next, particularly defect recombination at surfaces and Auger recombination in heavily-doped regions. The way in which these mechanisms contribute together to produce an *effective* lifetime is also considered. In order to justify the almost exclusive focus on lifetimes, a brief account of their critical impact on cell performance is given, including the effect on open circuit voltage, short circuit current and fill factor. Following that, various lifetime measuring methods are discussed, with special attention paid to the QSSPC technique. The relative advantages of this and other commonly used methods are considered in some detail. Finally, some useful surface passivation recipes are presented.

Chapter 2 examines the effect of phosphorus gettering on the bulk lifetime of mc-Si. Cast mc-Si was found to respond best when the dislocation density was low, and the concentration of mobile impurities high. However, low resistivity wafers were found to suffer from a concurrent thermal degradation of the bulk lifetime during high temperature steps. It has previously been suggested that precipitate dissolution may be responsible for this reduction, but specifically designed gettering experiments indicated that this might not be true. Some circumstantial evidence for a decrease in the crystallographic quality provides an alternative explanation for the thermal degradation. Edge-defined Film-fed Growth (EFG) mc-Si was found to respond to phosphorus gettering to a small extent, while the remaining recombination centres could be passivated by atomic hydrogen, consistent with previous studies. Secondary Ion Mass Spectroscopy (SIMS) revealed that Cu might be responsible for the low initial lifetimes.

Chapter 3 focuses on trapping in mc-Si. This effect distorts recombination lifetime measurements, and as such is somewhat of a nuisance. Nevertheless, it appears to be very common in this type of material, and so is important to understand in order to try to make sense out of such lifetime measurements. A minority carrier trapping model developed in the 1950's is shown to provide a good explanation for the unusual injection-level dependence caused by the effect. The lack of impact that trapping has on device performance can also be explained in terms of this model. The physical origin of the trapping centres is examined, with evidence pointing to both dislocations and boron-impurity complexes. Finally, a recently proposed method for correcting trap-affected lifetime data is tested and found to provide a useful extension of the range of usable data.

Chapter 4 is in some ways the culmination of the previous chapters, bringing the conclusions and techniques together to allow an in depth analysis of the recombination mechanisms in mc-Si cells. High efficiency 1.5 Ω cm mc-Si PERL cells fabricated at ANU produced reasonable efficiencies, but were almost entirely dominated by bulk recombination. This was also true for Passivated Emitter and Rear Cells (PERC) cells made on 0.2 Ω cm mc-Si. The PERL cells were found to have reduced fill factors due to the injection-level dependence of the bulk lifetime, an effect which is shown to be even more pronounced if a cell is dominated by interstitial Fe. SIMS results on cast mc-Si revealed both Cr and Fe, but further evidence suggests that these are present almost exclusively as precipitates, not interstitially. Lifetime techniques were applied to the commercial mc-Si process used by BPSolar, indicating that the emitter is the source of the greatest recombination loss in these cells, followed by the bulk and the rear Al BSF.

Chapter 5, while still based firmly on recombination and lifetime measurements, is not focused on mc-Si. This chapter introduces a new technique for determining the capture cross-sections of impurities in semiconductors in general. In the previous chapters, it was recognised that accurate knowledge of these cross-sections allows powerful diagnostic tools to be developed. In general however, these cross-sections are not well known. Injection-level dependent lifetime measurements, being extremely sensitive to impurities, offer an excellent possibility for determining these cross-sections if samples with controlled impurity doses are used. Chapter 5 applies this new technique, dubbed Injection-level Dependent Lifetime Spectroscopy (IDLS), to the acceptor level of FeB pairs. The results are more accurate than comparable results from the widely used Deep Level Transient Spectroscopy (DLTS) technique. Other future applications of IDLS are discussed.

CHAPTER 1

Carrier Lifetimes in Crystalline Silicon

The most relevant parameter for characterising carrier recombination in semiconductors is the recombination lifetime, which, not surprisingly therefore, has powerful monitoring and predictive properties. As such, the measurement and interpretation of this lifetime forms the basis around which this thesis is built. This chapter introduces some key concepts and techniques related to recombination lifetimes that are used extensively throughout the remainder of the thesis.

The term ‘lifetime’ in connection with semiconductors has traditionally been subject to a number of ambiguities and nuances that are often implicit, and hence must be understood from the context in which the term is used[16]. Firstly, *recombination* and *generation* lifetimes must be differentiated, since they may differ by orders of magnitude in non-equilibrium conditions, which prevail in most problems of interest. For example, the generation lifetime in a deeply depleted space-charge region of a device will often be very different to the corresponding recombination lifetime, despite the fact that the same localised states are responsible for both processes. Such a distinction is critical in many microelectronic devices in which the generation lifetime determines leakage currents. It is not particularly relevant to solar cells however, since thermal generation through defects plays no significant role in their operation. However, other sub-definitions of the term lifetime do need to be clarified.

Minority carrier lifetime obviously applies only to minority carriers, and as such has no meaning in conditions other than low-injection. The term arose from the importance of the minority carrier lifetime in controlling the recombination rate in the low-injection conditions that prevail in many devices. However, silicon solar cells, particularly highly efficient ones, often operate under mid-injection, especially at open circuit conditions. When the excess carrier concentration approaches and surpasses the dopant density, the electron and hole lifetimes become nearly equal, and the relevant parameter can be referred to as the *recombination* lifetime. In this thesis, such lifetimes are measured over large ranges of carrier densities, from low-injection to high-injection conditions. Therefore the term minority carrier lifetime is avoided where possible and replaced with the more general *recombination lifetime*.

In practice, the total recombination lifetime is usually the result of a number of independent processes. This is referred to as the *effective* recombination lifetime, and may, for example, comprise mostly of Auger and Shockley-Read-Hall recombination lifetimes. The final important distinction for the purposes of this work is between *effective* lifetimes and *apparent* lifetimes. This latter term is used for cases where the measured quantity does not actually represent recombination, but is the result of a distortion caused by trapping effects. This distinction is utilised throughout the thesis due to the ubiquitous presence of trapping effects in mc-Si.

In general, the recombination *rate* U for a given process can be more intuitively defined than the recombination lifetime. For example, Auger recombination in lowly-injected p-type silicon requires an electron and two holes, hence the recombination rate U_{Auger} must be proportional to np^2 . Once the rate is determined, the recombination lifetime can then be calculated by:

$$\tau = \frac{\Delta n}{U} \quad (1.1)$$

where $\Delta n = \Delta p$ is the excess carrier density when there is no trapping present.

The next section introduces specific expressions for the various recombination mechanisms that are important in crystalline silicon solar cells. Emphasis is given to *p*-type material, in keeping with the large majority of the samples studied in this work. Following that, the effective lifetime arising from these processes is discussed. The impact of these processes on cell performance is then considered, followed by a description of some techniques of lifetime measurement, particularly those used extensively in this thesis. Finally, the important issue of surface passivation and the various methods for achieving it are discussed.

1.1 Carrier recombination mechanisms

There are three fundamental recombination mechanisms in semiconductors which are necessarily present to some extent in any sample: radiative, Auger and multi-phonon recombination[17]. These mechanisms differ in the way the excess carrier energy is dispersed, being mediated by photons, electrons and phonons respectively. This section discusses the relative importance of these processes in crystalline silicon and their relevance to solar cells.

All three mechanisms can occur either from band-edge to band-edge, or via an intermediate level in the band-gap[17]. However, when recombination occurs from band to band, it occurs principally through the radiative and Auger processes. Multi-phonon processes are extremely unlikely in such cases, since many phonons (possibly as many as 20 at room temperature in silicon) need to be coordinated almost simultaneously. In addition, both carriers are free, and hence are not strongly coupled to the lattice, resulting in diminished possibilities for phonon emission. In contrast, recombination through intermediate levels is almost exclusively dominated by multi-phonon emission. In such cases a large number of phonons are still required, but, critically, one of the levels is a *localised* state that is strongly coupled to the lattice.

Multi-phonon recombination through intermediate levels is more commonly known as Shockley-Read-Hall (SRH) recombination after those who originally modelled its effect[18,19], although their model only applies to certain restrictive cases. This defect-mediated process is not ‘intrinsic’ in the sense that it requires the presence of localised levels within the band-gap, and hence can, in principle, be removed by producing a silicon crystal of perfect purity and structure. Nevertheless, it is very often the dominant process in solar grade silicon today.

SRH recombination can occur either as a result of surface states, which are typically caused by dangling bonds, or through bulk defects or impurities. These two cases are treated separately below. Grain boundaries in mc-Si can in some sense be thought of as internal ‘surfaces’, although the physical origin of the localised states there may be quite different to those at an external surface. Also, a second important manifestation of Auger recombination in solar cells, namely recombination in the heavily doped emitter regions, is discussed.

1.1.1 Radiative recombination

Radiative recombination is simply the process of optical absorption, which is the source of carrier generation in a solar cell, occurring in reverse. Consequently, it involves the emission of a photon with energy approximately equal to that of the band-gap, since thermalisation

ensures that any initial excess carrier energy is lost well before radiative recombination can occur. Of course, these emitted photons may be absorbed again before they escape from the crystal, a process that tends to reduce the overall impact of radiative carrier loss. However, such relatively low-energy photons are only weakly absorbed, and hence they are only ‘recycled’ to a significant extent if there is excellent light-trapping present.

The radiative recombination rate U_{rad} depends jointly on both the electron and hole concentrations, since one of each is required for the process to occur[20]. In p -type material this gives rise to the following expression:

$$U_{\text{rad}} = B\Delta n(N_A + \Delta n) \quad (1.2)$$

where B is a constant and the equilibrium electron concentration has been neglected. Hence, from Equation 1.1 the radiative recombination lifetime τ_{rad} is given by:

$$\tau_{\text{rad}} = \frac{1}{B(N_A + \Delta n)} \quad (1.3)$$

Radiative recombination is typically the dominant recombination process in direct semiconductors such as GaAs, and forms the basis for the operation of light emitting diodes in such materials. In indirect semiconductors such as silicon, the requirement for simultaneous photon *and* phonon emission (or absorption), in order to conserve both momentum and energy, makes such processes inherently less probable. Hence B has a small value of $1.0 \times 10^{-14} \text{ cm}^3 \text{ s}^{-1}$ for silicon[21].

In general, at least one other recombination mechanism will be dominant over radiative processes at any given injection-level in silicon wafers. This is illustrated in Figure 1.1, which shows the radiative lifetime as a function of excess carrier concentration Δn in comparison to Auger and Shockley-Read Hall (SRH) recombination lifetimes for $1\Omega\text{cm}$ p -type silicon, a typical resistivity for solar cells. The SRH curve depends strongly on the defect properties, as described below, but the one shown in the figure is quite typical. The figure shows that SRH recombination tends to dominate at low carrier concentrations, while Auger out-competes radiative recombination at higher values of Δn . For more lightly doped samples, radiative recombination can ‘overtake’ the Auger process in low-injection, but in these cases SRH recombination is usually completely dominant. For more heavily doped wafers, Auger alone significantly outweighs radiative recombination at all injection-levels. The general conclusion is that radiative recombination can usually be safely ignored in the analysis of measured recombination lifetimes in silicon solar cells.

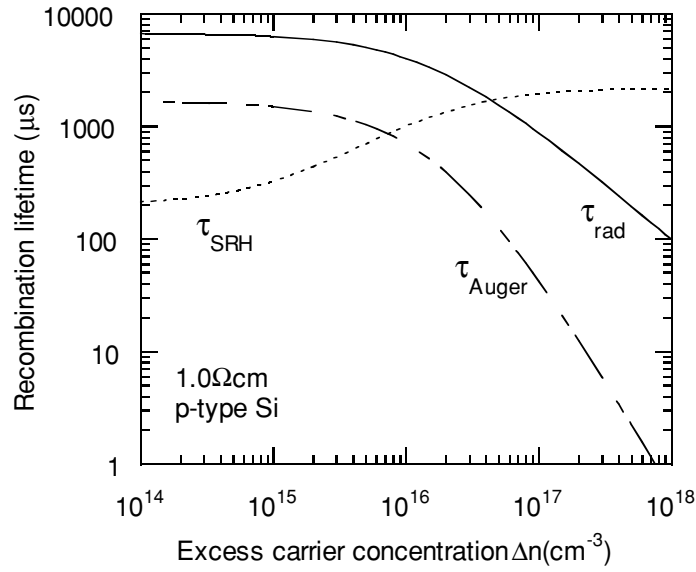


Figure 1.1. Radiative, Auger and SRH recombination lifetimes for 1Ωcm p-type silicon. The radiative and Auger curves are intrinsic, whereas the SRH curve is one of many possibilities for this material.

1.1.2 Auger recombination

Auger recombination occurs when the energy released by the recombination of an electron-hole pair is carried off by a third free carrier, and as such it is the reverse of impact ionisation, a common phenomenon in many microelectronic devices. In lowly-injected p-type silicon, the third carrier is most likely to be a hole, and the corresponding recombination rate U_{Auger} is given by[22]:

$$U_{\text{Auger}} = C_p \Delta n N_A^2 \quad (1.4)$$

where $C_p = 9.9 \times 10^{-32} \text{cm}^6 \text{s}^{-1}$ [23] is the low-injection Auger coefficient for p-type silicon. A similar expression holds for n-type silicon where $C_n = 2.8 \times 10^{-31} \text{cm}^6 \text{s}^{-1}$ [23]. The low-injection Auger lifetime then for p-type silicon is:

$$\tau_{\text{Auger}} = \frac{1}{C_p N_A^2} \quad \text{Low-injection} \quad (1.5)$$

Under high-injection conditions both carrier types are available to act as the third carrier, and the relevant expression is:

$$\tau_{\text{Auger}} = \frac{1}{C_a \Delta n^2} \quad \text{High-injection} \quad (1.6)$$

where $C_a = 1.66 \times 10^{-30} \text{ cm}^{-6} \text{ s}^{-1}$ [24] is the so-called *ambipolar* Auger co-efficient. As discussed in detail by Altermatt *et al.* [22], non-interacting free particles should result in C_a being equal to the sum of C_n and C_p . However, this is not observed in reality. Hangleiter and Hacker [25] argued that this could well be due to excitonic effects that result in increased Auger recombination rates at lower injection-levels, a phenomenon which has become known as Coulomb-enhanced Auger recombination. The effect largely disappears at high carrier concentrations ($> 1 \times 10^{18} \text{ cm}^{-3}$) due to charge screening, which prevents exciton formation.

Altermatt *et al.* provided a parameterisation of the carrier density dependence of the Coulomb-enhanced coefficients C_n and C_p by multiplying them by ‘enhancement factors’ g_{eeh} and g_{ehh} . Expressions for the carrier density dependence of the enhancement factors can be found in reference [22]. Glunz *et al.* then extended the parameterisation to allow the Coulomb-enhanced Auger lifetime to be calculated as a function of injection-level [26]. In their model the modified Auger coefficients C_n^* and C_p^* are functions of the enhancement factors, the dopant density and the low-injection and ambipolar Auger coefficients.

The final result is that the Auger lifetime can be accurately characterised at any injection-level of interest and for any likely dopant density, a significant improvement on what was possible only several years ago. In this thesis, this extension due to Glunz is used, based on Altermatt’s parameterisation of the enhancement factors, in conjunction with Dziewior and Schmid’s [23] C_n and C_p values, and Sinton and Swanson’s [24] value of C_a . A similar extension to all injection levels has recently been suggested by Altermatt *et al.* [27] that involves evaluating the enhancement factors at the total free carrier density for intermediate injection.

Like radiative recombination, Auger processes are intrinsic, meaning that their presence does not depend on the specific techniques used for silicon crystal growth (apart from the impact of the dopant density on their low-injection magnitudes of course), and are in this sense unavoidable. Unlike radiative losses however, they often contribute significantly to, or even dominate, the overall effective lifetime in silicon, particularly at high carrier densities. At lower carrier densities, in all but the best material with the best surface passivation, the lifetime is usually dominated by recombination through defects, as discussed in the next section.

1.1.3 Recombination through defects

Blakemore [17] develops the case of recombination through an arbitrary concentration of recombination centres N in a non-degenerate semiconductor sample with no significant drift or diffusion currents (that is, no electric fields or non-uniform carrier densities), under general illumination conditions (from true steady-state through to transient decay). It should be noted that these recombination centres can act also as traps (or even solely as traps), in which a carrier

is captured and subsequently injected back into the band from which it came. Although not contributing directly to recombination, trapping, by changing the free carrier concentrations, can nevertheless impact heavily on the overall carrier dynamics. The result is a pair of coupled (meaning the variables of interest are defined in terms of one another), first order differential equations in Δn and Δp for the electron and hole lifetimes τ_n and τ_p (these quantities need not be equal in this general case):

$$g_e - \frac{d\Delta n}{dt} = \frac{\Delta n}{\tau_n} = \frac{1}{\tau_{n0}} \left[\frac{(n_0 + n_1 + \Delta n)(\Delta n - \Delta p)}{N} + \frac{\Delta n n_1}{n_0 + n_1} \right] \quad (1.7)$$

$$g_e - \frac{d\Delta p}{dt} = \frac{\Delta p}{\tau_p} = \frac{1}{\tau_{p0}} \left[\frac{(p_0 + p_1 + \Delta p)(\Delta p - \Delta n)}{N} + \frac{\Delta p p_1}{p_0 + p_1} \right] \quad (1.8)$$

Here, g_e is the generation rate arising from external illumination and n_0 and p_0 are the electron and hole concentrations in thermal equilibrium (hence one will be given by the dopant density and the other by N_{dop}/n_i^2). τ_{n0} and τ_{p0} are sometimes known as the fundamental electron and hole lifetimes, and are related to the carrier thermal velocity v_{th} , the recombination centre density N and the capture cross-sections σ_n and σ_p of the specific centre in question:

$$\tau_{p0} = \frac{1}{N v_{\text{th}} \sigma_p} \quad \tau_{n0} = \frac{1}{N v_{\text{th}} \sigma_n} \quad (1.9)$$

The statistical factors n_1 and p_1 are the electron and hole densities when the Fermi level coincides with the recombination centre energy E_T :

$$n_1 = N_C \exp\left(\frac{E_T - E_C}{kT}\right) \quad p_1 = N_V \exp\left(\frac{E_C - E_G - E_T}{kT}\right) \quad (1.10)$$

where N_C and N_V are the effective densities of states at the conduction and valence band edges, and E_C and E_G the conduction band and band-gap energies.

The more concise equations on the left of Equations 1.7 and 1.8 deserve special note. These expressions define the carrier lifetimes in terms of the carrier densities and the generation rate, which may be a function of time, as mentioned above. As such, the lifetime defined in this way is valid for arbitrary illumination conditions, a feature that is later utilised in section 1.4.2 in the analysis of the quasi-steady-state photoconductance (QSSPC) technique for measuring lifetimes. With regard to the full equations, the aim here is to solve them for τ_n and τ_p in terms of either Δn or Δp (the remaining one being defined in terms of the other).

For the transient case, the strongly coupled Equations 1.7 and 1.8 can *not* be solved analytically, except in very specialised cases. As noted by Blakemore, the coupled nature of the

expressions largely arises because, in general, centres can act as both recombination sites and traps. If one type of carrier is trapped to any extent, the other type will necessarily be affected due to having less free carriers to interact with, and also because of the altered occupation rates of the recombination centres. Fortunately, under steady-state conditions, when the time derivative terms are zero, there do exist general analytic solutions for τ_n and τ_p . In this case, solving the simultaneous equations 1.7 and 1.8 results in cubic expressions for Δn and Δp . Taking the single positive real root of each of these equations produces the desired expressions for τ_n and τ_p . However, as Blakemore euphemistically states, they are far from being compact, and are not repeated here.

In samples where the recombination centre density N is relatively large, these full expressions should be used. However, if N is small compared to Δn , Δp and the dopant density, the long expressions reduce to those of the standard Shockley-Read-Hall model. A more direct route to the SRH equation from the general continuity equations 1.7 and 1.8 is to assume steady-state conditions and eliminate N by cross-substitution. Upon use of the identities $n_0/(n_0+n_1)=p_1/(p_0+p_1)$ and $p_1n_1=p_0n_0$ the following expression results:

$$g_e = \frac{\Delta n}{\tau_n} = \frac{\Delta p}{\tau_p} = \frac{\Delta n p_0 + \Delta p n_0 + \Delta n \Delta p}{\tau_{n0}(p_0 + p_1 + \Delta p) + \tau_{p0}(n_0 + n_1 + \Delta n)} \quad (1.11)$$

In the SRH model, N is small, meaning that trapping of carriers by the centres is negligible in comparison to the excess densities, and hence $\Delta n = \Delta p$. This leads to the standard SRH equation for the recombination lifetime $\tau_{SRH} = \tau_n = \tau_p$:

$$\tau_{SRH} = \frac{\tau_{n0}(p_0 + p_1 + \Delta n) + \tau_{p0}(n_0 + n_1 + \Delta n)}{n_0 + p_0 + \Delta n} \quad (1.12)$$

Although derived under steady-state assumptions here, it is possible to show that this expression is also valid for transient conditions. Equation 1.12 further reduces for p -type silicon, to:

$$\tau_{SRH} = \frac{\tau_{n0}(N_A + p_1 + \Delta n) + \tau_{p0}(n_1 + \Delta n)}{N_A + \Delta n} \quad (1.13)$$

This expression shows that the SRH lifetime is in general a function of the excess carrier concentration. Equation 1.13 is used to model defect-related injection-level dependent lifetime measurements in crystalline silicon wafers in several parts of this thesis.

Equation 1.13 can be further simplified in the cases of very low- and high-injection, and although these limiting cases are not generally directly applicable to lifetime measurements in regions of interest for solar cells, they are nevertheless instructive. In the special case of deep

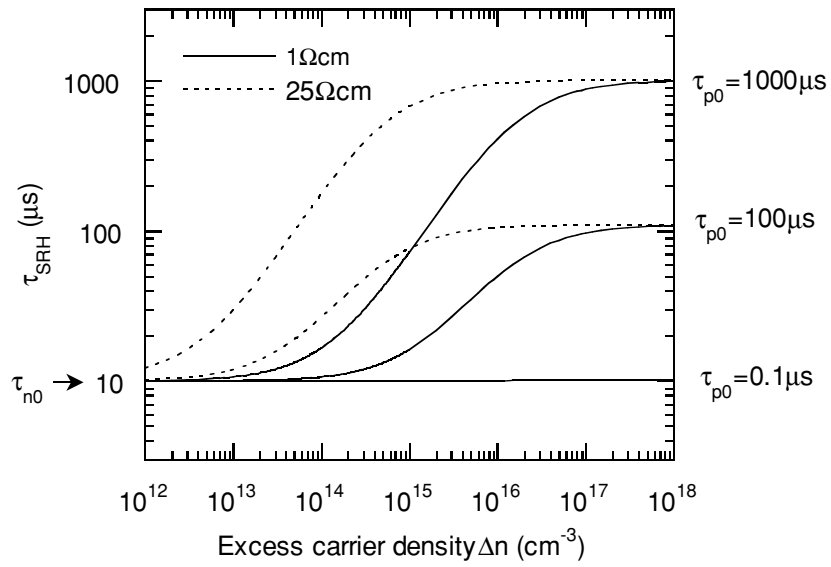


Figure 1.2. SRH recombination lifetimes for two different resistivities and different values of τ_{p0} .

centres (meaning that the energy level of the centre is near mid-gap), both n_1 and p_1 are much smaller than N_A and Δn , and the expression simplifies to:

$$\tau_{SRH} = \tau_{n0} \quad \text{deep centre, low-injection} \quad (1.14)$$

$$\tau_{SRH} = \tau_{n0} + \tau_{p0} \quad \text{deep centre, high-injection} \quad (1.15)$$

Since the characteristic lifetimes τ_{n0} and τ_{p0} essentially reflect the values of the capture cross-sections, it follows that deep centres with $\sigma_n \gg \sigma_p$ will result in the strongest injection-level dependence. This is revealed in Figure 1.2, which shows the SRH lifetime as a function of excess carrier density for several values of the characteristic lifetimes and dopant density. Another important feature is that the region of strong injection-level dependence is centred near the dopant density, which also happens to be the region that many solar cells (around 1 Ωcm) operate in. For states that can not be considered deep, the high- and low-injection limits are different, as discussed in detail in Chapter 5.

1.1.4 Surface recombination

Surface recombination is a special case of SRH recombination in which the localised states occur at the surface. Unlike bulk SRH centres however, these states do not usually occupy a single energy level, but rather form a set of states distributed across the band-gap. Surface recombination analysis is performed in terms of surface recombination velocities (SRV) instead of lifetimes, however, the principles are identical to bulk SRH recombination. A detailed

description of the analysis of the general case in which the SRV's have arbitrary magnitude and may be injection-level dependent can be found in Aberle[28]. In the simpler case of a sample with a constant bulk lifetime τ_b and a *small* constant SRV S that is the same on each surface, the effective lifetime is:

$$\frac{1}{\tau_{eff}} = \frac{1}{\tau_b} + \frac{2S}{W}. \quad (1.16)$$

The requirement that S be small arises from the assumption that the surface recombination rate is not limited by the diffusion of carriers to the surfaces. The accuracy of this expression for various sample thicknesses and values of S has been discussed by Sproul for carrier *decay* mode[29]. In general in this thesis we are concerned with *steady-state* conditions, but in many cases the region of validity of Equation 1.16 will be similar for the two. In the extreme case of infinite surface recombination velocity, the effective lifetime will be dominated by the transit time of carriers to the surfaces, provided the bulk lifetime is not very small. Under steady-state conditions with a uniform generation profile, the effective lifetime in this case is given by[30]:

$$\frac{1}{\tau_{eff}} = \frac{1}{\tau_b} + \frac{12D}{W^2} \quad (1.17)$$

where D is the carrier diffusivity. In low-injection conditions, the value of D for the minority carriers should be used, while in high-injection an ambipolar diffusivity is appropriate. Note that this expression is slightly different to that corresponding to transient decay mode, for which the second term on the right is $\pi^2 D/W^2$ [28]. This amounts to a 22% higher effective lifetime measured in decay mode for a sample with a long bulk lifetime. For lower bulk lifetimes, the difference is reduced. The discrepancy arises because carriers near the surface recombine quickly in decay mode, leaving those further away to diffuse to the surfaces, whereas in steady-state conditions carriers are constantly being generated near the surfaces, allowing their short lifetime to be incorporated throughout the entire measurement. It should be noted that neither lifetime is more 'correct' than the other from a fundamental viewpoint. However, it is definitely true that the steady-state result is more applicable to solar cells, which, of course, operate under steady-state illumination.

Equation 1.17 is used in Chapter 2 to estimate bulk lifetimes in samples with very high surface recombination velocities and low bulk lifetimes. Infrared illumination is used to ensure that the generation rate is uniform, a critical assumption in deriving the expression.

1.1.5 Emitter recombination

Another important source of carrier loss in silicon solar cells is recombination within the heavily doped emitter region. Such effects are difficult to model from a fundamental approach for a number of reasons. Usually the semiconductor is degenerate in this region, and the effects of band-gap narrowing, free carrier absorption, and the presence of dead layers and diffusion-related SRH defects (such as silicon interstitials), need to be considered. As a further complication, all of these effects in turn vary strongly as the dopant density changes with depth. Essentially however, the high recombination rates in this region are caused by Auger processes, and are exacerbated by the large number of minority carriers generated there by strongly absorbed high-energy photons. Furthermore, recombination at the emitter surface is typically lumped in with these effects also. Hence the quality of any emitter surface passivation can have a significant impact on the total recombination attributed to the emitter region.

Fortunately, it is possible from an empirical point of view to characterise total emitter recombination in terms of a single parameter, the emitter saturation current density J_{0e} . As alluded to above, this parameter incorporates recombination at the emitter surface as well as within the emitter bulk. It is possible to accurately and simply include surface effects since, in practice, the emitter is always in very low-injection (at least for non-concentrating cells), and consequently any SRH recombination at the surface will be injection-level independent, and will simply scale the parameter J_{0e} .

The effective recombination lifetime due to the emitter can be written as[31,32]:

$$\tau_{emitter} = \frac{qn_i^2 W}{J_{0e} (N_A + \Delta n)} \quad (1.18)$$

In low-injection (with respect to the base), this lifetime is injection-level independent, whereas under high-injection conditions, it decreases linearly with the excess carrier density. This provides the basis for a well known method of measuring J_{0e} values due to Kane and Swanson[31], whereby the slope of the high-injection lifetime determines J_{0e} . For accurate measurement, it is best to use lightly doped samples, since they provide the greatest injection-level range of data dominated by the emitter (see for example Figure 1.3). For more heavily doped samples, the linear region of interest overlaps with Auger recombination, making determination of J_{0e} less certain. With careful subtraction of the Auger components however, it is still possible to achieve such measurements.

Values for J_{0e} vary significantly, depending on the diffusion profile and the passivation quality. The lowest values achievable in practice are for ‘annealed’ thermally oxidised light phosphorus diffusions ($\sim 400 \Omega/\square$), which can be as low as 5 fAcm^{-2} , as shown by Kerr *et al.*[33]

in a recent study which updated the results of the original work performed King *et al.*[34]. At the other extreme, high J_{0e} values of around 3000 fAcm^{-2} also occur with light emitters, but when the surface is unpassivated (either bare or metallised)[28,35]. These values correspond to open circuit voltage caps (see section 1.3.1) of about 760mV (passivated) and 600mV (unpassivated)[33]. For more heavily doped emitters, the increased field-effect passivation reduces the importance of the surface. In fact, for phosphorus sheet resistances below around $20 \Omega/\square$, the emitter is completely ‘opaque’, and the J_{0e} value is insensitive to the surface conditions. Typical laboratory solar cells have emitters in the $100\text{-}200 \Omega/\square$ range, for which passivation is very important. Commercial solar cell emitters are generally in the $40\text{-}70 \Omega/\square$ range (except for structures with selective emitters such as buried-contact cells). The benefits of passivation in such cases are therefore reduced, but may still be significant.

1.2 The effective lifetime

In most practical cases two or more of the bulk recombination mechanisms described above may be important in a given sample at a given injection-level. For independent processes, the net recombination rate is the sum of the individual rates, resulting in an *effective* lifetime τ_{eff} . For example, when comprised of SRH, Auger and emitter recombination, τ_{eff} is given by:

$$\frac{1}{\tau_{\text{eff}}} = \frac{1}{\tau_{\text{SRH}}} + \frac{1}{\tau_{\text{Auger}}} + \frac{1}{\tau_{\text{emitter}}} \quad (1.19)$$

Typically, the different injection-level dependence of these mechanisms result in the effective lifetime having segments that are dominated by different processes. This is illustrated in Figure 1.3 for a substrate with $N_A = 1 \times 10^{14} \text{ cm}^{-3}$, an emitter characterised by a saturation current density of $2 \times 10^{-14} \text{ Acm}^{-2}$ (20 fAcm^{-2}) and a deep SRH centre with $\tau_{n0} = 1 \text{ ms}$ and $\tau_{p0} = 1 \text{ s}$. Such SRH parameters are very difficult to achieve in practice, but they serve as a useful example here. In low-injection, the sample is dominated by SRH recombination, while at intermediate to high-injection, emitter recombination takes over. It is this region which can be used to determine the value of J_{0e} using the method of Kane and Swanson described above. At the highest injection-levels, Auger recombination is the most important process. Such effective lifetime modelling is used in various parts of this thesis, and is an invaluable tool in analysing and identifying recombination processes in specific samples. The critical importance of these lifetimes in solar cell operation is discussed next.

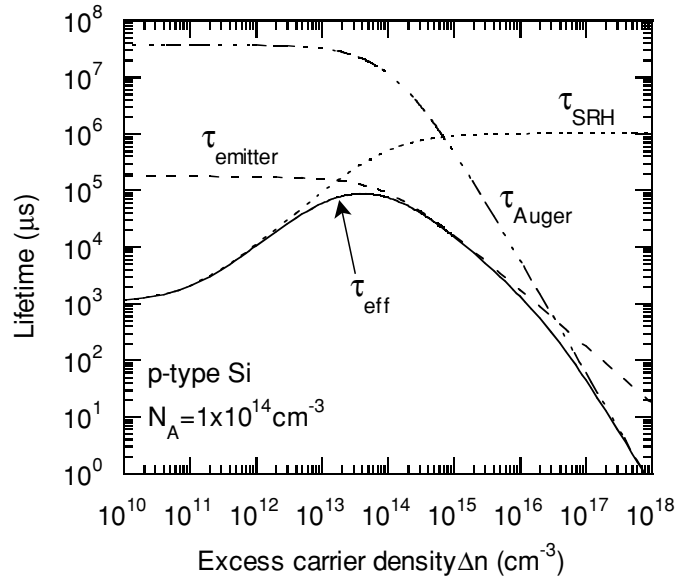


Figure 1.3. Effective lifetime made up of SRH, emitter and Auger terms. Each of these mechanisms dominates in turn as the excess carrier density increases.

1.3 Impact of lifetime on solar cell parameters

This section examines the specific impact of lifetimes on the three main performance parameters of a solar cell, namely: the open circuit voltage, short circuit current, and the fill factor (or equivalently, the ideality factor). The short circuit current is discussed only briefly since it is strongly influenced by the optical properties of a cell, which are of course crucially important, but, nevertheless, beyond the scope of this thesis. The open circuit voltage of a cell is much more critically dependent on the recombination dynamics within it, as is the fill factor, provided any parasitic effects caused by series and shunt resistances are not overwhelming.

1.3.1 Open circuit voltage

The open circuit voltage of a solar cell is determined by the product of the free carrier densities at the edge of the space-charge region in the base:

$$V_{oc} = \frac{kT}{q} \ln \left(\frac{\Delta n (N_A + \Delta n)}{n_i^2} \right) \quad (1.20)$$

where $n_i = 8.63 \times 10^9 \text{ cm}^{-3}$ is the intrinsic carrier concentration in silicon at 25°C [36]. Due to the direct relationship between Δn and τ_{eff} (Equation 1.1), it is obvious that the voltage is in turn dependent on the lifetime. Note that the logarithmic nature of the relation means that an increase

in the lifetime by an order of magnitude results in a voltage increase of about 60mV for a cell operating in low-injection at 25°C.

Equation 1.20 is used in several ways throughout this thesis. Firstly, it allows a lifetime value to be converted into an implied voltage, which is a more intuitive figure of merit for a wafer, since lifetimes themselves are generally strongly resistivity dependent. In fact, the value of Δn itself is directly measured at each illumination level during a photoconductance-based lifetime measurement, and this can be converted into an illumination- V_{OC} plot[30]. These implied curves can be compared with measured illumination- V_{OC} curves of finished cells, providing useful information on the source of non-idealities and revealing the presence of shunts, Schottky barriers and series resistance effects[37].

Secondly, the relationship between carrier densities and the V_{OC} in Equation 1.20 can be exploited to infer the effective lifetime of a substrate upon measurement of the V_{OC} . This is the basis of the QSS- V_{OC} technique for measuring lifetimes discussed in section 1.4.3. It is a very useful procedure when photoconductance lifetime measurements are not possible due to the presence of metal fingers or sheets, or, of particular relevance for mc-Si, if ‘trapping’ of minority carriers occurs in the injection range of interest.

Such calculations must be made with caution however, since Equation 1.20 refers to the carrier concentration at the junction edge. If a sample has a diffusion length considerably shorter than the substrate thickness, then non-uniform carrier profiles will result under white light illumination. The value of Δn measured in photoconductance-based techniques is the *average* excess carrier density in the base, which may be significantly lower than that at the junction edge in such cases. For such samples, infrared illumination will provide much more uniform profiles. An alternative although less accurate approach is to replace the sample width in Equation 1.20 with the carrier diffusion length[30].

1.3.2 Short circuit current

The short circuit current density J_{SC} of a solar cell is determined by the number of minority carriers (whether generated in the base or the emitter) that diffuse to the junction edge before recombining. Since the base is typically much thicker than the emitter, the majority of photons are absorbed in the base, despite the stronger absorption of white light near the front surface. In the simple case of long-base cells with an injection-level independent lifetime (and hence constant diffusion length), and ignoring contributions from the emitter, the one-dimensional diffusion equation can be solved in conjunction with the relevant continuity equation to give:

$$J_{sc} = qg_e L_e \quad (1.21)$$

where g_e is the uniform generation rate in the base and L_e the electron diffusion length (for p -type bases). In such cases then the short circuit current is proportional to the square root of the minority carrier lifetime in the base (we may refer to the minority carrier lifetime since in short circuit conditions the base is in low-injection).

Analytic expressions are also obtainable for short base cells with a constant surface recombination velocity at the rear surface, and also for certain non-uniform generation profiles. In more complex cases where the diffusion length and/or the rear surface recombination velocity is dependent on the local carrier density, the diffusion equation can be solved numerically, as is done in packages such as PC-1D[10]. This approach is used in Chapter 4 for modelling the short circuit current of cells dominated by recombination through interstitial Fe. A general trend is that as the diffusion length increases well above the cell thickness, the obtainable short circuit current saturates, as the vast majority of the carriers generated in the base will eventually diffuse to the junction. At that point further current gains can only be achieved by altering a cell's optical properties, or by refining the emitter. By contrast, the open circuit voltage continues to increase logarithmically with increasing lifetime in the base, since it is determined by the *density* of excess carriers there.

1.3.3 Ideality factor and fill factor

The fill factor is a dimensionless ratio, and in this sense it is a relative quantity. It does not reflect the magnitudes of the maximum power voltage and currents, but merely how they compare with their open circuit and short circuit counterparts. Therefore, in the absence of parasitic shunt and series resistances, the fill factor reveals how the voltage changes from open-circuit to maximum power in comparison to the 'ideal' case. In this ideal case the lifetime is assumed constant at all voltages, or in other words, injection-level independent. If the lifetime changes with injection-level, the carrier densities will depart from the ideal case, and an altered fill factor will result.

These considerations are commonly dealt with in terms of ideality factors. The local ideality factor n_{loc} is given by the slope of the illumination- V_{OC} graph, in which the illumination axis is plotted logarithmically. An illumination- V_{OC} plot is chosen instead of a photovoltaic I-V curve or J_{sc} - V_{OC} plot in order to avoid series resistance effects in the former and any non-linearity in the short circuit current in the latter. The local ideality factor is then given by:

Recombination process	Low-injection limit		High-injection limit	
	lifetime τ	ideality n	lifetime τ	ideality n
Radiative	constant	1	$\propto \Delta n^{-1}$	1
Auger	constant	1	$\propto \Delta n^{-2}$	2/3
Emitter	constant	1	$\propto \Delta n^{-1}$	1
SRH	constant	1	constant	2

Table 1.1. Low- and high-injection lifetime limits and ideality factors for various recombination mechanisms in silicon.

$$n_{loc} = \frac{q}{kT} \frac{dV_{OC}}{d(\ln I_{ll})} = \frac{q}{kT} \frac{dV_{OC}}{d\Delta n} \frac{d\Delta n}{dI_{ll}} I_{ll} \quad (1.22)$$

where I_{ll} is the illumination variable of arbitrary units, and the chain rule has been applied to obtain the right-hand expression. By taking the derivative of Equation 1.22 and noting that since $g_e \propto I_{ll}$ then $I_{ll} \propto \Delta n / \tau$, the following expression is obtained for n_{loc} :

$$n_{loc} = \frac{(N_A + 2\Delta n)}{(N_A + \Delta n) \left[1 - \frac{\Delta n}{\tau} \frac{d\tau}{d\Delta n} \right]} \quad (1.23)$$

This expression can be used to calculate ideality factors at any injection-level if the dependence of the lifetime on Δn is known. It becomes simplified under low- and high-injection limits, and the different idealities under these limits of specific recombination processes are listed in Table 1.1. The results indicate that, in the absence of parasitic effects and space-charge region recombination (which can produce a term with $1 \leq n \leq 2$ at low voltages[38-40]), any silicon solar cell should have ideality 1 at very low-injection levels. The validity of neglecting space-charge region recombination is discussed in detail in Chapter 4. At very high-injection, the ideality would reduce to 2/3 due to Auger recombination. Hence Auger dominated cells would actually have better fill factors than cells with ideality 1.

Figure 1.4 shows a modelled illumination- V_{OC} plot and the corresponding local ideality factors for 1 Ω cm p -type silicon with SRH recombination alone, and with the effects of emitter ($J_{0e} = 2 \times 10^{-14} \text{ A cm}^{-2}$) and Auger recombination added in turn. The SRH centre modelled has a very strong injection-level dependence, and is based on the parameters for interstitial Fe from Chapter 5. All three plots begin with ideality 1, as expected from Table 1.1. At high-injection they conform to the expected values from the table also. In the intermediate region, the ideality factor for the SRH only curve reaches very high values, almost 7. Such a curve is in a sense academic, since any real cell must have an emitter, and Auger recombination will always be present. Nevertheless, the curve illustrates the point that strong non-idealities can in principle occur through SRH recombination. When the other two processes are included, the intermediate

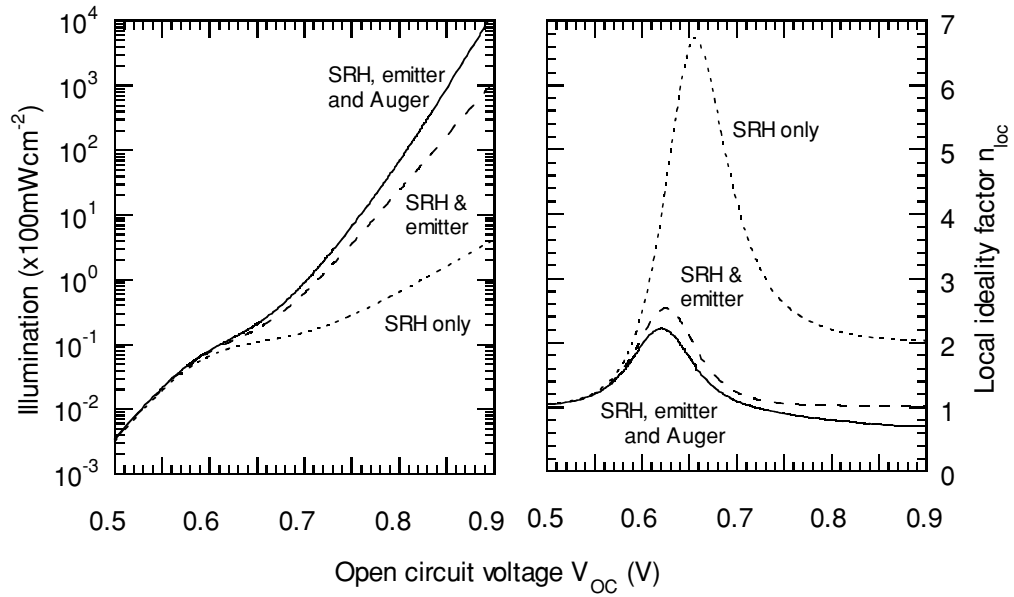


Figure 1.4. Modelled illumination- V_{OC} curves and the corresponding local ideality factors for $1\Omega\text{cm}$ p-type silicon with SRH only, SRH and emitter, and SRH, emitter and Auger recombination included.

ideality factor is reduced significantly, even for the low value of J_{0e} assumed, although it still has a peak above 2 in this case.

Such non-idealities at intermediate voltages caused by SRH recombination have been observed in the past in connection with recombination at oxide interface states[41-43], and more recently with boron-oxygen complexes in Czochralski silicon[44]. Chapter 4 discusses similar effects in high efficiency mc-Si cells, and links them with lifetime measurements dominated by bulk defects. A prerequisite to any such study, however, is a technique that allows accurate measurement of the recombination lifetime over a large range of excess carrier densities. These are discussed in the following section.

1.4 Lifetime measurement techniques

Due to the importance of the effective recombination lifetime in the performance of solar cells, and also in other microelectronic devices where the *generation* lifetime is often a critical parameter in controlling leakage currents, there have been many techniques developed over the decades with the objective of measuring lifetime[45]. This section provides a description of some of the methods most applicable to solar cells. Two techniques in particular, namely photoconductance decay (PCD) and the more recent quasi-steady-state photoconductance

method (QSSPC), are discussed in detail, due to their widespread use and special suitability to solar cell applications. Some other relevant voltage-based methods are also discussed briefly.

1.4.1 Transient photoconductance decay (PCD)

PCD involves the generation of excess carriers by a brief, sharp pulse of illumination that is rapidly turned off[45]. The resulting decay of carriers back to their equilibrium concentrations is monitored via the photoconductance, and the effective recombination lifetime calculated. In the absence of significant trapping, the excess carrier densities are equal, and the net excess conductance $\Delta\sigma$ will be given by:

$$\Delta\sigma = q\Delta n_{av}(\mu_n + \mu_p)W \quad (1.24)$$

where Δn_{av} is the average excess carrier density, μ_n and μ_p are the electron and hole mobilities and W the sample thickness. In conjunction with a carrier density dependent mobility model[46,47], this expression allows Δn_{av} to be calculated for each measured value of $\Delta\sigma$. The effective lifetime is then calculated by differentiating this time-dependent trace:

$$\tau_{eff} = -\frac{\Delta n_{av}}{d\Delta n_{av}/dt}. \quad (1.25)$$

There are currently two distinct variations of this technique in widespread use: microwave-detected PCD (μ W-PCD) and inductively-coupled PCD. The important difference between these methods arises from the way in which the excess carrier density, via the photoconductance, is detected.

In inductively-coupled PCD this is achieved via an inductive coil under the sample. Since the coil is calibrated over a large range of conductivities, the excess carrier density decay can be measured directly. By differentiating this trace, which may not be a pure exponential if the lifetime is injection-level dependent, a large number of lifetime values over a range of carrier densities is obtained. Figure 1.5 shows a typical inductively-coupled PCD trace with the corresponding lifetime versus excess carrier density curve in Figure 1.6. The particular apparatus at ANU (produced by Sinton Consulting) is excellent for samples with long lifetimes ($>100\mu s$) when used in PCD mode, but is less accurate for lower lifetimes due to the poor cut-off time of the flash-lamp. Such samples are best measured with the quasi-steady-state photoconductance (QSSPC) technique described in the next section.

The other widely used PCD method is μ W-PCD, in which the photoconductance is measured by means of the reflectivity of microwaves directed at the sample surface. Since this

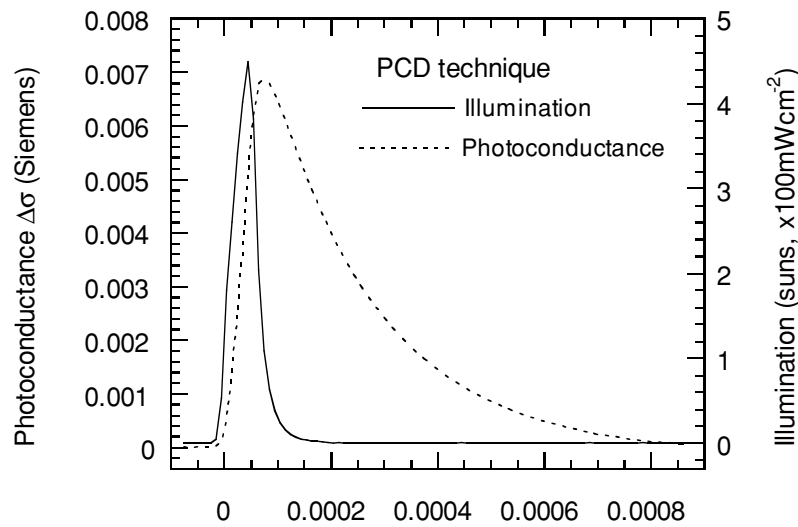


Figure 1.5. A typical inductively-coupled photoconductance decay (PCD) trace for a 0.3 Ωcm FZ wafer showing the sharp illumination peak and the ensuing carrier decay. The calculated effective lifetimes for this trace are shown in Figure 1.6.

reflectivity is a highly non-linear function of the free carrier density, this method is restricted to use as a small signal technique. This is no barrier to conducting low-injection lifetime measurements, but does cause a problem for higher carrier concentrations, which are the ones of interest in solar cells. This problem can be avoided by using a steady-state bias light to generate a background carrier density, upon which a small transient pulse is superimposed. Each bias-light setting will then result in one lifetime value, but the injection-level will remain unknown. However, in many cases it is critical that the measured lifetimes be reported at specific carrier densities, since the recombination lifetime is often injection-level dependent. Because the reflectivity signal contains no information about the absolute magnitude of the excess carrier density, the bias light must be calibrated so that the generation rate in the sample is known. Then, working back from the measured lifetime, the excess carrier concentration can be inferred, assuming no injection-level dependence of the lifetime! Hence, in order to perform accurate and reliable measurements at high carrier concentrations, a large number of measurements at lower concentrations are required to allow integration of the differential lifetimes in order to convert them into actual lifetimes[28,48-50].

As a result, inductively-coupled PCD measurements offer some very significant advantages over μW -PCD techniques. Firstly, the equipment is much less expensive and easier to maintain. Also, they provide accurate lifetime measurements over very large injection-level ranges in one quick flash, as opposed to many time-consuming individual traces taken at each bias-light setting necessary with μW -PCD. Most importantly, it is a large signal method, and as such an unambiguous measurement can be taken at any range of injection-levels without the need for previous measurements for integrating differential quantities. There is one potential

advantage of $\mu\text{W-PCD}$ however, and that is the ability to ‘map’ lifetimes with high resolution, down to a spot size of around 1mm. By comparison, the inductively-coupled version measures a region of several square centimetres. The point should be made however, that this feature may be a drawback in material like mc-Si where an area-averaged measurement will correlate better with cell performance.

One final point is that, unlike inductively-coupled PCD, $\mu\text{W-PCD}$ is not restricted to longer lifetimes, since the laser used for the small-signal pulse has a very rapid cut-off time. However, the next section describes a more general large-signal technique based on inductive-coupling that is valid over a very large range of lifetime values, while retaining the relative merits of inductively-coupled PCD over $\mu\text{W-PCD}$.

1.4.2 Quasi-steady-state photoconductance (QSSPC)

The inductively-coupled QSSPC technique was first suggested by Sinton and Cuevas in 1996[51]. It is essentially a steady-state method in which the effective lifetime is calculated via the expression

$$\tau = \frac{\Delta n_{av}}{g_e} \quad (1.26)$$

where g_e is the generation rate produced by the incident light. If the light source is held at a steady illumination, the sample will be in true steady-state, but will quickly suffer from heating and a changing lifetime. To avoid such heating, the incident light is slowly reduced to zero over several milliseconds. The decay is long enough however to ensure that the sample remains in steady-state in terms of recombination processes, except in cases of very long lifetimes as discussed below. The slowly decaying illumination also provides the added advantage of producing a large range of carrier densities, typically about one order of magnitude, over which the lifetime can be calculated.

The quantity Δn_{av} is determined at each point of the decay by Equation 1.24, as for PCD. However, the generation rate g_e is now required at each point also. It is determined by simultaneously measuring the intensity of the flash decay with a calibrated reference cell. The reference cell determines the flux of photons N_{ph} that generate electron-hole pairs in a sample in which all of the available photons are coupled into the wafer. Any real sample will only absorb a fraction f_{abs} of these available photons, the remainder being lost to reflection and transmission. The value of f_{abs} can be determined for a given sample by using charts for different thickness

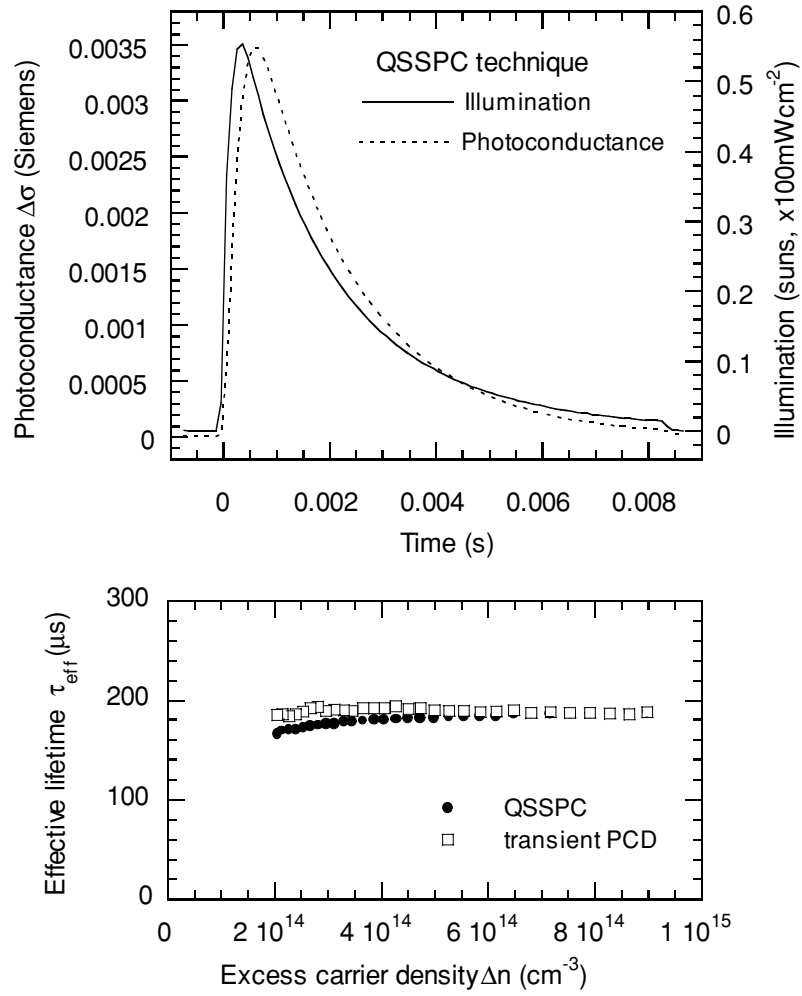


Figure 1.6. A typical quasi-steady-state photoconductance (QSSPC) trace for the same $0.3\Omega\text{cm}$ FZ wafer in Figure 1.5. The calculated effective lifetimes from both techniques are shown in the lower plot, and are in good agreement.

wafers with various oxides and other films present. Hence, the bulk generation rate in the wafer is:

$$g_e = \frac{N_{ph} f_{abs}}{W}. \quad (1.27)$$

Essentially then, the effective lifetime is proportional to the ratio of the photoconductance and the reference cell signal. Figure 1.6 shows a typical QSSPC trace and the corresponding lifetime versus excess carrier density curve. In contrast to inductively-coupled PCD, the QSSPC technique is well suited to *low* lifetime samples, since the carrier statistics are then closest to steady-state conditions during the flash. In long lifetime samples ($>100\mu\text{s}$ for our flash with a characteristic decay time of 2.3ms), the steady-state assumption begins to break down and the analysis becomes increasingly invalid.

Recently, Nagel *et al.*[52] pointed out that the two methods of ‘quasi-transient’ (PCD) and ‘quasi-steady-state’ are in fact limiting cases of a more general analysis method. They suggest replacing Equations 1.25 or 1.26 with the general expression:

$$\tau_{eff} = \frac{\Delta n_{av}}{g_e - \frac{d\Delta n_{av}}{dt}}. \quad (1.28)$$

This expression is identical to that in the continuity equations 1.7 and 1.8, and is valid for arbitrary generation conditions. Under true transient or steady-state conditions this expression reduces to Equation 1.25 or 1.26 respectively, as required. By using this generalised expression, the analysis of traces such as those in Figure 1.6 becomes valid even for long lifetime samples. As a result, the lifetimes shown in the lower plot of Figure 1.6, which were calculated using the generalised expression, reveal good agreement between the transient decay and quasi-steady-state signals. This analysis technique, in conjunction with the QSSPC apparatus, provides an excellent method for measuring a large range of actual (as opposed to differential) lifetimes (from around 0.1 μ s to several ms) over a large range of carrier densities (1×10^{12} to 1×10^{17} cm⁻³, depending on the lifetime). This method is adopted universally throughout this thesis.

1.4.3 Other techniques

There are many other techniques that have been developed for the purpose of measuring carrier lifetimes, and these have been comprehensively reviewed by Schröder[45]. Some relevant voltage-based techniques are briefly discussed here due to their suitability for solar cell applications.

The **Surface Photovoltage** (SPV) method has been used in many studies of impurities in silicon (for example Zoth and Bergholz[53]) and also for solar cell applications. It exploits the presence of a space-charge region induced by surface defects. When illuminated with weak light of varying wavelength, a photovoltage is created at the surface, the magnitude of which is related to the bulk diffusion length. The primary advantages of the technique are that no surface passivation treatment or junction formation is required, and the results are immune to trapping effects. It does however suffer from two major disadvantages that limit its usefulness in regard to solar cell applications. Firstly, the sample thickness must be much larger than the diffusion length, a requirement that is often not satisfied in crystalline silicon cells. Secondly, it is restricted to very low-injection measurements due to the delicate nature of the induced junction. The carrier densities probed are therefore far removed from those that prevail under normal cell

operating conditions, and may be different by orders of magnitude in samples with strong injection-level dependence.

Another common technique is **Open-Circuit Voltage Decay (OCVD)**. This method is similar to SPV in the sense that a voltage is measured from which the lifetime is inferred. Like SPV, it also possesses the advantage of being immune to trapping effects, which can plague photoconductance-based methods. However, since it uses a much more robust pn junction as opposed to an induced junction, a much larger range of carrier densities can be studied. This is achieved by applying a transient light pulse and monitoring the resulting voltage as it decays over a large range. The technique is, however, subject to junction capacitance effects, which can completely obscure the lifetime at low voltage[54].

An improvement on OCVD is the recently proposed **Quasi-Steady-State V_{OC} (QSS- V_{OC})** technique[37]. This is the equivalent of the QSSPC technique with respect to PCD. It has the advantages of OCVD, but due to being more steady-state in nature, is not affected as severely by junction capacitance. Specifically, if the flash lamp is arranged to decay much more slowly than the RC time constant of the junction capacitance, then the results will not be appreciably affected by the latter. This method is used in a number of occasions in the following chapters in situations where QSSPC was not applicable due to trapping effects or excessive conductance from metal fingers.

1.5 Surface passivation techniques

In many places throughout the thesis it is desirable to reduce the impact of surface recombination to the extent that the measured lifetimes, within experimental error, reflect only contributions from the bulk. In principle, this is not unduly difficult for mc-Si wafers, which tend to have lower bulk lifetimes than single-crystal float zone (FZ) samples of the same resistivity. There are therefore a number of potential passivation schemes that could perform adequately. However, there are some other difficulties associated with mc-Si wafers that need to be considered in choosing the most appropriate passivation method.

Firstly, mc-Si wafers are subject to significant changes in bulk lifetime when processed at high temperatures. If a high temperature process is to be used then, it should be relatively short and at temperatures which are not too high (say less than 900°C). This counts against dry oxidation, which requires long growth times at high temperatures to achieve reasonable thickness. Also, these oxides often have strongly injection-level dependent surface recombination velocities, even when forming gas annealed, which can complicate interpretation of effective lifetimes. The injection-level dependence is usually reduced by ‘annealing’, but this introduces other problems associated with bulk hydrogenation, as discussed below. Steam

oxides can be grown much more quickly at lower temperatures, but are significantly poorer in passivating quality, unless annealed, in which case they are subject to the same hydrogenation uncertainties. One final point is that the passivating properties of oxides may be somewhat dependent on the crystal orientation, an uncontrollable parameter when studying mc-Si, although in many cases the surface recombination velocities will still be low enough for practical purposes.

Another alternative is to deposit films of plasma-enhanced chemical vapour deposited (PECVD) SiN. These films have excellent passivating properties and are deposited at low temperature ($\sim 400^\circ\text{C}$)[55]. This makes them ideal for the purposes of Chapter 5, in which single-crystal FZ material deliberately contaminated with Fe requires a high quality, low temperature passivating scheme with no diffusions. However, when applied to mc-Si, PECVD nitride films can significantly increase the bulk lifetime due to hydrogenation of bulk defects[56,57]. Although this is of course desirable in terms of cell performance, such effects can obscure other changes in lifetime that may be the subject of an experiment. As shown in Chapter 2, annealing of oxides results in similar hydrogenation effects.

Other alternatives for mc-Si are chemical passivation by means of HF or iodine/ethanol solutions. HF can provide excellent passivation without any high temperature treatments[58], but poses a serious safety risk, and as such is not considered appropriate for routine use. Iodine in ethanol also apparently provides good passivation[49,59] on single-crystal samples. However, in attempts to implement its use on mc-Si samples we found that its effectiveness was critically dependent on the surface conditions, which were often quite rough (even after etching) and beyond our direct control. As a result, it was not possible to have the required degree of confidence in the lifetimes measured in this way.

Corona charging of dielectric layers represents another attractive option for passivating mc-Si wafer surfaces. By selecting the appropriate charge, the surfaces can be driven into strong depletion, resulting in very effective field-effect passivation[26,60]. It does however require the presence of an insulating film at the surfaces, which is typically a thermally grown oxide. For the reasons mentioned above, it is desirable to avoid such oxidations. Recently a new method proposed by Schmidt[61] made use of a layer of baked photoresist instead of an oxide layer. The resulting passivation was again excellent on polished single-crystal wafers whilst avoiding high temperature steps. Unfortunately, when we applied this method to mc-Si wafers, the passivation was found to be very unreliable. This is most likely due, again, to the surface roughness of mc-Si wafers.

Keeping all of these considerations in mind, the passivation scheme chosen as the standard throughout this thesis was a light phosphorus diffusion with a thin *in-situ* grown thermal oxide. The diffusion was performed at 840°C for 25 minutes, resulting in a sheet resistivity of $200\text{--}250\Omega/\square$. An oxide was then grown at 900°C for 20 minutes, giving an oxide

thickness of 15-20nm, followed by a 10 minute anneal in nitrogen. The wafers were then forming gas annealed (a process which does not cause significant bulk hydrogenation, as shown in Chapter 2) at 400°C for 25 minutes. Although not an ideal solution, since high temperatures are involved, this scheme provides high quality, reliable passivation with very little injection-level dependence around typical cell operating conditions. The temperatures are relatively low, and the oxide growth time is relatively short in comparison to plain oxidation, since oxide growth rates are faster on diffused surfaces. The presence of the diffusion also reduces the dependence of the passivation quality on crystal orientation. Finally, the gettering action of the light diffusion, which could potentially be a problem, is only slight, as shown in Chapter 2.

1.6 Summary

In general, the effective lifetime is a complicated parameter that may be made up of a number of distinct processes, all of which may have different magnitudes and injection-level dependence. For samples with particular properties it may be that the effective lifetime is dominated by one mechanism alone, a situation which greatly facilitates the study of that particular mechanism. However, even then, the effective lifetime is very likely to exhibit some injection-level dependence, especially around the carrier densities of relevance for solar cell operation. It is surprising then that lifetime values are regularly reported in the literature as *single* values, with no reference to the excess carrier density at which they were measured or how the value may relate to the operating conditions of a finished device. In fact, it often seems that injection-level dependent lifetimes are considered a complicating nuisance. Viewed from a different perspective however, they present an opportunity to gain greater insight into the underlying electronic processes, and possibly, in many cases, the best such opportunity.

By using a simple, robust method for measuring effective lifetimes, in this case the QSSPC technique, it is possible to focus attention on the physical processes behind the measurements, and also on their consequences for devices. These two issues are essentially the main themes of this thesis, and they are explored with the aid of the techniques and equations developed in this chapter. The following chapter applies some of these methods to the important problem of improving the effective lifetime of mc-Si wafers through physically removing bulk SRH recombination centres, a process known as gettering.

CHAPTER 2

Gettering and Thermal Degradation in Multicrystalline Silicon

2.1 Introduction

Impurities in silicon have direct, detrimental impacts on cell performance, as discussed in the previous chapter. However, some types of impurities can be removed from the bulk of a wafer by mechanisms that are known collectively as ‘gettering’. The common feature of these gettering processes is that they concentrate impurities in a specific region of a wafer, for example at the surfaces, which can then be either physically removed by etching, or isolated from the active device regions. Techniques using purposely applied regions that can later be removed are referred to as ‘extrinsic’ gettering, while those that take advantage of internal features such as dislocations, grain boundaries, oxygen precipitates or micro-defects are known as ‘intrinsic’ gettering. The latter are commonly used in microelectronics where a large portion of the wafer is electronically isolated from the device, a situation that rarely occurs in solar cells.

Gettering techniques differ by the way in which they ‘capture’ impurities at the gettering sites, some relying on precipitation at defects, others on solubility and diffusivity changes between different layers and temperatures, others still resulting from more complex non-equilibrium processes involving silicon-interstitials or dopant atoms. However, the critical feature of all gettering processes is the very large segregation coefficients achieved between the gettering region and the bulk, sometimes as high as 10^7 [62]. For applications to solar cells, gettering steps may be deliberately incorporated into a cell fabrication process, usually near the beginning, or, more preferably from a cost perspective, may occur coincidentally during another process step, such as emitter diffusion.

Phosphorus gettering is probably the most widely studied method for solar cell applications, primarily due to its ease of application and widespread use for emitter formation. In this chapter, phosphorus gettering of cast multicrystalline silicon is studied. The effectiveness of the gettering is found to depend on the crystallographic quality of the material, and hence on the part of the ingot from which a wafer is sawn. Also, the ‘mobility’ of the lifetime-limiting impurities, which can be indirectly measured using a new cross-contamination technique, is shown to strongly affect the gettering efficiency.

The ultimate aim of any gettering step is, of course, to improve the lifetime of the substrate. However, low resistivity mc-Si suffers from thermal degradation of the lifetime under high temperature steps, a mechanism that appears to occur independently of any gettering action. In this chapter it is shown that these competing mechanisms of gettering and thermal degradation lead to a resistivity-dependent optimum gettering time. Possible origins of the thermal degradation effect are examined, the main candidates being metallic ‘poisoning’, whereby previously precipitated impurities become mobile and diffuse through the bulk, or alternatively a deterioration in the crystallography.

Three further phosphorus gettering studies are also presented in this chapter. The first provides a more detailed study of the gettering response of wafers along the length of ingots, in this case produced by BPSolar. These ingots are found to behave quite differently to the Eurosolare ingots studied previously. The second extra study explores the response of a different Eurosolare ingot that suffered from a power ‘black-out’ during its growth, lending it peculiar crystallographic features that can be understood in terms of the previous conclusions. The final piece of work examines gettering of ribbon grown Edge-defined Film-fed Growth (EFG) mc-Si, a promising low-cost photovoltaic material[56,63]. As a starting point however, a brief overview of the various gettering techniques commonly employed in the broad field of silicon device processing is presented.

2.2 Gettering techniques for silicon devices

The physical mechanisms underlying the various gettering techniques available have been extensively studied, primarily because of their relevance in the microelectronics industry. These mechanisms are, however, complex and varied, and some remain poorly understood. For example, gettering of iron to heavily boron-doped silicon has been attributed recently to the different solubilities of interstitial Fe in the heavily- and lightly-doped regions[64]. Another study however, concluded that the ‘capture’ of Fe as FeB pairs in the heavily doped layer was responsible[65]. In any case, a common feature of all gettering methods is that they comprise three distinct fundamental processes: release of impurities, diffusion to gettering sites, and capture at the gettering sites[66]. Any one of these three mechanisms may limit the gettering efficiency. Generally they all exhibit strong temperature dependence, which should be considered when analysing any particular gettering process.

A comprehensive and recent review of transition-metal gettering in silicon has been provided by Myers *et al.*[67]. They suggest five distinct categories of gettering mechanisms, based on the underlying physics of the ‘capture’ part of the process. These five groups are: metal-silicide precipitation, segregation into second phases, atomic trapping at defects, interactions with electronic dopants, and finally phosphorus gettering, which is a special case. Each of these is briefly discussed below with a particular focus on their potential benefits and limitations with respect to solar cell applications.

Firstly, **metal-silicide precipitation** is based on the precipitation of super-saturated metals at specifically introduced or naturally occurring lattice-defect precipitation sites. As the gettering temperature, and hence the metallic solubility, is lower than the temperature at which the impurities were originally dissolved in the silicon during ingot growth, the metals precipitate preferentially at the gettering sites. Such a technique is limited in its effectiveness by the difference of the solubility limits at the original ingot growth temperature and the gettering temperature, which often results in a smaller segregation coefficient than other techniques. Naturally, using lower gettering temperatures produces greater segregation, but the reduced diffusivity of the metals requires much longer gettering times, especially when the entire bulk of the wafer must be gettered as for solar cells.

Many studies on this type of gettering have been performed for applications in microelectronics. The precipitation sites sometimes take the form of a band of structural defects formed by ion-implantation of electronically inert species such as H or He[68]. Precipitation sites may also be introduced by mechanical damage of the wafer rear, or by depositing a film of polycrystalline silicon. Internal precipitation at defects caused by oxygen complexes is also often used. These techniques are unlikely to be cost-effective for solar cell production, except

for the possible exception of back-side mechanical damage. Nevertheless, cavity gettering by H and He implantations in cast mc-Si has been investigated and found to provide effective gettering[69], despite competition from grain boundaries and other defects which also act as precipitation sites. As discussed below, it is likely that the gettering effectiveness in such real cases is driven not only by precipitation, but also by atomic trapping at defects, a physically distinct process.

Segregation into second phases involves the presence of a specifically introduced region comprised of silicon and some other species, usually boron or aluminium, present in high concentrations. Gettering to phosphorus doped regions also occurs via this mechanism, but due to the dominance of other processes, it is treated separately below. In gettering by segregation into a second phase, the solubility of the metallic impurities is much higher in the gettering layer than in the wafer bulk, and so, at temperatures high enough to allow sufficient mobility, the metals are collected in the gettering layer. It should be noted that in using the term ‘phase’ we are not referring to a particular molecular arrangement of dopant and silicon atoms, although in some cases these have been identified. Here we simply mean a region that is doped heavily enough to have dramatically increased solubilities for metallic species. This type of gettering is not restricted by the solubility of the metals in the wafer bulk since it does not rely on precipitation, and consequently can achieve much higher gettering efficiencies than precipitation gettering. Gettering by segregation into second phases has been described in heavily boron-doped layers[64], and also in Al-Si alloyed layers[62,70]. The latter case, in which a layer of Al is deposited and then annealed at temperatures higher than the Al/Si eutectic temperature (577°C) to produce a molten Al/Si alloyed layer, is widely employed in silicon solar cell processes, even if only as a by-product of back-surface-field formation, and is often referred to as Liquid Aluminium Layer (LAL) gettering[71].

Experimental evidence has suggested that segregation coefficients as high as 10^7 can be achieved with LAL gettering, significantly higher than possible with precipitation gettering[62]. For non-precipitated metallic impurities, LAL gettering is usually impurity-diffusion limited. It is therefore easier to model than precipitation gettering, which is typically limited by the inherently more complex precipitation kinetics. Plekhanov *et al.* modelled the more complex case of LAL gettering of precipitated Fe, a process that is essentially limited by the rate at which the precipitates dissolve[71]. They found that using a ramped gettering process with decreasing temperatures should result in the best gettering efficiency. A high initial temperature is necessary to sufficiently dissolve the precipitates, while the time at each gettering step must increase as the temperature decreases due to the decreasing mobility of the impurities. In later sections of this chapter we apply their suggested regime to phosphorus gettering of mc-Si.

Gettering achieved by **atomic trapping at defects** superficially appears similar to the case of precipitation gettering by mechanical damage or other crystal imperfections, described

above. They are, however, fundamentally different processes. Trapping at defects is analogous to atomic bonding and can occur whenever an impurity diffuses near a ‘vacant’ defect, irrespective of the solubility limit of the metal species. Assuming sufficient mobility, these two processes then are ultimately limited by different mechanisms: precipitation gettering by the solubility limit, and trapping at defects by the availability of vacant defects and the bonding ‘cross-section’. In reality however, these two distinct types of gettering very often occur simultaneously in a sample, and for many practical purposes the distinction between them is largely academic.

Gettering via **interactions with electronic dopants** is essentially an electrostatic process. Dissolved metal impurities carry an electronic charge, as do the deliberately introduced dopant atoms. If these charges are opposite the resulting attraction causes bonding of the two species, which results in segregation between lightly- and heavily-doped regions. Again, this process is not limited solely by solubility limits, but due to the relatively weak metal/dopant bonds, lower temperatures (<800°C) have been found to provide better gettering efficiencies. Of course, at these lower temperatures the mobility of the metal atoms is much less, meaning that this type of gettering is not as attractive for deep gettering, as required for solar cells. However, it has been widely studied in relation to shallow gettering of Fe by B-doped layers for microelectronic applications[65].

Phosphorus diffusion gettering is treated as a distinct category, and remains poorly understood in general. Phosphorus gettering studies of Co[72] and Au[73] in silicon have revealed much larger segregation coefficients than can be explained by either precipitation gettering or segregation to the second highly-doped phase, although these processes must also be present to some extent. Also, for these systems, electronic dopant interactions would actually be repulsive instead of attractive, and would hence be a force opposing gettering. Many studies have implicated the generation of silicon self-interstitials as the cause of the enhanced segregation[72-76]. These defects are created in large quantities during phosphorus diffusion, and are also responsible for the familiar ‘hump’ in diffused phosphorus profiles. The interactions of these self-interstitials with metallic impurities are complex and are the focus of on-going research, but seem to be at least part of the reason for the very high segregation coefficients achievable with phosphorus diffusions.

As alluded to above, in many practical cases more than one of the listed types of mechanisms will occur concurrently. In some cases it has been shown that the simultaneous action of two types of gettering results in a synergistic effect that provides greater segregation than would be expected if the mechanisms acted ‘independently’. The most notable example of such effects in relation to solar cells has been the synergistic action of phosphorus and LAL

gettering[77,78], in which the self-interstitials produced by the phosphorus diffusion also enhance the effectiveness of the LAL gettering, as predicted from modelling by Tan *et al.*[79].

The next section presents results of phosphorus gettering of cast mc-Si wafers, as studied by QSSPC-measured lifetimes. There have been many previous studies of phosphorus gettering of silicon in general[66,80], and also of this material in particular, but here we present new work on the relationship between the gettering efficiency and both the crystallographic quality of the material and the amount of non-precipitated impurities.

2.3 Phosphorus gettering of Eurosolare multicrystalline silicon ingots

Increases in minority carrier lifetime in mc-Si wafers after a phosphorus gettering process are well documented[66,81]. Cast mc-Si is generally solidified in a controlled manner from the bottom to the top of the melt. Previous work has shown that the bottom of the resulting ingot tends to contain crystallographic defects and dissolved oxygen, as well as other impurities from the crucible walls, which consequently affect the lifetime[82,83]. It has also been established that lifetimes before gettering are generally poor at the top of an ingot due to transition metal impurity segregation[84,85].

Since phosphorus gettering is very effective at removing non-precipitated transition metals from the active regions of silicon devices, it seems reasonable to expect that wafers from the top of a mc-Si ingot would have higher lifetimes after gettering. However, Sopori *et al.* and others have found that gettering is not effective when the dislocation density is above a threshold value of about 10^6 cm^{-2} [86]. It has been suggested that in such cases the impurities are precipitated at dislocations, grain boundaries and other microdefects, where they serve to increase the recombination at such centres, and from which they are difficult to getter[87-89].

In order to systematically study the gettering response of wafers from various regions of different quality ingots, we have measured dislocation densities (using a defect etch), and, indirectly, the concentration of ‘mobile’ impurities. This was done using a novel cross-contamination technique, which involved measuring the lifetime degradation of high quality FZ wafers placed very close to the mc-Si samples during a high temperature step. A proportion of the mobile impurities diffusing out of the surface of the mc-Si sample diffuses into the adjacent float zone wafer and consequently degrades its lifetime. The lifetime of the control wafer thus decreases monotonically with increasing concentration of mobile impurities in the test wafer, allowing ‘dirty’ and ‘clean’ samples to be discriminated in a qualitative way.

Combining the results of the gettering experiments, the defect etching, and the cross-contamination experiments, a more coherent picture of the prominent lifetime limiting factors emerges.

2.3.1 Experimental Methods

The *p*-type mc-Si material used in this study was grown by directional solidification at Eurosolare SpA, Italy. While one of the two ingots examined can be considered of standard quality (ingot 6, average grain size $\approx 40 \text{ mm}^2$), the second suffered from anomalous growth conditions, resulting in generally poor crystallography (ingot 8, average grain size $\approx 5 \text{ mm}^2$). The resistivity of wafers from each ingot was measured using a contactless inductive coupling device, and found to decrease from the bottom to the top for both ingots, as expected due to boron segregation, ranging from 0.9 to 0.8 Ωcm for the standard ingot, and from 1.5 to 1.0 Ωcm for the defective one. The total ingot length prior to sawing was 18cm. Under normal industrial conditions the top 3cm are discarded, but for this study they were retained.

Minority carrier lifetimes were measured using the QSSPC technique as described in detail in Chapter 1. Surface passivation was achieved by the standard light phosphorus diffusion and in-situ oxidation also described in Chapter 1, followed by the usual 25 minute forming gas anneal at 400°C. The sheet resistivity of the diffused layer was typically 250 Ω/\square . Single-crystal 1 Ωcm float zone (FZ) wafers were included in the batches as controls, and measurements of the effective lifetimes in these wafers indicated that the quality of the surface passivation was sufficient to unambiguously measure bulk lifetimes of up to 200 μs in the multicrystalline samples. None of the lifetimes measured for such samples in this study exceeded 50 μs , indicating that the measured lifetimes almost entirely relate to the bulk.

The passivating layers were then etched off and the wafers given a 3 hour 900°C POCl_3 gettering diffusion, terminated by a 20 minute dry oxidation. This gettering treatment was chosen because previous studies in our laboratory had shown it to be the most effective[81], although later work revealed that this is not true for all resistivities, as discussed in section 2.3. The sheet resistivity of the gettering diffusion was typically 7 Ω/\square , with a phosphorus glass layer visible. The heavily diffused layers were then etched off and the wafers re-passivated with another light diffusion, identical to the initial process, with another oxide layer formation and forming gas anneal. The lifetimes were then re-measured. After the entire process the wafers were about 40 μm thinner due to the etches, resulting in an average post-getter wafer thickness of around 320 μm .

In a second phase of the experiment, controlled cross-contamination experiments using FZ control wafers were conducted to determine the extent of out-diffusion of impurities at high temperatures, and hence indirectly evaluate the concentration of mobile impurities in the mc-Si samples. Each mc-Si sample was ‘sandwiched’ between two control wafers, which absorbed out-diffusing impurities. The distance between the controls and the samples was about 5mm. The control wafer upstream of a sample should receive a lower dose of impurities than the downstream wafer, which is likely to be subjected to impurities on both surfaces due to turbulence in the gas stream. This was confirmed by experiments that showed, for sufficiently contaminated samples, that upstream control wafers had lifetimes 2 to 3 times larger than the downstream controls.

Clearly it is important to avoid impurities from upstream groups of wafers contaminating the controls surrounding other multicrystalline wafers further downstream. To minimise the risk of this happening, the separation between each group of three wafers was kept as large as possible (about 10cm). Also, wafers that were known to contain large concentrations of diffusive impurities were placed at the downstream end of the boat. As a result of these measures, contamination from upstream wafers was negligible, as was indicated by the lifetimes of the control wafers in front of each sample.

To achieve cross-contamination, the wafers were given the standard light phosphorus diffusion and oxidation as described in Chapter 1. This process served the dual purpose of allowing out-diffusion of impurities, and also provided surface passivation for lifetime measurement.

A further useful application of the cross-contamination effect was employed to confirm that the gettering process was complete after the three hour heavy phosphorus diffusion. Contaminated control wafers from the first passivating light diffusion and oxidation were included alongside mc-Si wafers in the etch/getter/etch/passivation process, in order to evaluate the ‘cleanliness’ of the mc-Si wafers after the gettering treatment. Since the lifetimes of the control wafers recovered to near their normal uncontaminated values, it seemed that out-diffusion from the mc-Si samples ceased at some point during the three hours, implying that gettering was indeed ‘complete’. This conclusion is corroborated by further evidence presented in section 2.6, in which ‘double’ gettering of wafers revealed no further change in lifetime.

In addition to the experiments described above, one wafer from each region of each ingot was mechanically polished, chemically cleaned and etched, and then defect etched in Yang’s etchant, which contains chromium trioxide and dilute hydrofluoric acid[90]. This defect etch provides good delineation of dislocations for a range of crystal orientations, although, like other commonly used etches, it apparently does not etch all orientations with equal speed[91]. Nevertheless, when applied to the wafers studied here, it was found to reveal dislocations on every grain if left for long enough, in this case two minutes at room temperature, after which the

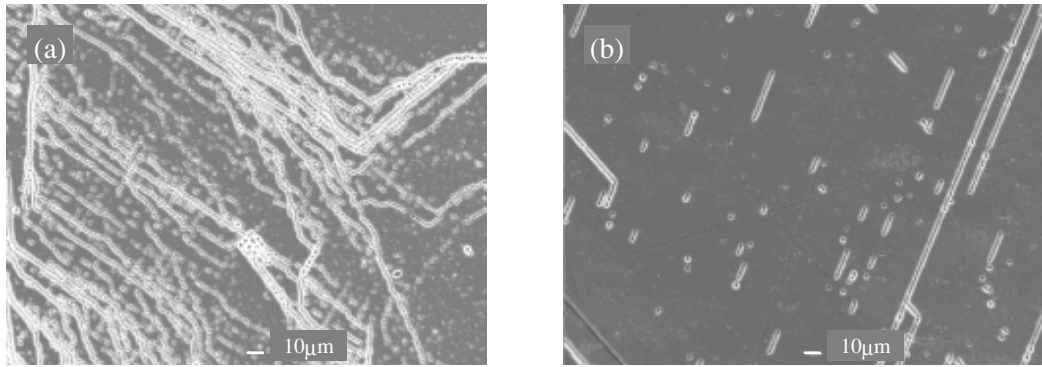


Figure 2.1. SEM micrographs of defect etched samples, showing etch pits corresponding to dislocations. Part (a) is from wafer 300, ingot 6 (high dislocation density), and part (b) from wafer 50, ingot 8 (moderate dislocation density).

etch pits increased in size but not in number. SEM micrographs were taken of suitably etched areas, and dislocation densities calculated for each sample.

2.3.2 Results and Discussion

2.3.2.1 Dislocation density distribution

The dislocation density was found to be very non-uniform across the surface of the wafers. Some regions had essentially no dislocations, while other areas were extremely heavily dislocated (as high as 10^8cm^{-2}). This non-uniformity has previously been attributed to the slightly different breaking-strengths of different grain orientations, resulting in thermally-generated dislocations accumulating in the ‘weakest’ grains[92]. Figure 2.1 shows SEM micrographs of a moderately and heavily dislocated region as revealed by pits caused by Yang’s etch. The left-hand image is very highly dislocated, and corresponds to a local dislocation density of about 10^7cm^{-2} . Such regions have been thought responsible for significant lifetime degradation in other studies[88,91].

Figure 2.2 depicts the change in dislocation density along ingots 6 and 8 respectively. They increase towards the top of the ingots, as expected due to the rapid cooling that occurs there at the end of the casting process. The dislocation density values plotted in these figures are *average* values for each region. Due to the highly non-uniform distribution of the dislocations, it is difficult to estimate such an average value without very time consuming pit counting, even with the aid of image filtering software. The values in the figure were obtained by manually counting pits in a typical heavily dislocated region on each wafer, estimating the proportion of the wafer surface which was heavily dislocated, and then ‘distributing’ the dislocations across the entire wafer. Such a process results in large uncertainties, as reflected in the figure.

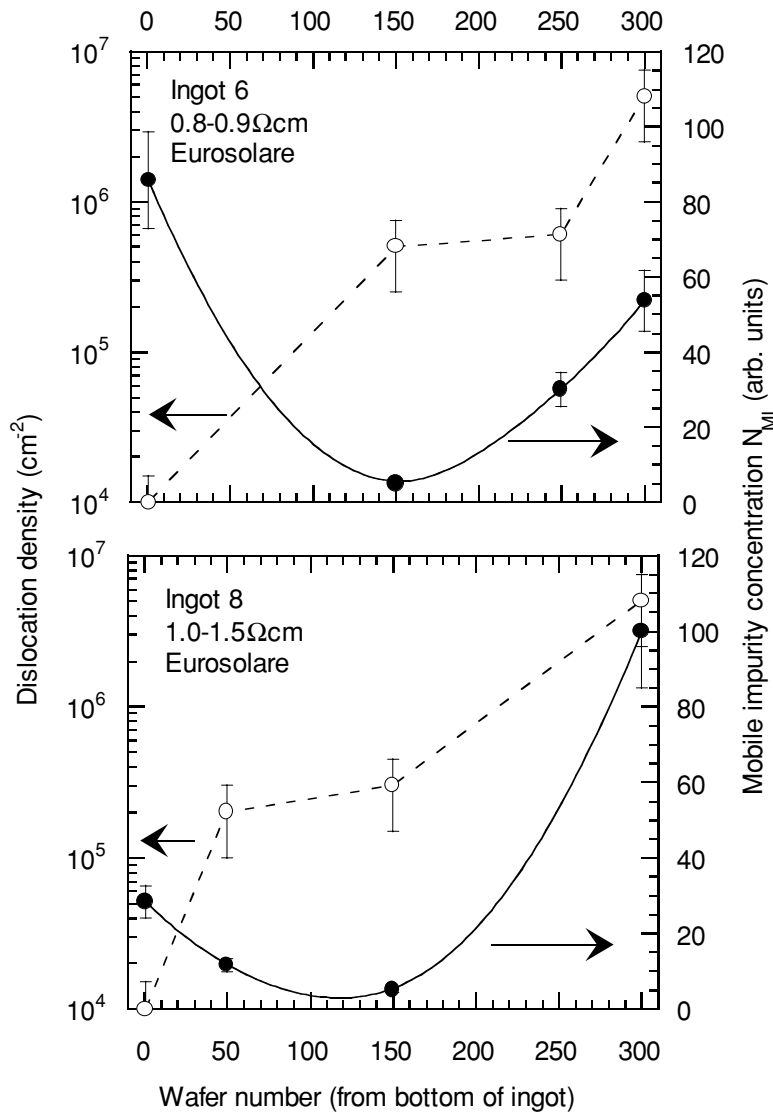


Figure 2.2. Average dislocation densities and estimated relative mobile impurity concentrations as a function of wafer number for both mc-Si ingots.

Nevertheless, the massive variation in average dislocation density along the ingot length allows clear trends to be observed.

2.3.2.2 Mobile impurity distribution (cross-contamination)

The results of the cross-contamination experiments are presented in Table 2.1 in the form of effective lifetimes of the downstream control wafers (τ_{FZ} , in μs , measured at a carrier concentration of $1 \times 10^{14} \text{ cm}^{-3}$), and a relative mobile impurity concentration (N_{MI} , arbitrary units). This latter value is calculated from the lifetime values by noting that the recombination lifetime of a sample dominated by Shockley-Read-Hall recombination is inversely related to the impurity concentration (see Chapter 1). The values are normalised, with the most contaminated

Ingot, Wafer no.	τ_{FZ} (μ s)	N_{MI} (arb. units)
6, 1 (bottom)	175	86
6, 150	3000	5
6, 250	500	30
6, 300 (top)	280	54
8, 1 (bottom)	530	28
8, 50	1300	12
8, 150	3000	5
8, 300 (top)	150	100

Table 2.1. Cross-contamination results. τ_{FZ} is the average lifetime of downstream control FZ wafers. N_{MI} provides an estimate of the relative concentrations of mobile impurities in the corresponding mc-Si wafers.

sample (ingot 8, wafer 300) having a value of $N_{MI}=100$. In an uncontaminated environment, the high resistivity (50-1000 Ω cm) FZ control wafers would yield a lifetime of around 4ms at a carrier concentration of $1 \times 10^{14} \text{cm}^{-3}$ under the light phosphorus diffusion conditions. The most heavily contaminating mc-Si samples degraded the control wafer lifetime to 150 μ s while the least contaminated resulted in 3ms. High resistivity FZ samples were chosen since, at least for deep levels, they are more sensitive to SRH recombination due to the lesser presence of Auger recombination. Also, the effective surface recombination velocity of the passivating diffusion is lower than for more heavily doped substrates.

Of course, it is difficult to accurately relate the degraded FZ lifetimes to the concentration of mobile impurities in the initial mc-Si test samples, primarily because it is unclear what proportion of impurities out-diffuse and whether the various samples contain the same relative proportions of different types of impurity. Furthermore, surface recombination still plays a role in the effective lifetimes of the less contaminated FZ wafers. However, the calculated values of N_{MI} portray a picture, if not entirely accurate in a quantitative sense, of the relative contamination in the various parts of the ingots. The results for both ingots are shown in Figure 2.2. Note that the error bars shown for the N_{MI} values merely reflect uncertainty in the effective lifetime measurements of the FZ wafers, and are not an estimate of the accuracy of the cross-contamination method itself. The figure reveals that the central regions of the ingots contain relatively few mobile impurities, while the relatively high density found at the bottom is most likely caused by contamination from the crucible. Those at the top are probably due to metallic segregation during solidification.

The proportion of impurities transferred during the cross-contamination process can be crudely estimated as follows. Comparing the lifetime of the relevant FZ wafer (175 μ s) with the mc-Si wafers from the bottom of ingot 6 (1 μ s from Figure 2.4), and assuming the impurities are ‘deep’ recombination centres (meaning lifetimes of different resistivities are directly

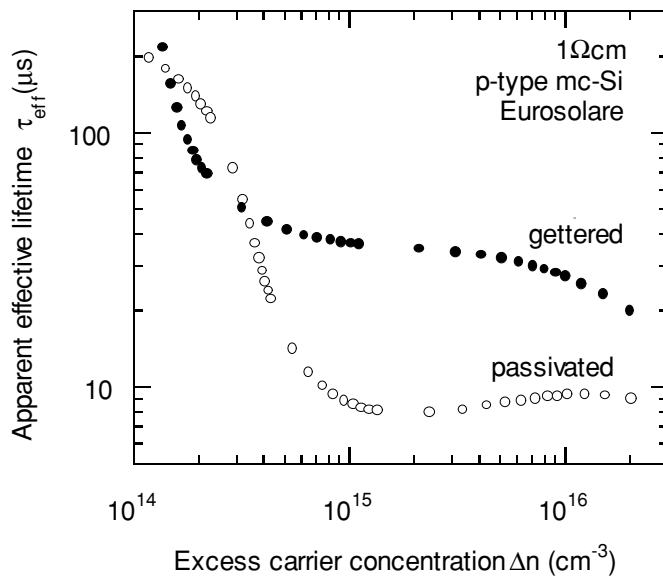


Figure 2.3. Injection-level dependent ‘apparent’ lifetime measurements of a cast mc-Si wafer before (passivated) and after gettering. The term apparent is used due to the presence of trapping, evident as rapidly increasing lifetimes as the carrier concentration decreases.

comparable), it would appear that approximately 1 in 200 impurities are successfully transferred to the FZ wafer during the cross-contamination process, which seems a plausible proportion.

2.3.2.3 Gettering results

Recombination lifetimes are often strongly injection-level dependent, therefore it is important to compare values at the same carrier density when comparing lifetimes of different samples, and also of the same sample after different process steps. Further, mc-Si samples are subject to trapping effects that distort the lifetime measurement, as discussed in Chapter 3. For the purposes of this section, the important point is that a carrier density greater than $10^{15} cm^{-3}$ must be used to comfortably avoid the trapping effects in all samples. Consequently, the lifetime measurements presented in this section were all taken at a carrier density of $3 \times 10^{15} cm^{-3}$. Figure 2.3 shows a typical lifetime versus injection-level curve for a mc-Si sample before and after gettering, with the trapping effect evident as a rapid increase in ‘apparent’ lifetime at lower carrier densities. The lifetime of this sample at $3 \times 10^{15} cm^{-3}$ increased from 8 to $32 \mu s$ after phosphorus gettering.

The results for both passivated and gettered samples are shown in Figure 2.4 for ingots 6 and 8. Several samples from each region were processed in order to ensure that the results reflect real trends, not merely the ‘random’ variations that occur across the surface of any mc-Si wafer. The uncertainty in the lifetime measurements themselves, as shown by the error bars, is

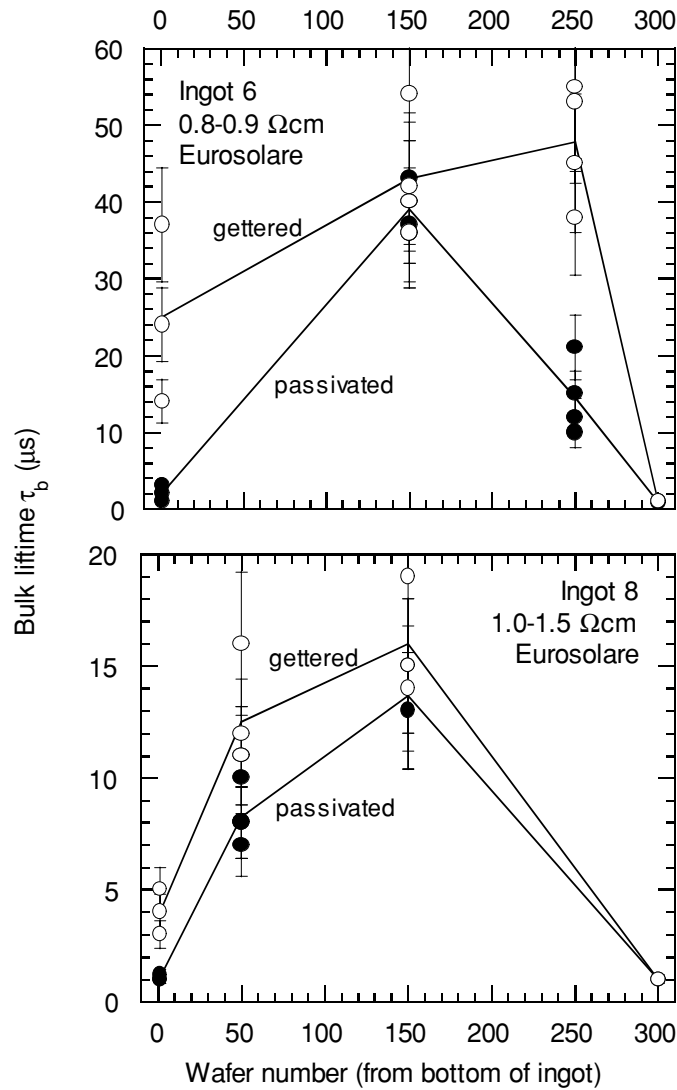


Figure 2.4. Bulk lifetimes measured at a carrier density of $3 \times 10^{15} \text{ cm}^{-3}$ before and after gettering as a function of wafer number for both ingots.

estimated to be about 15%. The figure reveals obvious gaps in the data at wafers 50 and 250 for ingot 6 and 8 respectively. Unfortunately these wafers were not available from the manufacturer. A more comprehensive study of the gettering response along the length of two BPSolar cast mc-Si ingots is presented in section 2.5. However, the results presented here are sufficient to draw some important general conclusions.

The bottom of both ingots show very poor pre-gettering lifetimes of about $1 \mu\text{s}$. The dislocation density is low at the bottom for both ingots, while the mobile impurity concentration is very high for ingot 6 and moderately high for ingot 8. It seems possible then that the poor lifetimes in these wafers arise from the presence of these mobile impurities. After gettering, the lifetimes of these bottom wafers improve significantly: by approximately a factor of 12 and a factor of 4 for ingot 6 and 8 respectively. The larger increase for ingot 6 may reflect the greater mobile impurity concentration in these wafers. These relative lifetime increases are the largest

of any of the wafers studied, and are due to the combination of low dislocation densities and high levels of mobile impurities. It is worthwhile noting that these bottom wafers would be suitable for cell fabrication after a gettering step, whereas without one, such wafers are normally discarded. To further illustrate this point, the implied voltage technique described in Chapter 1 suggests that an increase in lifetime from $2\mu\text{s}$ to $25\mu\text{s}$ at 1-sun illumination corresponds to an open circuit voltage increase from about 560mV to 620mV, for a $1\Omega\text{cm}$, $300\mu\text{m}$ thick wafer with an optical absorbed fraction of 0.85 after anti-reflection coating. Typical commercial mc-Si cells have open-circuit voltages of around 590-600mV, which of course includes limitations due to the emitter and rear surface passivation, as well as the bulk.

In contrast to the bottom wafers, those from the top do not respond to gettering at all. Their pre-getter lifetimes are also very low, about $1\mu\text{s}$. However, the high dislocation densities at the top of both ingots suggest that their lifetimes are limited by dislocations and other defects, which are possibly decorated with impurities. Consequently their lifetimes do not increase after gettering, irrespective of the high concentration of mobile impurities. These results confirm the suggestion by Sopori *et al.*[86] that there is a 'threshold' value of the dislocation density of about 10^6 cm^{-2} , above which gettering is ineffective.

As noted, these wafers exhibited high concentrations of mobile impurities. A simple model of impurity behaviour might suggest that highly dislocated samples would contain most of their impurities in a precipitated state. Previous work has shown that such 'trapped' impurities are not easily getterred[93]. Consequently, high dislocation density wafers might be expected to exhibit relatively low mobility of impurities at standard processing temperatures, resulting in low out-diffusion. However, the cross-contamination data suggests that this is not the case for the highly dislocated wafers studied here. It was not possible to determine whether the out-diffusing impurities are coming from precipitated states at dislocations, grain boundaries or microdefects, or from interstitial sites in the bulk of the grains. In any case, it seems that their effect on the total recombination lifetime of these samples is small, and these mobile impurities are in an electronic sense 'surplus'.

Turning next to the central region of the two ingots, it can be seen that the response to gettering is again marginal. For these wafers, the dislocation density is moderate and the mobile impurity concentration very low. Hence it seems that such wafers do not respond to gettering because there is little to getter. The lifetimes of these wafers then, both before and after gettering, are dominated by crystallographic defects with their associated ungetterable metallic decoration.

The final samples to consider are those not at the ends, nor in the centre. Wafers numbered 250 and 50 all showed a significant response to gettering for ingots 6 and 8 respectively. These samples had dislocation densities similar to the central wafers, but contained significantly more mobile impurities. Upon extraction of these impurities through gettering, the

lifetimes increased up to values similar to the central wafers for the two ingots, indicating that the limit imposed by the crystallography had been reached.

Although the trends for the two ingots are similar, the magnitudes of the lifetimes for ingot 6 (the standard ingot) are larger than for ingot 8 (the defective ingot): $48\mu\text{s}$ compared to $14\mu\text{s}$ for the central wafers. It is tempting to suggest that this is a reflection of the smaller average grain size in ingot 8. However, wafers from the top of ingot 8 had the largest grain size of *all* the wafers (even compared with ingot 6), and yet displayed the lowest lifetimes after gettering, illustrating that the visual appearance of mc-Si samples is often poorly correlated to the electronic quality. It seems then that the generally lower lifetimes in ingot 8 must be related to other non-visible crystallographic defects.

A lifetime of $48\mu\text{s}$ should allow for open circuit voltages of up to 640mV for ingot 6. Bearing in mind the higher resistivity of ingot 8 ($1.0\text{--}1.5\Omega\text{cm}$ as opposed to $0.8\text{--}0.9\Omega\text{cm}$), $14\mu\text{s}$ is a relatively low lifetime, and corresponds to a maximum achievable open circuit voltage in the vicinity of 600mV.

In summary, the largest increase in lifetime after phosphorus gettering was found in samples with low dislocation densities and high concentrations of mobile (and hence getterable) impurities. The lifetime of samples with dislocation densities above 10^6cm^{-2} remained low after gettering, despite their high initial concentration of mobile impurities. It is possible that the dislocations and microdefects in such samples are, from a recombination point of view, saturated with impurities. Those found out-diffusing previously had little impact on the recombination lifetime, and, consequently, their removal does not result in a lifetime increase.

2.4 Gettering and thermal degradation of low resistivity multicrystalline silicon

The two ingots studied in the previous section are of typical resistivity for commercial mc-Si cell production, in other words around $1\Omega\text{cm}$. However, there are a number of reasons for examining lower resistivity material. Firstly, as wafering technology continually improves, and yield issues regarding the processing of thinner wafers are resolved, industry is moving towards thinner mc-Si substrates. The main driving factor here is the significant cost savings associated with producing more wafers per ingot. A potential added bonus of thinner wafers however, is that the required diffusion length to maintain cell current is reduced, provided that sufficient light-trapping exists to negate optical losses arising from the thinner substrates. It then becomes plausible to consider using more highly doped substrates that will produce greater voltages but similar currents.

A second consideration, which is of particular relevance to mc-Si cells, relates to the greater presence of Auger recombination in more heavily doped wafers. As has been shown in the gettering results presented here, the recombination lifetime of mc-Si samples is usually appreciably less than single-crystal FZ material, due to the presence of impurities and defects. However, as the dopant density increases, the relative importance of SRH recombination through defects diminishes in comparison to Auger recombination. For deep SRH recombination centres, the low-injection recombination rate is independent of the dopant density, while for shallow levels it may be either independent or linearly dependent (see Chapter 5). By comparison, in low-injection Auger recombination proceeds at a rate that is proportional to the square of the dopant density. As Auger recombination is a fundamental process that occurs in any material, it follows that the lifetime gap between mc-Si and single crystal silicon should be reduced for lower resistivity material.

A further potential benefit of using lower resistivity mc-Si material is that ohmic contact can be made directly to the base using aluminium, without the need for alloying. This allows greater freedom in cell process design, and opens the possibility of using more effective rear passivation schemes such as SiN, as opposed to aluminium alloyed back-surface fields. Hence there are strong incentives to study low resistivity mc-Si material. In this section the electronic behaviour of such material, and, in particular, the poorly understood but important ‘thermal degradation’ of bulk lifetimes, are examined.

Thermally-induced degradation of the recombination lifetime in low resistivity mc-Si has been documented by several researchers[94-96]. It appears to occur independently of the type of process step performed, whether oxidation, diffusion or annealing in an inert atmosphere such as nitrogen. However, such material can also be improved through gettering by any of the means described in section 2.2, and any high temperature gettering process will necessarily involve both these competing mechanisms. Since gettering is most effective during the initial stages, when the concentration of impurities in the bulk is relatively high, it follows that there will exist an optimum gettering time which will result in a maximum bulk lifetime, after which the lifetime will decrease due to thermal degradation.

The aim of this section is to explore the nature of this trade-off between the beneficial effects of gettering and the detrimental effects of thermal degradation, particularly as it applies to samples of different resistivities. This latter point is important, since it appears that the strength of the thermal degradation effect is strongly dependent on the dopant density, a dependence that in turn affects the optimum gettering time.

The physical origin of the thermal degradation is also examined. Previous workers have proposed mechanisms for this lifetime reduction, the most accepted probably being the dissociation of impurity precipitates at high temperature[71,79,94]. Plekhanov *et al.*[71] have modelled this dissociation, and concluded that certain variable temperature gettering regimes

should result in an increase in lifetime by making use of the changing dissociation rates and impurity diffusivities at different temperatures. In this section results from such a gettering step are presented which indicate that no corresponding lifetime increase occurred. However, it is found that high temperature oxidations resulted in a significant increase in the dislocation density in the low resistivity samples, suggesting a possible alternative explanation for the reduced lifetime.

As a starting point, experimental evidence of the resistivity-dependent thermal degradation effect is presented and discussed.

2.4.1 Evidence of thermal degradation

2.4.1.1 Process monitoring of mixed resistivity high-efficiency cells

Process monitoring by lifetime measurements has become a well established technique for determining the relative impacts of process steps on device performance[97]. In the laboratories at ANU, it is routinely used for this purpose, and also to ensure processes are within specification. For the purposes of this section, process monitoring of a batch of high-efficiency FZ and mc-Si cells of mixed resistivities provides a good example of the thermal degradation of low resistivity mc-Si wafers, and more generally of the different behaviour of mc-Si and single-crystal FZ silicon.

The particular cell design attempted was a Passivated Emitter, Rear Locally-diffused (PERL) cell[98,99], with texturing performed by isotropic etching of photolithographically-defined ‘tubs’[100,101], and a selective emitter comprised of two diffused regions. The lifetimes were measured using the QSSPC technique at various stages of the process, as indicated below by an asterisk. To avoid severely surface-limited lifetime measurements, they were performed at points when passivating oxides or light diffusions were covering most of the surfaces. The wafers were given a forming gas anneal (FGA) at 400°C for 25 minutes prior to each lifetime measurement to improve the oxide interface quality.

1. 3 hour 900°C phosphorus gettering. Diffusion etched away.
2. 150nm thick 900°C steam oxidation for ‘tubs’ masking, FGA *
3. ‘Tubs’ etched, 180nm 900°C steam oxidation for diffusion mask, FGA. *
4. Light phosphorus emitter diffusion, 1100°C TCA masking oxide, FGA. *
5. Heavy phosphorus and boron diffusions into fingers and dots, FGA. *
6. Final thin TCA oxide growth at 900°C for emitter passivation, FGA. *
7. Metallisation, FGA and antireflection coating.

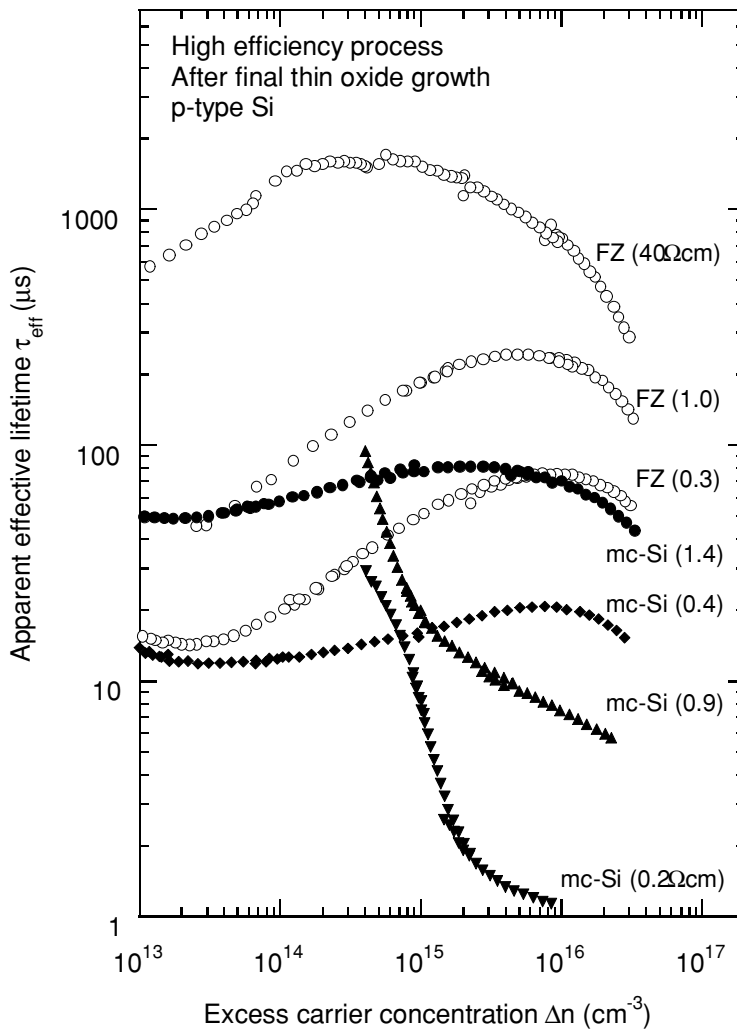


Figure 2.5. Injection-level dependent lifetimes of single-crystal FZ and mc-Si cell pre-cursors after the final thin emitter passivating oxide growth and immediately prior to metallisation.

As an example of the injection-level dependent lifetime measurements obtained, Figure 2.5 depicts the lifetime curves after the final thin passivating oxide growth. Comparing the three FZ samples with the 1.4 and 0.4Ωcm mc-Si samples reveals a stronger injection-level dependence for the FZ wafers. This is due to the fact that they are rear-surface limited, and are hence subject to the well-documented injection-level dependent surface recombination velocity of the rear oxide-silicon interface[41,43]. Forming gas annealing after metallisation reduces this dependence significantly, although lifetime measurements are not possible then due to the excessive conductance of the metal. In contrast, the two mc-Si samples (1.4 and 0.4Ωcm) are limited by bulk recombination centres. This is also true for the two other mc-Si wafers (0.9 and 0.2Ωcm), however they are also subject to strong trapping effects which distort the lifetime at lower carrier concentrations. To allow meaningful comparison between samples, and to avoid the trapping effects, lifetimes discussed in this section were all recorded at a carrier density of $1 \times 10^{16} \text{ cm}^{-3}$. This is higher than the carrier density required in section 2.3 due to the fact that

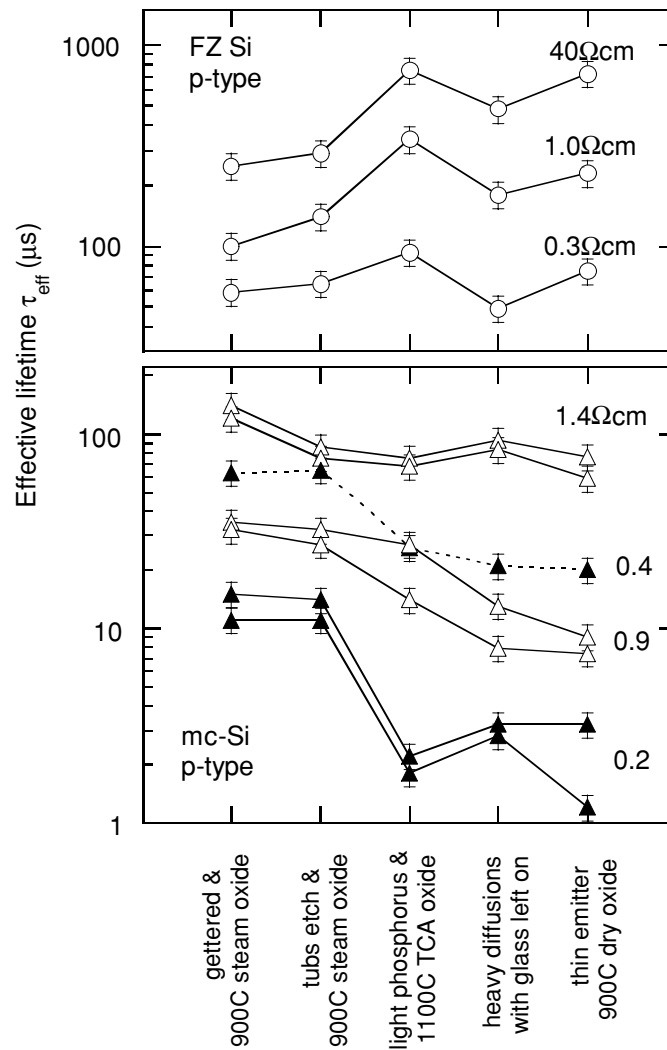


Figure 2.6. Effective lifetimes measured at a carrier density of $1 \times 10^{16} \text{ cm}^{-3}$ for FZ (top) and mc-Si (bottom) cell precursors at various stages during cell processing.

here we consider lower resistivity material, which typically has larger trap densities, an observation that is consistent with results in Chapter 3.

Figure 2.6 presents these lifetimes as measured after the five process stages outlined above. The top half of the figure shows the results for the FZ wafers, which all follow the same trend independent of resistivity. For these wafers, all the measurements are surface dominated, and the lifetime results essentially reflect the quality of the overall surface passivation present at each step. The results show that the total surface passivation is best at points 4 and 6, which seems reasonable as the surfaces are then passivated by TCA oxides, as opposed to steam oxides.

The bottom half of Figure 2.6 shows the results for the mc-Si substrates of various resistivities. Their behaviour is different to that of the FZ cells, and also varies between the different resistivities. All these mc-Si measurements are bulk-dominated, and hence they reflect

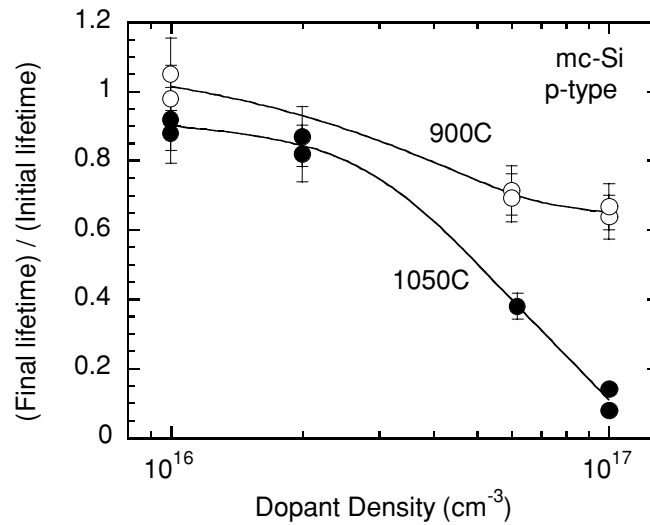


Figure 2.7. Ratio between final and initial recombination lifetimes in mc-Si before and after a 900°C and 1050°C oxidation for 30 minutes, versus dopant density. The solid lines are guides to the eye.

changes in the bulk recombination properties at each point in the process. The most notable observation from these values is that the lower resistivity substrates suffered from a significant lifetime drop after the step involving an 1100°C TCA oxidation, with the 0.2Ωcm wafers decreasing by about an order of magnitude. For the 1.4Ωcm wafer, the corresponding drop was much less. This effect is the resistivity-dependent ‘thermal degradation’ often observed in mc-Si. It was not observed in the FZ wafers, at least to the degree allowed by the surface passivation.

The process monitoring of this batch of cells revealed, if ‘accidentally’, the importance of understanding the thermal degradation of the lifetime in mc-Si. The next section presents experiments that were targeted at elucidating the nature of the resistivity dependence of the phenomenon.

2.4.1.2 High temperature oxidation of mc-Si

Several Eurosolare grown mc-Si wafers of varying resistivity were subjected to either a 900°C or a 1050°C dry oxidation step for 30 minutes. Lifetimes before and after oxidation were all measured at a carrier concentration of $1 \times 10^{16} \text{ cm}^{-3}$, again to avoid trapping effects. Surface passivation was provided by the oxide, which was given a forming gas anneal prior to lifetime measurement. Control FZ wafers of similar resistivity were included to ensure the surface passivation was sufficient to allow the lifetimes measured on the mc-Si samples to be interpreted as bulk recombination lifetimes. The data is presented in Figure 2.7 as the ratio of

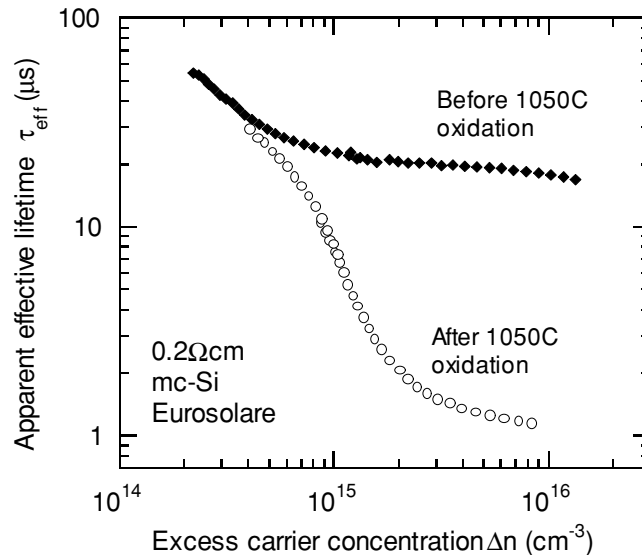


Figure 2.8. Apparent lifetime versus excess carrier concentration for a 0.2Ωcm mc-Si wafer before and after a 1050°C oxidation. The apparent lifetime increases rapidly as the carrier density decreases, revealing the presence of trapping effects. These are more pronounced after the oxidation step, implying an increase in the trap density.

these lifetimes post- and pre-oxidation. Prior to oxidation, the samples were phosphorus gettered for 60 minutes in order to maximise the recombination lifetime, and hence increase the sensitivity of the experiment. The average pre-oxidation lifetimes were 130, 60, 50 and 17μs for the 1.5, 0.8, 0.3 and 0.2Ωcm wafers respectively.

Clearly the higher temperature oxidation results in greater thermal degradation. In fact, the more highly doped samples experience a massive reduction in lifetime, dropping by about 90% after the 1050°C oxidation, a similar result to that of the 1100°C oxidation in the cell process of the previous section. This is more explicitly illustrated in Figure 2.8, which shows the injection-level dependent lifetime curve of a 0.2Ωcm wafer before and after such a 1050°C oxidation. However, Figure 2.7 reveals that the more lightly-doped wafers are much more resilient. These results are also consistent with those presented in the previous section, in which the high resistivity mc-Si wafers did not suffer unduly from thermal degradation during any of the high temperature steps. This resilience offers an explanation for the success of high efficiency cell processes when applied to higher resistivity mc-Si material[101]. Standard PERL designs involve a large number of high temperature oxidations and diffusions, as typified by the previous section, which severely degrade low resistivity material but leave high resistivity substrates relatively unchanged.

An interesting observation made during the lifetime measurements of these samples was that the trapping effect was noticeably more pronounced after the 1050°C oxidation step for the most highly-doped wafers, as shown clearly in Figure 2.8. This increase in the trap density is referred to again in section 2.4.3.2 in relation to the physical origin of thermal degradation.

2.4.2 Optimum gettering times for low resistivity mc-Si

As mentioned previously, the concurrent effects of thermal degradation and impurity gettering that occur during phosphorus diffusion of low resistivity mc-Si, should result in an optimum gettering time. In this section the optimum time is determined for Eurosolare mc-Si wafers of various resistivities under gettering at 900°C. At higher temperatures the optimum times would be shorter due to the more rapid nature of both gettering and thermal degradation.

2.4.2.1 Experimental methods

Gettering experiments were performed at 900°C for times of 20, 60, 120 and 180 minutes on mc-Si wafers with resistivities of 0.2, 0.4 and 1.4Ωcm. During gettering, POCl₃ vapour and O₂ comprised 0.1% and 7% of the gas stream respectively. The sheet resistances resulting from these gettering diffusions were 130, 25, 15 and 10Ω/□ for the four times above. Two wafers of each resistivity, taken from adjacent slices within the ingots, were processed for each gettering time to provide greater confidence in the results.

The most appropriate method of surface passivation must be considered in this experiment. The gettering diffusions provide some surface passivation, although in all cases except the 20 minute gettering process, the resulting diffusion is so heavy as to limit the effective lifetime through emitter recombination. Consequently, in order to measure the bulk recombination lifetime, the heavily-doped phosphorus layer was etched off, and the samples re-passivated. This was achieved by the standard light phosphorus and thin in-situ oxidation described in Chapter 1, followed by a forming gas anneal. This etching and passivation step was not performed on the samples gettered for 20 minutes, since the gettering layer itself provided sufficient passivation. The quality of the surface passivation was monitored by including FZ single-crystal silicon wafers of comparable resistivities in each batch of wafers.

2.4.2.2 Results and discussion

Lifetimes were again measured at a carrier concentration of $1 \times 10^{16} \text{cm}^{-3}$ to avoid trapping effects, and also to allow direct comparison between samples. The quality of the surface passivation was sufficient to allow lifetimes about an order of magnitude larger to be measured

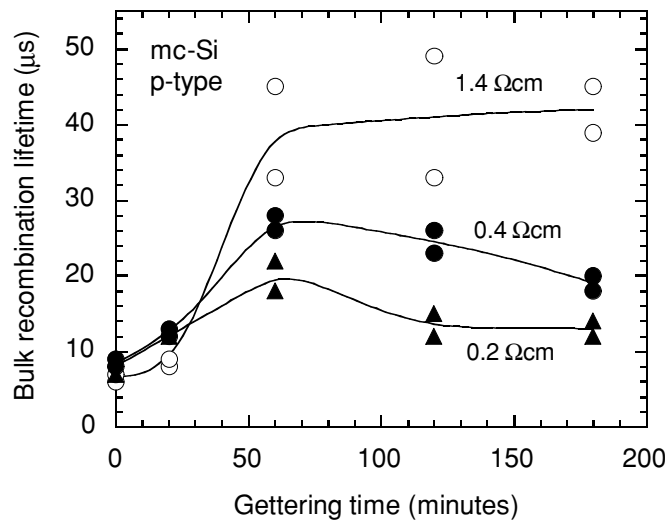


Figure 2.9. Bulk recombination lifetime versus gettering time for different resistivity mc-Si wafers after gettering at 900°C. The lines are guides to the eye.

on the FZ control wafers of comparable resistivities, and so the effective lifetimes measured on the mc-Si wafers can be interpreted as bulk recombination lifetimes.

Figure 2.9 shows the results of lifetime measurements on the mc-Si wafers of various resistivity subjected to various gettering times. During this gettering procedure, the two competing mechanisms of impurity gettering and thermal degradation are simultaneously at work. Initially, gettering is the dominant mechanism, due to the abundance of easily gettered impurities, and the recombination lifetime increases dramatically. This occurs similarly for all three resistivities. However, as the efficacy of the gettering is reduced, after about 60 minutes, the behavior of the lifetimes is strongly resistivity-dependent, and the effects of thermal degradation begin to impact significantly on the lower resistivity samples. However, for the higher resistivity wafers, the recombination lifetime becomes effectively constant.

Figure 2.9 suggests that all samples reach a maximum lifetime, or close to it, after 60 minutes. However, it seems reasonable to suppose that the optimum gettering time would exhibit some dependence on the substrate resistivity, considering the stronger thermal degradation in the lower resistivity samples. More experiments close to the 60 minute point may reveal such a dependence more explicitly, with more heavily-doped samples expected to require shorter gettering times.

After gettering for 60 minutes, recombination lifetimes were typically two to three times higher than in the untreated wafers. Of particular note are the results for the 0.2Ωcm material, which exhibited lifetimes above 20μs in one case. Such a bulk lifetime corresponds to an implicit open-circuit voltage of around 670mV for a 185μm thick cell. Of course the challenge with achieving such voltages in practice lies in minimising the thermal degradation of the lifetime during subsequent cell processing. Chapter 4 presents results of PERC cells made on

this 0.2Ωcm material, with the best result being a V_{OC} of 649mV for a 185μm thick cell without antireflection coating. The loss of voltage is due precisely to thermal degradation during oxidation for rear surface and emitter passivation. Stocks[102] and Kerr[103] have measured V_{OC} =659mV and 655mV respectively in slightly thicker cells made with this material, but with antireflection coatings, as described in Chapter 4.

These gettering results are relevant for any attempt to introduce gettering steps into commercial cell fabrication processes, which have previously been seen as undesirable due to the long gettering times required. This work shows that, particularly for low resistivity wafers, long gettering times (more than one hour), are not only unnecessary but actually detrimental. Further reductions in gettering time can potentially be achieved as industry moves towards thinner substrates. However, there still remains the challenge to develop an industrially feasible cell fabrication process that is capable of fully exploiting high bulk recombination lifetimes. One such candidate is the buried contact sequence[3], and its application to mc-Si is actively being studied[11].

2.4.3 Physical origin of thermal degradation

It would be of great value to have a clear understanding of the physical cause of the observed thermal degradation. As mentioned above, one proposed explanation is based on the dissolving of metallic precipitates, which inject interstitial metallic ions into the bulk, resulting in a reduced recombination lifetime[71]. This process, sometimes referred to as metallic ‘poisoning’, is essentially the reverse process of intrinsic precipitation gettering described in section 2.2. In this section we firstly examine the precipitate dissolution model and its applicability to the mc-Si wafers studied here, and finally consider an alternative explanation based on a change in the crystallographic quality.

2.4.3.1 Precipitate dissolution model

In the precipitate dissolution model proposed by Plekhanov *et al.*[71], it was suggested that lower lifetimes can result from what is essentially an *incomplete* gettering process. In this model, slowly dissolving precipitates may actually create an *increase* in the concentration of interstitial metallic impurities, even while gettering is still active. For this to occur, the gettering temperature must be higher than the temperature of precipitate formation. Modelling of such dissociation behavior has revealed that a decrease in the recombination lifetime can be expected for constant temperature gettering treatments if the dissociation rate and metallic solubility are

Temperature (°C)	Ramp-down time from previous temperature (min)	Time at temperature (min)
1180	-	1.0
1100	11	1.5
1000	14	2.5
900	20	5
800	30	10
700	30	40

Table 2.2. Temperature and time intervals as used in the variable gettering process based on modelling performed by Plekhanov *et al.*

high enough to generate excess metallic interstitials, and subsequent cooling fast enough to ‘freeze’ them in. Such an effect provides a potential explanation for the observed thermal degradation.

Plekhanov *et al.* suggested that a significant improvement in lifetime could be gained by using variable temperature instead of constant temperature gettering. This conveniently provides a method of experimentally testing the applicability of their model to the samples studied here. The initial gettering temperature suggested is 1200°C, followed by ramping down in steps of 100°C, and remaining at each temperature for increasing periods of time. The high initial temperatures allow for rapid and near-complete precipitate dissociation, and the calculated ramping down allows the freed impurities to be gettered whilst their solubility and diffusivity are sufficiently high. It should be noted that Plekhanov *et al.* were specifically modelling Liquid Aluminium Layer (LAL) gettering, whereas in this study phosphorus gettering has been used. However, despite this apparently major difference, the two situations should be comparable due to the fact that the primary limiting mechanism in Plekhanov’s model is the dissolution of the precipitates, a process that is independent of the specific gettering mechanism used. Alternatively stated, the segregation coefficients for both LAL and phosphorus gettering are sufficiently large to ensure that precipitate dissolution remains the limiting mechanism.

In order to test the validity of the precipitate dissolution model, a variable temperature gettering procedure was performed on 0.2 and 1.0Ωcm mc-Si wafers, according to Plekhanov’s regime. Table 2.2 lists the times used at each temperature and the intervals between each temperature. The latter values are longer than those modelled by Plekhanov due to the inherently slow cooling rate of the furnace used, but this extra time should actually result in more complete gettering, as mentioned in Plekhanov’s article. The sheet resistance of the final gettering diffusion was 2.2Ω/□.

The bulk recombination lifetimes after the variable temperature gettering step are given in Table 2.3. For comparison, values for sister wafers given the standard 900°C constant

Wafer, resistivity (Ωcm)	τ after variable temp. getter (μs)	τ after 900°C getter (μs)
E4A, 0.2	7	17
E4D, 0.2	9	22
12B, 1.0	56	46
12D, 1.0	79	97
78D, 1.0	73	159
78B, 1.0	20	54

Table 2.3. Bulk lifetimes of various mc-Si wafers after the variable temperature and the standard 900°C gettering processes.

temperature gettering for 60 minutes are also shown. For the 0.2 Ωcm wafers, the variable temperature gettering lifetimes of 7 and 9 μs were as low as those in non-gettered material (see Figure 2.9). For the 1.0 Ωcm material there is also no improvement in gettering efficiency, and in fact they also seem to yield poorer lifetimes. The results indicate that the degradation of the lifetime is not caused by precipitate dissolution, at least not by precipitates with properties similar to those modelled by Plekhanov *et al.* It is of course possible that the precipitates present in these samples have a dissociation energy much larger than those authors used. If this were true, however, a much longer gettering time, even for variable temperature gettering procedures, would be required. Unfortunately, little information is currently available concerning the magnitudes of such dissociation energies.

A further manifestation of the inappropriateness of the precipitate properties used by Plekhanov when explaining the observations presented here is evident in Figure 2.9. For constant temperature gettering at 900°C, the reduction in lifetime should occur within a time frame of 10 to 100 seconds according to the modelled results of Plekhanov. However, Figure 2.9 reveals that this process occurred in a time scale of something like 100 minutes for the mc-Si samples studied. These considerations suggest that either the precipitates are much more strongly bonded than assumed in the modelling, or that the thermal degradation is caused by some other mechanism.

One final important inadequacy of the precipitate dissolution model is that it does not provide an insight into the cause of the observed dopant density dependence of the thermal degradation. Given these facts, an alternative explanation for the observed behaviour was sought. Considering that the thermal degradation effect is absent from FZ silicon, and that one of the fundamental differences between FZ silicon and mc-Si is the presence of many more crystallographic defects in the latter, it seems natural to examine the role of these defects in thermal degradation.

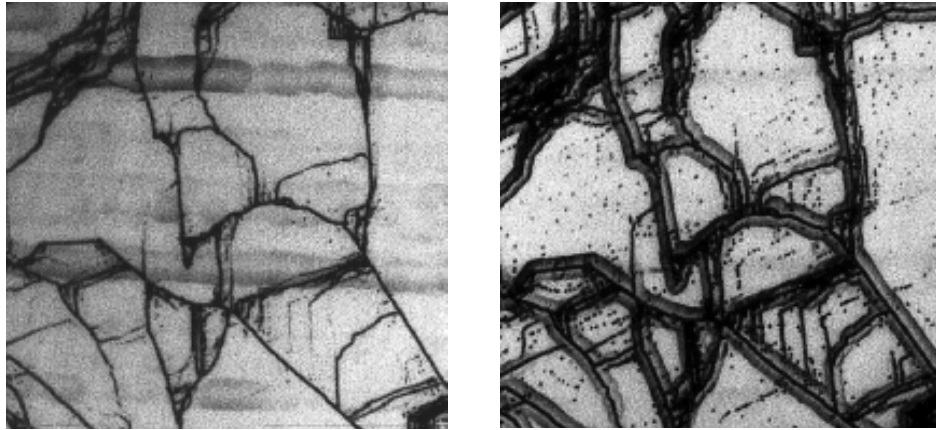


Figure 2.10. Optical images of a section of the same $0.2\Omega\text{cm}$ mc-Si wafer before (left) and after (right) a 30 minute 1050°C oxidation. The wafer has been dislocation etched to reveal dislocations as small pits. The trenches in the right-hand figure are due to a previous silicon etch. Magnification is approximately $50\times$.

2.4.3.2 Generation of crystallographic defects

In this section, the change in the dislocation density of mc-Si samples of various resistivities is monitored before and after a high temperature step, and the results discussed in relation to the thermal degradation of the low resistivity lifetimes. Dislocation etches were again performed using Yang's etch[90], which reveals such defects on crystals of various orientation.

Figure 2.10 shows optical images of a section of a $0.2\Omega\text{cm}$ mc-Si wafer before and after a 1050°C oxidation. Initially, the sample was bright-etched in a HF/HNO_3 solution to obtain a smooth surface, and then dislocation etched. The first image reveals grain boundaries and a few dislocations distributed within the grains on the sample before oxidation. The wafer was then HF/HNO_3 etched again to obtain a fresh surface, and oxidised. This second etch resulted in trenches along the grain boundaries due to the very closely packed defect etch pits there. After oxidation and lifetime measurement, the oxide was etched off, and about $20\mu\text{m}$ of silicon etched from the surfaces with HF/HNO_3 to remove any surface damage acquired during oxidation. The samples were then finally dislocation etched once more. The trenches from the second etch remained, and are evident in the second image, which was taken after the final dislocation etch. Nevertheless, the trenches do not obscure the clear increase in the concentration of dislocations within the grains, and in several places new grain boundaries have propagated.

A $1.4\Omega\text{cm}$ mc-Si sample was subjected to the same treatment as above, and although in some places the dislocation density increased, in general there were much fewer new dislocations than in the $0.2\Omega\text{cm}$ case. A tentative explanation of the source of these dislocations might be the large mismatch factor of boron in silicon, coupled with existing stresses in the

multicrystalline structure, which may result in dislocation creation at high temperatures or during rapid temperature changes (such as during cool-down). Considering that these thermal degradation effects were not observed in FZ silicon, it seems that existing grain boundaries and other crystallographic defects in mc-Si act in some critical way as seeding sites for dislocation creation.

Further indirect evidence in support of an increase in dislocations comes from the fact that the trap density increases in the heavily degraded 0.2 Ω cm samples, as mentioned in section 2.4.1.2. Work presented in Chapter 3 establishes a correlation between the presence of trapping states and dislocations[104].

Whether the increase in the dislocation density is directly related to the thermal degradation of the lifetime, or merely a coincidental occurrence, is not conclusively established by the results presented here. However, it seems a plausible, if speculative, alternative to the dissolution of precipitates model. In reality it may be that some combination of the two mechanisms occurs, whereby increased mobility of metallic impurities and a greater concentration of dislocations results in more widespread decorated defects, which would certainly contribute to a reduced recombination lifetime.

2.5 Gettering of BPSolar multicrystalline silicon ingots

Section 2.3 discussed the response of two cast mc-Si ingots produced by Eurosolare to phosphorus gettering. As a result of that initial work, it was realised that more samples along the ingot length should be studied to reveal the detailed gettering trends. Unfortunately, as mentioned, wafers from other regions were not available for those ingots. As a result, a more comprehensive gettering study was performed on wafers from two ‘bricks’ (11 \times 11cm blocks) cut from standard cast mc-Si ingots (of resistivity 1 Ω cm and 1.5 Ω cm) produced by BPSolar.

In the previous study of Eurosolare wafers, the gettering temperature and time used was 900°C for 3 hours. In light of the results of the gettering optimisation work in section 2.4, it seemed that this treatment may have been excessive. Therefore, a series of gettering experiments at lower temperatures and shorter times were performed on the new BPSolar material to determine the optimum gettering regime. Temperatures of 850, 870 and 900°C for times of 30 and 60 minutes were tried.

Another important driving factor behind conducting these cooler and shorter gettering experiments was the observation that the commercial belt diffusion for emitter formation at BPSolar’s plant in Villawood, Sydney, also produced effective gettering. Their phosphorus diffusion process consists of coating one side of the wafers with a phosphorus source at room

temperature and feeding the wafers onto a conveyor belt that takes them through a large quartz furnace. The diffusion time is 10-15 minutes and the temperature 860-880°C. The resulting sheet resistance of the diffused layer is approximately 45-70 Ω/\square . Such diffused regions proved, in some cases, to be as effective at getting as our laboratory based POCl₃ diffusions. A more detailed comparison between the getting action of these two types of diffusion is given elsewhere[105,106].

When attempting getting at lower times and temperatures with POCl₃ diffusions, it is important to maintain a reasonable level of phosphorus incorporation into the wafers. This is generally not a consideration for the commercial belt diffusion, since the surfaces are completely saturated with phosphorus. The main driving factors for phosphorus incorporation at a given temperature are the percentage of POCl₃ in the furnace and the oxygen/POCl₃ ratio. A lower than usual O₂ concentration of 1.1% and a relatively high 0.2% POCl₃ were used here, in comparison with the usual 7% and 0.1% as used in section 2.4.2.1. These conditions resulted in heavier diffusions than would be obtained under normal flow rates, and produced a sheet resistance of about 70 Ω/\square at 870°C for 30 minutes and also at 850°C for 60 minutes. Both these getting steps resulted in almost identical improvement of the electronic quality, and proved to give the best results of the various conditions examined. The improvements after getting at 900°C for 30 and 60 minutes and at 870°C for 60 minutes were marginally less, possibly due to slight thermal degradation. However, the results after getting at 850°C for 30 minutes revealed that getting was incomplete in that case.

Once again, surface passivation was achieved by the standard light phosphorus diffusion at 840°C followed by a short oxidation at the same temperature, and a forming gas anneal at 400°C. The fact that the 850°C getting step for 30 minutes produced incomplete getting suggests that this passivation step should cause even less getting, which is of course desirable in order to measure the change in lifetime before and after the deliberate getting step. The expected getting action of the passivating diffusion is further reduced considering that the oxygen and POCl₃ flows were returned to normal, resulting in significantly less phosphorus incorporation. Indeed, the following section presents evidence that indicates the getting effect of the passivating diffusion is minimal. After the intentional getting diffusion, the wafers are etched 5-10 μm per side to remove the heavy diffusion and then passivated again by the standard 840°C diffusion and thermal oxidation process.

The result of getting at 870°C for 30 minutes is shown in Figures 2.11 and 2.12 for the two different ingots. The values shown are the average of four measurements taken in each quarter of the large 11×11cm wafers provided by BPSolar. There was significant variation between these quarters, with one quarter in particular consistently showing lifetimes approximately half those of the other quarters. It is quite possible that this particular quarter was

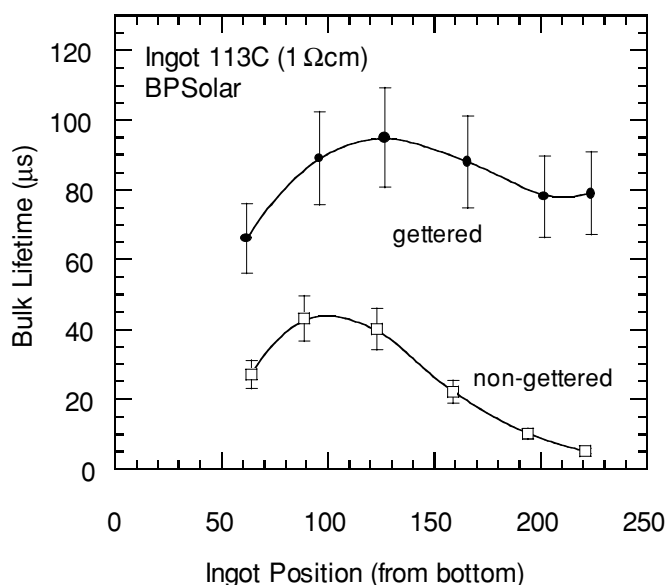


Figure 2.11. Response of a 1Ωcm BPSolar mc-Si ingot to gettering at 870°C for 30 minutes.

in fact the very corner of the ingot from which the smaller bricks were cut. Note that the brick from ingot 113C (Figure 2.11) did not include wafers below number 60, since these are routinely recycled after casting. The reason for this is revealed by ingot 94G (Figure 2.12), which shows that these wafers have low bulk lifetimes that do not respond to gettering. For wafers from other parts of the ingots, gettering resulted in an increase of the lifetime. This improvement is particularly important for the regions that showed a low lifetime before gettering (top of the ingot), bringing their quality up to essentially the same level as the other regions. These results are referred to again in Chapter 4, where the performance limitations imposed by various elements of the industrial cell process are measured and compared.

It should be noted that the response of these two ingots is in some significant respects contrary to that observed in the Eurosolare material. There is a large region at the bottom of the BPSolar ingots that does not improve after gettering, whereas the corresponding Eurosolare wafers improved dramatically. Dislocation density etches of the BPSolar ingots revealed that they had very low dislocation densities at the bottom, as did the Eurosolare wafers. However, it seems that for the BPSolar ingots there must have been a high density of other micro-defects that dominate the lifetime and/or prevent effective gettering of the impurities. The response from wafers at the top of the ingots was also opposite for the two manufacturers. The Eurosolare material remained very low, while the BPSolar wafers improved significantly. This is again most likely due to different crystallographic defect profiles of the two types of material. Dislocation etches over the full length of the BPSolar ingots revealed that they were in general less dislocated than the Eurosolare material[107]. The possibility of some of the ingots being

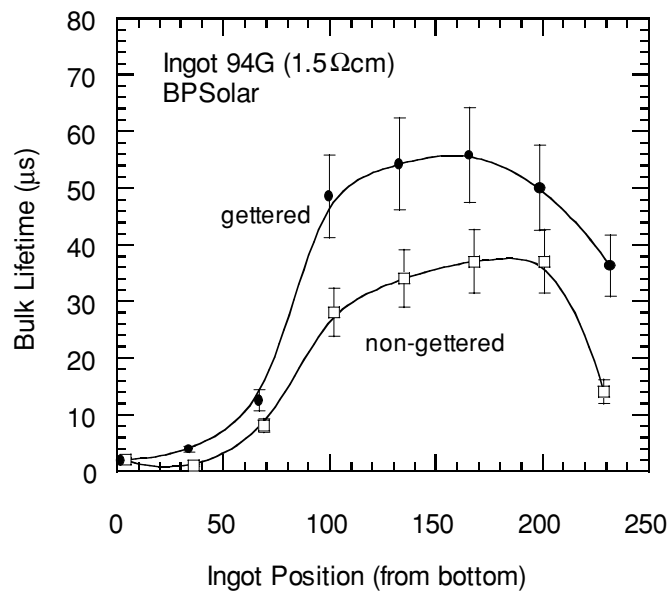


Figure 2.12. Response of a 1.5Ωcm BPSolar mc-Si ingot to gettering at 870°C for 30 minutes.

labelled back-to-front was discounted by measuring the slight decrease in resistivity from the bottom to the top of an ingot, which arises from boron segregation.

In general, these results highlight the strong influence of the casting process on the electronic properties of the wafers. Hence, the conclusions reached in section 2.3 regarding Eurosolare material are not necessarily valid for mc-Si grown by other manufacturers, unless the growth techniques are known to be very similar.

2.6 Gettering of a ‘black-out’ multicrystalline silicon ingot

In this section a further study of a more complete Eurosolare ingot than that studied in section 2.3 is presented, with the added difference that the ingot in question suffered from a power black-out approximately half way through the casting process. This black-out resulted in disturbance to the crystallography of the upper half of the ingot, leading to some interesting gettering properties which can be understood in terms of the previous conclusions. This ingot had a resistivity of 0.9Ωcm, and so should not be overly subject to the thermal degradation effects discussed previously.

A further aim of this third study was to verify that two assumptions heavily relied upon in the previous studies were in fact valid. The first of these assumptions was that the light phosphorus diffusion (840°C for 25 minutes) and oxidation used to passivate the wafers for the initial ‘non-gettered’ lifetime measurement did not itself cause significant gettering. Some

evidence for this came in section 2.5 in which gettering at 850°C for 30 minutes was found to be incomplete. However, it is important to verify that any gettering arising from the passivating diffusion was minimal, not merely incomplete. This was examined by initially passivating the samples with a thin steam oxide grown at 800°C for 60 minutes. This low temperature was chosen to avoid excessive thermally activated defect reactions which may alter the pre-gettered lifetime. However, while allowing faster growth at lower temperatures, steam oxide passivation is generally of poor quality in comparison to other oxide growth methods, even after a forming gas anneal. Fortunately, it can be greatly improved by depositing corona charges onto the oxide surface. In this way it was possible to measure the pre-gettered bulk lifetimes and compare them to those obtained with the passivating light phosphorus diffusion.

The results are presented in Figure 2.13. The oxidised results represent the corona-charged steam oxide passivation on non-gettered wafers. In comparison, data for the light phosphorus passivating diffusion reveal that indeed some gettering has occurred despite the very light nature of the diffusion (about $250\Omega/\square$). However, significantly more gettering occurs during the subsequent three hour gettering step, and so broadly speaking the gettering trends established in the study in section 2.3 are valid, although the magnitudes of the non-gettered lifetimes may be somewhat overstated.

All effective lifetimes were measured at an excess carrier concentration of $5 \times 10^{15} \text{cm}^{-3}$. Once again FZ controls were included to ensure that surface passivation was adequate enough to allow the effective lifetimes measured on the mc-Si wafers to be interpreted as bulk lifetimes. Although this was expected to be true for the previously well characterised light passivating diffusion and thin oxide, it was important to verify this for the low temperature steam oxide. A $1\Omega\text{cm}$ FZ wafer with the steam oxide and FGA yielded a lifetime of $122\mu\text{s}$ at an excess carrier concentration of $5 \times 10^{15} \text{cm}^{-3}$. After corona charging, this value doubled to $250\mu\text{s}$, implying sufficient passivation. As a comparison, the corresponding effective lifetimes of FZ wafers after the standard passivating conditions, after gettering/etching/re-passivating, and after double gettering/etching/ re-passivating, were 250, 275 and $310\mu\text{s}$ respectively.

The second assumption was that the gettering action after the three hour gettering step was ‘complete’ in the sense that further improvements could not be made (excluding the possibility of improvements from very long gettering times due to dissolving precipitates, as modelled by Plekhanov). This was tested by simply applying a second three hour gettering treatment to the wafers, etching the diffusion and re-passivating again. Figure 2.13 also shows results for these double-gettered samples. The lifetimes did not increase after this second gettering step, implying that the initial three hour treatment was sufficient to ‘complete’ gettering, at least of any easily getterred non-precipitated impurities. Some of these wafers in fact appear to have suffered a reduction in lifetime.

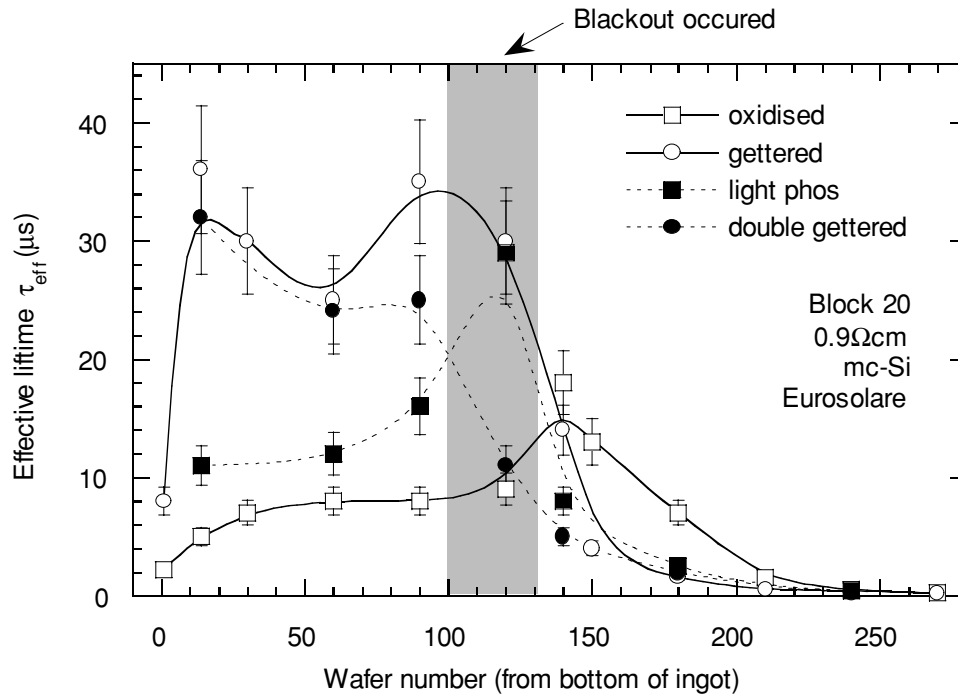


Figure 2.13. Bulk lifetime measurements of wafers from a cast mc-Si ingot that experienced a power black-out during growth. Measurements are shown for as-cut wafers (oxidised) lightly phosphorus diffused, gettered and double gettered.

The other obvious feature of this plot is the rapid decrease in all lifetimes after the black-out occurred. This is most likely due to a large increase in the density of crystallographic defects caused by the uncontrolled solidification rate, although the visible appearance of the wafers does not change significantly. These defects ‘trap’ impurities such that they can not be easily gettered, as discussed previously. However, there is a further interesting observation to be made from the post black-out data. The wafers in this region appear to suffer from thermal degradation of the bulk lifetime, as evidenced by reductions after the light phosphorus diffusion and again after the gettering treatment. This is consistent with the suggestion that thermal degradation is related to the crystallography, and that dislocations and other defects may help to ‘seed’ further defect propagation during high temperature steps.

One final observation to be made from Figure 2.13 is that the full response to gettering of this Eurosolare ingot occurs almost from the very bottom. Ingot 8 in section 2.3 had a larger region of lower post-getter lifetimes, while the relevant data was missing for ingot 6, the standard ingot.

2.7 Gettering of Edge-defined Film-fed Growth (EFG) multicrystalline silicon

The mc-Si studied so far in this chapter was grown by directional solidification of large ingots, which were then sawn into bricks and subsequently wafered. However, there exist other techniques of silicon growth which result in substrates with similar grain structure and hence are also classified as mc-Si. These techniques, collectively known as ‘ribbon silicon’, are fundamentally different in that they produce silicon in sheets or ‘ribbons’ directly from the melt, which are then diced into smaller wafers. There are obvious cost benefits in this approach due to eliminating the expensive and wasteful wire-saw step needed to create wafers from a solid ingot. Unfortunately, due to the nature of the crystallisation process for ribbon silicon methods, the recombination lifetimes tend to be shorter than for cast mc-Si[56]. The primary reasons for this are that the temperature profiles during crystallisation are much more difficult to control than for bulk ingots, resulting in high dislocation densities. Also, each wafer is in closer contact with potential contamination sources, namely the gaseous atmospheres and any dies used to define growth. Currently there are three main ribbon silicon growth methods used commercially[108]: Edge-defined Film-fed Growth (EFG) manufactured by ASE Americas, dendritic web silicon made by Ebara Solar, and string ribbon silicon produced by Evergreen Solar. Two other techniques, namely Ribbon Grown on Substrates (RGS, made by Bayer) and Silicon Sheet from Powder (SSP, various institutes, see reference [108]) are currently being actively pursued at the research level.

EFG material has shown promise as a cost-effective alternative to cast mc-Si that can still achieve reasonable efficiencies (around 14% routinely[109]). It can be grown relatively thinly, especially when grown as a cylinder[110] (75-100 μm), which reduces the required diffusion length for a given efficiency, and the loss rate of input silicon is very low (less than 13%). The density of crystallographic defects is high however, with many dislocations and twin arrays, although many of these are relatively inactive electrically[109].

A recent study of EFG material by Rohatgi *et al.*[56] showed that phosphorus gettering improved the bulk lifetime, but only from an initially low 1-2 μs to about 3-5 μs . A greater improvement could be achieved by simultaneous phosphorus and LAL gettering (up to 7-15 μs). The lifetime could be increased again through synergistic hydrogenation effects arising from an 850°C simultaneous anneal of an aluminium layer and a SiN_x layer. This process resulted in lifetimes of 12-26 μs for the 3 Ωcm material. In this section, phosphorus gettering of EFG material is examined and the results compared to these previous studies. In particular, a lower temperature hydrogenation method is applied which produces similar lifetime improvements

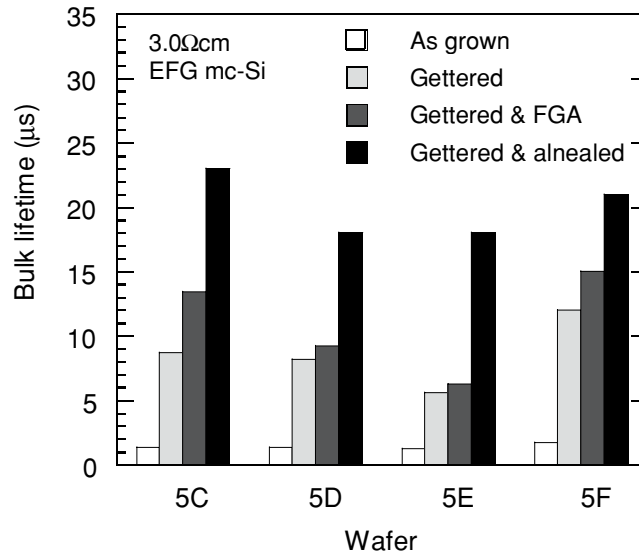


Figure 2.14. Bulk lifetimes measured at an excess carrier concentration of $1 \times 10^{15} \text{ cm}^{-3}$ for four EFG mc-Si wafers. Results are shown for the as-grown state, gettered, gettered with forming gas anneal (FGA), and gettered with 'alneal'.

without the presence of a LAL. Also, Secondary Ion Mass Spectroscopy (SIMS) is applied to the phosphorus gettering layer in an attempt to identify the gettered impurities.

2.7.1 Results and discussion

Figure 2.14 shows the results of the gettering treatment on four separate 3Ωcm EFG samples. The as-grown lifetime measurements were estimated using the QSSPC technique on the samples with no surface passivation treatment. This was made possible by the very low magnitude of the bulk lifetime, although it was necessary to use infrared light for these measurements, since white light results in most of the generation occurring close to the surface, which decreases sensitivity to the bulk. Assuming infinite surface recombination velocities, a wafer of thickness W (cm), with *steady-state uniform generation* (provided by infrared light), will yield an effective lifetime given by the following expression[30], as discussed in section 1.1.4:

$$\frac{1}{\tau_{eff}} = \frac{1}{\tau_b} + \frac{12D_n}{W^2} \quad (2.1)$$

where D_n is the electron diffusivity ($\approx 31 \text{ cm}^2/\text{s}$ for 3Ωcm material). The second term on the right is referred to as the transit time, which represents how long it takes the generated carriers, on average, to diffuse to the surfaces where they instantly recombine. By measuring the effective lifetime, Equation 2.1 can be then used to calculate the bulk lifetime. In the case of finite

surface recombination velocities, which is more representative of wafers with native oxides present, Equation 2.1 can be expressed as an inequality, providing an upper limit for the bulk lifetime:

$$\frac{1}{\tau_b} > \frac{1}{\tau_{eff}} - \frac{12 D_n}{W^2} \quad (2.2)$$

Equation 2.2 has been used to calculate the as-grown lifetimes of Figure 2.14, which are strictly only upper bounds. Note that in using infrared illumination, the absorbed fraction f_{abs} , an important parameter in the QSSPC lifetime calculation, must be known, since it may differ significantly from that for white light. By calibrating against samples of known electronic properties, the absorbed fraction for the EFG samples (thickness of 300 μ m) was found to be 0.52, compared with 0.68 for white light. This lower value is primarily due to extra transmission through the wafer thickness.

The reported lifetimes were all taken at a carrier density of $1 \times 10^{15} \text{cm}^{-3}$ to avoid trapping effects, and to allow direct comparison with the results of Rohatgi *et al.* who also used this value. This relatively low value is made possible by the fact that, in general, the EFG samples exhibited lower trap densities than the cast mc-Si discussed in the previous sections. This may be at least partially due to the lower boron concentration, which is often correlated with the trap density as discussed in Chapter 3.

Phosphorus gettering was performed using a high POCl_3 flow at 900°C for 60 minutes, resulting in a sheet resistance of 25 Ω/\square . This treatment was chosen as a result of the gettering time optimisation of section 2.4.2. After gettering, the heavy diffusion was etched off in dilute HF/HNO_3 solution, and the standard light phosphorus diffusion (250 Ω/\square) and thin in-situ oxide grown for surface passivation. At this stage the lifetimes were measured again, and the results are depicted as ‘gettered’ in Figure 2.14. Due to the presence of surface passivation and the longer bulk lifetimes, white light was used for these measurements, and all subsequent ones, due to its greater ease of use. 1 Ωcm FZ control samples were included in the batches to monitor the effectiveness of the surface passivation. After the light diffusion and thin oxide passivation they yielded a lifetime of 80 μs , suggesting they were subject to some cross-contamination, but nevertheless indicating that the values measured on the EFG wafers are again essentially bulk lifetimes.

The as-grown bulk lifetime upper limits ranged from 1.3-1.7 μs , in good agreement with the values determined by Rohatgi *et al.* on the same material (1-2 μs)[56]. However, the post gettering lifetimes in Figure 2.14 are longer than those reported by Rohatgi (6-12 μs compared to 3-5 μs). This discrepancy is most likely due to the different gettering treatments used: Rohatgi *et al.* used a spin-on dopant source diffused at 925-930°C for 6 minutes, resulting in a lighter

gettering diffusion of $45\Omega/\square$. After a concurrent phosphorus and aluminium gettering step, however, they achieved $7\text{--}15\mu\text{s}$, comparable to our phosphorus gettering alone. Note that all these post-gettering lifetime values are substantially lower than corresponding values for cast mc-Si (in the range $30\text{--}60\mu\text{s}$ for the standard Eurosolare ingot in section 2.3), despite the higher resistivity of the EFG material.

As mentioned above, hydrogenation of bulk defects can lead to further substantial increases in the lifetime of EFG and other ribbon silicon materials, as well as cast mc-Si. To achieve this type of passivation, there needs to be sufficient atomic hydrogen diffusing through the bulk during the relevant annealing step. In the work by Rohatgi *et al.*, this atomic hydrogen was generated by a thin Plasma-Enhanced Chemical Vapour Deposited (PECVD) film of SiN_x applied to the front of the wafers (on top of the diffusion). These films are rich in hydrogen due to the presence of silane and often also ammonia during their deposition. During annealing the hydrogen is injected into the silicon in the form of molecular and atomic hydrogen. The proportion of atomic hydrogen is apparently increased by the interaction of silicon interstitials[111], which are generated by the simultaneous alloying of aluminium on the opposite surface, with the molecular hydrogen. The net result is a larger concentration of atomic hydrogen diffusing throughout the wafer bulk, passivating defects in the process.

To investigate alternative ways of generating similar increases in the bulk lifetime, two different methods that may introduce atomic hydrogen into the bulk were tried, and the results are also shown in Figure 2.14. The first was through the application of a forming gas anneal (FGA) at 400°C for 30 minutes. The forming gas used contains 5% molecular hydrogen diluted in argon, and so it is not immediately clear that atomic hydrogen will be present in the wafer in significant quantities. However, a FGA is well known to reduce the density of recombination centres at the oxide interface by passivating dangling silicon bonds with atomic hydrogen, and consequently reduces the surface recombination velocity[28]. Accordingly, the control FZ wafer included in the experiment increased in effective lifetime from 80 to $185\mu\text{s}$ after a FGA. It seems possible then that this presence of atomic hydrogen may also passivate bulk defects.

The results in Figure 2.14, labelled ‘gettered & FGA’, show, however, that any such bulk passivation is minimal. In fact the very slight increase in lifetime is most likely due to improved surface passivation. This suggests that the availability of atomic hydrogen is low using a standard FGA process, although sufficient to passivate the relatively few and more easily accessible interface defects. Certainly the diffusivity of atomic hydrogen at 400°C is large enough to ensure it diffuses throughout the wafer bulk if present. Stavola[112] cites a diffusivity value of $D_H=2.3\times 10^{-6}\text{cm}^2\text{s}^{-1}$ at 400°C , which implies a diffusion length of $200\mu\text{m}$, enough to penetrate to the centre from each side, after only three minutes. Vyvenko *et al.*[57] also recently

showed that atomic hydrogen introduced by remote hydrogen plasma was sufficiently diffusive at 310°C to penetrate about 100µm into the bulk of cast mc-Si wafers after 60 minutes.

The second attempt to incorporate atomic hydrogen was by ‘alenealing’, in which a layer of aluminium (1000Å in this case) is evaporated onto the surfaces before applying the FGA as usual. This technique is often used to achieve very low surface recombination velocities for oxides, either on diffusions or on bulk silicon, in high-efficiency devices[28]. The improved passivation of interface states arises from the greater availability of atomic hydrogen, caused by residual water vapour within the aluminium. Indeed, as the anneal temperature is lower than the aluminium/silicon eutectic temperature, the generation of atomic hydrogen can not be due to interstitials injected by alloying of the aluminium. Nevertheless, the significant lifetime increases shown in Figure 2.14 are testimony to the greater availability of atomic hydrogen. In fact, the alenealed lifetimes are comparable to those measured by Rohatgi after their bulk hydrogenation step, supporting their interpretation of the results. A second alenealing step with a fresh aluminium layer for a further 30 minutes resulted in no further increase in the lifetime, suggesting that the bulk passivation had ‘saturated’.

2.7.2 SIMS analysis of gettering layer of EFG material

Naturally it would be valuable to identify the impurities present in the as-grown EFG material. One approach is to apply Secondary Ion Mass Spectroscopy (SIMS) to the surface of a wafer that has been phosphorus gettered, with the heavy gettering diffusion remaining. SIMS is well suited to this application since it can analyse impurities to a depth of a few microns, deep enough to traverse most diffusion profiles. Another advantage is that the gettering action of the diffused layer significantly increases the concentration of impurities in the near-surface region, making them more easily detected. This is a critical factor in analysing metallic impurities in silicon, since their bulk concentration is typically less than 10^{14}cm^{-3} . Assuming this value, if all the impurities are gettered to the top half a micron in a 300µm wafer, the resulting concentration in that thin layer would be $6 \times 10^{16}\text{cm}^{-3}$, which is approximately the sensitivity limit of SIMS. The gettering action then ‘magnifies’ the sensitivity of SIMS by more than two orders of magnitude.

Figure 2.15 shows the SIMS profile for an EFG wafer with the gettering layer intact. The traces for Fe and Cr are inconclusive and may be affected by surface contamination during sample mounting. However, the Cu trace is much more significant and is most likely due to gettering from the bulk. Using numerical phosphorus diffusion models that account for the well known concentration-dependent diffusion induced ‘kink’[113-115], the junction depth after the

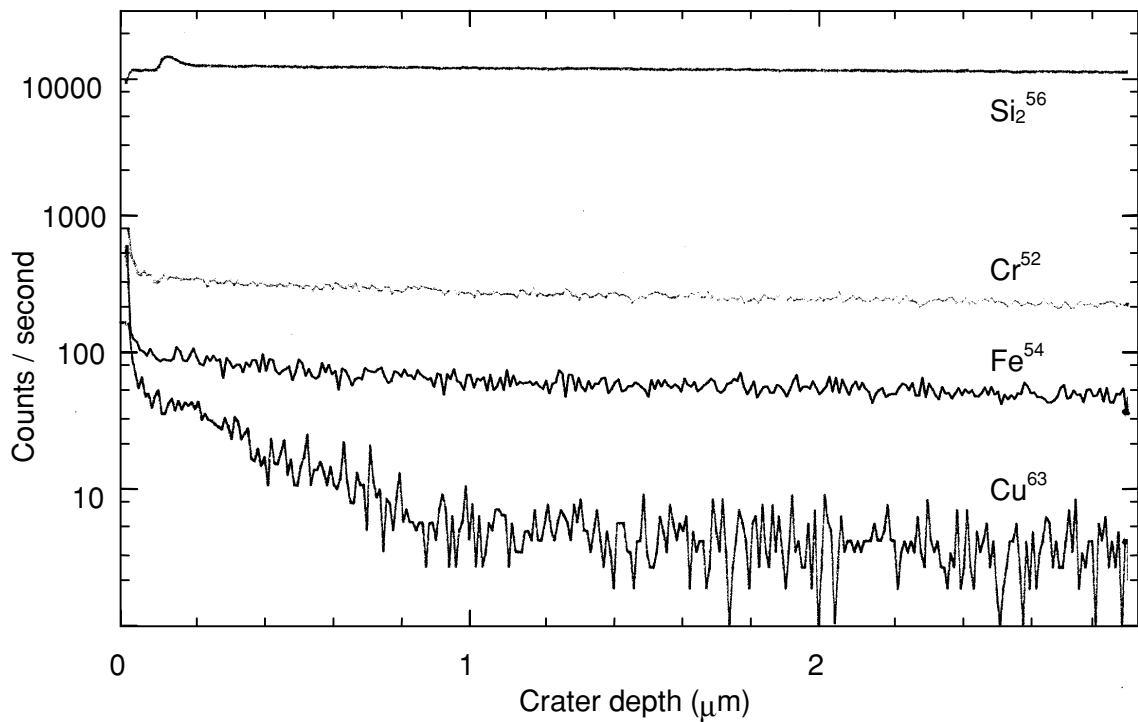


Figure 2.15. SIMS profile of an EFG mc-Si wafer with the phosphorus gettering layer still present. The junction depth is expected to be approximately $1.2\mu\text{m}$.

gettering diffusion is estimated to be $1.2\mu\text{m}$, in good agreement with the observed Cu profile. By comparison with profiles from samples of known Cu content, the results suggest an approximate equivalent Cu dose of 10^{13} - 10^{14}cm^{-2} , corresponding to a bulk concentration of 3×10^{15} - $3\times 10^{16}\text{cm}^{-3}$. These are high concentrations, and suggest that the recombination strength of the Cu centres, whether in the form of precipitates, substitutional or interstitial Cu, or even as Cu-Cu pairs[116], is low. By comparison, using the SRH recombination formula and the relevant energy levels and capture cross-sections of Chapter 5, a concentration of $3\times 10^{15}\text{cm}^{-3}$ of interstitial Fe would result in a lifetime of merely $0.07\mu\text{s}$ at an excess carrier concentration of $1\times 10^{15}\text{cm}^{-3}$, compared with the measured value of approximately $1.5\mu\text{s}$. This latter point is discussed further in Chapter 4 in connection with similar SIMS analysis on cast Eurosolare mc-Si wafers, which revealed the presence of both Fe and Cr, but not Cu.

Previous studies of the effect of Cu contamination have indeed shown that, at least in p-type silicon, Cu produces relatively weak recombination centres[116]. In fact, work by Naito and Nakashizu[117] revealed that for surface doses of the order 10^{13} - 10^{14}cm^{-2} , Cu related centres were about 2 orders of magnitude weaker than was the case for Fe, in broad agreement with the approximate calculations above. Hence it seems plausible that the high levels of Cu found in the EFG material could be responsible for the low lifetimes before gettering. Unfortunately, there is currently little consensus on values for energy levels and capture cross-

sections of Cu related recombination centres[116], making it impossible to model their impact on lifetimes using SRH theory. If such information were available, the injection-level dependent lifetime curves of the EFG samples could be used to confirm Cu centres as the lifetime killing culprits. The potential benefit of this type of lifetime analysis is the motivation behind the work in Chapter 5, where injection-level dependent lifetime curves of samples with known impurities are used to calculate their energy levels and cross-sections in order that they may be identified in ‘real’ silicon samples. For the current purposes however, it is only possible to state that Cu may be at least responsible for the low as-grown lifetimes in EFG material.

2.8 Summary

The work presented in this chapter has focused on gettering in mc-Si. Cast mc-Si produced by Eurosolare was found to respond best to gettering when the dislocation density was low and the concentration of mobile impurities high. In low resistivity mc-Si, an independent ‘thermal degradation’ of the lifetime occurs in parallel with the gettering action. Since the gettering efficiency diminishes with time, the competing mechanisms result in a resistivity-dependent optimum gettering time, after which the lifetime begins to degrade. Nevertheless, low resistivity material has potential for high efficiency cells, provided that these thermal degradation effects are kept in mind.

Previous modelling has shown that the thermal degradation may be due to dissolved metallic precipitates, which inject interstitial metals into the bulk. Variable temperature gettering experiments designed to avoid these problems actually resulted in lower lifetimes than the standard gettering treatment, implying that either the modelled precipitate properties (most likely the dissociation energy) are massively underestimated, or that the phenomenon is caused by some other mechanism. Some evidence of increased crystallographic damage after high temperature steps has been presented which may offer a plausible alternative explanation of the thermal degradation effect.

Gettering of cast mc-Si ingots produced by BPSolar was also studied. In general these wafers improved after gettering, but the details of the response were somewhat different to the Eurosolare material, reflecting the strong dependence of the electronic properties on the precise casting methods used. Finally, phosphorus gettering of EFG mc-Si, a material produced by a very different technique, was also found to result in improved lifetimes. These could be further increased by injecting atomic hydrogen into the wafer bulk. Although a different technique of hydrogen incorporation was used here, the results agree well with those from previous studies. SIMS of gettered layers of EFG material revealed that the low as-grown lifetimes may be due to Cu contamination, although this is difficult to prove conclusively due to the lack of information

available about the energy levels and capture cross-sections of Cu-related recombination centres.

CHAPTER 3

Minority Carrier Trapping in Multicrystalline Silicon

3.1 Introduction

Recombination of charge carriers in silicon at low excess carrier concentrations generally proceeds via the Shockley-Read-Hall mechanism through localised states in the band-gap, as discussed in Chapter 1. During this process, the localised states must interact with carriers from both the valence and conduction bands for recombination to occur. However, it is also quite possible for these states, by having a minutely small capture cross-section for one type of carrier, to effectively interact with only one band[17,118]. In this case, carriers are captured by the level for a certain period of time before being ejected back into the band from which they came. Such states are referred to as ‘traps’, as opposed to recombination centres, although, unfortunately, there are many instances in the literature where recombination centres are also called traps, sometimes causing ambiguity and confusion. For the purposes of this thesis, the term ‘traps’ refers to states that effectively interact with one type of carrier only.

Experimental evidence of the existence of traps came in several forms in the early 1950's. The first was through drift mobility experiments, in which the time taken for carriers to drift from one side of a sample to the other, under the influence of a small electric field, was monitored[119]. It was found that there was a significant component of carriers that 'lagged' behind, resulting in skewed arrival-time profiles and artificially low calculations of the mobility. The lagging was attributed to temporary trapping of carriers and their subsequent re-injection into their original band. In silicon, such trapping was observed at room temperature, unless the sample was under strong bias illumination, in which case the traps were said to be 'saturated'[119,120]. Trapping was also observed in drift mobility measurements of germanium at lower temperatures[121].

Very soon after, further evidence of trapping came in the form of photoconductance decay[119,120,122,123] and injected carrier decay[124] measurements in single-crystal silicon and germanium. At that time, crystal growth techniques were only just beginning to be refined. Consequently, there were many impurities and crystallographic defects present, some of which must have given rise to these trapping effects. As ingot growth techniques matured in the following decades, trapping effects disappeared in single-crystal material, and the research focus shifted to the more important recombination properties. However, with the recent advent of relatively cheap but electronically poor multi-, poly- and nanocrystalline silicon (and other compound semiconductor materials), primarily for photovoltaic applications, it is not surprising that trapping effects have re-surfaced, and are now found to be ubiquitous in many such materials. These trapping centres cause significant problems in photoconductance-based lifetime measurements by creating anomalous effects which 'mask' the recombination lifetime, a critical parameter in cell performance. Currently, these methods for measuring lifetimes are the most widely used techniques, and so an understanding of trapping effects and their impact on the photoconductance is an important field of study.

In this chapter, trapping effects in modern cast mc-Si for photovoltaic applications are examined. Their detrimental effect on photoconductance-based lifetime measurement techniques is discussed, and an old theoretical model from 1955 due to Hornbeck and Haynes[119], and also Fan[125], is modified to suit the QSSPC technique, and shown to provide a good explanation for the observed effects. The physical origin of the states that cause trapping is also explored, with the evidence suggesting that both crystallographic and impurity-related levels can act as traps. A recently proposed technique for adjusting photoconductance-based lifetime measurements to correct for the effect of traps is also examined, and found to provide a useful improvement in the carrier density range over which accurate data can be acquired. This correction technique, which often significantly improves the accuracy of lifetime measurements under standard 1-sun illumination, may prove to be useful for in-line process monitoring in industrial applications. At the end of the chapter, other recently proposed

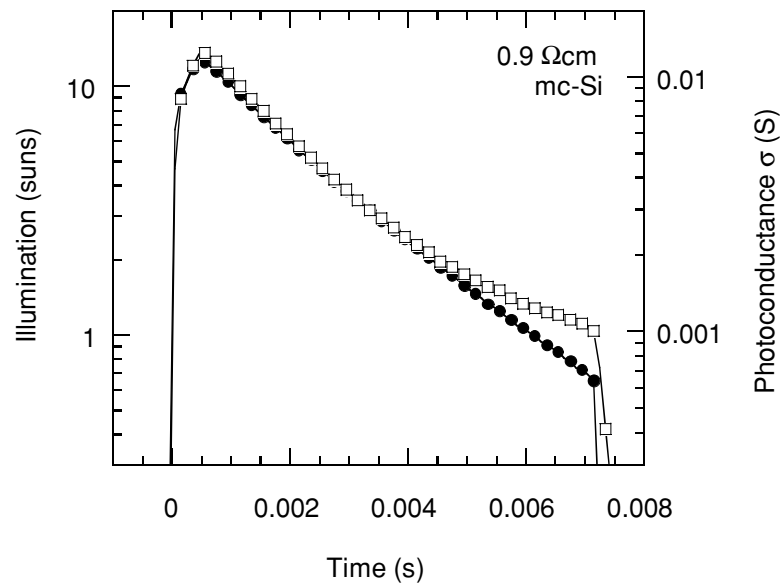


Figure 3.1. Photoconductance versus illumination for a passivated mc-Si wafer, showing the anomalous effects caused by trapping at low light intensities.

explanations for the anomalous photoconductance effects that are attributed here to trapping are discussed.

Firstly though, experimental evidence of trapping is presented, along with some initial attempts to explain the phenomena. These attempts ultimately proved to be inadequate, but nevertheless lead eventually to a more satisfactory explanation.

3.2 Anomalous QSSPC and PCD lifetimes at low excess carrier concentrations

Unusual behaviour of the photoconductance versus illumination, or, alternatively, the lifetime versus carrier density, has been observed in numerous photovoltaic materials, including cast mc-Si,[104,126], silicon ribbons[56,63,127], polycrystalline CdTe and CdS[127,128], and to a small extent Czochralski silicon[129]. In QSSPC measurements, the photoconductance ceases to decrease as rapidly as the illumination after a certain point, as shown in Figure 3.1, resulting in an ‘apparent’ recombination lifetime that increases, often dramatically, as the carrier concentration decreases. For PCD measurements, the transient photoconductance decays more slowly than the conventional exponential, resulting in a long ‘tail’ in the trace. However, although trapping affects both QSSPC and PCD lifetime measurements, the resulting lifetime curves are not in general comparable, especially at excess carrier densities well below the trap density[17,119]. These discrepancies arise from the more complex, time-dependent carrier

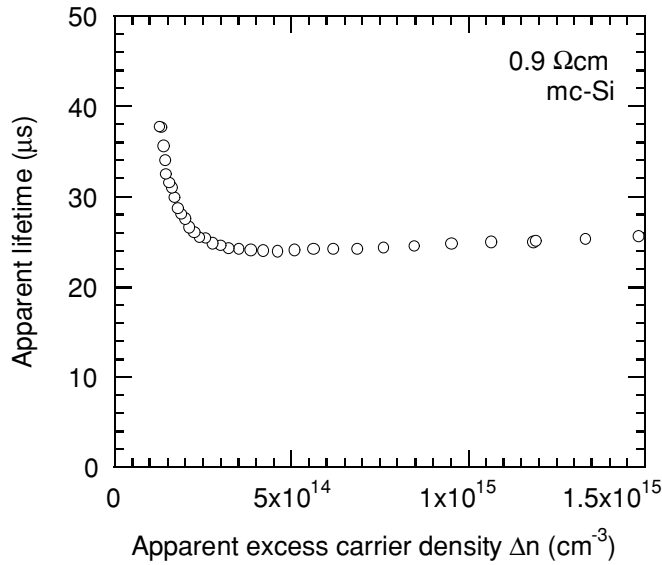


Figure 3.2. ‘Apparent’ lifetime versus excess carrier density calculated using the data in Figure 3.1.

dynamics present in transient decay mode. In this chapter, the more tractable QSSPC case is considered, although analytic expressions also exist for the transient case under certain simplifying conditions.

Figure 3.2 depicts the ‘apparent’ lifetime versus carrier density data arising from the QSSPC trace in Figure 3.1. This sample, as were all other 0.9Ωcm wafers studied in this chapter, was a Eurosolare wafer from the centre of ingot 6 as described in Chapter 2. It had been gettered for three hours at 900°C, etched, and then passivated with the standard light phosphorus diffusion (840°C for 30 minutes, giving $R_{\text{sheet}} \approx 250 \Omega/\square$) and thin in-situ oxidation (900°C for 20 minutes) followed by a forming gas anneal (400°C for 25 minutes). The high quality passivation thus achieved means the measurements reflect bulk effects. Note that for the QSSPC technique the apparent lifetime is essentially the ratio of the two curves in Figure 3.1, which results in the rapidly increasing apparent lifetime data at low carrier densities in Figure 3.2. This effect has been found to occur in every one of the many cast mc-Si wafers measured in our laboratory, although often at very different carrier densities.

If such a rapidly increasing lifetime truly reflected the minority carrier recombination lifetime, such measurements would imply improved cell performance at 1-sun illumination levels, according to Figure 3.1, and, while appearing unusual, would be greatly welcome. Specifically, the open circuit voltage, which can be predicted from a measurement of the minority carrier lifetime as described in Chapter 1, should reflect the changing lifetime data if this data is driven by minority carrier recombination. Unfortunately such an improvement is not observed, as discussed in the following section, indicating that the observed effect is not related to recombination.

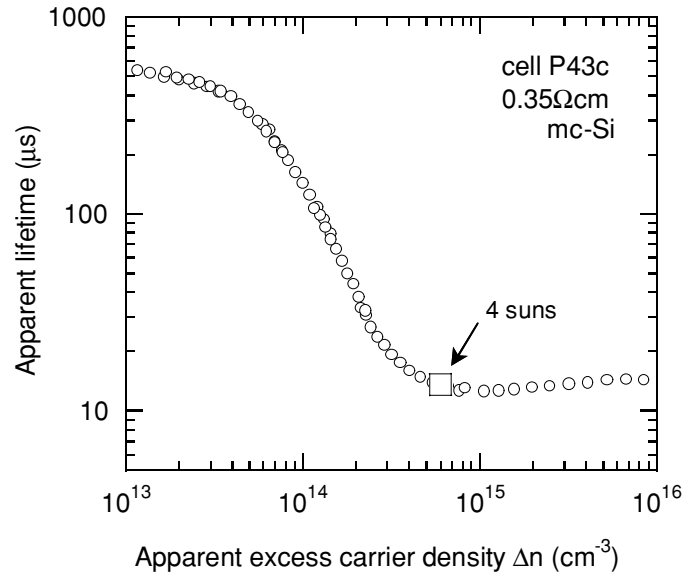


Figure 3.3. ‘Apparent’ lifetime versus excess carrier density for a 0.35Ωcm cell pre-cursor just prior to metallisation.

3.2.1 Quasi-steady-state V_{oc} measurements

The fact that the unusual low excess carrier density behaviour does not reflect recombination is well illustrated by the following example. Figure 3.3 depicts the apparent lifetime curve for a Eurosolare 0.35Ωcm cast mc-Si cell precursor, clearly showing the anomalous behaviour. Note that the apparent lifetime reaches values as high as 500μs at the lowest carrier densities. This wafer was processed as a PERL cell, identically to those described in Chapter 2. The apparent lifetime measurement was taken after etching fingers and dots through the front and rear passivating oxides respectively, but prior to metallisation. Hence the electronic properties of the wafer should not change markedly between lifetime measurement and V_{oc} measurement after metallisation. The apparent lifetime measured under 4-sun illumination is shown to act as a marker for the point at which the anomalous effect begins, in order to allow comparison with the following illumination- V_{oc} graph.

The apparent lifetime data may be used to predict how the V_{oc} should vary with changing light intensity, assuming the lifetime data reflects recombination, following the technique outlined in Chapter 1. This ‘implied’ V_{oc} curve can then be compared with the measured illumination- V_{oc} data acquired after metallisation. This comparison is shown in Figure 3.4. The results reveal that above the 4-sun illumination point, the two curves agree well, indicating that the lifetime data in this region does indeed reflect minority carrier recombination (note that the excess carrier densities are still below the dopant density of $N_A=5 \times 10^{16} \text{ cm}^{-3}$, and so we may still

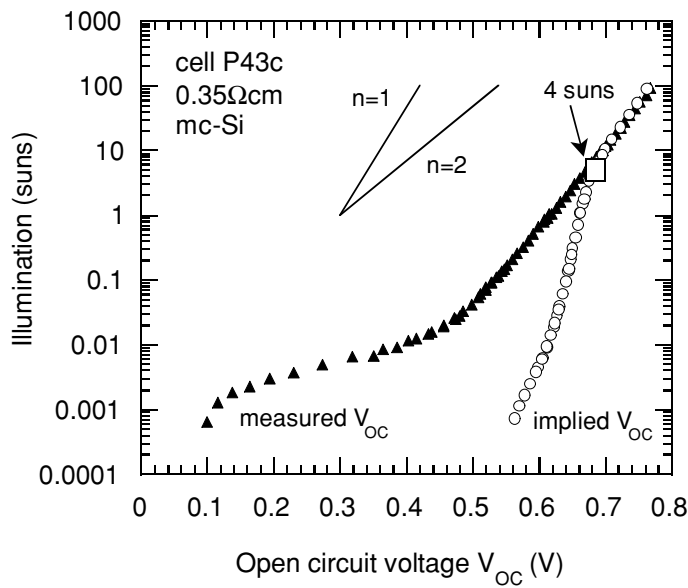


Figure 3.4. Measured and implied illumination- V_{OC} curves for the cell-precursor from Figure 3.3. Ideality factors of $n=1$ and $n=2$ are also shown.

refer to minority carriers). However, below the 4-sun point the curves rapidly diverge. The measured V_{OC} curve continues with a largely unchanged ideality factor of between 1 and 2 down to around 0.5V, below which it is affected by a shunt. This curve of course, in the non-shunted region at least, reflects the minority carrier recombination lifetime. Obviously this is not the case for the *implied* V_{OC} curve as calculated from the apparent lifetime data, which must therefore be affected by other phenomena. The next section discusses some preliminary attempts to explain the discrepancy between these two curves.

3.2.2 Long flash lifetime measurements

Initially, it seemed that the unusual behaviour may be due to ‘slow’ traps, which would fill with electrons during the high-intensity part of the flash, and then empty their electrons back into the conduction band during the remaining part of the measurement[126]. Such an effect would clearly cause the photoconductance to unduly increase at lower intensities, and hence may explain the observed apparent lifetimes. Essentially, this slow trapping model implies that the assumption of the sample being in steady-state breaks down. Fortunately, it is easily tested, since the effect of the traps ‘emptying’ will change if the decay time of the flash is altered significantly. Specifically, if a much more slowly decaying flash is used, the slow traps should have less impact on the measurement, since the number of filled and empty traps will be closer to being in steady-state for a longer portion of the flash.

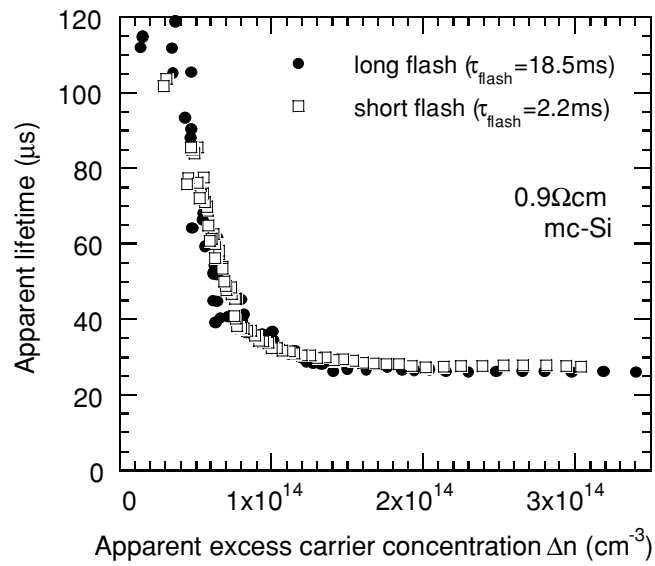


Figure 3.5. Apparent lifetime versus excess carrier density for a passivated 0.9Ωcm mc-Si wafer using two different flash decay times.

Figure 3.5 shows the results from such an experiment. Once again a getterred, etched and passivated 0.9Ωcm cast mc-Si wafer was measured using the QSSPC technique. Two exponentially decaying flashes were used, with characteristic decay times of 18.5 and 2.2ms. The results clearly show that there is no measurable difference between the onset and extent of the trapping effect. Of course, it is possible that the ‘emptying’ time of the traps is much longer than either flash decay length used, in which case the difference may not be detectable. However, if the trap emptying time were so long, it should not have time affect the measurements at all! Just to be sure, however, true steady-state lifetime measurements were also performed.

3.2.3 True steady-state lifetime measurements using staircase LED illumination

Despite their potential usefulness, true steady-state lifetime measurements are difficult to perform in practice due to potential heating of the sample. Such heating significantly alters the intrinsic carrier concentration, which can have quite profound impacts on the electronic properties of a sample. To achieve true steady-state measurements without too much heating, an infrared (950nm) LED array was employed. It could be programmed to produce light pulses of sufficient length to ensure the photoconductance reached steady-state, but still short enough to prevent heating. Furthermore, the array could produce ‘staircase’ pulses that allowed several carrier densities to be probed within each pulse, as shown in Figure 3.6.

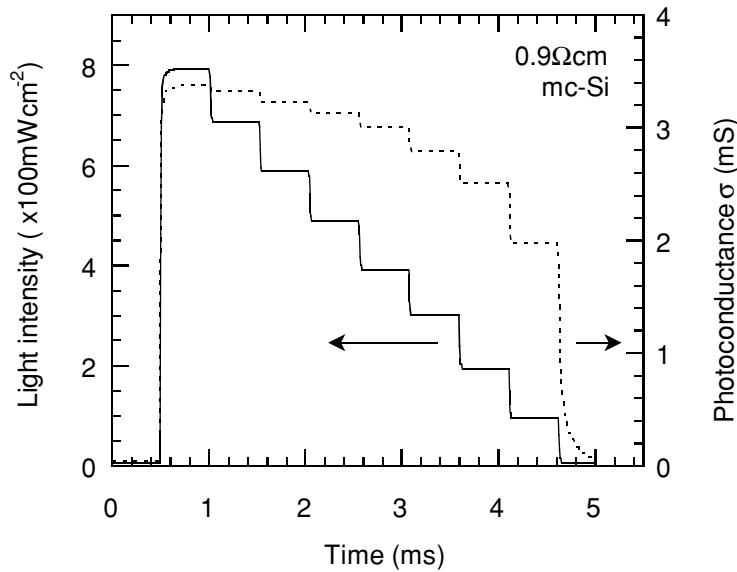


Figure 3.6. Staircase pulse and resultant photoconductance of a passivated $0.9\Omega\text{cm}$ mc-Si wafer produced by an infrared LED array which allows true steady-state photoconductance measurements at several different excess carrier densities.

Due to the relatively low intensity of the infrared light there was a significant amount of electronic noise in the photoconductance signal. To avoid this problem, the array was programmed to produce repeated staircase pulses, with sufficient intervals to minimise heating. The pulses were then averaged as they were acquired by the oscilloscope. To allow direct comparison between the steady-state LED lifetime measurements and the standard QSSPC measurement, infrared light was also used for the latter through the use of a silicon filter ($\sim 1050\text{nm}$). This is important in order to negate the effects of different carrier profiles caused by different wavelength illumination, particularly in relatively low bulk lifetime material. The absorption factors f_{abs} for the $320\mu\text{m}$ thick sample under the two infrared light sources, which are required in calculating the generation rate and therefore the lifetime, were estimated using calibrated samples of similar thickness and optical properties. These calibration samples had excellent passivation and relatively long, injection-level independent bulk lifetimes, and were hence relatively immune to changes in the generation profile. The absorption factors thus determined were 0.52 and 0.49 for the LED array and the silicon filter respectively.

The staircase pulse in Figure 3.6 allows 8 different carrier densities to be examined. Note that for 1 sun illumination the photoconductance is still 60% of its value at 8 suns, indicating that the apparent lifetime is increasing rapidly with decreasing carrier density, typical of the anomalous effect described. The comparison of the results from the LED array and the QSS illumination using the silicon filter is shown in Figure 3.7 for a passivated $0.9\Omega\text{cm}$ mc-Si wafer (a different sample to the last section). The results agree well and prove conclusively that the unusual apparent lifetime behaviour is not caused by carrier release from ‘slow’ traps.

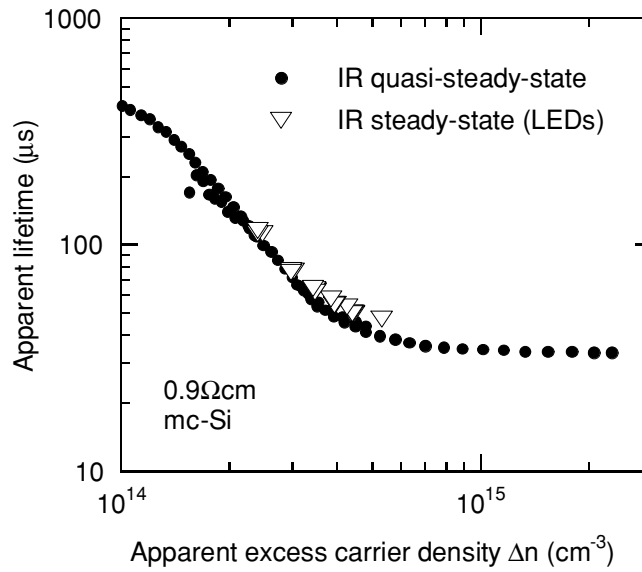


Figure 3.7. Apparent lifetime versus excess carrier density for the same mc-Si wafer from Figure 3.6 using an infrared LED array for steady-state measurement and an infrared flash lamp for QSSPC measurement.

Considering the fact that the effect appears to be steady-state in nature, it seems logical to consider the effect of *fast* traps rather than slow ones. In this case, changing the flash decay would have no impact on the behaviour of the fast traps, since their trapping and release dynamics would always remain in steady-state. In the next section, a trapping model developed in the mid 1950's and based on such fast traps, which are characterised by filling and emptying times much shorter than the flash decay, is applied to our data and found to provide a more coherent explanation.

3.3 Hornbeck-Haynes trapping model

Hornbeck and Haynes[119] developed a trapping model to explain unusual photoconductance data measured in single-crystal silicon. Their model was essentially the same as a slightly earlier one developed independently by Fan[125]. These trapping models were quite widely applied in those times, and featured in a number of general textbooks on semiconductor physics, notably Smith[118] and Blakemore[17]. Trapping states were understood to represent an extreme case of SRH recombination, in which the cross-section for one type of carrier capture was so small as to render such capture events negligible.

While the main focus of Hornbeck and Haynes' paper was on the analysis of trapping in transient photoconductance decay (PCD), this section concentrates on the steady-state situation, adapting their model for use with the QSSPC technique. The steady-state case was chosen here

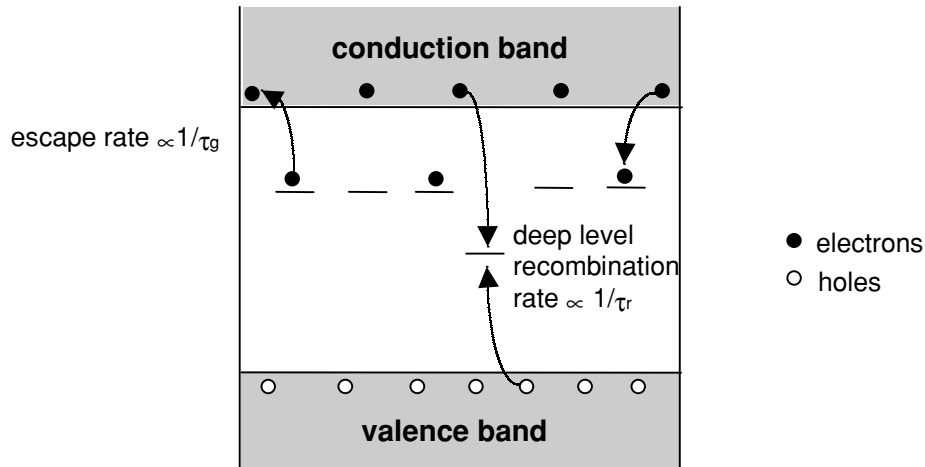


Figure 3.8. Energy band diagram showing the main features of the Hornbeck-Haynes trapping model. There are two distinct types of localised state in the band-gap, one type traps and releases only minority carrier electrons, the other interacts with both bands to produce recombination.

because it allows lower recombination lifetimes to be measured in comparison to inductively-coupled PCD techniques, as discussed in Chapter 1. This is an important consideration when dealing with generally lower quality materials such as mc-Si. Also, the development of the trapping model is more straight-forward in steady-state conditions due to disappearance of several time-dependent terms, as discussed below.

3.3.1 Trapping statistics

The main features of the Hornbeck-Haynes model are illustrated in Figure 3.8 in the form of an energy band diagram. A fundamental assumption of the model is that SRH recombination only occurs through a specific set of deep recombination centres. The *total* recombination lifetime may of course be injection-level dependent, in accordance with standard SRH, Auger or emitter recombination models. As well as the deep levels, there is a set of physically distinct, relatively shallow levels (nearer the conduction band for *p*-type silicon), which trap electrons, but do not contribute directly to recombination. In other words, their cross-section for hole capture is vanishingly small. Minority carriers are trapped by these levels at a rate proportional to $1/\tau_t$, where τ_t is the mean time before trapping when all the traps are empty, or simply the ‘trapping time’. The trapped carriers escape back to the conduction band at a rate proportional to $1/\tau_g$, with τ_g the ‘escape time’, or alternatively the mean time spent in a trap. The escape time is assumed to be independent of the proportion of traps occupied. Under steady-state conditions the trapping and escape rates are in balance.

The relevant density relating to these traps is the density of normally-empty traps, $N_{T(\text{empty})}$, which is dependent on the temperature and the Fermi level. Multicrystalline silicon for

photovoltaic applications is generally *p*-type, ranging in resistivity from 0.2-3Ωcm. Hence the Fermi level is quite close to the valence band, resulting in almost all of the traps being empty when in equilibrium at room temperature. Consequently, the density of normally empty traps is simply equal to the total trap density N_T . It should be remembered however, that this may not be the case for largely different resistivities or temperatures, an issue which is considered again in section 3.4.2.

In order to establish a physical picture of the effect of the traps, firstly consider the case when the carrier concentration is much greater than the trap density N_T , a condition that can be obtained with strong illumination. In such a situation the proportion of electrons in traps is small, even if most of the traps are full, and the excess *free* hole and electron densities, Δp and Δn respectively, are hence effectively equal. Recombination proceeds as usual through the deep centres, and the photoconductance reflects the true effective lifetime of the material.

As the carrier concentration decreases to near and eventually below N_T , the proportion of excess electrons in traps rises. Charge neutrality requires that $\Delta p = \Delta n + n_T$, where n_T is the trapped electron concentration. However, Δn must have the same value as if no traps were present, since it is determined by recombination through the deep levels, which operate independently of the traps. Hence, as the trapped electron concentration n_T begins to be appreciable, the excess hole concentration becomes significantly *higher* than the level that would be expected without traps. The result is a larger photoconductance and therefore an increased ‘apparent’ lifetime that does not reflect the effective recombination lifetime. The essential point then is that the traps *remove* some of the electrons from the recombination channels, allowing the photo-generated carriers to build up until steady-state is reached.

The excess photoconductance $\Delta\sigma$ (due to the *untrapped* carriers) will in general be given by:

$$\Delta\sigma = q(\mu_p \Delta p + \mu_n \Delta n)W \quad (3.1)$$

where μ_n and μ_p are the electron and hole mobilities. Substituting for Δp gives:

$$\Delta\sigma = q\Delta n(\mu_n + \mu_p)W + qn_T\mu_p W \quad (3.2)$$

This is essentially the standard expression used in the QSSPC technique as outlined in Chapter 1, with an additional term involving n_T . The Hornbeck-Haynes model provides a way of calculating n_T , and hence allows the effect of traps on QSSPC measurements to be modelled.

According to the Hornbeck-Haynes model, the differential equations describing the carrier populations in *p*-type material under steady-state or transient conditions can be written as:

$$\frac{d\Delta n}{dt} = g_e - \frac{\Delta n}{\tau_r} + \frac{n_T}{\tau_g} - \frac{\Delta n(1 - n_T / N_T)}{\tau_t} \quad (3.3)$$

$$\frac{dn_T}{dt} = -\frac{n_T}{\tau_g} + \frac{\Delta n(1 - n_T / N_T)}{\tau_t} \quad (3.4)$$

where g_e is the photogeneration rate of electron-hole pairs. The terms on the right-hand sides of Equations 3.3 and 3.4 are each associated with physical processes, and the construction of these equations can be understood as follows. In Equation 3.3, which represents the change in untrapped or *free* electrons, the first two terms are the standard ones representing gain and loss of carriers due to generation and recombination respectively. The third term represents a gain of carriers through ‘escape’ from traps, and the fourth represents carrier loss through trapping of free carriers. Equation 3.3 is essentially the negative of these last two terms, as it must be since it represents the change in the density of *trapped* carriers. Note that the term $1 - n_T / N_T$ is simply the fraction of traps that are empty.

In the steady-state case, the left hand sides of the above equations are both zero, reducing the relations, after some manipulation, to:

$$\Delta n = g_e \tau_r \quad (3.5)$$

$$n_T = \frac{N_T \Delta n}{\Delta n + N_T \tau_t / \tau_g}. \quad (3.6)$$

Equation 3.5 implies that, for a given photogeneration rate, the density of free electrons Δn remains equal to that expected when no traps are present, as stated before. Equation 3.6 is the desired expression for evaluating the extra photoconductance term in Equation 3.2.

In standard QSSPC measurements, the ‘apparent’ carrier lifetime τ_{app} is calculated from the excess conductivity and the photo-generation rate by implicitly assuming $\Delta n = \Delta p$, as discussed in Chapter 1:

$$\tau_{app} = \frac{\Delta \sigma}{g_e (\mu_n + \mu_p)}. \quad (3.7)$$

When trapping is present, the calculated apparent lifetime will be in error for two reasons: firstly due to the large number of extra holes that would not otherwise be present, and also because the implicit assumption of equal free hole and electron densities breaks down. This second point results in improper mobility weighting in Equation 3.6. The excess carrier density Δn commonly determined in the QSSPC technique is also calculated from the measured photoconductance, and hence will also be incorrect for the same reasons, and so is similarly referred to here as the ‘apparent’ excess carrier density.

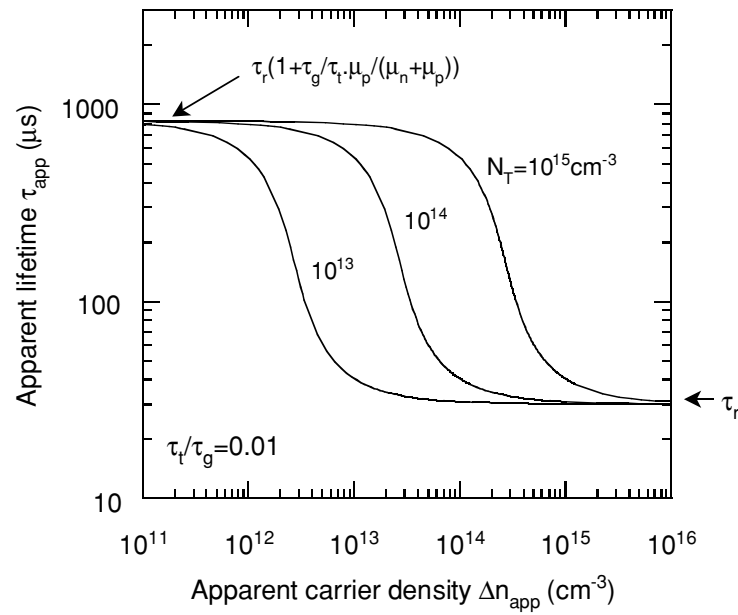


Figure 3.9. Modelled apparent lifetime versus apparent excess carrier density, showing how the parameter N_T affects the output of the Hornbeck-Haynes model.

The Hornbeck-Haynes model, expressed by equations 3.5 and 3.6, in conjunction with equations 3.2 and 3.7, can be used to generate apparent lifetime versus apparent excess carrier density plots that are directly comparable with curves measured using the QSSPC technique. There are three free parameters in the model to adjust: τ_r , the ratio τ_t/τ_g , and N_T . The recombination lifetime τ_r is in effect determined by the measured lifetime at carrier concentrations high enough to saturate trapping effects, although if it exhibits strong injection-level dependence this is not necessarily accurate. For the moment however, in order to bring out the features of the trapping model, we shall assume that the recombination lifetime is constant with injection-level.

Figure 3.9 illustrates the effect of changing the trap density N_T . In this case $\tau_t/\tau_g=0.01$ and $\tau_r=30\mu\text{s}$. Firstly, note that at high carrier concentrations when $\Delta n \gg N_T$, then $\tau_{app} \rightarrow \tau_r$, as expected. However, as the carrier concentration decreases to values near and below the trap density, the apparent lifetime begins to increase dramatically. From Equations 3.2, 3.6 and 3.7 it is possible to show that at very low carrier densities, when $\Delta n \ll N_T \tau_t/\tau_g$, then τ_{app} approaches the constant value:

$$\tau_{app} = \tau_r \left(1 + \frac{\tau_g}{\tau_t} \frac{\mu_p}{(\mu_n + \mu_p)} \right) \quad \text{low excess carrier densities} \quad (3.8)$$

as also shown in the Figure.

Figure 3.9 reveals that changing the trap density merely shifts the transition region between these two limiting values horizontally, or, alternatively, this parameter determines the

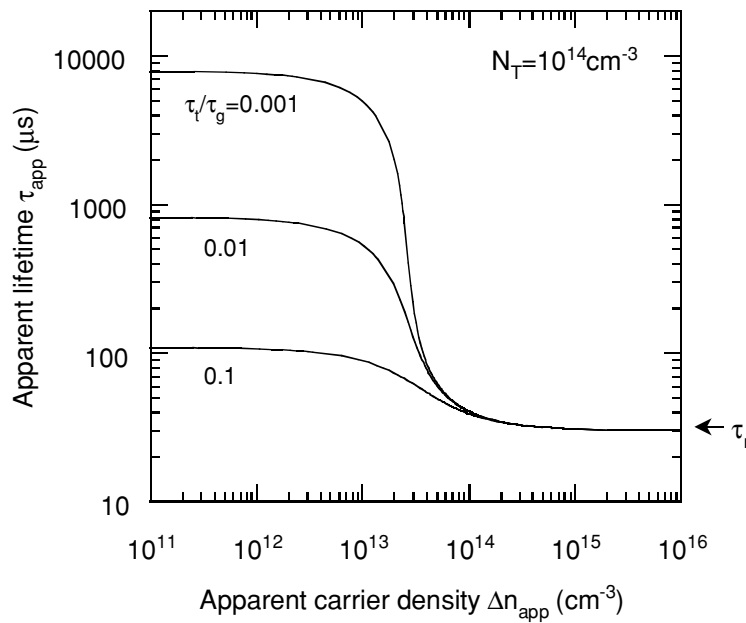


Figure 3.10. Modelled apparent lifetime versus apparent excess carrier density, showing how the parameter τ_t/τ_g affects the output of the Hornbeck-Haynes model.

carrier density at which trapping ‘begins’. Conveniently, this behaviour allows the trap density to be easily determined by fitting the model to real measurements.

Figure 3.10 shows the impact of different values of τ_t/τ_g for a trap density of $N_T = 1 \times 10^{14} \text{ cm}^{-3}$ and a recombination lifetime of $\tau_r = 30 \mu\text{s}$. As can be seen from Equation 3.7, changing this ratio simply changes the constant apparent lifetime value at very low carrier densities, the region in which the photoconductance is totally dominated by the behaviour of the traps. In this region, due to the abundance of empty traps, a value of $\tau_t/\tau_g = 0.01$ for example means that electrons only spend 1% of their time untrapped. In the opposite limiting case when traps only hold carriers for very short periods of time compared to how long it takes them to be trapped, i.e. when $\tau_t/\tau_g \gg 1$, Equation 3.7 shows that $\tau_{app} \approx \tau_r$, and the traps have virtually no impact. Essentially then, this parameter determines the ‘strength’ of the trapping effect. A useful consequence of the ‘independent’ action of N_T and τ_t/τ_g is that it allows them both to be determined unambiguously by fitting the model to experimental data.

The third parameter in the trapping model is the recombination lifetime τ_r . The impact of changing its value is trivial: the entire curve simply shifts up or down with the value of τ_r . That this should be the case follows from the linear dependence of both the low and high carrier density limits of τ_{app} (Equation 3.7) on τ_r . In this sense then, the relative impact of the traps is independent of the magnitude of the recombination lifetime.

As a more general consideration, the reader may wonder why only *minority* carrier traps have been discussed so far. Of course, if high-injection conditions prevail then neither carrier

type is in the majority, and so traps that affect *either* carrier type will impact on the photoconductance similarly. However, this does not seem to be observed in practice, probably because to act as high-injection traps in standard mc-Si, the trap density would need to be very high indeed. Under low-injection conditions however, only *minority* carrier traps have an observable impact on the photoconductance. This is because it is the minority carrier density that determines the recombination rate, and so majority carrier traps, if present, would not result in a build-up of minority carriers. Essentially then, majority carrier traps may exist, but they will have no observable impact on the photoconductance unless they occur at a concentration greater than the dopant density.

It should be mentioned at this point that, in reality, it is of course possible, and even very likely, for a state in the band-gap to act sometimes as a trap and sometimes as a recombination centre[17]. In general, such situations must be dealt with by using the full expressions for both Δn and Δp given in Chapter 1, section 1.1.3. Fortunately there are many situations where the analysis is greatly simplified by the dominance of one action over the other. In the SRH recombination model for example, the centres are considered to produce no significant trapping. It is important to recognise that this lack of trapping action is only achieved by assuming that the density of centres is much less than the excess carrier densities considered, and is in no way a reflection of the energy level or cross-section values.

In contrast, the Hornbeck-Haynes model is based on a two-level system in which one level acts solely as a trap and the other solely as a recombination centre. This second centre is in fact directly analogous to a SRH centre. In this case, the trap level acts solely as such due to having an extremely small cross-section for one type of carrier. Therefore, using two centres in parallel as described by the full expressions, reduces to the Hornbeck-Haynes model when one centre has a cross-section that is effectively zero, and the other centre has a small concentration. Additional SRH centres can easily be added in parallel if necessary. Although this may seem a restrictive requirement, experimental evidence presented in section 3.4.2.4 shows that this assumption is indeed satisfied by the trapping centres found in cast mc-Si in this work.

3.3.1.1 Energy level of trapping states

From the ratio τ/τ_g , as determined by fitting the trapping model to experimental data, it is possible to estimate the depth of the trap below the conduction band E_C-E_T as shown by Hornbeck and Haynes[119]. The principle of detailed balance implies that the trapping and escape rates are equal:

$$\frac{n}{\tau_t} = \frac{n_T}{\tau_g} \quad (3.9)$$

where n is the density of untrapped electrons. Furthermore, in thermal equilibrium, the following relations must also hold:

$$n = N_C \exp\left(\frac{-(E_C - E_F)}{kT}\right) \quad (3.10)$$

$$n_T = N_T \exp\left(\frac{-(E_T - E_F)}{kT}\right) \quad (3.11)$$

where E_F is the Fermi level, k is Boltzmann's constant and $T=300\text{K}$. N_C is the effective density of states in the conduction band, with a value of $2.86 \times 10^{19} \text{cm}^{-3}$ [130]. Combining these equations results in the following expression for the trap energy level:

$$E_C - E_T = kT \ln\left(\frac{N_C \tau_g}{N_T \tau_t}\right) \quad (3.12)$$

This expression is strictly only valid in thermal equilibrium when the principle of detailed balance holds and the concept of a unique Fermi level is applicable. In such cases $n=n_0 \approx n_i^2/N_A$. However, when the excess carrier concentrations are small, as is the case in the region that determines the ratio τ_t/τ_g , then $n=\Delta n$ and Equation 3.12 should not be too far in error, as implicitly assumed by Hornbeck and Haynes.

3.3.2 Comparison with experimental data

In this section, the Haynes-Hornbeck model is compared with experimental QSSPC apparent lifetime curves of mc-Si wafers that exhibit trapping effects. The model is found to explain the data well for a range of mc-Si samples with varying recombination lifetimes and trap densities. The energy levels of the traps are also calculated via Equation 3.11 and discussed.

3.3.2.1 QSSPC lifetime curves

Figure 3.11 shows QSSPC lifetime curves for four $0.9\Omega\text{cm}$ Eurosolare cast mc-Si wafers. These wafers had been gettered, etched and passivated in the usual fashion, as described earlier. These wafers actually came from ingot 6 which was studied in Chapter 2, and the four samples came from the bottom (wafer#1), centre (#150), near top (#250) and top (#300) of the ingot. As a result, their recombination lifetimes vary significantly, in accordance with the discussion of

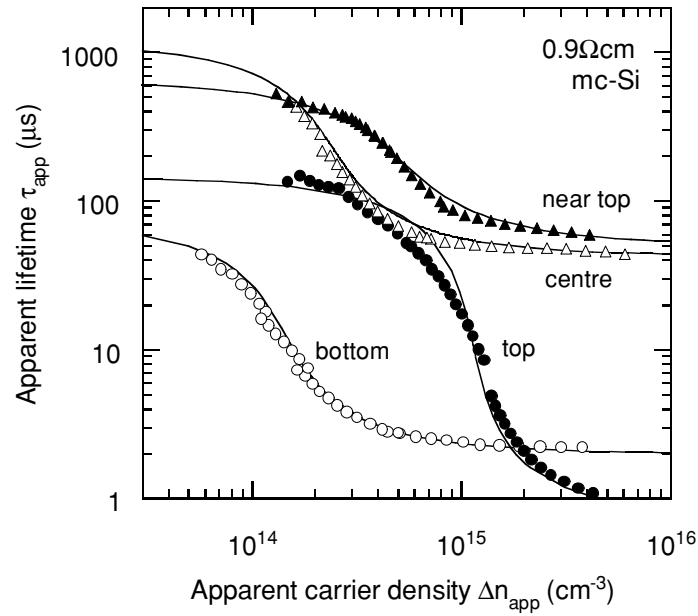


Figure 3.11. Measured apparent lifetime versus apparent excess carrier density for four mc-Si wafers from different regions of an ingot. The Hornbeck-Haynes trapping model is shown as a solid line for each sample.

Wafer no.	Recom. lifetime τ_r (μ s).	Trap density N_T (cm^{-3}).	Trap/escape ratio τ_t/τ_g .	Trap energy $E_C - E_T$ (eV).
1 (bottom)	2.0	5.1×10^{14}	.008	0.404
150	43	9.0×10^{14}	.01	0.383
250	51	1.7×10^{15}	.025	0.344
300 (top)	0.75	4.0×10^{15}	.0015	0.398

Table 3.1. Values of the trapping model parameters for the four 0.9 Ω cm mc-Si samples shown in Figure 3.11.

Chapter 2. Each of these wafers clearly shows the dramatic increase in lifetime at lower carrier densities, which is diagnostic of trapping effects, since other sources of injection-level dependence such as SRH recombination are very unlikely to produce such behaviour. The solid lines in Figure 3.11 depict the Hornbeck-Haynes model fitted to the data. The parameters used to generate the fits are listed in Table 3.1. For these samples, the recombination lifetime τ_r was assumed constant. While providing adequate results in this case, in later sections τ_r needs to be modelled explicitly to account for the injection-level dependence of SRH and emitter recombination.

Note that the carrier density at which trapping begins to affect the measurements, which is roughly equivalent to the trap density, varies quite strongly between the samples. The results show that the trapping model is capable of describing the behaviour of mc-Si wafers with widely different recombination lifetimes over a broad range of carrier densities. For the three samples with the highest recombination lifetimes τ_r , the model fits the data very well. All these samples have diffusion lengths close to or greater than the sample thickness (300 μ m). However,

for the sample with the lowest lifetime (top), the diffusion length is only around 50 μm , causing the white light illumination to produce a somewhat non-uniform carrier distribution across the thickness of the wafer. The simplified analysis of the QSSPC data no longer calculates the carrier density correctly, resulting in the apparent lifetimes becoming ‘stretched’ along the horizontal axis. Hence the fit for this sample is not as convincing as the other samples, and the trap density estimate is subject to greater uncertainty. This problem can be avoided by illuminating with infrared light, which provides more uniform photo-generation. Unfortunately, our flash does not produce sufficient infrared light to generate high enough carrier densities. Nevertheless, the white-light data from this sample has been included for completeness.

The calculated energy levels of the traps are also listed in Table 3.1. The average value is 0.38eV below the conduction band, which is actually quite deep, and as such may reasonably be expected to act as a recombination centre. It is possible that the inability of these states to participate in recombination arises from Coulombic repulsion of majority carriers due to the states being charged, rather than purely by virtue of the energy difference between the states and the valence band. Alternatively, the breakdown of the thermal equilibrium assumption in deriving the trap energy level expression may cause the results to be inaccurate.

3.3.2.2 Effect of traps on open circuit voltage

From a theoretical point of view, minority carrier traps result only in a relative increase in the majority carrier concentration. The density of free (untrapped) minority carriers remains exactly as would be the case if the traps were absent. Hence if the trap density is significantly less than the dopant density (always true in the samples studied here), the excess majority carriers will not significantly change the total majority carrier population. Consequently we would not expect the presence of traps to noticeably affect device voltage. This was confirmed by Figure 3.4 in section 3.2.1, which compared the implied V_{OC} calculated from the apparent lifetime with the measured V_{OC} .

Two more such comparisons are presented in Figure 3.12 for two different wafers. The mc-Si sample in Figure 3.12 a) had a relatively low trap density ($2 \times 10^{13} \text{cm}^{-3}$), in fact low enough to be insignificant at 1 sun illumination levels. Consequently, the value of the implied V_{OC} agrees well with the measured V_{OC} (612mV and 616mV) at 1 sun. However, the implied V_{OC} curve is affected by trapping at illumination levels below about 0.2 suns.

A second example is shown in Figure 3.12 b). In this case the trap density is high ($1 \times 10^{16} \text{cm}^{-3}$), and causes a drastic over-prediction of V_{OC} at 1 sun (by about 100mV). This example serves to illustrate how trapping can cause difficulty in process monitoring in standard mc-Si. The solid line on the figure represents a constant extrapolation of the recombination

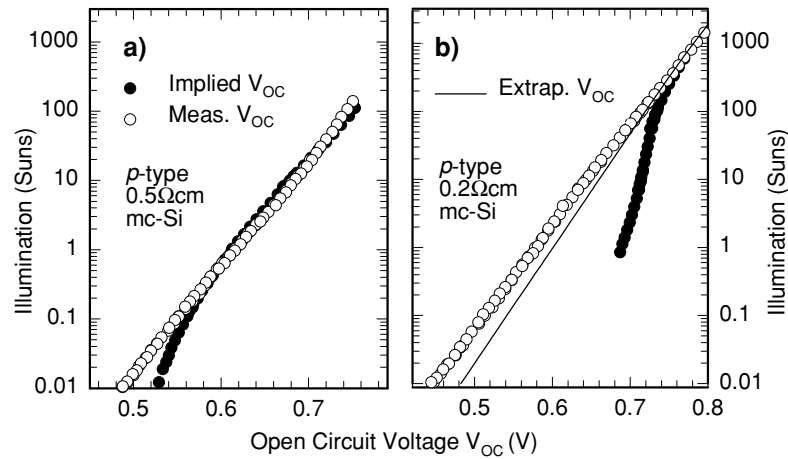


Figure 3.12. Measured and implied illumination- V_{OC} curves for two mc-Si cells with very different trap densities. The solid line in part b) is generated by extrapolating a constant recombination lifetime from 0.75V to lower voltages, and hence represents an ideality of $n=1$.

lifetime as measured above $1 \times 10^{16} \text{cm}^{-3}$, to lower injection regions. Such an extrapolation predicts a V_{OC} at 1 sun of 602mV, as compared with the measured V_{OC} of 585mV. The discrepancy between these values is due to the injection-level dependence of the recombination lifetime at lower injection levels, which is masked by the trapping centres. This masking often occurs in standard $1 \Omega \text{cm}$ mc-Si at 1 sun levels, making substrate monitoring difficult. It is a significant issue for in-line commercial applications of contactless photoconductance lifetime techniques, whether steady-state or transient in nature. This problem is the motivation for the work in section 3.5, which attempts to validate a recently proposed method for correcting trap-affected lifetime data. In the next section however, the physical origin of the localised states that cause trapping in cast mc-Si is studied and discussed.

3.4 Physical origin of trapping centres

Figure 3.13 shows measured QSSPC apparent lifetime curves for a $0.9 \Omega \text{cm}$ mc-Si wafer both before and after gettering. The Hornbeck-Haynes trapping model is also fitted to the data in order to determine the trap densities. Gettering was performed for 60 minutes at 900°C under a heavy POCl_3 flow, then the gettered layer was etched and the sample passivated using the standard light phosphorus and in-situ oxidation of Chapter 1. The figure shows that the gettering treatment had a two-fold effect, firstly to increase the recombination lifetime (from around $8 \mu \text{s}$ to $35 \mu \text{s}$), and secondly to reduce the trap density (from $2 \times 10^{15} \text{cm}^{-3}$ to $7 \times 10^{14} \text{cm}^{-3}$ as determined by the fits). It seems then that the gettering treatment removed some of the centres responsible for the trapping effects, as well as removing recombination centres. However, there still remains

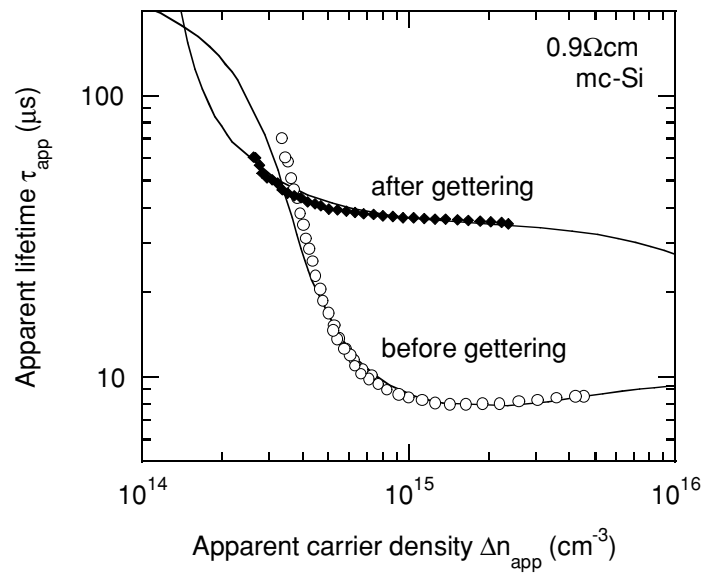


Figure 3.13. Measured (symbols) and modelled (lines) apparent lifetimes for a mc-Si wafer before and after gettering. The wafer had been passivated with a light phosphorus diffusion and thin oxide prior to both measurements.

a significant quantity of trapping centres after gettering. Hence we broadly classify trapping centres in two categories: those which can be removed by gettering, and those which cannot. We firstly examine the physical origin of traps ‘left behind’ in gettered wafers.

3.4.1 Correlation with dislocation density in gettered material

During the 1960’s it was thought that the presence of dislocations could explain trapping effects in single-crystal silicon[131,132]. Consequently, it seems logical to look for a similar correlation in the mc-Si studied in this chapter. Since dislocations will not be removed by gettering, they present a possible explanation of the ‘residual’ traps that remain after other types of traps have been removed. The fact that wafers from the top, centre and bottom of the Eurosolare mc-Si ingots studied in Chapter 2 had markedly different dislocation densities provides a convenient opportunity to observe whether any such correlation exists.

Figure 3.14 shows a plot of trap density against dislocation density for the samples in Table 3.1, plus data from five additional samples from the same ingot. The dislocation density, which was determined by counting etch pits on scanning electron micrographs as described in Chapter 2, is highest at the top of the ingot, probably due to high thermal stresses resulting from rapid cooling at the end of the casting process. The plot reveals that a correlation does indeed appear to exist between the densities of trapping centres and dislocations for this mc-Si ingot. It is interesting to note however, that there is no such correlation between the trap or dislocation

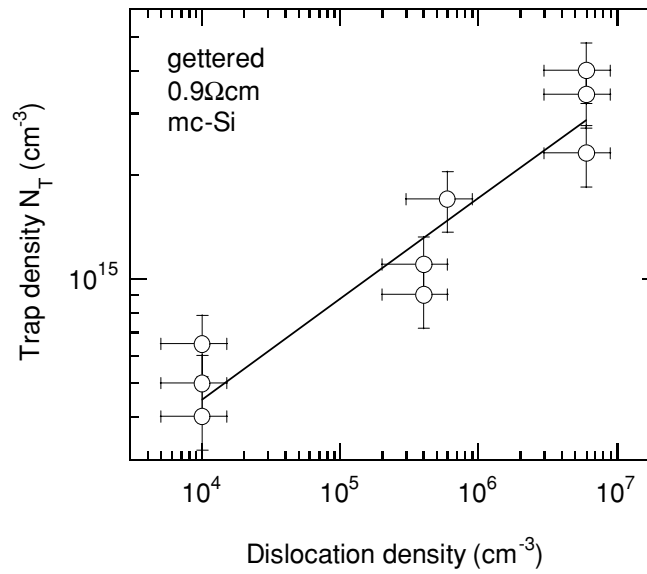


Figure 3.14. Trap density versus dislocation density in gettered 0.9Ωcm mc-Si. Trap densities were determined by fitting the trapping model to apparent lifetime curves. The solid line is a guide to the eye.

density and the recombination lifetime (see Table 3.1), suggesting that recombination, even in the gettered material, is not caused merely by dislocations.

It seems then that dislocations offer a possible explanation for the trap density in gettered material. It is possible that the dislocations themselves are directly responsible for the trapping states, or alternatively, the dislocations may act as precipitation sites for other impurities that actually cause the trapping. Such precipitated impurities are common in cast mc-Si, and are known to be very difficult to getter[88,133]. If they were responsible for trapping, their presence would result in the type of correlation with dislocation density in Figure 3.14. However, as mentioned, they are unlikely to be responsible for the ‘mobile’ traps that are removed by gettering. The next section applies cross-contamination techniques to study these ‘getterable’ traps.

3.4.2 Correlation with dopant density in non-gettered material

It is of course difficult to separate the effects of crystallographic defects and impurities when both are present in significant quantities, as occurs in mc-Si. However, studying single-crystal FZ wafers of ‘perfect’ crystallography which have been deliberately cross-contaminated with mobile impurities from mc-Si samples, provides a direct way of ‘removing’ the complicating effects of crystal defects. Such an approach was used in Chapter 2 to measure the concentration of mobile recombination centres in mc-Si wafers to better understand their

response to gettering. In this section, the fact that trapping centres also apparently migrate from the mc-Si to the FZ wafers is exploited to gain insights into the physical origin of the mobile traps.

3.4.2.1 Cross-contamination experiments

As mentioned, an important advantage of the cross-contamination experiments is that they allow the study of trapping and recombination centres in a material that is practically free of crystallographic defects. They also provide a way of examining the correlation between the background doping levels and the magnitude of the trapping effects by contaminating FZ wafers of different resistivities. This is generally not possible with mc-Si wafers, which come only in a narrow dopant density range, and in which a similar crystal quality cannot be guaranteed.

Cross-contamination of p-type FZ Si wafers was achieved by the standard 840°C light phosphorus diffusion, thin thermal oxide growth at 900°C and a forming anneal at 400°C as described in Chapter 1. This served the dual purposes of effusion of impurities from the non-gettered mc-Si to the FZ Si and also passivation of the surfaces for lifetime measurements. To ensure measurable trapping effects in the FZ wafers, non-gettered mc-Si samples with high trap densities of around $7 \times 10^{15} \text{cm}^{-3}$ were used. These were in fact wafers from the top of the standard ingot #6 from Chapter 2 and also the previous section of this chapter. Table 3.1 shows that after gettering, these wafers had a trap density of around $4 \times 10^{15} \text{cm}^{-3}$, meaning that approximately half the traps are apparently caused by mobile, easily gettered impurities.

Figure 3.15 shows apparent lifetime measurements of two such cross-contaminated FZ samples of 0.35 and 8Ωcm resistivity. At higher injection levels the data reflect the recombination lifetimes, however at around $1 \times 10^{14} \text{cm}^{-3}$ and $2 \times 10^{12} \text{cm}^{-3}$ for the 0.35 and 8Ωcm samples respectively, trapping effects begin to dominate. The presence of the contaminating species in the FZ material has two effects on lifetime – firstly the introduction of minority carrier traps and the associated increase in apparent lifetime at low carrier densities, and secondly the introduction of recombination centres and the resulting Shockley-Read-Hall (SRH) dependence of the recombination lifetime on injection-level. The presence of the emitter caused by the phosphorus diffusion in these samples also impacts on the effective lifetime measurements at the highest injection levels. This is particularly noticeable in the 8Ωcm case as a decreasing lifetime as the carrier density increases above $1 \times 10^{15} \text{cm}^{-3}$.

As well as experimental data, Figure 3.15 shows fit lines for the Hornbeck-Haynes trapping model. However, the fitting procedure is more complex than that used in section 3.3, where the recombination lifetime τ_r was assumed constant. The curves in Figure 3.15 clearly

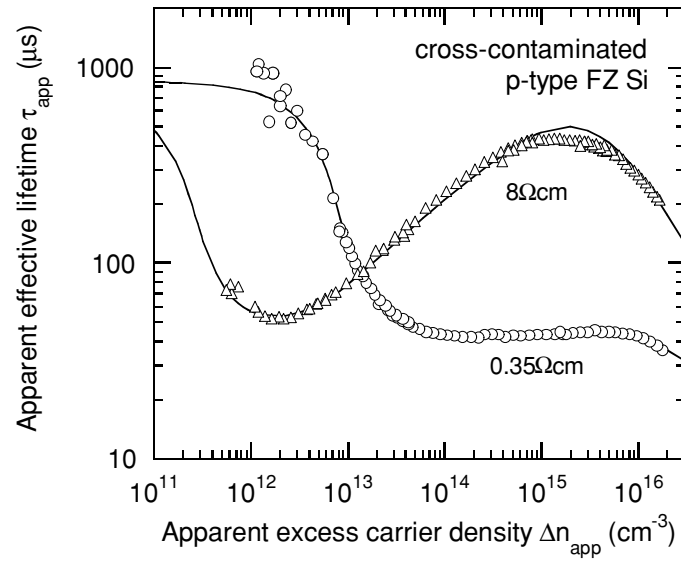


Figure 3.15. Apparent lifetime versus apparent excess carrier density for 0.35 and 8Ωcm cross-contaminated FZ Si wafers. The open symbols are QSSPC data. The solid lines represent the trapping model, with the recombination lifetime τ_r modelled by two SRH centres and an emitter term.

show an injection-level dependence at carrier densities higher than the region where traps dominate. This is typical of SRH recombination centres, and also of emitter recombination, as mentioned above. As a result, for p-type Si, τ_r must be modelled by:

$$\frac{1}{\tau_r} = \frac{1}{\tau_{SRH}} + \frac{1}{\tau_{emitter}} \quad (3.13)$$

where τ_{SRH} and $\tau_{emitter}$ are defined in Chapter 1. The SRH lifetime is characterised by the energy level of the recombination centre and the capture time constants for electrons and holes τ_{n0} and τ_{p0} . The emitter term is characterised by the emitter saturation current density J_{0e} . The values of J_{0e} used in the fitting procedure were measured experimentally for each sample under high injection conditions[31,32] and were typically $5 \times 10^{-14} \text{ A cm}^{-2}$. Auger recombination was not an important contributor in these cross-contaminated wafers, and so was not included in the modelling.

To obtain an accurate fit to the experimental data in Figure 3.15, it was necessary to model τ_r with *two* SRH centres and an emitter term. Having two centres meant that there were six fit parameters (two energy levels and four capture time constants) for the SRH contribution to τ_r , resulting in a large number of possible sets of parameters that provided reasonable agreement. As a consequence, it is not possible to uniquely determine τ_{n0} and τ_{p0} or the energy level of the recombination centres from these experiments. However, for any of these sets of parameters that provide a good fit, the possible values of the *trap* density N_T are restricted to a

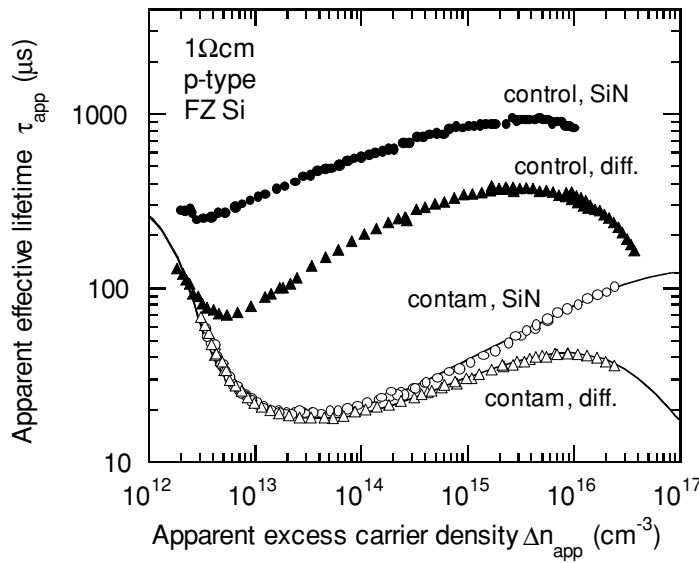


Figure 3.16. Apparent lifetime versus apparent excess carrier density for a contaminated (open symbols) and a clean (solid symbols) $1\Omega\text{cm}$ FZ sample with emitter-passivation (triangles) and SiN-passivation (circles). The solid lines for the contaminated cases represent the trapping model fitted with two SRH centres only for the SiN case and with two SRH centres and an emitter term for the emitter passivated case.

narrow range. Hence we are in a position to accurately specify N_T , even if we can infer little about the nature of the SRH centres.

Before moving on to discuss the cross-contamination results further, there is the important question of whether the trapping and recombination effects observed in the contaminated FZ wafers are related to bulk or surface states. At the surfaces there exist relatively heavily doped phosphorus layers, in which impurities are in general highly soluble. Hence it is conceivable that the impurities adsorbed onto the surfaces of the FZ wafers during cross-contamination remain in the thin diffused regions. Also, the oxidised surfaces themselves may be impacting on both the trapping and recombination activity. To determine if this was indeed the case, a contaminated $1\Omega\text{cm}$ sample was etched to remove the phosphorus layers. The sample was then re-passivated with PECVD silicon nitride (SiN) films deposited at 400°C [55], and the lifetimes re-measured. The results are depicted in Figure 3.16, with data also from a $1\Omega\text{cm}$ FZ control sample that was not cross-contaminated.

The results for the emitter-passivation and SiN-passivation agree very well. There is a difference at higher injection levels, but this is due entirely to the presence of emitter recombination in the diffused sample, which is of course not present in the SiN-passivated sample. The trapping model with two SRH centres was fitted for both these cases, with an emitter term also included for the diffused case. The fit shown for the SiN-passivated data is simply that for the diffused case with all trapping and SRH parameters the same, except with $J_{0e}=0$ (i.e. no emitter recombination). Note that the slight dip in lifetime at the upper end of the

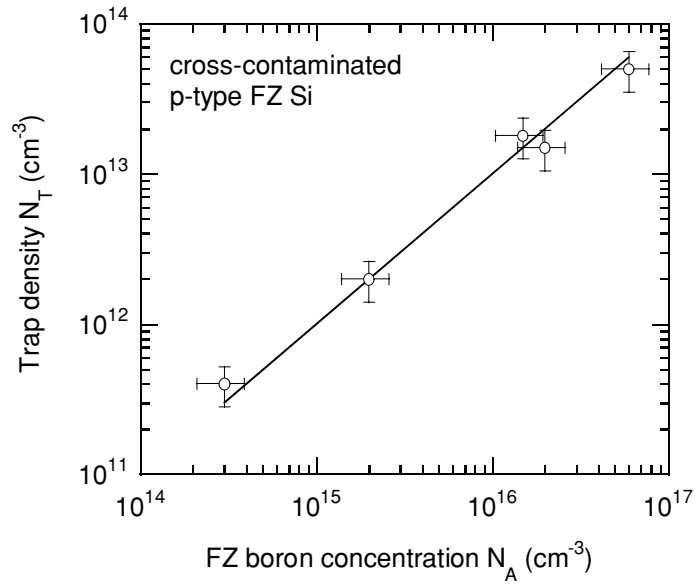


Figure 3.17. Boron concentration N_A versus trap density N_T for cross-contaminated boron-doped p-type FZ wafers of different resistivities. The solid line represents a linear fit of $N_T = 0.001N_A$.

SiN passivated control sample is caused by Auger recombination, not emitter recombination. As mentioned, Auger recombination did not impact significantly on the contaminated samples.

The curves for the SiN-passivated and diffused *control* samples (non-contaminated) in Figure 3.16 are useful in interpreting the overall results. The fact that both these curves represent significantly higher apparent lifetimes at all injection-levels (when comparing the two diffused samples or the two SiN coated samples), strongly indicates that the increased recombination activity in the contaminated wafer reflects mainly bulk apparent lifetimes. More important though for the purposes of this section is the increased trapping evident in the contaminated samples. The clean samples also show evidence of trapping, which is most likely caused by surface states, but have lower trap densities than the contaminated wafers. Also, the fact that the trap density of the contaminated wafer is the same for both passivation schemes, while it is quite different for the two passivation methods on the clean wafer, suggests that the computed trap densities for the contaminated cases relates to a volume concentration, while that for the clean case reflects surface properties. Hence we may interpret the trap densities in the contaminated wafers as being caused by bulk states arising from effused impurities from the mc-Si wafers.

The bulk trap density was determined for a range of contaminated FZ wafers of resistivity from 0.3 to 1000 Ωcm . For the 1000 Ωcm case the trap density was so small ($< 1 \times 10^{11} \text{cm}^{-3}$) as to be unmeasurable. The results for the other wafers are shown in Figure 3.17 as a function of boron concentration in the FZ substrate. There is a clear linear relationship between these two variables, implying that the traps are related to boron-impurity pairs. Multicrystalline samples with lower trap densities and higher recombination lifetimes (and hence lower mobile impurity

concentrations) than those used in the experiments above were also used to cross-contaminate 1Ωcm FZ wafers. The corresponding trap densities in these FZ wafers were lower than for the heavily contaminated FZ wafers, indicating that a relationship exists between trap density and mobile impurity concentration that is qualitatively similar to that in Figure 3.17. The impurities responsible for the trapping centres have clearly come from the mc-Si, and hence must be highly mobile in silicon at high temperatures in order to effuse effectively. Prime candidates for such an impurity are transition metals.

There is however another possible cause of the correlation with the dopant density in Figure 3.17 that needs to be considered. Since the Fermi level will change significantly for the various resistivity FZ wafers, it is possible that the proportion of ‘empty’ traps in thermal equilibrium may also change, even though the total trap density may be the same for each wafer. Smith[118] discusses this possibility, and gives an expression for the proportion of ‘cocked’ traps β (i.e. those which are empty and ready to trap minority carriers) in thermal equilibrium as a function of the Fermi level:

$$\beta = \frac{1}{1 + 2 \exp\left(\frac{E_F - E_T}{kT}\right)} \quad (3.14)$$

However, for the p-type FZ material used in this study, the Fermi level is always many times kT below the trap level, which from Table 3.1 is possibly around 0.38eV below the conduction band, and certainly no deeper. Hence, for all of the resistivities used in this study $\beta=1$, or in other words, all available traps are ‘cocked’.

The linear nature of the relationship between the trap density and the dopant density in the FZ material suggests, therefore, that boron-impurity complexes are responsible for the trapping centres in the non-gettered mc-Si. Moreover, the linearity implies that there should be one boron atom in each of these complexes, suggesting the possibility of boron-impurity pairs. Such pairs are well documented for FeB[53] and CrB[134] in silicon, and are also known to exist, although less well studied, for other metals such as Co[135]. A well known property of such pairs is that they can often be dissociated under strong illumination (FeB pairs) or low temperature thermal annealing (both FeB and CrB). The next section discusses the response of traps in non-gettered mc-Si to these two treatments.

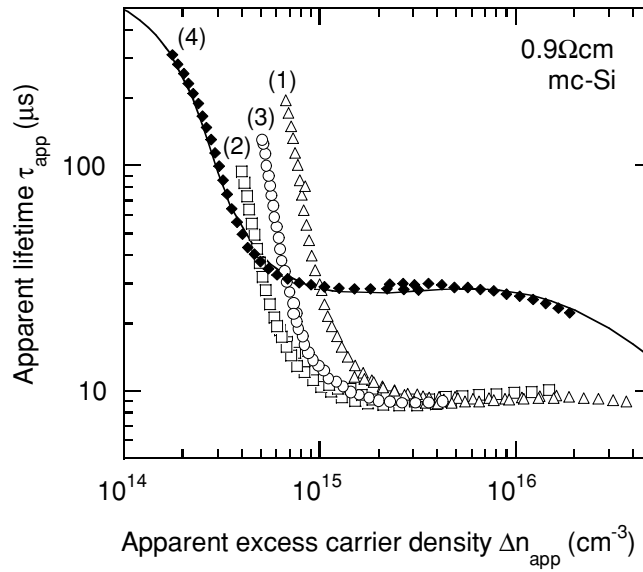


Figure 3.18. Apparent lifetime versus apparent excess carrier density for a mc-Si sample as measured (1) six months after any thermal treatment and after lightsoaking (2) directly after thermal annealing at 200°C for 10 minutes (3) 7 days after thermal anneal and (4) after gettering. The results for thermal annealing and lightsoaking of the sample after gettering are not shown as they lie on top of curve (4). The solid line through curve (4) represents the trapping model fitted to the data.

3.4.2.3 Light-soaking and thermal annealing behaviour of traps

Figure 3.18 illustrates results for a 0.9Ωcm mc-Si wafer before and after gettering. However, before the gettering treatment, the wafer was subjected firstly to strong lightsoaking (one hour at two suns) and then a 10 minute 200°C anneal, with lifetime measurements in between. After gettering, this procedure was repeated. For the non-gettered case, the lightsoaking had no impact on either the recombination lifetime or the trap density. However, the 200°C anneal, while not affecting the recombination lifetime, did result in a decrease in the trap density from $2.7 \times 10^{15} \text{ cm}^{-3}$ to $1.3 \times 10^{15} \text{ cm}^{-3}$. The wafer was re-measured again after one week (before gettering), and the trap density was found to have increased again to $1.9 \times 10^{15} \text{ cm}^{-3}$. These results are consistent with the suggestion that in non-gettered wafers, boron-impurity pairs or complexes cause some of the traps. These complexes can evidently be dissociated through annealing, after which they slowly re-associate at room temperature, in a similar way to FeB and CrB pairs in silicon. Note however that we can rule out FeB pairs as the cause of the traps since they should be dissociated by the lightsoaking, and also because such dissociation should result in a significant change of the recombination lifetime, which was not observed (see Chapter 5 for a detailed discussion of FeB pairs). Furthermore if FeB pairs were present in such high concentrations, the recombination lifetime would necessarily be much smaller. Similar

arguments can be used to rule out CrB pairs, which would also cause a much lower recombination lifetime. Hence it seems likely that some other impurity ‘bonds’ with the boron to cause the traps. SIMS studies were performed on gettered mc-Si wafers with the gettering layers intact, as discussed in Chapter 4, but no other likely candidates for the trapping states were found, possibly because of the relatively poor sensitivity of SIMS.

As a final piece of evidence, Figure 3.18 also shows the same sample after gettering. As is usual, the recombination lifetime has increased, and the trap density decreased (to $9.5 \times 10^{14} \text{ cm}^{-3}$), indicating the trap-causing impurity-boron complexes have been removed by the gettering. The sample was then lightsoaked and annealed at 200°C again. In both cases the recombination lifetime and trap density remained completely unchanged, confirming that the remaining traps are not boron-impurity related.

A further interesting result of this study is that the boron-impurity centres that cause trapping apparently act *only* as traps. In other words, they do not also act as recombination centres, at least not dominant ones, as evidenced but the unchanged recombination lifetime during thermal annealing. This is in keeping with one of the underlying assumptions of the Hornbeck-Haynes trapping model, confirming the validity of applying it to these samples.

The main conclusion from this section then is that there appears to be two types of trapping centres in mc-Si, one related to dislocations and the other to boron-impurity pairs or complexes. The latter can be removed by phosphorus gettering, and can also be dissociated by thermal annealing, while the dislocation-related states remain after gettering. In either case, the trapping distorts recombination lifetime measurements, often at carrier densities of interest for solar cell operation. The next section is devoted to validating a proposed technique for correcting, at least partially, such trap-affected lifetime data.

3.5 A method for correcting trap-affected lifetime data

The usefulness of any lifetime technique is of course contingent upon reliable measurement of the effective recombination lifetime in the injection range of interest. Photoconductance-based measurement techniques such as microwave-detected photoconductance decay ($\mu\text{W-PCD}$) and QSSPC, are currently the only widely used methods able to determine lifetimes under low-, mid- and high-injection conditions, but are unfortunately subject to trapping effects. Surface photovoltage (SPV) diffusion length measurements, on the other hand, are not subject to trapping effects, precisely because they rely on measurement of the *voltage* across an induced junction at the surface. Due to the delicate nature of this induced junction, however, SPV measurements are restricted to very low-injection conditions that are far

removed from those under which a solar cell operates. Free-carrier absorption (FCA) techniques, which can measure under mid- and high-injection conditions, are also subject to trapping effects. It would be useful then to be able to mitigate the effect of trapping centres, either physically or analytically, in order to extend the range of useful data obtainable using the μ W-PCD and QSSPC techniques.

Recently, a method has been proposed by Sinton that corrects, at least partially, for the effects of traps on QSSPC data[136]. The correction involves adjusting injection-level dependent lifetime data, through the use of a ‘bias-light’ term, in order to extend the range of usable data into lower carrier densities. The improved data potentially provides more accurate knowledge of lifetimes near cell operating conditions, and hence allows better process monitoring. This section examines the efficacy of this correction method, and determines guidelines for its proper application. This is achieved by examining the effect of the correction on modelled lifetime curves and verifying the conclusions with experimentally measured QSSPC lifetime data.

Modelled trapping curves are generated in the same way as in the previous section with an effective recombination lifetime τ_r generated by an emitter term and a SRH term (which may arise from either the bulk or the surfaces). Due to the general dominance of these two mechanisms in mc-Si under cell operating conditions, Auger and radiative recombination are negligible in all cases considered here. These curves are used in the following sections to investigate the effectiveness of the bias-light correction method, which can also be easily incorporated into the modelling. The ideal result would be for the correction method to cause the trap-affected curve to fall on top of the underlying recombination lifetime curve. Of course, it is possible to achieve this by fitting the full Hornbeck-Haynes model with SRH and emitter recombination to the measured data, and then ‘turning off’ the traps. This is however very time consuming. The potential advantage of the bias-light correction is that it is very easily and quickly applicable to measured data, and so can potentially be deployed in-line. It should be stressed that the bias-light correction considered here does not involve *physically* applying a bias-light during measurement, but is merely descriptive of the analytical data correction employed.

3.5.1 The bias-light correction method

As discussed in Chapter 1, the QSSPC technique is based on the simultaneous measurement of the excess photoconductance $\Delta\sigma$ via an inductively-coupled coil, and the generation rate g_e (cm^{-3}) via a reference cell. The generation rate is given by:

$$g_e = \frac{IN_{ph}f_{abs}}{W} \quad (3.15)$$

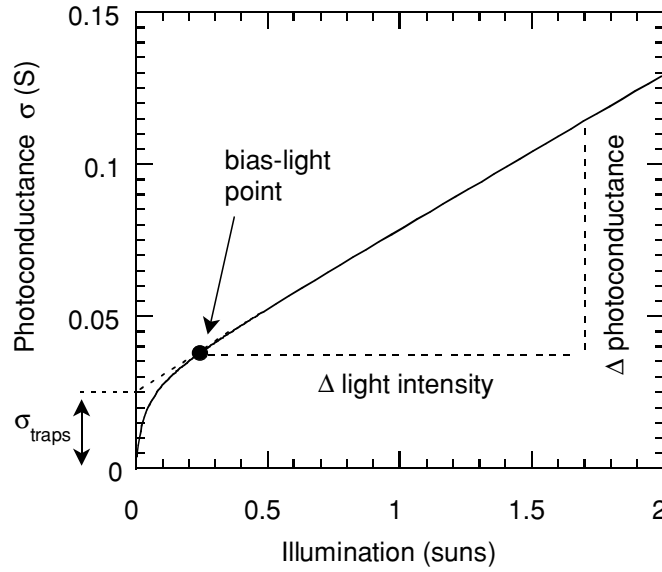


Figure 3.19. Photoconductance versus light intensity for a sample affected by trapping.

where I is the light intensity in units of ‘suns’ (1 sun=100mW/cm²), N_{ph} is the incident photon flux density under standard 1 sun illumination, and W is the sample width (cm). The quantity f_{abs} is the fraction of incident photons absorbed, and is a function of the particular optical properties of the sample. It accounts for optical losses due to reflection from the front surface and transmission through the wafer.

The apparent excess carrier concentration Δn_{app} is determined by:

$$\Delta n_{app} = \frac{\Delta \sigma}{qW(\mu_n + \mu_p)} \quad (3.16)$$

where q is the electronic charge and μ_n and μ_p the electron and hole mobilities. The apparent lifetime is then given by $\tau_{app} = \Delta n_{app} / g_e$. An implicit assumption in this analysis is that the excess electrons and holes contribute equally (weighted for their mobilities) to the excess photoconductance. This is not true when minority carrier traps are present. Firstly, the fact that some minority carriers are trapped means that the majority carriers contribute more heavily to the excess photoconductance. Secondly, since the trapped minority carriers are unable to recombine, the concentration of majority carriers increases until a new balance between generation and recombination is attained. The result is an abnormally large excess photoconductance, driven by majority carriers, at low carrier densities, hence the ‘apparent’ subscripts of the calculated variables above.

The bias-light correction attempts to overcome this problem by effectively subtracting out the trap-induced excess photoconductance[136]. The analysis is then carried out relative to this ‘baseline’ photoconductance. This is illustrated in Figure 3.19, which shows a linear plot of

photoconductance versus light intensity for a constant recombination lifetime sample affected by trapping. The plot shows the rapid increase in photoconductance at low illumination due to trapping, and also shows the positioning of the bias-light at the point where it is just sufficient to fill the traps.

The correction involves determining the *change* in generation Δg_e relative to the generation due to the bias-light (or traps):

$$\Delta g_e = \frac{(I - I_{bias})N_{ph}f_{abs}}{W} \quad (3.17)$$

The carrier density at the bias-light intensity, Δn_{bias} , can be read directly from the measured data. The corrected effective lifetime is then given by:

$$\tau_{eff-corr} = \frac{\Delta n_{app} - \Delta n_{bias}}{\Delta g_e} \quad (3.18)$$

where Δn_{app} is determined by Equation 3.16. Essentially then, the corrected lifetime is proportional to the ratio of incremental photoconductance to incremental light intensity, as shown on Figure 3.19. Note that although the method involves subtracting out terms to account for the traps, the method is still a *large-signal* approach. In other words, the incremental photoconductance may be much larger than the ‘baseline’ value, and as such the resultant corrected lifetimes reflect actual, not differential, quantities. This is appropriate for application to the QSSPC technique, which is similarly a large-signal method, unlike μW -PCD[48,50].

Once the corrected lifetimes are calculated, the question arises as to which carrier density should each lifetime be ascribed to. Because of the large imbalance between hole and electron populations in the trapping region, it is necessary to estimate the minority carrier density Δn (for *p*-type material) at each data point, and plot the lifetime values against this variable, since it is the relevant parameter for solar cell operation. This is achieved by extrapolating the data from above the bias point to the photoconductance axis, as shown on Figure 3.19. The value at the axis approximates the photoconductance due to the traps, σ_{traps} . The minority carrier density Δn is then estimated as:

$$\Delta n = \frac{\Delta \sigma - \sigma_{traps}}{qW(\mu_n + \mu_p)}. \quad (3.19)$$

The fully corrected data is plotted in the form of $\tau_{eff-corr}$ versus Δn . The following sections examine the effect of this correction method on modelled trap-affected lifetime curves. In all cases, the recombination lifetimes and corrected lifetimes are plotted against minority carrier density Δn , whereas the trap-affected curves are plotted against apparent carrier density Δn_{app} .

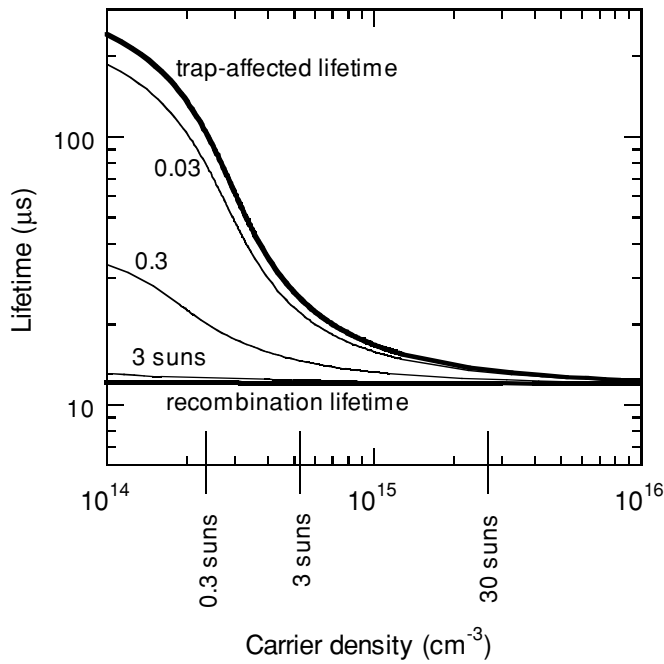


Figure 3.20. Case 1: Modelled constant recombination lifetime. The recombination lifetime is $12\mu\text{s}$, and the trap density $1 \times 10^{15}\text{cm}^{-3}$. The impact of the bias-light correction is shown for bias-light intensities of 0.03, 0.3, 3 and 30 suns, the latter coinciding with the recombination lifetime curve. The corresponding bias carrier densities are shown on the horizontal axis. For the 0.03 suns case the value is $5.8 \times 10^{13}\text{cm}^{-3}$.

Bias carrier densities Δn_{bias} are always expressed as apparent carrier densities. The discussion is divided into three distinct cases, each characterized by a different injection-level dependence of the underlying recombination lifetime. It should be noted that the correction procedure sometimes gives rise to spurious asymptotic effects near the bias carrier density. These have been numerically smoothed out in the following examples.

3.5.1.1 Case I: constant recombination lifetime

The simplest case to consider is that of an injection-level *independent* recombination lifetime. Such a situation is not entirely realistic, but is nevertheless commonly presumed, as discussed in Chapter 1. For our current purposes, it provides a convenient starting point for understanding the effect of the bias-light correction. Figure 3.20 shows the constant recombination lifetime case, with $\tau_r = 12\mu\text{s}$, a trap density of $1 \times 10^{15}\text{cm}^{-3}$, and a trapping time to escape time ratio $\tau_t/\tau_g = 0.01$. Such values are typical of commercial solar grade mc-Si. Note that the trap-affected lifetime, which corresponds to that which would be measured using the QSSPC technique, is notably different from the underlying recombination lifetime, even at carrier densities considerably higher than the trap density.

Also shown on Figure 3.20 is the result of adjusting the trap-affected data using the bias-light correction with several different values of the bias-light intensity. On the horizontal carrier density axis, the bias carrier density is shown for each bias-light intensity. A value of 0.03 suns results in very little change in the data, since then only a small fraction of the $1 \times 10^{15} \text{cm}^{-3}$ traps are occupied, and the photoconductance is still a measure of trap filling and emptying rather than free minority carrier generation and recombination. As the bias-light intensity increases, the corrected curve more closely approximates the recombination lifetime curve. In fact, in this constant lifetime case, the larger the bias, the better the correction. At bias-light intensities above about 30 suns (giving bias carrier densities above $2 \times 10^{15} \text{cm}^{-3}$), the correction is close to exact, since the bias carrier density is higher than those at which the measured lifetime is severely affected by trapping.

This illustrates an important aspect of the bias-light correction. As the bias carrier density increases, the corrected values are ‘based’ on points that more closely resemble the recombination lifetime *at the bias carrier density*. When the recombination lifetime is constant, this results in a good correction for *all* injection-levels. However, if the recombination lifetime varies with injection-level, as caused by emitter or SRH recombination, the corrected values may be ‘based’ on a value that does not apply at other carrier densities – in the case of emitter recombination the lifetime will be too small at higher bias carrier densities. This is shown explicitly in the next case.

3.5.1.2 Case II: decreasing lifetime with increasing excess carrier density

Figure 3.21 depicts the case where the effective lifetime decreases at larger carrier densities due to recombination in the emitter. Such recombination is characterized by the emitter saturation current density J_{0e} , which in this case was chosen to have a value of $2 \times 10^{-12} \text{Acm}^{-2}$. This relatively high value was chosen for reasons discussed below, and as modelled here for a $1 \Omega \text{cm}$ p -type substrate of thickness $300 \mu\text{m}$ and 15% reflectance, results in a low-injection lifetime cap of $12 \mu\text{s}$, or, alternatively, a 1-sun V_{OC} cap of 603 mV. Again, a trap concentration of $1 \times 10^{15} \text{cm}^{-3}$ has been used to generate trapping effects.

The significant impact of the traps on the ‘measured’ lifetime is obvious, and once again a bias-light intensity of 0.03 suns generates little improvement. However, the behavior for larger bias-light intensities is different to the constant lifetime case. The best correction is achieved with a bias of 3 suns. This is essentially the minimum bias required to fill the traps, and as such it provides the most accurate extrapolation to the axis (as shown in Figure 3.19) which is necessary to estimate the minority carrier density. The figure indicates that the 3 suns correction

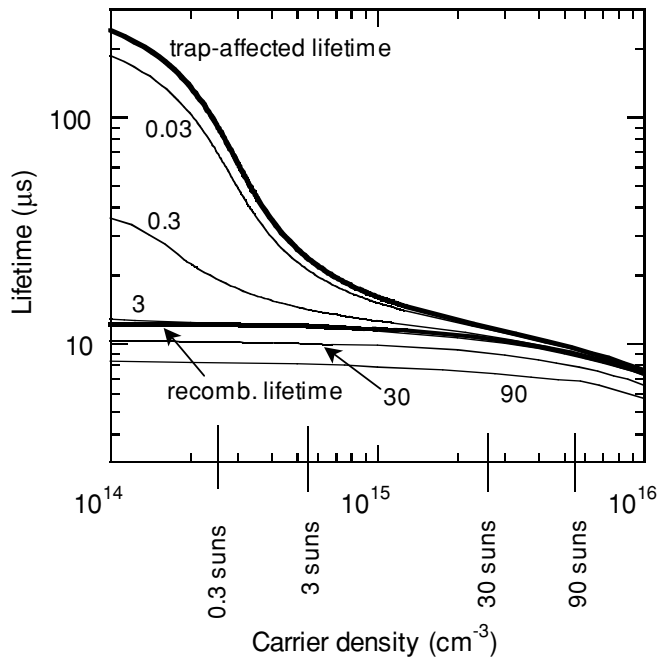


Figure 3.21. Case 2: Modelled emitter recombination dominated lifetime, with $J_{0e}=2\times 10^{-12} \text{ A cm}^{-2}$. The low-injection recombination lifetime is again $12\mu\text{s}$, and the trap density $1\times 10^{15} \text{ cm}^{-3}$. The impact of the bias-light correction is shown for bias-light intensities of 0.03, 0.3, 3, 30 and 90 suns. The corresponding bias carrier densities are shown on the horizontal axis. For the 0.03 suns case the value is $5.8\times 10^{13} \text{ cm}^{-3}$.

is very good at least down to a density of $1\times 10^{14} \text{ cm}^{-3}$, which represents a significant improvement in the range of usable data available. In fact, the usable data now extends down past 1-sun open-circuit conditions, allowing much greater accuracy in monitoring cell processes and predicting device performance. For very large bias terms, such as the 30 and 90 suns cases, the bias carrier density is well above the region where trapping dominates, and consequently the extrapolation to the axis is less accurate. Furthermore, at these high carrier densities, the dependence created by the emitter recombination causes the extrapolation to reflect high-injection conditions, and is irrelevant to the low-injection region of interest. Consequently these large biases cause the corrected lifetime to underestimate the recombination lifetime in the trap-affected region.

The crucial questions then become: which is the best bias-light intensity to use (i.e. what is the minimum bias required to just fill the traps), and over what range is the ensuing corrected data accurate? From Figure 3.21, it can be seen that the optimum bias of 3 suns corresponds to a bias carrier density of about $5\times 10^{14} \text{ cm}^{-3}$. In fact any bias carrier density in the range $3\text{--}7\times 10^{14} \text{ cm}^{-3}$ will give adequate results. This range straddles the carrier density at which the trap-affected lifetime is approximately twice the effective lifetime in the region just above the point where trapping begins. In other words, a good guideline for determining the best bias is to simply increase the bias until the bias carrier density is at the point where the uncorrected

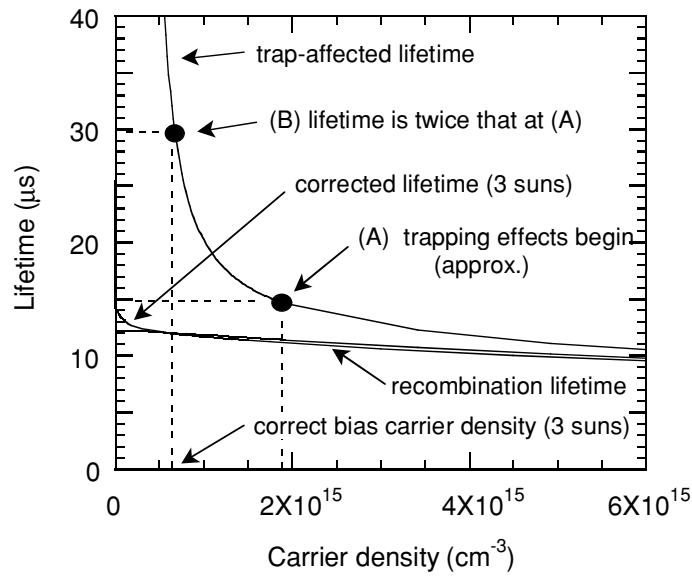


Figure 3.22. Case 2: Linear horizontal axis version of Figure 3.21. The method for determining the optimum bias begins by estimating, by visual inspection, the point on the trap-affected data where trapping begins to impact (point (A)). The lifetime at this point is then doubled. The data point corresponding to this new value (point (B)) gives the bias carrier density corresponding to the optimum bias.

lifetime is approximately doubled due to the traps. This can be done easily by visually inspecting the graphed data, and is made easier by viewing a linear plot as opposed to the logarithmic one of Figure 3.21. Figure 3.22 shows the same data on a linear scale, and the caption describes again the method for determining the optimum bias. Although such visual inspection is subject to uncertainty, the relative broadness of the optimum ensures that such uncertainties are small, and are more than outweighed by the ease of applying the method. An equivalent, alternative approach is to increase the bias-light until the corrected lifetime at the bias carrier density is half the uncorrected value. Care needs to be exercised with this second approach, as more than one bias-light value may satisfy this criteria. Finally, note that the properly corrected data is sufficiently accurate for all carrier densities greater than or equal to the bias carrier density.

While the accuracy of this method is independent of the magnitude of the trap density or the low-injection recombination lifetime, it does depend somewhat on the value of J_{0e} , since it determines the steepness of the high-injection slope. However, values of J_{0e} which are less than $2 \times 10^{-12} \text{ A cm}^{-2}$ will give rise to cases with milder dependence, and in the extreme case will approach Case 1 with a constant lifetime. We found that using a bias of 3 suns was very adequate also for that case, noting that a direct comparison is valid since all other parameters are the same. Consequently, we can state that this method for determining the appropriate bias level is valid for all emitters with $J_{0e} \leq 2 \times 10^{-12} \text{ A cm}^{-2}$. This is a large value, and should easily cover most practical industrial and laboratory cases.

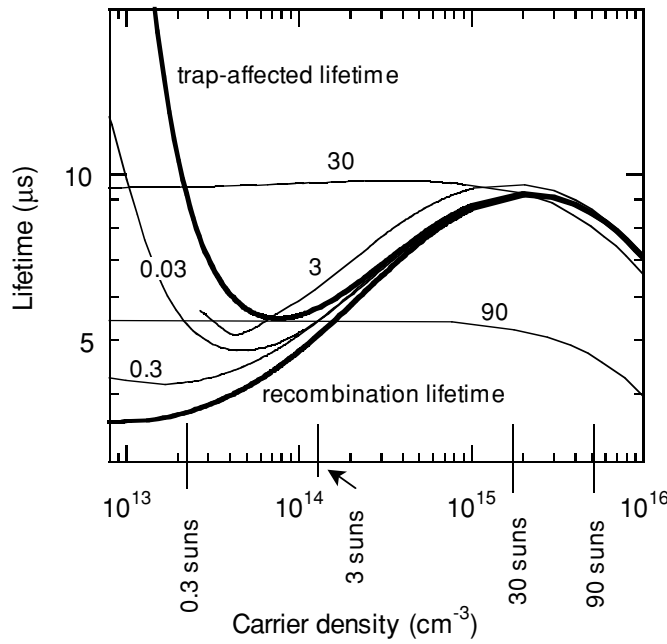


Figure 3.23. Case 3: Modelled SRH recombination dominated lifetime, with $E_{SRH}=E_C-0.4\text{eV}$, $\sigma_n=9\times10^{-15}\text{cm}^2$ and $\sigma_p=9\times10^{-17}\text{cm}^2$, $N_{SRH}=2\times10^{12}\text{cm}^{-3}$ and an emitter term of $J_{0e}=2\times10^{-12}\text{Acm}^{-2}$. The trap density is $1\times10^{14}\text{cm}^{-3}$. The impact of the bias-light correction is shown for bias-light intensities of 0.03, 0.3, 3, 30 and 90 suns. The corresponding bias carrier densities are shown on the horizontal axis. For the 0.03 suns case the value is $9.0\times10^{12}\text{cm}^{-3}$.

As mentioned, a bias of 3 suns was also adequate for Case 1. The procedure outlined above for determining the optimum bias is therefore applicable to both Cases 1 and 2. The final case to consider is that in which SRH recombination centres, either in the bulk or at the surfaces, give rise to a different type of injection-level dependence.

3.5.1.3 Case III: increasing lifetime with increasing excess carrier density

Figure 3.23 illustrates the case where SRH recombination dominates the lifetime dependence at low- to mid-injection levels. The effects of emitter recombination are retained as before, with $J_{0e}=2\times10^{-12}\text{Acm}^{-2}$. SRH recombination is also included, which manifests itself as an increasing lifetime as the carrier density moves from low- to mid-injection. The recombination properties of the SRH centres used were: energy level $E_{SRH}=E_C-0.4\text{eV}$ where E_C is the conduction band energy; electron and hole capture cross-sections $\sigma_n=9\times10^{-15}\text{cm}^2$ and $\sigma_p=9\times10^{-17}\text{cm}^2$ respectively; and a volume density $N_{SRH}=2\times10^{12}\text{cm}^{-3}$. These values are typical of interstitial metallic impurities such as iron in silicon. Once again traps were included in this case, but this time with a density reduced by an order of magnitude to $1\times10^{14}\text{cm}^{-3}$, in order to

allow the SRH behavior to dominate in the mid-injection range. This type of injection-level behavior is often seen in mc-Si samples with a relatively low trap density.

As in the previous cases, the lowest bias value of 0.03 suns is not sufficient to overcome the traps. As the bias is increased further, to 0.3 suns, the corrected curve moves towards the actual recombination lifetime curve, as expected. As the bias is increased still further however, the corrected curve starts to rise again, as in the 3 and 30 sun cases. This occurs due to the bias carrier density now being above the trapping region, where it is subject to the injection-level dependence of the recombination lifetime. The cause is the same as in Case 2, but this time with the opposite effect due to the opposite injection-level dependence. At the highest bias level of 90 suns, the corrected data shifts back down again, since in this case the emitter recombination dominates the recombination lifetime at the bias carrier density.

Consequently, the question as to which bias level to choose for the best correction is easier to answer in this case. A good rule is to simply increase the bias carrier density from below the measurement range to the point where the low-injection data falls to its lowest point. This occurs at a bias of 0.3 suns in Figure 3.23, which is an order of magnitude less than in the previous two cases, consistent with the lower trap density. Once again, the corrected data has reasonable accuracy at carrier densities greater than the bias carrier density, $2 \times 10^{13} \text{ cm}^{-3}$ in this case. Specifically, the correction overestimates the recombination lifetime by about 15% at the bias carrier density, whereas the uncorrected data, at the same carrier density, overestimates by about a factor of three (200%). In fact the uncorrected data only achieves an accuracy of 15% at about $1.5 \times 10^{14} \text{ cm}^{-3}$, hence the correction procedure pushes the range of usable data about an order of magnitude lower in terms of carrier densities than would otherwise be available.

3.5.2 General guidelines for applying the bias-light correction

Use of the proposed bias-light term to correct for trapping effects in QSSPC lifetime measurements of mc-Si improves the accuracy of the results in the region where trapping partially affects the measurement. Under most realistic conditions, the resulting corrected data is accurate to within about 20-30% at the bias carrier density, with improving accuracy at higher carrier densities. This generally represents an extra order of magnitude of usable data, in terms of carrier densities, than would otherwise be available. This can be very significant for commercial mc-Si, which often suffers from trapping effects at carrier densities corresponding to maximum-power conditions. Below the bias carrier density, the corrected data may behave erratically and should be discarded. Also, asymptotic affects, arising from the correction procedure, may occur near the bias carrier density.

The central question of deciding which is the best bias value to choose can be conveniently divided into two distinct cases:

1. Measured lifetime immediately above trapping region *decreases or is constant* with increasing carrier density: increase the bias until the bias carrier density is at the point where the uncorrected lifetime is approximately doubled due to the traps.

2. Measured lifetime immediately above trapping region *increases* with increasing carrier density: simply increase the bias until the corrected lifetime reaches a minimum at the lower carrier densities.

Essentially these guidelines reflect the desire to use just enough bias intensity to fill the traps, but not more. Both cases above can be performed by visual inspection of the QSSPC data, since the relatively broad optimum results in reasonable data for bias values varying by about a factor of 3. A general working principle which follows from the above guidelines, and which should always be observed, is that *the bias carrier density must always be less than the carrier density at which the lifetime is to be reported*. If it is not possible to achieve this while observing the guidelines above, then the trap density is too high to allow accurate correction at the desired carrier density.

3.5.3 Example of corrected measurements on 0.4Ωcm mc-Si

The previous three cases were based purely on modelled lifetime curves, although the recombination and trapping parameters used to create them are representative of standard mc-Si. In this section, real data from a 0.4Ωcm mc-Si wafer is subjected to the bias-light correction procedure outlined above. In order to assess the accuracy of the correction, it is of course necessary to have knowledge of the underlying recombination lifetime for the sample, across the whole injection-level range. This was achieved by processing the wafer into a solar cell with excellent emitter and rear surface properties, allowing the bulk to totally dominate the cells behavior. The illumination- V_{OC} curve under quasi-steady-state conditions was then measured, and the effective recombination lifetime curve inferred from the results, as detailed in Chapter 1. Such QSS V_{OC} measurements are immune to the effects of trapping, hence we are able to observe the recombination lifetime across a broad range of injection-levels. However, to obtain reliable recombination lifetime data with this technique, care needs to be taken to avoid the effect of shunts. Also, accurate temperature control is essential, as the lifetime varies exponentially with the measured voltage, which in turn varies approximately linearly, over a small range, with temperature.

The QSS V_{OC} recombination lifetime measurements are shown in Figure 3.24, as well as the trap-affected lifetime curve measured by the QSSPC method prior to metallisation. At

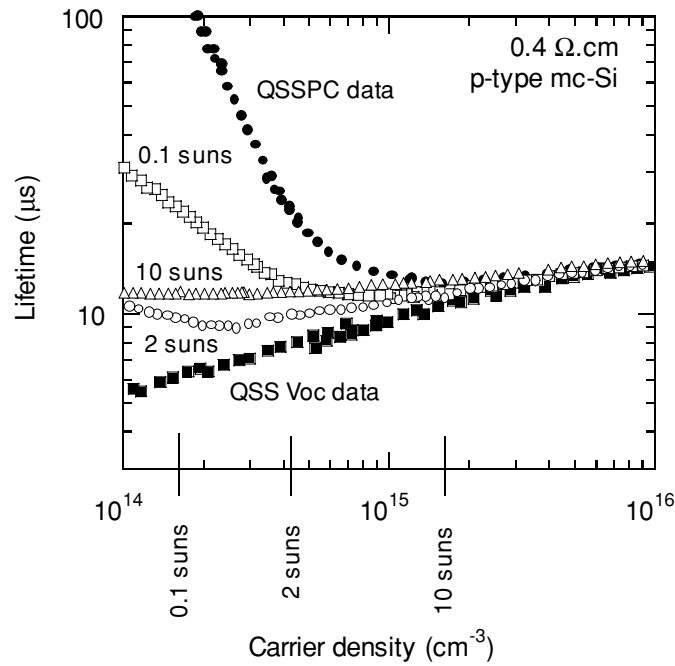


Figure 3.24. Trap-affected QSSPC lifetime and illumination- V_{OC} recombination lifetime measurements for a $0.4\Omega\text{.cm}$ mc-Si wafer. The impact of the bias-light correction on the measured data is shown for bias-light intensities of 0.1, 2 and 10 suns. The corresponding bias carrier densities are shown on the horizontal axis.

carrier densities above about $4 \times 10^{15} \text{cm}^{-3}$, the two methods are in good agreement. Below this value however, the QSSPC data becomes increasingly inaccurate as trapping effects dominate. The QSSPC data is then corrected using the bias-light method. This sample is qualitatively like Case 3 above, with SRH recombination apparent at low- to mid-injection, and we find that the conclusions reached in Case 3 hold here also. Again, the 0.1 sun bias is insufficient to provide satisfactory correction. The 2 suns case causes the corrected lifetime to reach its minimum at low-injection, while increasing the bias further to 10 suns causes the corrected curve to rise again. A bias-light intensity anywhere between 1-3 suns will give satisfactory results, corresponding to a bias carrier density range of about $3\text{--}6 \times 10^{14} \text{cm}^{-3}$. In a case such as this, the optimum bias is easy to determine, since it only needs to be increased until the corrected data reaches its lowest point at the lower carrier densities, as for Case 3 above. Note, however, that the optimum bias carrier density is very near the point where the non-trapping lifetime is doubled by the effect of traps, which is the method for determining the best bias value for Case 2 situations.

The corrected data once again has significantly improved accuracy for carrier densities above the bias carrier density. In this case, the corrected and uncorrected data overestimate the recombination lifetime at the bias carrier density by about 20% and 200% respectively. Clearly, some residual SRH dependence exists in the trap-dominated part of the data, and is extracted by the correction method. At carrier densities lower than the bias carrier density, however, these

SRH traces are overwhelmed by the trap-induced photoconductance, and the corrected data is unreliable.

3.6 Other explanations for anomalous photoconductance effects

Although the Hornbeck-Haynes trapping model seems to provide a good explanation of the anomalous photoconductance effects discussed in this chapter, it is worthwhile discussing some other potential explanations for such effects that have been proposed recently. There are two specific alternatives that will be examined in turn. The first is based on the slow release of carriers stored in the space-charge region at oxidised surfaces, and has been used to explain unusual transient decay in single-crystal wafers[137,138]. The second is based on theoretical modelling of bulk SRH recombination centres that occur at a density *equal* to the dopant density, resulting in extremely injection-level dependent recombination lifetimes[139]. Hence this second approach is referred to here as the ‘defect-compensated’ model. The relevance of these two alternatives to the data presented in this chapter from mc-Si samples is discussed.

3.6.1 Release of carriers from a space-charge region

In recent papers[137,138], Hahneiser *et al.* studied the origin of long carrier decay times (in the millisecond range) in single-crystal silicon wafers that had one oxidised surface and one bare surface. In such wafers the decay time is expected to be quite low (about 10 μ s, depending on the wavelength), due to the very high surface recombination velocity at the rear bare surface. By using time resolved microwave photoconductivity (TRMC) measurements, they were able to observe three distinct phases in the carrier decay. There was an initial period in which carriers did not have time to diffuse to the rear surface, hence little recombination occurred. This was followed by a period dominated by the decay of bulk carriers at the rear surface, and then a much longer decay due to the slow release of carriers that were ‘stored’ in the space-charge region at the oxidised surface. As they were released, these carriers diffused to the rear and recombined.

It is possible that such phenomena occur in the mc-Si wafers studied in this chapter, although in this case the recombination of the slowly released carriers would occur in the bulk rather than at the rear surface. However, the nature of the slow release from the space-charge region means that the effect is essentially transient in nature. Hence, using different flash decay

rates with the QSSPC technique should produce changes in the observed long lifetimes. In particular, using true steady-state illumination would result in the complete elimination of the effect, since when the carriers are ‘stored’ they do not contribute to the conductance. As shown in the preceding sections, the phenomenon observed in the mc-Si wafers studied here was unaltered by the use of steady-state illumination, indicating that the impact of any carriers stored in, and slowly released from, the oxide-induced space-charge regions is negligible.

3.6.2 Single-level recombination in defect-compensated semiconductors

Even more recently, Karazhanov[139] presented another alternative explanation for the very strong injection-level dependence discussed in this chapter. He proposed that the phenomenon observed in mc-Si could be explained by a single set of recombination centres, provided they have a certain energy level and capture cross-sections. Under these conditions, the effect is most pronounced when a sample is exactly ‘compensated’, meaning that the density of recombination centres N_{SRH} equals the dopant density N_{A} . When this occurs, the single localised level acts as both a trap and a recombination centre, and can produce photoconductance effects similar to those observed in this chapter.

The fundamental distinction between the Hornbeck-Haynes model considered here and Karazhanov’s model is that the former is based on a system involving *two* energy levels: relatively shallow trapping centres and deeper recombination centres, while the latter only has a *single* level. As discussed, an important feature of the Hornbeck-Haynes model is that, in a broad sense, the trapping and recombination effects are ‘de-coupled’, meaning that it is possible to have varying degrees of trapping and recombination in a given sample. This cannot occur in a single-level model such as Karazhanov’s.

Karazhanov fitted the single-level model to experimental data published jointly by the current author[140] (in fact it was the data in Figure 3.7) and suggested that this single-level model, due to its greater simplicity, was a more satisfactory explanation for the anomalous effect. There are however a number of considerations which strongly favor the two-level model (or more generally a multi-level model) as the more satisfactory explanation.

Firstly, the single-level model requires the sample to be ‘compensated’ for the effect to occur fully. As a result of fitting the model to the experimental data, Karazhanov found that the recombination centre density N_{SRH} , and therefore the dopant density N_{A} , in the particular sample modelled should be $4 \times 10^{14} \text{cm}^{-3}$. However, although unfortunately not mentioned in the article the data was taken from, this *p*-type sample had a resistivity of $0.9 \Omega \text{cm}$, corresponding to a

dopant density of $N_A=2\times 10^{16}\text{cm}^{-3}$, in contradiction to the prediction of the single-level model. As a more general objection, considering that mc-Si samples always display the anomalous effect at some apparent excess carrier density, it seems an unlikely coincidence that compensation would occur in every case.

A second consideration is that, as mentioned above, a single-level system implies a direct correlation between the extent of the anomalous effect and the degree of recombination in any given sample, or, rephrased using the terminology of this chapter, between the trap density N_T and the recombination lifetime. The results in Table 3.1 show that there is no such correlation between these parameters for the four samples listed, which, importantly, all had the same dopant density. This apparent separation between trapping and recombination was precisely the reason why a two-level system was originally proposed. Furthermore, the 200°C annealing experiments of non-gettered mc-Si wafers in section 3.4.2.3 provided direct evidence of the distinct physical origins of trapping and recombination centres in the material studied.

Finally, a further consideration relates to the measured and implied illumination- V_{OC} curves of solar cells fabricated on these mc-Si substrates. The measured curve must of course reflect the underlying recombination lifetime. However, we find that this is not the case, and in fact the measured and implied curves diverge significantly below the trap density, as shown in Figure 3.4 for example. In the single-level model, it is possible to generate such a divergence by virtue of differences between the majority and minority carrier lifetimes that arise from trapping by the centres. However, it is not clear that the carrier dynamics of the single-level model could produce a good explanation of the implied and measured illumination- V_{OC} data in a qualitatively accurate and self-consistent manner, a criteria which is well satisfied by the Hornbeck-Haynes model.

3.7 Summary

The anomalous photoconductance behaviour often observed in cast mc-Si wafers, and also other modern photovoltaic materials, has been explained using a minority carrier trapping model originally developed by Hornbeck and Haynes in the mid-1950's. The model allows the apparent injection-level dependence of the lifetime to be understood, and explains the lack of impact of these apparent lifetimes on cell voltage. The physical origin of these minority carrier traps in cast mc-Si was found to be related to the presence of dislocations, and also of boron-impurity pairs or complexes. Their thermal annealing behaviour has also been explained in terms of these boron-impurity complexes.

A simple method for numerically correcting trap-affected lifetime data has been examined in detail, and found to extend the range of carrier densities over which useful data is available by approximately an order of magnitude. This may often be of importance for predicting and monitoring cell performance and processes. Also, other possible explanations for the observed anomalous photoconductance effect have been considered. However, in contrast to the Hornbeck-Haynes model, they fail to explain all of the observed features of the anomalous effect.

CHAPTER 4

Recombination in Multicrystalline Silicon Solar Cells

4.1 Introduction

Recombination of charge carriers is the primary determinant of the open circuit voltage achievable in a solar cell, although the optical properties also have an important, but lesser influence. This recombination can occur in the bulk, emitter, or space-charge region, or at the front or rear surfaces. For a particular cell design and substrate type, one or more of these recombination mechanisms may come to dominate the electronic performance of the cell. For example, the highest efficiency single-crystal PERL (Passivated Emitter Rear Locally-diffused) cells, produced at UNSW[8], are apparently dominated by bulk recombination at open circuit conditions, while at maximum power, surface recombination at the rear oxide interface also becomes important[41,43]. Such information is useful in allowing further research efforts to be focussed in the appropriate areas.

In this chapter, high efficiency cast mc-Si PERL cells made at ANU are similarly analysed and found to be dominated almost entirely by bulk recombination at both open circuit

and maximum power. The injection-level dependence of the bulk lifetime results in higher ideality factors near maximum power, and hence lower cell fill factors. Other possible causes of the non-ideal behaviour, most notably space-charge region recombination, are discussed and shown to be negligible in the cells examined. To further illustrate the impact bulk centres can have on fill factors, cells that are dominated by bulk recombination through interstitial Fe, which has a strong injection-level dependence, are modelled. The fill factor is shown to be affected even for interstitial Fe concentrations as low as $1 \times 10^{11} \text{ cm}^{-3}$.

As a complement to the high efficiency mc-Si PERL cell study, analysis of the relative importance of the various recombination mechanisms in commercial mc-Si solar cells, produced by BPSolar in Villawood, Sydney, is then presented. The results suggest that the most important source of recombination in these cells is the emitter, followed by both the bulk and the rear surface, which have approximately equal importance. The significance of these results for future research is considered.

Further work on the physical origin of the bulk recombination centres in cast mc-Si is also discussed. SIMS analysis of gettered layers revealed the presence of Cr and Fe, but in concentrations too large to be present solely as interstitial impurities. Various experimental results are drawn together to conclude that these metals are most likely present as precipitates at extended defects, where their recombination activity is undoubtedly important, but currently poorly characterised.

Finally, some attempts at making high-efficiency PERC (Passivated Emitter and Rear Cell) devices on low resistivity cast mc-Si are presented. These substrates had shown excellent effective lifetimes after the optimised gettering process of Chapter 2, promising very high open circuit voltages, which were largely realised.

4.2 Injection-level dependent bulk lifetimes in multicrystalline silicon PERL cells

Multicrystalline silicon solar cells have achieved excellent results recently using various high-efficiency cell designs. Rohatgi *et al.*[141] recorded an efficiency of 18.6%, independently confirmed, in a cell with a full area Al BSF and evaporated front contacts. This efficiency was later matched, although not independently confirmed, by a full aluminium rear (but not alloyed) long-base $0.2 \Omega \text{ cm}$ cell with evaporated contacts reported by Stocks[102]. Recently, both these results have been eclipsed by a new record of 19.8% for a PERL cell made by Zhao *et al.*[101], based on their standard high efficiency PERL process for single-crystal cells. However, although impressive, the best mc-Si cells still fall well short of their single-crystal counterparts

at 24.7%[8]. It is useful then to compare the limiting mechanisms in these two types of cells in order to illuminate the path to further improvements. For the ultra-high efficiency single-crystal cells, it has been shown that the primary factor limiting the open circuit voltage is bulk recombination in the base[7]. At maximum power conditions, performance is further affected by the injection-level dependence of the surface recombination velocity of the rear oxide. This leads to a 'kink' in the J_{SC} - V_{OC} curve, resulting in ideality factors greater than unity, and hence lower fill factors[41,43].

Here we examine the limiting mechanisms in similar high-efficiency mc-Si cells. The recombination lifetimes of cell pre-cursors have been determined experimentally as a function of injection-level, and modelled with Shockley-Read-Hall (SRH) statistics and an emitter recombination term. Analysis of the results shows that the open circuit voltages are primarily limited by recombination in the bulk of the cells, as with the single-crystal cells mentioned above. However, the behaviour of these bulk SRH centres has a similar effect to the surface recombination velocity of the rear oxide in the single-crystal cells. Specifically, the bulk lifetimes exhibit a strong injection-level dependence that leads to a hump in the illumination- V_{OC} curve. Importantly, the injection-level dependence around one-sun maximum power conditions is quite strong, resulting in ideality factors greater than unity and therefore causing reduced one-sun fill factors. Note that the quality of the rear surface passivation of these mc-Si cells is similar to that of the single-crystal cells, but since the bulk lifetimes are significantly lower, the rear surface has a much reduced impact on cell parameters.

Using a simple analytic method to convert the lifetime measurements into implied I-V curves, we find that the measured fill factors and voltages agree well with the predicted values, provided the devices satisfy certain conditions. Conventionally, ideality factors greater than unity have been explained by the presence of junction recombination. However, we find, similarly to Aberle *et al.*[41,43], that such an explanation is not valid for these cells. The non-idealities and hence reduced fill factors are explained much more plausibly, in the absence of series resistance, by the bulk lifetime injection-level dependence.

4.2.1 Experimental Methods

Solar cells were fabricated on 1.5 and 0.4 Ω cm boron-doped cast mc-Si wafers grown by directional solidification at Eurosolare, Italy. The PERL cell process used is essentially the same as that outlined in Chapter 2, section 2.4.1.1. Photolithographically defined contacts on lightly-doped ($>100\Omega/\square$), oxide-passivated emitters ensured low emitter recombination losses. Point-contacts through an aluminium-annealed (alannealed) oxide on the rear of the 2 \times 2cm cells

similarly afforded very low rear-surface recombination losses. To ensure good ohmic contact to the base, particularly on the $1.5\Omega\text{cm}$ substrates, localised boron diffusions were included. Edge effects were avoided by the use of a planar diffusion through a 4cm^2 window in a thermal oxide that extended well beyond the cell boundaries.

It is well known that cell fabrication processes can affect recombination lifetimes significantly. This is particularly true for mc-Si, which is often prone to lifetime degradation during high temperature steps such as oxidations, as discussed in detail in Chapter 2. As a result, in order to make accurate correlations between substrate lifetimes and final cell parameters, it is crucial that the lifetime measurements be performed near the end of the fabrication process. Since the presence of metal contacts makes accurate excess-photoconductance measurements impossible on our system, lifetimes were measured just prior to metallisation and immediately after the opening of contact-holes through the front and rear (annealed) passivating oxides. To verify that the metallisation process did not impact on the substrate lifetime, the contacts were almost completely removed on one of the finished cells and the lifetimes re-measured. The results revealed no discernible change.

After metallisation, the one-sun I-V curves of the cells were measured, as were their illumination- V_{OC} profiles. The latter was achieved by monitoring the open-circuit voltage on an oscilloscope while simultaneously monitoring the intensity of an exponentially decaying flash lamp[37,136].

4.2.2 Analytic Modelling Techniques

Recombination lifetimes measured with the QSSPC techniques were modelled using SRH and emitter recombination terms, in identical fashion to the cross-contaminated FZ wafers in Chapter 3. Due to the low defect-related lifetimes in these samples ($<100\mu\text{s}$), and the fact that the cells operate at low excess carrier densities, Auger recombination plays no role in these devices, and is subsequently neglected. Also, the passivating quality of the annealed oxides was sufficiently high to ensure that recombination at the surfaces was insignificant in comparison to other effects. This was verified experimentally, as explained in the discussion section below. The recombination lifetime is then given by:

$$\frac{1}{\tau_r} = \frac{1}{\tau_{SRH}} + \frac{1}{\tau_{emitter}} \quad (4.1)$$

where τ_{SRH} is the SRH bulk recombination lifetime and $\tau_{emitter}$ an effective emitter recombination lifetime as discussed in Chapter 1.

The emitter recombination lifetime is determined by:

$$\frac{1}{\tau_{emitter}} = \frac{J_{0e}(N_A + \Delta n)}{qn_i^2 W} \quad (4.2)$$

where J_{0e} is the emitter saturation current density, W the cell thickness and $n_i = 8.63 \times 10^9 \text{ cm}^{-3}$ the intrinsic carrier concentration in silicon at 25°C . This is a simplified expression that is only valid when recombination in the emitter is not limited by the diffusive transport of carriers from the bulk to the emitter, and a nearly uniform carrier profile exists. It is a good approximation only when J_{0e} is relatively small, or when the contribution of the emitter to the total recombination is small, both of which are true for the cells analysed here under one-sun operating conditions.

The values of W and N_A are known by measurement. The emitter saturation current density J_{0e} is determined from the slope of a linear fit to the high excess carrier density part of the inverse lifetime curve, where the emitter dominates, as described in Chapter 1. By adjusting the remaining unknown SRH parameters, namely τ_{n0} and τ_{p0} , a fit can be obtained for the mid- to high-injection-levels. However, a further complicating issue is the presence of trapping centres, which cause an abnormally large photoconductance at injection-levels equal to and less than the trap density (between 1×10^{13} and $1 \times 10^{14} \text{ cm}^{-3}$ in these samples), in turn causing the apparent lifetime to increase dramatically with decreasing injection-level. In order to circumvent this problem, the Hornbeck-Haynes trapping model of Chapter 3 was fitted to the apparent lifetime data, with the modelled recombination lifetime as an input, and the traps subsequently ‘turned off’. This procedure involves introducing two more parameters to the fitting process, namely the trap density N_T and the trapping-time to escape-time ratio τ_t/τ_g . By doing so, the recombination lifetime can be calculated at lower injection-levels than would otherwise be possible. The procedure is more time consuming than using the bias-light correction of Chapter 3, but is in general more accurate. Nevertheless, as with the bias-light method, the accuracy of this technique decreases rapidly with decreasing injection-level. Consequently, trapping sets an effective lower limit to the injection-levels at which accurate recombination lifetime measurements can be made.

Figure 4.1 provides an example of a lifetime curve that exhibits all of the features mentioned above. Below $2 \times 10^{13} \text{ cm}^{-3}$, trapping dominates, as indicated by the decrease in apparent lifetime with increasing injection-level. Between 2×10^{13} and $2 \times 10^{15} \text{ cm}^{-3}$, the dependence of the lifetime with injection-level is reversed as SRH recombination dominates, while above $2 \times 10^{15} \text{ cm}^{-3}$ the dependence is reversed yet again as emitter recombination takes over. Figure 4.1 also shows the constituent parts as well as the total lifetime model as fitted to the experimental data. To obtain a good fit, it was necessary to use *two* independent SRH

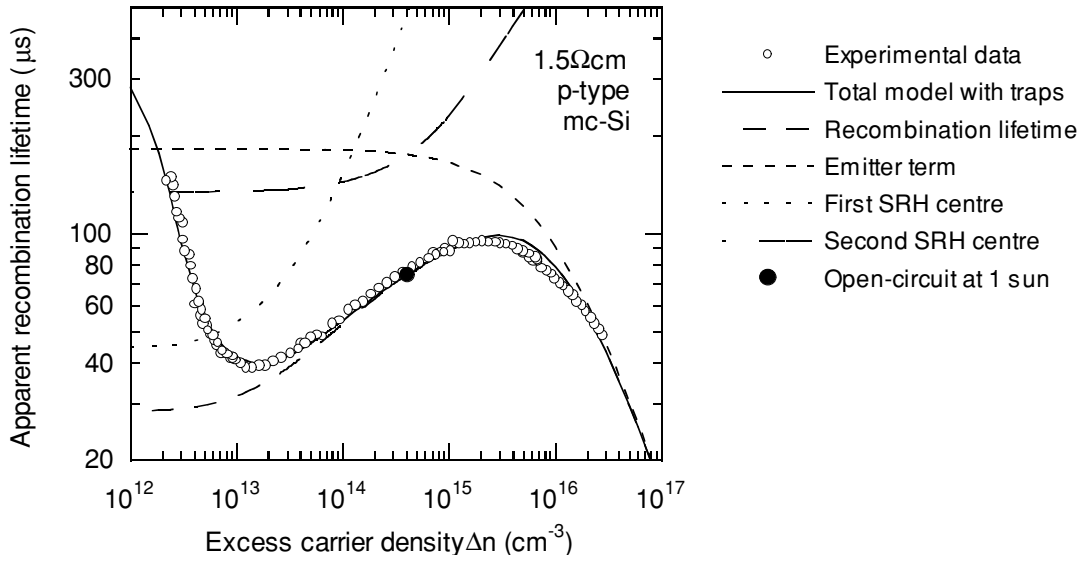


Figure 4.1. Apparent lifetime versus excess carrier density for a 1.5Ωcm mc-Si cell precursor. As well as showing the total injection-level dependent model, the constituent parts, namely the two SRH centres and the emitter term, are also shown. The solid circle represents open-circuit conditions under one-sun illumination.

centres, an emitter term, and the effect of trapping centres. Note that the recombination lifetime is also shown as extrapolated from regions above the onset of trapping to well below it by ‘turning off’ the traps in the model. As mentioned, the accuracy of such an extrapolation is uncertain at low carrier densities, but it serves to show, in qualitative terms, the expected injection-level dependence of the recombination lifetime in this region.

With an expression for the injection-level dependence of the recombination lifetime, we can then proceed to predict the illumination- V_{OC} curve of a substrate upon metallisation. As discussed in Chapter 1, it is possible to do this at all measured illumination levels, since a knowledge of the lifetime at each illumination level equates to a knowledge of the carrier densities. The implied V_{OC} is then:

$$V_{OC} = \frac{kT}{q} \ln \left(\frac{\Delta n (N_A + \Delta n)}{n_i^2} \right) \quad (4.3)$$

It is important to note that an implicit assumption in this method is that the carrier densities do not vary significantly in terms of their spatial profiles in the base, or in other words that the carrier concentration at the junction edge is equivalent to the average carrier density. This generally amounts to requiring the minority carrier diffusion length in the base to be comparable to or larger than the base thickness.

The implied illumination- V_{OC} curve can be compared with the measured illumination- V_{OC} curve after metallisation. The short circuit current density J_{SC} of the cells was measured as a function of illumination, and found to be linear over the measurable range. Consequently, the

implied and measured illumination- V_{OC} curves can easily be converted to J_{SC} - V_{OC} curves by using the factors 23.4 and 34.4 $\text{mAcm}^{-2}\text{sun}^{-1}$ for the 0.4 and 1.5 Ωcm cells respectively. The large difference between these short-circuit current density values is due to the lack of an antireflection coating on the 0.4 Ωcm cell.

It is possible to take the analysis of the recombination lifetime data further still. Noting that the currents are linear with illumination, the implied illumination- V_{OC} curve, as calculated from the lifetime expression, can be converted into an implied photovoltaic I-V curve by invoking the superposition principle, and neglecting the effects of series resistance. The resulting fill factor reflects only non-idealities arising from injection-level dependent effective lifetimes. This is essentially the same process used in Sinton's[37,136] technique for converting *measured* illumination- V_{OC} curves into I-V curves. In this technique, the voltages are measured at open circuit, so that series resistance effects are absent, although in this case the effects of any post-metallisation shunting present will be incorporated into the fill factor. Finally of course, there is the measured fill factor of the cell from the standard photovoltaic I-V curve, which includes series resistance as well as the other effects. There are then *three* fill factors that can be fruitfully compared in this work: the implied fill factor (from the lifetime measurement), the V_{OC} -mode fill factor (from the illumination- V_{OC} measurement) and the photovoltaic-mode fill factor (from the standard I-V curve). Comparisons between these various fill factors reveal the relative importance of changing lifetimes, shunts and series resistance effects in reducing the final photovoltaic-mode fill factor.

4.2.3 Results and Discussion

Figures 4.1 and 4.2 illustrate lifetime data for two different mc-Si cell pre-cursors, with base resistivities of 1.5 and 0.4 Ωcm . Both show the same general behaviour, being dominated by traps at low injection, then exhibiting some SRH dependence, and finally being dominated by the emitters at high injection. Note however that the magnitudes of the lifetimes are quite different, with values of 65 and 20 μs for the 1.5 and 0.4 Ωcm material respectively at an excess carrier density of $1 \times 10^{16} \text{cm}^{-3}$. This drop reflects the change in resistivity, and was also observed in similar material in Chapter 2 at the end of the same cell process, which gave comparable lifetimes of 70 and 20 μs (see Figure 2.6).

The lifetime model described above was fitted to both these curves, and also shown separately are the curves due to the SRH centres and the emitter needed to achieve the total fit. Note that it was necessary to employ two SRH centres to achieve a good fit in both cases. In fact it is possible that even more than two types of recombination centre are important in these

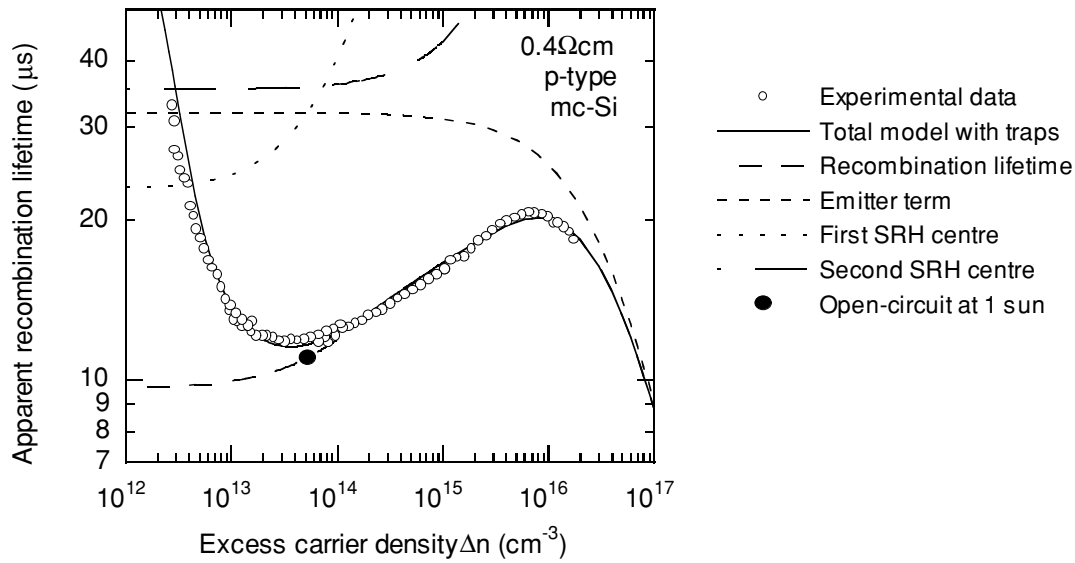


Figure 4.2. Apparent lifetime versus excess carrier density for a 0.4Ωcm mc-Si cell precursor. The two SRH curves and the emitter term are shown separately. The solid circle represents open-circuit conditions under one-sun illumination.

Sample type, resistivity	Dopant density N_A (cm ⁻³)	Thickness W (cm)	Emitter sat. current J_{0e} (Acm ⁻²)	Trap density N_T (cm ⁻³)	Trap/escape ratio τ_e/τ_g	Elec.-capt. time const. τ_{n0} (s)	Hole-capt. time const. τ_{p0} (s)	τ_{n0}/τ_{p0} ratio
Multi 1.5	1.0×10^{16}	0.028	1.9×10^{-13}	9×10^{12}	0.02	3.33×10^{-5}	1.11×10^{-2}	0.003
						1.09×10^{-4}	1.09×10^{-3}	0.1
Multi 0.4	4.0×10^{16}	0.032	3.0×10^{-13}	9×10^{12}	0.02	2.13×10^{-5}	7.09×10^{-3}	0.003
						3.33×10^{-5}	3.33×10^{-4}	0.1

Table 4.1. Fit parameters for Figures 4.1 and 4.2. Two sets of electron- and hole-capture time constants appear for each sample, since two independent SRH recombination centres were required to obtain a satisfactory fit.

samples, although two are sufficient to fit within measurement uncertainty (estimated to be 15%). Indeed, in similar modelling work, Robinson *et al.*[43] found that the ‘kink’ in the illumination- V_{OC} curve predicted by a single SRH centre was much sharper than any that they measured experimentally. They concluded that the presence of more than one type of centre would ‘smooth out’ the kink, which is precisely the effect of the two centres used here.

The fit parameters are presented in Table 4.1. It is interesting to note that the ratio between the electron- and hole-capture time constants, τ_{n0}/τ_{p0} , for the first and second SRH centres, are the same for the two wafers of different resistivities. The capture time constants are related to the concentration of SRH recombination centres N_{SRH} and the electron and hole capture cross-sections σ_n and σ_p through the relations $\tau_{n0} = 1/(v_{th}\sigma_n N_{SRH})$ and $\tau_{p0} = 1/(v_{th}\sigma_p N_{SRH})$, where $v_{th} = 1.1 \times 10^7$ cm s⁻¹ is the thermal velocity of electrons and holes at 300K. The fact that these ratios are equal reflects that, although they may be present in varying amounts, the same two *types* of recombination centre are present for each resistivity. It seems reasonable to expect

this to be the case, considering that the wafers were cast by the same manufacturer using the same technique.

The curves of most consequence in Figures 4.1 and 4.2 are the recombination lifetime curves, i.e. the sum of the SRH and emitter terms, but with the traps turned off. It is these curves which are later used to calculate the implied illumination- V_{OC} and implied I-V curves. At this stage however, it is useful to establish if the observed SRH dependence arises from surface or bulk states. The front surface can be ruled out, since recombination there is characterised by the emitter term, and has essentially no injection-level dependence when the base is in mid- to low-injection. Hence, if caused by surface recombination, it must be due to the rear.

These substrates enjoyed an annealed oxide on the rear that in general provides excellent passivation[28]. Single-crystal float zone (FZ) samples of comparable resistivity which were processed in parallel with the mc-Si samples, yielded effective lifetimes approximately an order of magnitude larger than the mc-Si samples, with very little injection-level dependence. This suggests that the mc-Si samples are bulk limited, but does not constitute definite proof, since the grain orientations of the mc-Si samples are random and hence the oxide growth is less predictable, potentially leading to poorer passivation[142]. However, when subjected to a corona discharge[60] on the rear oxide, the lifetimes of the FZ wafers increased further due to the field-enhanced passivation, revealing that, although the initial passivation was good, these wafers were rear-surface limited. When a similar charge layer was deposited on the rear of the mc-Si wafers however, no increase was observed. Consequently, we may tentatively assert that the SRH dependence of the mc-Si samples arises from bulk properties.

This conclusion is further supported by direct measurements of the surface recombination velocity of similar annealed oxides on mc-Si samples from the same $1.5\Omega\text{cm}$ ingot performed by M. Kerr[140]. Those experiments revealed that in the carrier density range of interest here, the SRV was around 50cm/s . Using Equation 1.16 of Chapter 1 (without the factor 2 since only the rear surface is considered here), shows that this SRV value results in the effective and bulk lifetimes being equivalent to within 10% for an effective lifetime of $50\mu\text{s}$. It seems then that the measured effective lifetimes of the mc-Si samples are essentially bulk-driven.

Another important feature of these graphs is the solid circle representing the recombination lifetime and injection-level which occur under one-sun illumination. This is the point which determines the open circuit voltage at one-sun, and the behaviour of the lifetime below this point will influence the fill factor. If the lifetime decreases below the one-sun point, a reduced fill factor will result. For the $1.5\Omega\text{cm}$ substrate, the one-sun point occurs quite near the maximum lifetime, with a strong SRH dependence below. Since there exists a significant injection-level range below the one-sun point that is not affected by trapping, we can use this data to determine the implied illumination- V_{OC} and one-sun I-V curves, and hence predict the implied fill factor for this cell with some accuracy. In fact, this was precisely the reason for

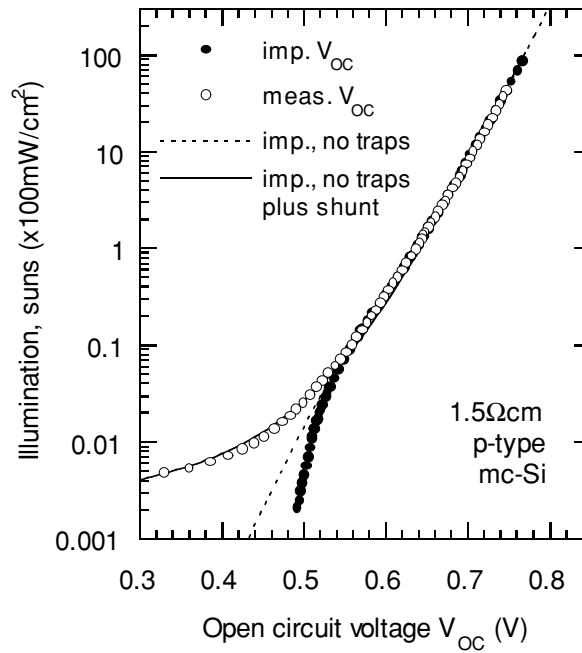


Figure 4.3. Implied and measured illumination- V_{OC} curves for the $1.5\Omega\text{cm}$ cell. The dotted line represents the implied voltage calculated from the recombination lifetime in Figure 4.1. The solid line also includes the effect of a shunt resistance of 2400Ω .

Sample	Imp. V_{OC} (V)	Meas. V_{OC} (V)	Implied FF (from τ_r curve)	V_{OC} -mode FF (from illum- V_{OC})	PV-mode FF (from I-V curve)
Multi 1.5	642	644	0.790	0.797	0.785
Multi 0.4	616	614	0.827	0.823	0.806

Table 4.2. Implied and measured V_{OC} and fill factors (FF) for the two mc-Si cells.

studying this particular sample, since in general mc-Si exhibits a much larger trap density. This can be seen in the case of the $0.4\Omega\text{cm}$ substrate, for which the onset of trapping occurs very close to one-sun open circuit conditions, compromising the accuracy of the recombination lifetime measurements around maximum power conditions.

After lifetime measurements, these substrates were metallised, and the illumination- V_{OC} curves measured. Figure 4.3 shows the results for the $1.5\Omega\text{cm}$ cell, together with the implied illumination- V_{OC} data as calculated from both the apparent and recombination lifetimes from Figure 4.1. The curve predicted by the apparent lifetime is in good agreement at high voltages, but then diverges rapidly due to trapping effects. The recombination lifetime is somewhat better, but still inaccurate due to a shunt that occurred during metallisation, evident at voltages below about 0.55V. The final fit on Figure 4.3 is for the recombination lifetime with the effects of a shunt resistance of 2400Ω included. There is good agreement between this curve and the measured curve, which is reflected by an excellent correlation between the one-sun implied and

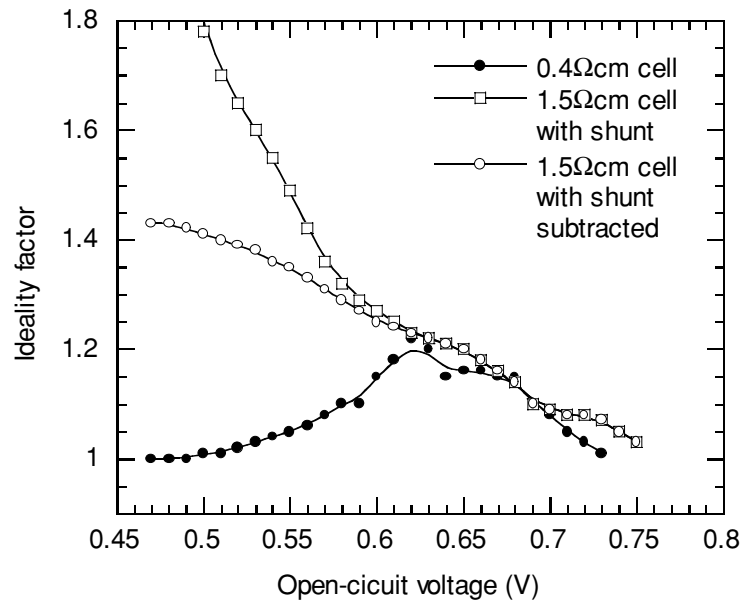


Figure 4.4. Measured ideality factors for the $1.5\Omega\text{cm}$ (with and without shunt) and $0.4\Omega\text{cm}$ cells. The lines are guides to the eye.

measured V_{OC} values given in Table 4.2. Fortunately, the shunt resistance is large enough to not significantly affect the performance of the cell near one-sun maximum power, and so has little affect on the fill factor. Note that for this cell, the three different fill factors in Table 4.2 are almost within the likely uncertainty limits. There is a small drop from 0.797 to 0.785 from V_{OC} -mode to photovoltaic-mode, which is probably due to series resistance. However, an ideal cell would have a fill factor of 0.835, as discussed below, indicating that the observed low fill factor values are mostly caused by factors other than series or shunt resistances.

A further manifestation of the shunt is that the apparent ideality factor for this cell decreases monotonically from values greater than 2 in low voltage regions, towards a value of 1 in high-injection, due to emitter recombination, as shown in Figure 4.4. Also shown is the ideality for this cell with the effect of the shunt resistance subtracted, revealing again that the shunt alone is not sufficient to fully explain the change in ideality.

Figure 4.5 shows the corresponding illumination- V_{OC} results for the $0.4\Omega\text{cm}$ cell. This cell did not suffer from any noticeable shunting at lower voltages. This raised a further consideration however, namely the possibility of junction capacitance effects distorting the values at lower voltages. Such effects can arise if the characteristic decay time of the flash is not considerably longer than the equivalent RC constant relating to the junction capacitance, an issue which is discussed in Chapter 1. This possibility can be tested, however, by using flashes of different decay length. Two such measurements for a 1.8ms and a 4.0ms flash are shown in the figure, and result in very similar curves, implying that the measurements are not overly affected by junction capacitance. This conclusion is further supported by the dark I-V curve that

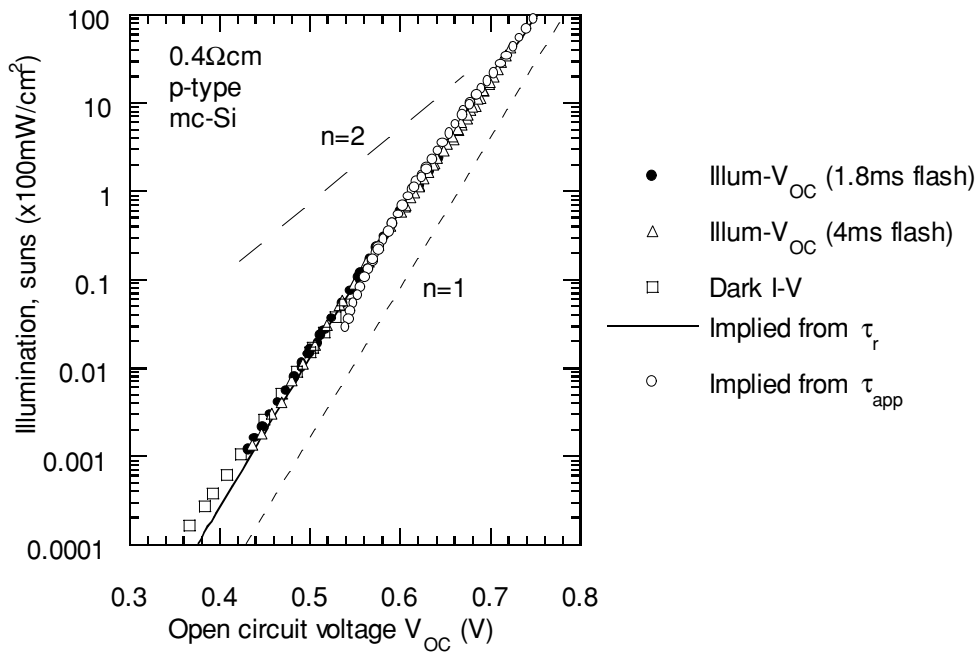


Figure 4.5. Implied and measured illumination- V_{OC} curves for the $0.4\Omega\text{cm}$ cell. The solid line represents the implied voltage calculated from the recombination lifetime in Figure 4.2. Idealities of $n=1$ and $n=2$ are also shown.

was measured in steady-state and is also shown on the figure. It is possible that junction capacitance occurs at lower voltages, but in that case the impact on the fill factor would be very small.

The corresponding local ideality factor curve for the $0.4\Omega\text{cm}$ cell, calculated from the measured illumination- V_{OC} data, is shown in Figure 4.4. This cell is qualitatively different to the previous device in that the ideality begins at 1, increases a little, and then returns to 1 at high voltages. This is significant when considering the physical origin of the non-idealities, as discussed in the following section.

4.2.3.1 Junction recombination as an alternative explanation of non-ideal behaviour

A common explanation for ideality factors greater than 1 in silicon solar cells at low voltages is recombination in the space-charge region, typically expressed through the double-diode model[143,144]. In this model, the $n=2$ term is considered to arise from SRH recombination in the junction itself, and the transition between this term, which is dominant at low voltages, and the $n=1$ term, which arises from bulk and emitter recombination, causes the broad sweep of intermediate idealities. Figure 4.5 shows the result of applying this model to the

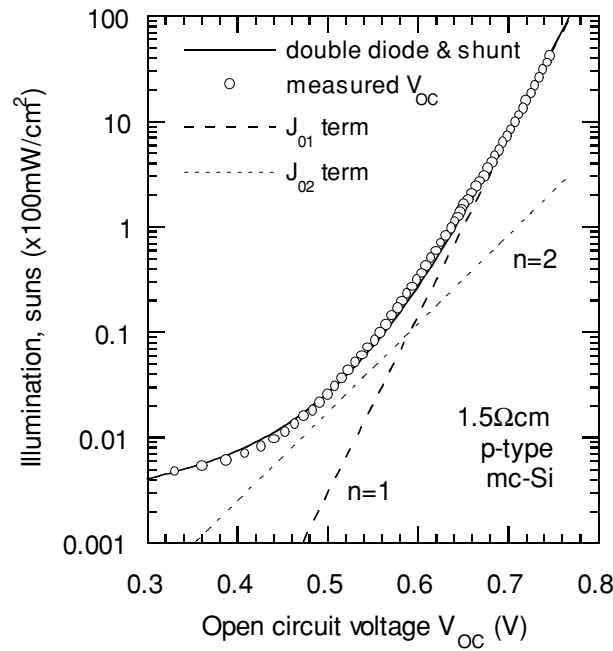


Figure 4.6. Double-diode model fitted to the measured illumination- V_{OC} data of the $1.5\Omega\text{cm}$ cell.

data, and shows that, indeed, a good fit is attainable in the case of this $1.5\Omega\text{cm}$ cell when the same shunt of 2400Ω is included in the model. The value of the dark saturation current J_{O1} (the pre-factor of the ideality one term in the double-diode model), was required to be $J_{O1}=4.0\times 10^{-13}\text{Acm}^{-2}$, twice as high as the measured value of the emitter saturation current of $J_{Oe}=1.9\times 10^{-13}\text{Acm}^{-2}$. The difference is caused by recombination in the base, which is assumed to be injection-level independent and is lumped into the J_{O1} term in the double-diode model. The required value for the ideality two pre-factor, J_{O2} , was $3.7\times 10^{-8}\text{Acm}^{-2}$. Such a reasonable fit of the double diode equation might lead one to the premature conclusion that the non-idealities are caused by junction recombination.

Fortunately, the situation is clarified by the data from the $0.4\Omega\text{cm}$ cell, the illumination- V_{OC} plot for which is shown in Figure 4.5. In this case there is no complicating shunt, and the implied voltage curve calculated from the recombination lifetime and the measured voltages agree well over the entire range, except at very low voltages where the extrapolation of the recombination lifetime into the trapping region is uncertain. Ideality factors of $n=1$ and $n=2$ are also shown on this plot, and reveal that for this cell the ideality changes from values near one to slightly greater than one, and then back to one as the voltage increases, as shown explicitly in Figure 4.4. The lack of a shunt in the $0.4\Omega\text{cm}$ cell therefore allows us to rule out the influence of junction recombination on the ideality factor in the voltage range of interest, since it is not possible to achieve the observed ideality dependence with the standard double-diode model. It seems likely that a similar dependence is occurring in the $1.5\Omega\text{cm}$ cell, but that the low-

injection behaviour is masked by the presence of the shunt, leading to a dependence that *could* be interpreted as junction recombination. Upon subtracting the shunt, the 1.5Ωcm cell still shows non-idealities at lower voltages than the 0.4Ωcm cell, but this is due to the more pronounced injection-level dependence of the lifetime below one-sun open circuit conditions in the 1.5Ωcm cell, as revealed in Figures 4.1 and 4.2.

As further evidence against the presence of junction recombination, we make use of an analytic model that allows an estimation of the magnitude of the recombination current in this part of a device. Corkish and Green[145] developed an expression for an effective upper bound (which they termed $J_{rg}(1)$) on the junction recombination saturation current density, (which is equivalent to the pre-factor of the ideality 2 term, J_{O2} , in the double diode equation), that holds under the general conditions of asymmetric junctions and capture time constants. Using the recombination parameters determined for the 1.5Ωcm cell from the lifetime modelling in Table 4.1, we find that $J_{O2} \leq 2 \times 10^{-9} \text{ Acm}^{-2}$. This value is much less than that determined above by fitting the double-diode model, implying that the vast majority of the $n=2$ term in the double-diode fit does not in fact arise from junction recombination. This point is further illustrated by the following observation: under a forward bias of 0.55V, which is close to maximum-power for the cell in question, this upper bound represents a current loss of at most $85 \mu\text{Acm}^{-2}$ compared to the observed loss of more than 1mAcm^{-2} when compared to a cell with ideality 1 (see Figure 4.7). Modeling the 0.4Ωcm cell in a similar way reveals an even smaller junction recombination current ($J_{rg} \leq 3 \times 10^{-10} \text{ Acm}^{-2}$). Remembering that these figures represent upper bounds, it seems clear that junction recombination plays a minor role in these devices, at least at voltages that are likely to impact on the fill factor. In general then, the double-diode model, while in some cases allowing an accurate fit, does not provide meaningful insights into the physical nature of the recombination processes. This is consistent with other work by Hovel which concluded that junction recombination is unlikely to be important for silicon cells[146], except possibly when they are thin ($< 50 \mu\text{m}$) and have very short defect-related lifetimes ($\ll 1 \mu\text{s}$), or if they have multiple junctions[147].

As described above, the implied illumination- V_{OC} data can be used to predict the fill factor of the finished cells via an implied I-V curve. Figure 4.7 shows the photovoltaic-mode I-V curve and the implied I-V curves for the 1.5Ωcm cell. For the implied curve, the measured value of J_{SC} (34.4 mA/cm^2) is used to scale the current axis. Good agreement between the measured and implied curves is evident in the fill factor values of 0.785 and 0.790 respectively, as summarised in Table 4.2. This agreement indicates that series resistance only has a small impact on this cell. Also shown on the figure is the I-V curve expected for a similar cell, but with a constant recombination lifetime below open circuit conditions. The effects of emitter

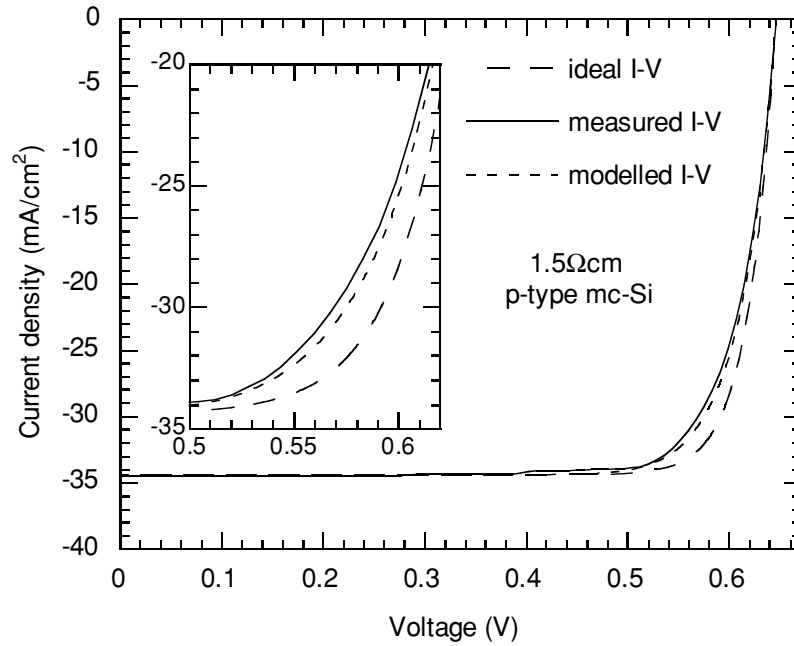


Figure 4.7. Implied and measured one-sun I-V curves for the 1.5Ωcm cell. The inset shows a magnified version of the maximum-power region. The ‘ideal’ constant lifetime I-V curve is for a cell with no injection-level dependence below open-circuit, resulting in a higher fill factor.

recombination are retained for high injection, leading to an ideality of one for all injection-levels in this case (as discussed in Chapter 1). This curve represents an ‘ideal’ cell, and yields a fill factor of 0.835. Thus the low measured fill factor can be attributed almost entirely to the injection-level dependence of the bulk-lifetime, an ‘intrinsic’ property of the material, and not to device design problems such as series or shunt resistance, or edge effects, nor to junction recombination. It is interesting to note that the highest efficiency mc-Si cell made to date by Zhao *et al.*[101], on similar 1.5Ωcm material with a similar cell structure, also achieved a fill factor of 0.795. It seems quite possible that this cell may also have been affected by the injection-level dependence of the bulk lifetime.

The interpretation of the implied I-V curve is more complicated in the case of the 0.4Ωcm cell. Table 4.2 shows that all three fill factor values are larger for the 0.4Ωcm cell than for the 1.5Ωcm cell. The basic reason underlying this fact is that the higher dopant density and lower lifetimes cause this cell to be in lower injection at one-sun, and hence further from the region of strongest SRH dependence. The implied and V_{OC} -mode values (0.827 and 0.823) are again in good agreement, indicating that the small reduction from the ideal value is due to the slight injection-level dependence of the bulk lifetime at maximum power. There is however a significant difference between these values and the photovoltaic-mode fill factor of 0.806. This discrepancy is caused by series resistance, which was more pronounced in this cell.

4.2.3.2 Validity of assumptions in the modelling

It is important to consider the possible impact of injection-level dependent lifetimes on J_{SC} , as non-linearities in J_{SC} as a function of illumination would invalidate the use of the superposition principle. For the $1.5\Omega\text{cm}$ cell, the minority carrier diffusion length in the base is always greater than the base thickness, resulting in essentially uniform carrier profiles in the base at all times. It is reasonable then to expect a linear J_{SC} response from this cell, which was verified experimentally by monitoring J_{SC} over a large illumination range. However, the analysis of the $0.4\Omega\text{cm}$ cell is potentially complicated by the fact that the minority carrier diffusion length in the base is less than the base thickness (about half at worst). The result is spatially non-uniform carrier profiles, a situation that may be further exacerbated by the injection-level dependent lifetime, potentially jeopardizing the validity of superposition. Despite this, this cell also exhibited a very linear J_{SC} response. This linearity stems from the fact that, in short circuit conditions, the excess carrier density in the base is very low, and the effective lifetime is essentially constant. This remains true even for very high illumination levels. The net result is that the diffusion length in short circuit conditions is essentially independent of the illumination level, giving rise to a linear current response irrespective of whether the diffusion length is longer or shorter than the base thickness.

4.2.3.3 Conclusions

To summarise this section, a high-efficiency PERL cell design applied to gettered mc-Si wafers results in devices whose electronic performance (i.e. open circuit voltage and fill factor) is limited almost wholly by the bulk recombination lifetime. This contrasts with equivalent single-crystal cells, which tend to be limited by a combination of bulk recombination and surface recombination at the rear oxide. Further improvements in high-efficiency mc-Si cells therefore have to stem from increased bulk lifetimes. Treatments such as gettering can help to improve lifetimes, but only to an extent. Consequently it seems that non-ideal fill factors are often an intrinsic property of the material, and are not always caused by device issues such as series and shunt resistances, nor by junction recombination.

Injection-level dependent bulk recombination lifetimes are of course not restricted to mc-Si. Boron-doped Czochralski (Cz) silicon, widely used for commercial solar cell applications, is known to suffer from light-induced bulk lifetime reductions due to boron-oxygen complexes[129]. Due to its commercial relevance, this effect has been the subject of intense research recently[148]. These complexes exhibit a moderately strong injection-level

dependence, and often dominate cell performance. Not surprisingly then, the injection-level dependence of these centres near one-sun maximum-power operation has recently been shown to result in a reduced fill factor in such Cz cells[44], provided the emitter properties and surface passivation are sufficiently good to allow the bulk lifetime to have an impact.

Yet another example of these effects is provided by FZ wafers which were deliberately cross-contaminated with impurities from mc-Si samples, as in Chapters 2 and 3. These contaminated wafers exhibited reduced recombination lifetimes due to the presence of metallic impurities from the mc-Si wafers, and as a consequence of the strong injection-level dependence of the lifetime, resulted in implied V_{OC} curves with idealities of around 1.35 at one-sun. This point is further illustrated in the next section, where the impact on fill factors of one particular metallic impurity that is often present in silicon, namely interstitial Fe, is modelled.

From a more general point of view, the results of this section emphasise that the classic assumption of low-injection, in which the lifetime is assumed constant to simplify analysis, is not always applicable to real cells. In many real devices the effective lifetime may have residual injection-level dependence even at carrier concentrations two or three orders of magnitude below the dopant density. Therefore, even if a device technically operates in low-injection, which may be defined as the excess carrier density being much less than the dopant density, a constant lifetime cannot necessarily be assumed at open circuit, nor even at maximum-power. In fact, possibly the only condition in which it is safe to assume *a priori* that there is no injection-level dependence is when a cell is in short circuit.

4.3 Impact of interstitial iron on c-Si cells

It is interesting to consider what the physical source of the two SRH centres used to model the lifetimes in the mc-Si cells in the previous section might be. The ratios between the electron- and hole-capture time constants do not coincide well with those expected from the known capture cross-sections for interstitial Fe (Fe_i), a common metallic lifetime killer in mc-Si[149], and unfortunately the capture cross-sections are not well known for most other metals. Also, considering that the wafers used in these experiments were phosphorus gettered, and the gettering layer was removed before emitter formation, they are expected to have a relatively low interstitial metallic impurity content. Therefore, as discussed in detail in section 4.5, the bulk recombination in such wafers is attributed to metallicity decorated crystallographic defects. Such complexes are known to be common in mc-Si and largely impervious to gettering[88], but are not currently well characterised in terms of capture cross-sections.

However, standard commercial cell processes may conceivably result in a significant quantity of interstitial metals remaining in the bulk, despite the beneficial gettering effects of

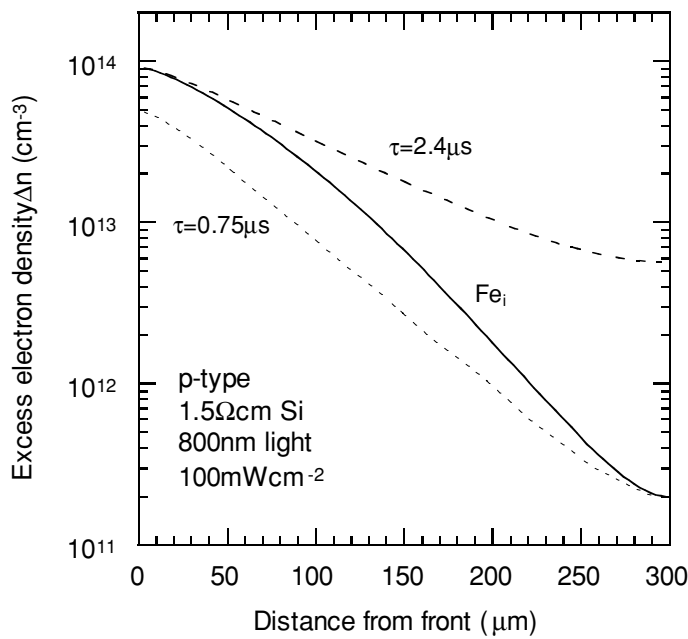


Figure 4.8. Carrier profiles at open circuit conditions under 800nm illumination for a sample with $[Fe_i] = 4.3 \times 10^{12} \text{ cm}^{-3}$, which gives rise to $\tau_{n0} = 0.42 \mu\text{s}$ and $\tau_{p0} = 300 \mu\text{s}$. Also shown are profiles for constant lifetimes of 0.75 and 2.4 μs .

emitter and Al back-surface-field formation[150]. This can occur through processes such as metallic ‘poisoning’ during relatively low temperature anneals, as discussed in Chapter 2. Therefore, it is of interest to consider the effects such recombination centres may have on device performance, apart from the obvious reduction in voltage and current due to decreased diffusion lengths. By using the capture cross-sections for Fe_i from the literature as listed in Chapter 5 (and also Table 4.3), it is possible to model the effect of different levels of Fe_i contamination not only on the V_{OC} and J_{SC} , but also on the fill factor. Although the results presented in this section are specifically for Fe_i , many other impurities and defects in silicon have similarly asymmetric cross-sections. The results then serve the more general purpose of exploring qualitatively the effect of such recombination centres on cell fill factors.

In the modelling, it is assumed that a negligible proportion of the Fe is present in the form of FeB pairs, a perfectly safe assumption for cells operating under constant illumination[53]. There are a number of other issues however that make the simplified analytic modelling approach used in the previous section inappropriate in this case. At higher Fe_i concentrations, the diffusion length of minority carriers in the base becomes significantly less than the cell thickness. This fact, coupled with the strong injection-level dependence of the lifetime due to the highly asymmetrical cross-sections, can cause large spatial non-uniformity in the carrier profiles. This is illustrated in Figure 4.8, which shows the shape of the minority carrier profile for a sample with $[Fe_i] = 4.3 \times 10^{12} \text{ cm}^{-3}$ under 800nm illumination calculated using PC-1D[10]. Also shown are two profiles for constant lifetimes of 0.75 and 2.4 μs . A single wavelength was

chosen for this illustrative plot because it results in almost exponential profiles for these constant lifetime cases, as shown in the figure. They are not quite perfectly exponential due to surface effects, but nevertheless act as useful comparisons to the profile for Fe_i .

The figure reveals that for the Fe_i case, the higher lifetime in regions of high carrier density causes the profile to broaden in those regions and generally become more step-like. The result in this case is a *less* uniform profile than would be generated by a constant lifetime equal to the low-injection Fe_i lifetime. However, under certain conditions, the profiles generated by Fe_i are actually *more* uniform than would be produced by a comparable low-injection constant lifetime. This occurs when the magnitude of the diffusion lengths are high enough (i.e. low enough iron concentrations) to cause the ‘step’ to push past the rear surface, or, in other words, for the wafer to be largely in mid-injection. However, in the case shown the diffusion lengths are too short for this to occur, and the result is a highly non-uniform profile. The important point for our current purposes is that these uneven profiles cause the calculation of the open circuit voltage to become complicated, since for this the carrier density at the junction edge is required.

These non-uniform profiles also impact on the calculation of the emitter recombination term, which becomes increasingly dependent on the rate of diffusion of carriers from the base. As a result, PC-1D was used to accurately model the impact of a changing Fe_i concentration on cell parameters. To ensure only the impact of the bulk lifetime was being observed, rear surface recombination velocities were set to zero. Junction recombination was verified to have very little impact, with the method described above revealing an upper bound on J_{rg} of about $2 \times 10^{-12} \text{ A cm}^{-2}$. This low value is due to the fact that the hole capture cross-section is much larger than that for electrons in the p-type side of the junction where the space-charge region mostly lies[145].

Figure 4.9 shows the impact of differing levels of interstitial Fe on V_{OC} and J_{SC} modelled for a $1.5 \Omega \text{ cm}$ cell of thickness 0.03 cm , and with an emitter characterised by a saturation current density of $J_{0e} = 3.0 \times 10^{-13} \text{ A cm}^{-2}$. 85% of the incoming light is assumed to be coupled into the cell. The results show that for Fe_i concentrations below 10^{10} cm^{-3} , the voltage of such a cell is dominated totally by the emitter, which caps the V_{OC} at 647 mV . Also the short circuit current is essentially independent of the Fe concentration at these low Fe levels because the bulk diffusion length is many times longer than the cell thickness. As the interstitial Fe concentration increases, the current begins to fall as the low-injection diffusion length decreases below the cell thickness. V_{OC} begins to drop also as the lifetime at open circuit decreases. Note that the V_{OC} curve shows a ‘kink’ which is caused by the injection-level dependence of the bulk lifetime producing an accelerated decrease in the open circuit lifetime as the recombination centre density increases. This kink is absent from the J_{SC} curve, because the low-injection lifetime never experiences any injection-level dependence, even at very high iron concentrations.

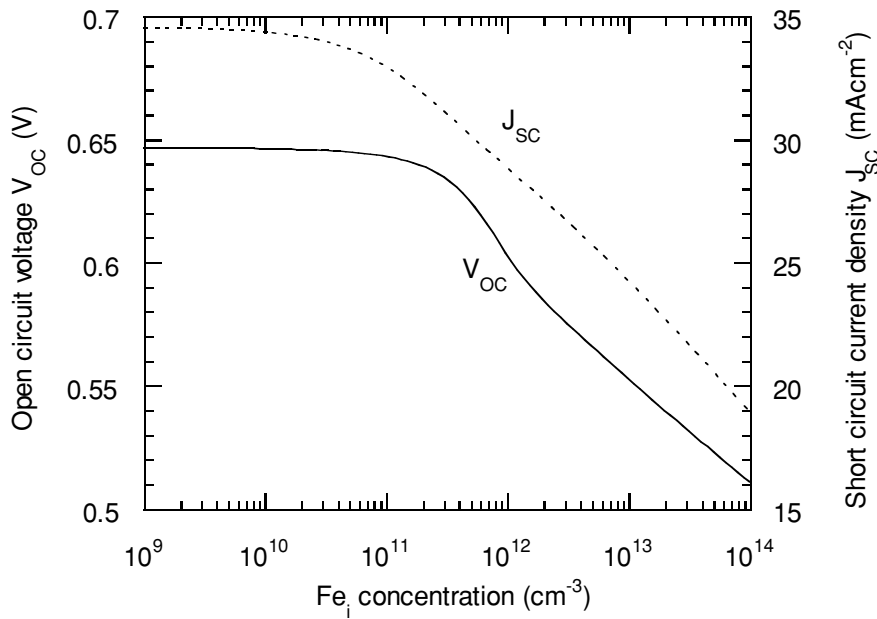


Figure 4.9. Effect of Fe_i concentration on V_{OC} and J_{SC} as modelled for a $1.5\Omega cm$ cell of thickness $0.03cm$ and with $J_{0e}=3\times 10^{-13} A/cm^2$.

Of more interest however is the behaviour of the fill factor, which is shown in Figure 4.10. For very low Fe_i levels, the injection-level dependence of the effective lifetime, being dominated by the emitter, is very slight, and results in an ideal fill factor of 0.835. As the Fe_i concentration increases though, the fill factor begins to degrade due to the increasing SRH dependence around maximum power point. As this dependence approaches open circuit conditions, V_{OC} begins to drop also, as mentioned. At around $5\times 10^{11} cm^{-3}$ Fe_i concentration, the strongest part of the SRH dependence is centred near one-sun maximum power conditions, limiting the fill factor to 0.785. As the Fe_i level increases further still, the lifetime becomes low enough to take the one-sun carrier density below the strongest SRH dependence, and the fill factor begins to recover. At these high Fe_i levels however, the voltage and current drop off very quickly due to the decreasing magnitude of the bulk lifetime.

As the Fe_i concentration increases above $1\times 10^{13} cm^{-3}$, a different effect begins to dominate. The decreasing magnitude of the open circuit voltage causes the ‘ideal’ fill factor to decrease also, a well-known property of $p-n$ junction diodes[20]. This effect occurs even for the case where the lifetime is injection-level independent. To illustrate this point, Figure 4.10 also shows the fill factor curve for a recombination centre that has such an injection-level independent lifetime. It also suffers from fill factor reduction due to lower voltages at high recombination centre densities. For the case of the Fe_i fill factor curve, the compounding influences of injection-level dependent lifetimes *and* low voltages result in a large fill factor reduction at high Fe_i concentrations.

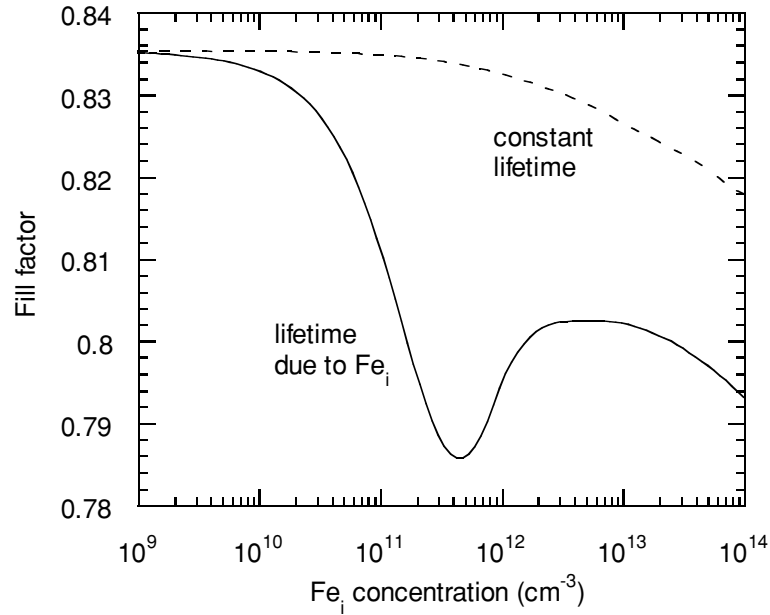


Figure 4.10. Effect of Fe_i concentration on fill factor as modelled for a $1.5\Omega\text{cm}$ cell of thickness 0.03cm and with $J_{0e}=3\times 10^{-13}\text{ A/cm}^2$. Also shown is the fill factor curve for a recombination centre that has an injection-level independent bulk lifetime (which is equal to the high-injection lifetime of Fe_i).

The physical reason for the dramatic injection-level dependence of the SRH lifetimes for Fe_i , and hence the poor fill factors, is the large asymmetry between the electron and hole capture cross-sections, which differ by about three orders of magnitude. Other common metal-related defects, notably CrB pairs, have largely unequal capture cross-sections also (see Table 4.3). These results then serve to illustrate the detrimental impact metallic impurities can have not only on V_{OC} , but also on the fill factor, and provide a plausible alternative to junction recombination as an explanation for non-ideal behaviour.

It is interesting to note that a recombination centre which gives rise to the opposite injection-level lifetime dependence, i.e. a lifetime that *decreases* as the injection-level increases, could result in fill factors *larger* than the ‘ideal’ constant lifetime case, although of course the overall cell efficiency would be less than if the centres were absent. Under certain conditions, shallow centres can cause such a dependence, as discussed in detail in Chapter 5. However, it seems that in practice such centres rarely dominate the lifetime of a sample. Auger recombination causes a quadratically decreasing lifetime with increasing carrier concentration under high-injection. Hence, cells operating in high-injection may also have better than ideal fill factors, provided that Auger recombination dominates recombination and resistive effects are not overwhelming.

In contrast to the high efficiency structures examined in this and the previous section, the following section considers commercially produced large-area mc-Si cells fabricated at BPSolar

in Villawood, Sydney. The cells are analysed using lifetime techniques to determine which regions of the cell place the most stringent limits on cell performance. Also, the effect of injection-level dependent lifetimes on the fill factor is considered, along with other important fill factor losses such as shunt and series resistances. The conclusions are markedly different from the high efficiency devices, reflecting the cruder cell fabrication techniques generally used in industrial production of mc-Si cells.

4.4 Recombination mechanisms in commercial multicrystalline silicon cells

In a complete commercial mc-Si cell, the effective lifetime comprises not only the bulk lifetime, but also components due to the emitter and the aluminium-doped back-surface-field (Al BSF) regions. Junction recombination is not considered here for reasons outlined in the previous sections. The electronic properties of the BSF are particularly relevant when the diffusion length is comparable to the wafer thickness (typically about 250 μm), which is usually the case for standard mc-Si samples after emitter diffusion, as discussed in detail in Chapter 2. By using a combination of QSSPC effective lifetime and QSS- V_{OC} measurements, the impact of the emitter and BSF regions has been evaluated in terms of dark saturation current densities. By determining the relative impact of these process steps on the effective lifetime, and therefore the final cell open circuit voltage and short circuit current, a clearer picture of which aspects of the process need to be improved emerges. The main sources of fill factor reduction in commercial cells are also considered.

4.4.1 Bulk lifetime limitation

As discussed in Chapter 2, the bulk lifetime of standard BPSolar mc-Si wafers is typically in the range of 40-60 μs after the gettering benefits of an emitter diffusion for wafers from regions other than the bottom of an ingot. These lifetimes were generally measured at carrier densities considerably higher than occur under one-sun illumination, a necessary precaution to avoid trapping effects. Typically, the recombination lifetime at one-sun would be lower due to SRH injection-level dependence. A reasonable general figure for the one-sun bulk lifetime might then be 45 μs for 1 Ωcm mc-Si wafers. Such a value places a limit on the achievable open-circuit voltage of 640mV for a wafer with a thickness of 250 μm and total global reflectance of 15%, which are typical values for these TiO_x -coated, screen-printed cells. Measured open circuit

voltages in completed devices rarely achieve more than 600mV, and so are clearly not limited to any large degree by the post-diffusion bulk lifetime, except in the case of wafers from the bottom of an ingot. Assuming that thermal steps subsequent to the emitter diffusion do not cause dramatic changes to the bulk lifetime, the lower final cell voltages must be due to recombination in the emitter or at the rear surface, or a combination of both.

4.4.2 Limitation due to emitter recombination

The relatively low sheet resistance and high surface dopant concentration of the industrial diffusion ($45\text{--}70\Omega/\square$), which is necessary to allow ohmic contact of the screen-printed metal fingers, is a source of significant additional recombination. In order to quantify this recombination, single-crystal $1\Omega\text{cm}$ float-zone (FZ) wafers were subjected to the industrial emitter formation step. The resulting lifetime was measured to be $26\mu\text{s}$. The rear surface had already been passivated at the ANU with a standard light POCl_3 diffusion and thin oxide as described in Chapter 1. When present on both surfaces, this passivation scheme yielded an effective lifetime of $300\mu\text{s}$, and indicates that the heavy commercial diffusion dominates the effective lifetime of $26\mu\text{s}$. This value implies a limit on the achievable open circuit voltage of 626mV.

These conclusions were confirmed by a separate experiment in which the emitter contribution to the dark saturation current density J_o , was determined from high-injection effective lifetime measurements of high resistivity (greater than $50\Omega\text{cm}$) FZ wafers[31,32]. A dark saturation current density of $J_{oe} = 8.2 \times 10^{-13} \text{Acm}^{-2}$ was measured at 25°C . This J_o value places a limit on the achievable open-circuit voltage of 625mV, for a $1\Omega\text{cm}$ wafer of thickness $250\mu\text{m}$ and reflectance of 15%, in good agreement with the experiment described above.

4.4.3 Limitation due to Al BSF

The relatively long diffusion lengths in these cells make them sensitive to the rear surface, where additional recombination can occur. While Al BSF formation provides a lower surface recombination velocity than plain metal on silicon, the passivation may still be poor enough to impact on performance. In the BPSolar process, the BSF is formed by alloying screen-printed aluminium paste. After etching the excess aluminium in HCl to make the use of the photoconductance tester possible, the measured lifetime on single-crystal $1\Omega\text{cm}$ FZ wafers with a high quality front surface passivation was $46\mu\text{s}$, which is equivalent to an implied

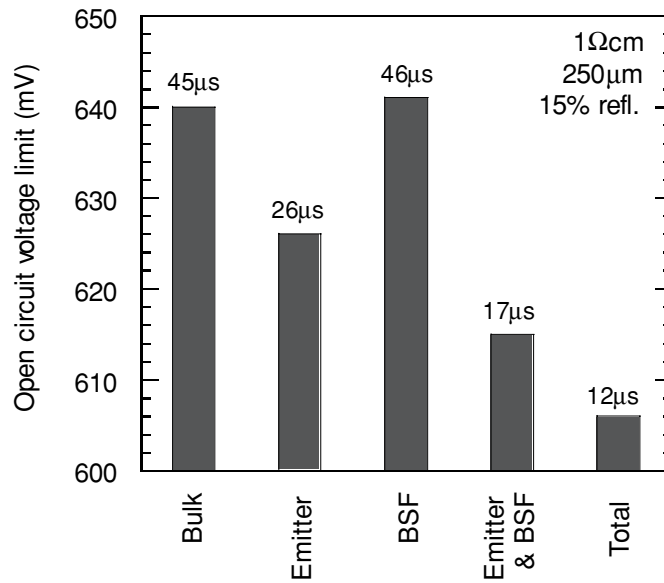


Figure 4.11. Voltage and lifetime caps imposed by typical bulk, emitter and rear surface recombination in commercial mc-Si cells.

voltage of 641mV. We also used an alternative method based on probing the voltage between the *n*-type diffusion and *p*-type Al-doped layer as a function of light intensity[37]. This measurement does not require full contacts to the cell, since no current is drawn from it. The measured $V_{oc}=640\text{mV}$ is in excellent agreement with the lifetime evaluation. The quality of the BSF layer can also be expressed in terms of a saturation current density of $J_{o(\text{BSF})}=5\times 10^{-13}\text{Acm}^{-2}$, or alternatively as a surface recombination velocity of around 500cm/s. These results suggest that the aluminium BSF is less restrictive than the phosphorus diffusion.

As a final verification of these results, a further experiment was performed. Rather than using a high-quality laboratory prepared passivation on one surface, 1Ωcm FZ wafers were subjected to both the standard front industrial phosphorus diffusion and rear BSF process steps on the front and back respectively. After etching the excess aluminium at the rear, a one-sun lifetime of 17μs was measured, which is equivalent to an implied voltage of 615mV. This was corroborated by probing the open-circuit voltage before etching the metal, which resulted in a measurement of 611mV. By adding the inverse lifetimes of the individual emitter and BSF limits as previously determined (the inverse bulk lifetime is negligible in these FZ wafers), we would expect the results to be 17μs and 615mV, in good agreement.

These results are summarised graphically in Figure 4.11. It depicts the voltage and lifetime caps imposed separately by the emitter, the BSF and a bulk lifetime of 45μs, as well as the combined emitter and BSF limit, and the combination of all three recombination mechanisms. The combination of all three results in a voltage cap of 606mV, a slight overestimation of those observed in completed mc-Si cells, which are typically around 590mV

but in some cases up to 602mV. The lower voltages in the finished cells are due partly to shunting, and also to the presence of silver strips (non-BSF regions) on the rear of the cells. It is also possible that the bulk lifetime degrades somewhat during Al BSF and front contact paste firing, further reducing the final voltage (although it may also improve).

4.4.4 Fill factor effects

Fill factors in the large-area screen-printed mc-Si cells are usually quite poor, generally in the range 0.73-0.75. The largest contributing factor to these low values is series resistance caused by the screen-printed fingers. Shunting at the cell edges also plays a role in reducing the fill factors, as it is usually present to some extent even after plasma etching of the edges. A third potential source of reduced fill factors is injection-level dependence of the bulk lifetime, as described previously for the mc-Si PERL cells and for Fe_i. By comparing illumination-V_{OC} curves with photovoltaic-mode I-V curves, it is possible to determine the relative importance of these mechanisms.

It should be mentioned that there is also the possible impact of lateral variations of the effective lifetime across different grains. To a large extent, these effects will be subsumed within the area-averaged lifetime measurements. However, they may cause a slightly lower fill factor than would thus be expected. This did not appear to be important in the mc-Si PERL cells studied above, but may be important in lower lifetime cells with larger variations. This could be a useful area for future work, particularly regarding lateral variation of the effective lifetime caused by the silver strips on the rear. These regions have very high surface recombination velocities, and although they only cover approximately 10% of the cell rear, they may have a significant impact on cell fill factors.

Unfortunately it is difficult to directly measure the recombination lifetime in typical mc-Si samples near maximum power due to the presence of trapping, making it impossible to generate an implied I-V curve, as was done in the previous sections. However, by using the recombination parameters determined for the 1.5Ωcm cell in section 4.2 (but without the shunt), it is possible to gain some indication of the impact of the bulk injection-level dependence on commercial cell fill factors. Using the J_{oe} and J_{o(BSF)} values determined above, the result is an implied V_{OC} of 606mV, and an implied fill factor of 0.815. The reduction in the fill factor is not as severe as for the high efficiency 1.5Ωcm cell, since the relatively high saturation currents of the heavily doped regions in the commercial cell ‘dampen’ the injection-level dependence of the total effective lifetime. Hence it seems that the injection-level dependence of the bulk recombination centres may be partly responsible for the low fill factor values in commercial

cells, but is certainly not the major cause. It should be remembered however that the injection-level dependence of the bulk lifetime might be more severe in standard cells.

The V_{OC} -mode fill factor of these commercial cells (measured by the QSS V_{OC} technique), which includes shunting effects but not series resistance, is generally around 0.77-0.79. The largest reduction occurs in photovoltaic-mode, which of course includes series resistance, and which generates fill factors in the range of 0.73-0.75. If we compare this with the implied value of 0.815 due to recombination only, it seems that series resistance accounts for roughly half of the fill factor loss, while shunting and injection-level dependent lifetimes appear to be responsible for approximately a quarter each. More work is required in this area to fully elucidate the cause of the low fill factors in commercial mc-Si cells.

4.4.5 Conclusions

In general, the results indicate that the emitter region warrants particular attention if attempts to boost cell voltages are to be made. Of course, the major obstacle in achieving this is the need to have a relatively low sheet resistance in order to allow acceptable ohmic contact of the front fingers. To reduce the impact of emitter recombination, a selective emitter process could be implemented, which would have the added benefit of allowing heavier diffusions under the fingers to reduce the impact of series resistance on the fill factor[9]. There are currently many groups investigating low-cost ways of achieving selective emitters, ranging from the use of partial diffusion barriers[151] to auto-doping and double-source methods[152]. Passivation of the lightly-doped section of the selective emitter would then become critical. Low temperature SiN is being increasingly recognised as an excellent approach to achieving this[28].

Passivation of the current heavy emitter by oxide growth or SiN deposition may also result in improvements, but the likely presence of a ‘dead’ layer may cause such gains to be modest or even non-existent. Improved rear surface properties could be achieved through a locally-contacted rear structure with a passivating film, again such as SiN, elsewhere.

4.5 Analysis of possible bulk recombination centres in multicrystalline silicon

In Chapter 2, results of Secondary Ion Mass Spectroscopy (SIMS) analysis of ribbon-grown EFG mc-Si were presented. Heavily doped gettering layers were shown to contain

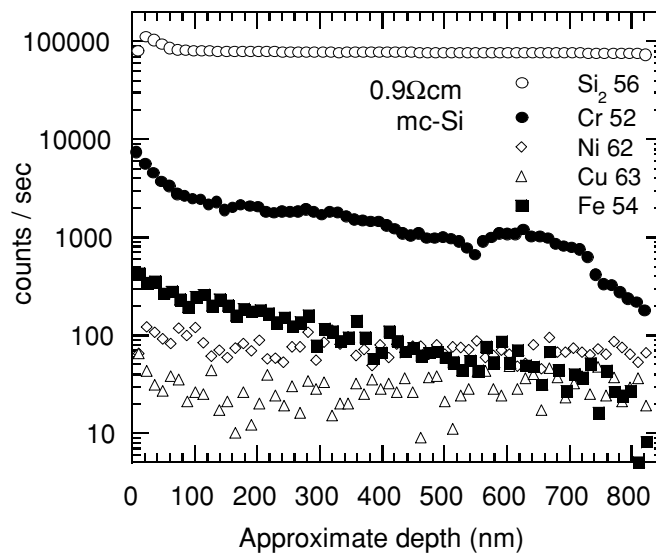


Figure 4.12. SIMS profile of a Eurosolare mc-Si sample with a heavily doped gettering layer intact. The junction depth is estimated to be approximately $1.2\mu\text{m}$.

significant amounts of Cu, suggesting it may have been responsible for the low bulk lifetimes before gettering. In this section, similar experiments on cast mc-Si from Eurosolare are discussed. In this case, the gettering layers were found to contain considerable quantities of Cr and Fe. Since the energy levels and capture cross-section of interstitial Fe and Cr, and also of FeB and CrB pairs, are reasonably well known, it is possible to investigate whether or not the injection-level dependence of the lifetimes caused by the gettered impurities corresponds to any of these centres. This was not possible for Cu in the EFG material since the cross-sections for Cu-related centres are almost completely unknown.

The results suggest that the vast majority of the available Fe and Cr in the cast mc-Si samples must reside in precipitates, since if they were present as interstitial impurities the recombination lifetimes before gettering would necessarily be much lower than observed.

4.5.1 SIMS profiles of multicrystalline silicon

Figure 4.12 shows the SIMS profile of a $0.9\Omega\text{cm}$ cast mc-Si wafer with a phosphorus gettering layer present at the surface. This was a heavily contaminated wafer, with a bulk lifetime of around $1\mu\text{s}$ before gettering and approximately $2\mu\text{s}$ after gettering. The junction depth of the diffusion is estimated to be approximately $1.2\mu\text{m}$. Since the secondary ion yield varies strongly between different isotopes, the absolute magnitude of the signal is not always an accurate indication of the presence of trace impurities. Rather, a signal that decreases over roughly the same distance as the gettering layer is a more reliable indicator. The plot shows that

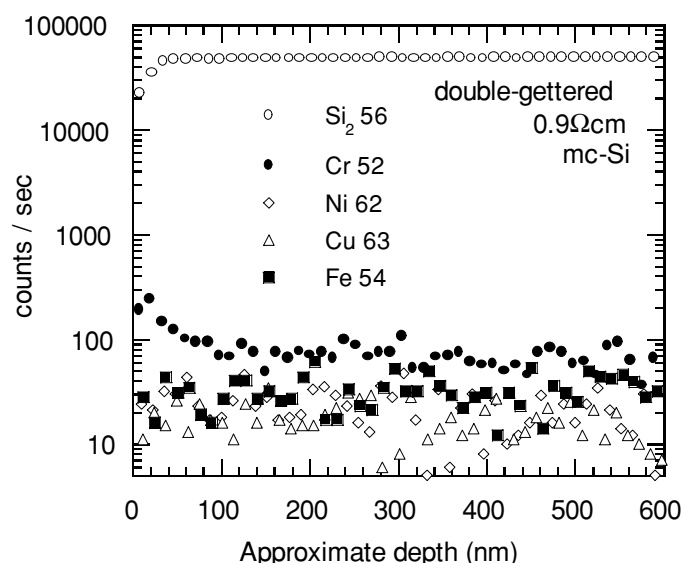


Figure 4.13. SIMS profile of a Eurosolare mc-Si sample that was gettered twice, the second heavily doped gettering layer remaining for SIMS analysis. The junction depth is estimated to be approximately $1.2\mu\text{m}$.

there is a definite trace of both Cr and Fe in this sample. Ni and Cu however do not appear to be present in sufficient concentrations to be detected using this technique.

To ensure that the observed traces genuinely reflected gettering from the bulk as opposed to surface contamination or other artifacts, a second sample was analysed, but in this case the gettering layer was etched off and the sample given a second heavy gettering diffusion prior to SIMS profiling. Note that similar ‘double-gettering’ experiments performed on the same material in Chapter 2 resulted in no further lifetime increase, implying that gettering was complete after the initial diffusion. Hence, this double-gettering should result in many fewer impurities in the second diffused layer. Figure 4.13 shows the results, which suggest that the concentration of all four metallic species dropped or remained below the detection limit, as expected.

Figure 4.14 shows a comparison between the single- and double-gettered profiles for both Fe and Cr. These plots reveal the presence of Fe and Cr in the single-gettered wafers more directly. The profiles of the double-gettered sample can be considered as upper bounds on the noise levels for the two impurities. Considering that there may be some impurities still present in the diffused region of the double-gettered sample, it is possible that the actual noise levels are lower than this. In the single-gettered wafer, ^{54}Fe occurs at concentrations slightly above this apparent limit, while for ^{52}Cr the signal is considerably higher.

As discussed in Chapter 2, the sensitivity limit of SIMS is not as low as electronic techniques such as DLTS or lifetime-based methods. The best SIMS systems available have sensitivities of no better than $5 \times 10^{14} \text{cm}^{-3}$ for the isotopes ^{54}Fe and ^{52}Cr [153]. The particular SIMS apparatus at ANU has a bulk sensitivity limit considerably worse than this (at least an

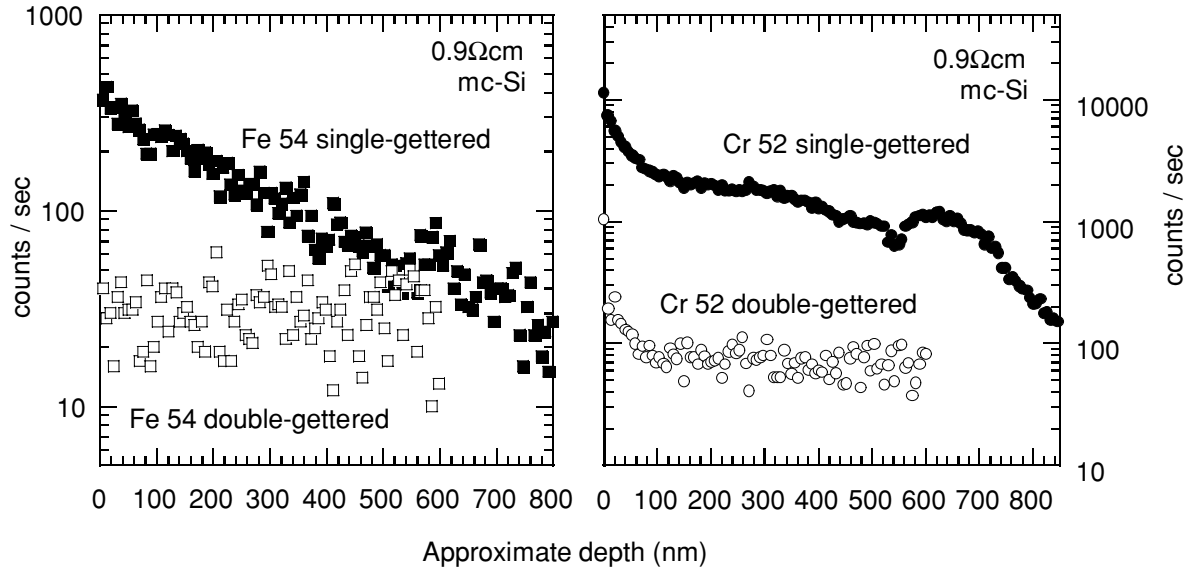


Figure 4.14. SIMS profiles for Fe and Cr isotopes in single- and double-gettered wafers. Data taken from Figures 4.12 and 4.13.

order of magnitude[154]), but for our current purposes we shall assume these optimistic values to obtain lower bounds. Since the ^{54}Fe trace in Figure 4.14 indicates concentrations not far above the noise level, we may assume a minimum concentration of $5 \times 10^{14} \text{ cm}^{-3}$ for ^{54}Fe over the approximate junction depth of $1 \mu\text{m}$. As stated above, the observed trace may be considerably further above the *real* noise limit, meaning the actual concentration would be greater. This implies a lower bound on the distributed ^{54}Fe concentration throughout the bulk of the $300 \mu\text{m}$ wafer of $2 \times 10^{12} \text{ cm}^{-3}$. Considering that the natural abundance of ^{54}Fe is approximately 6%, this in turn suggests a minimum total Fe concentration of around $3 \times 10^{13} \text{ cm}^{-3}$.

The profile for ^{52}Cr is approximately an order of magnitude higher than that for ^{54}Fe . However, considering that the relative abundance of this isotope is 52%, also an order of magnitude higher, the resulting minimum Cr concentration when distributed throughout the bulk is again around $3 \times 10^{13} \text{ cm}^{-3}$. It should be stressed once more that this is a very optimistic lower bound. If we assume this value for the Cr concentration, interstitial Cr and CrB pairs present at these levels would cause the bulk lifetime to be 0.02 and $0.04 \mu\text{s}$, respectively, at an excess carrier concentration of 10^{15} cm^{-3} using the cross-section data from Table 4.3. These values are much lower than those actually measured in such non-gettered mc-Si wafers, which yield lifetimes of around $1 \mu\text{s}$. Hence, it seems that the vast majority of the Cr present must occur in some other form. Further evidence in support of this conclusion is presented in the next section.

In a similar manner, assuming a total Fe concentration of $3 \times 10^{13} \text{ cm}^{-3}$ results in bulk lifetimes of 3 and $0.6 \mu\text{s}$ for interstitial Fe and FeB pairs respectively. These results suggest that either of these centres *may* provide a plausible explanation for the observed lifetimes. In the

next section, this possibility is tested further by comparing the measured injection-level dependence of the recombination lifetimes in non-gettered material with that expected for interstitial Fe and Cr, and also for FeB and CrB pairs. The thermal annealing and light-soaking responses of non-gettered mc-Si wafers are also discussed.

Recombination centre	Energy level (eV)	σ_n (cm ²)	σ_p (cm ²)	Source
Fe _i	E _V +0.38	5×10 ⁻¹⁴	7×10 ⁻¹⁷	Istratov <i>et al.</i> [155].
FeB acceptor	E _C -0.23	3×10 ⁻¹⁴	2×10 ⁻¹⁵	Istratov and Chapter 5, this thesis.
Cr _i	E _C -0.22	2.3×10 ⁻¹³ *	1.1×10 ⁻¹³ *	Mishra[134].
CrB	E _V +0.27	1.4×10 ⁻¹³ *	1×10 ⁻¹⁴	Mishra and Conzelmann <i>et al.</i> [156].

Table 4.3. Energy levels and capture cross-sections for Fe and Cr related recombination centres. The values marked with an asterisk(*) are calculated from Mishra's capture coefficients $C_{n,p} = \sigma_{n,p} v_{th}$, assuming a value of $v_{th} = 1.1 \times 10^7 \text{ cm s}^{-1}$.

4.5.2 Modelling multicrystalline silicon lifetime data with chromium- and iron-related centres

In material that has not been gettered, the bulk lifetime $\tau_{\text{non-gett}}$ can be written in terms of two components:

$$\frac{1}{\tau_{\text{non-gett}}} = \frac{1}{\tau_{\text{impurity}}} + \frac{1}{\tau_{\text{gett}}} \quad (4.4)$$

where τ_{impurity} is the lifetime due to the getterable impurities, and τ_{gett} is the lifetime after gettering, or alternatively, the lifetime caused by those centres which can not be gettered. Of course it is necessary to provide adequate surface passivation to avoid surface effects, and this was achieved by applying light phosphorus diffusions with thin oxides, as described in Chapter 1.

By measuring the injection-level dependent lifetimes before and after gettering, it is possible then to determine the injection-level dependence of the gettered impurities alone via:

$$\frac{1}{\tau_{\text{impurity}}} = \frac{1}{\tau_{\text{non-gett}}} - \frac{1}{\tau_{\text{gett}}} \quad (4.5)$$

This subtraction technique was also used in a recent study of boron-oxygen complexes in Czochralski silicon[129].

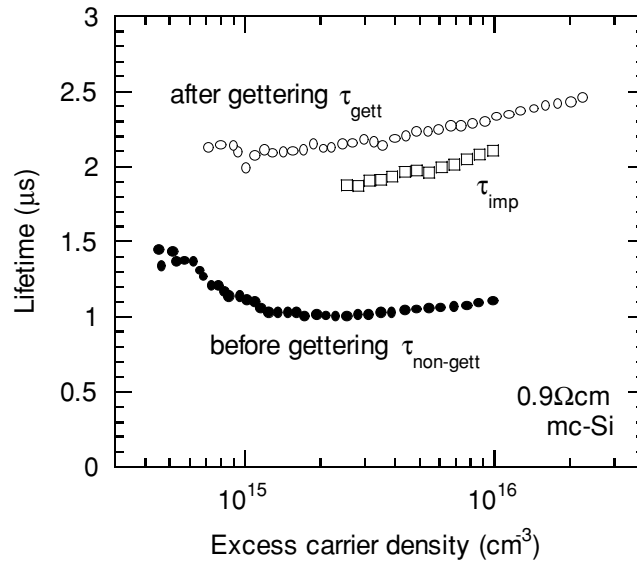


Figure 4.15. QSSPC lifetime versus excess carrier density for a mc-Si wafer before and after gettering. Also shown is the lifetime curve of the removed impurities, as calculated by subtracting the inverse of the two QSSPC curves.

Figure 4.15 shows the result of such a procedure for a ‘sister’ wafer of those used for the SIMS analysis above. The range over which the subtracted data is available is small due to the presence of trapping in the non-gettered wafer, but nevertheless displays some injection-level dependence that can be modelled. Note that the trapping effect is absent in the gettered lifetime data, indicating that the trap density has been reduced, as was found to occur in Chapter 3.

Figure 4.16 illustrates the result of attempting to fit SRH curves for interstitial Fe, Cr, and also FeB and CrB pairs to the subtracted data. Clearly the only centre capable of adequately explaining the injection-level dependence is interstitial Cr. However, to match the magnitude of the measured lifetime a low interstitial Cr concentration of $4 \times 10^{11} \text{ cm}^{-3}$ is required. This value is two orders of magnitude below the generous lower bound implied by the SIMS profile, once again implying that the Cr must mostly occur in other forms. Note that for interstitial Fe and FeB pairs, the required concentrations are comparable to the lower bounds from the SIMS results, as discussed in the previous section, but they have incorrect injection-level dependences. These results imply that, of the centres considered, only interstitial Cr could explain the results, and even then the vast majority of the Cr is required to be present in some much more electronically benign form, such as in precipitates.

However, if interstitial Cr does exist, even in the low concentrations speculated, then it should be detectable using a low temperature (200°C) anneal[134]. For the resistivity in question, interstitial Cr forms CrB pairs over a period of many days at room temperature. Therefore, after waiting a sufficiently long time after the final high temperature step, measurements taken before and after annealing should result in significantly different lifetime

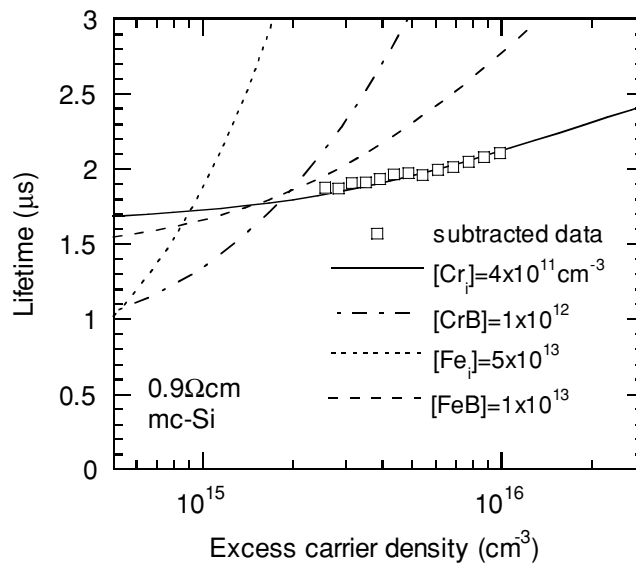


Figure 4.16. Subtracted data from Figure 4.14 modelled with SRH curves for interstitial Fe and Cr, and FeB and CrB pairs using the energy levels and cross-sections from Chapter 1.

curves. However, these mc-Si samples revealed no such change, in parallel with the annealing results presented in Chapter 3, where the trap density was found to change markedly but the recombination lifetime was completely stable. It is possible that CrB pairs do not form as readily in mc-Si as they do in single-crystal wafers, which would explain the lack of annealing response, but it is difficult to imagine why this might be true. It seems more likely that the accurate fit of interstitial Cr to the subtracted data is merely a coincidence, and that the recombination is actually caused by some other type of centre.

Although the injection-level analysis counts against both interstitial Fe and FeB pairs as the dominant centre, further proof comes from the lack of response to light-soaking of the non-gettered mc-Si wafers, again as shown in Chapter 3. Such a light-soaking treatment should result in a different lifetime curve due to breaking up of FeB pairs, which form within several hours at room temperature for moderate resistivity[53]. Hence it seems that neither interstitial Cr nor Fe, nor their dopant pairs, can be held accountable for the low lifetimes in the non-gettered mc-Si material. However, it may occur to the reader that a combination of these centres might provide an explanation. Inspection of the injection-level dependences in Figure 4.16 reveals that this is not possible, since no linear combination of the inverse lifetimes will produce a total lifetime curve of the required shape.

An obvious question remains as to the state of the Cr and Fe revealed in the SIMS profiles, considering we have ruled out interstitial sites and dopant pairs. It is likely that the high concentrations of these metals reside almost exclusively as precipitates in the wafer bulk. Since each precipitate may contain many such metal atoms, the total density of centres is greatly reduced, meaning that even if the recombination activity of each precipitate (or alternatively

their effective ‘cross-sections’) is large, the resulting impact on the bulk lifetime will be lower than if the metals occurred on interstitial sites. Such precipitates have been observed in cast mc-Si by several authors[88,157].

One particular study by McHugo *et al.*[88] used high resolution x-ray fluorescence (XRF) mapping to reveal extended crystallographic defects that were heavily decorated by Cr, Fe and Ni in cast mc-Si. The decorated regions correlated well with areas of reduced diffusion length, as identified by light-beam induced current (LBIC) mapping. The Fe and Cr distributions in particular were found to be locally very high, with equivalent surface concentrations up to 10^{17}cm^{-2} . Such concentrations are many orders of magnitude higher than the solubility limits of these metals in silicon at any reasonable processing temperature, allowing the authors to conclude that they must be present as some form of precipitate. Even more recent work has shown that in the case of Fe, the precipitates may occur in the form of either oxides or silicates[133]. It seems likely that the Cr and Fe observed with SIMS profiling in this chapter come from such precipitates.

The results presented above were for Eurosolare cast mc-Si. Very recent work using Neutron Activation Analysis (NAA)[45] has revealed that Fe and Cr also exist in considerable quantities in BPSolar cast mc-Si, both before and after gettering. Prior to gettering, typical concentrations of Fe and Cr were $1\times 10^{13}\text{cm}^{-2}$ and $6\times 10^{13}\text{cm}^{-2}$ respectively (these values are equivalent implant doses). For 300 μm thick wafers these equivalent doses correspond to bulk concentrations of $3\times 10^{14}\text{cm}^{-3}$ and $2\times 10^{15}\text{cm}^{-3}$ respectively. These are in very broad agreement with the SIMS results on Eurosolare material. The preliminary NAA spectra also revealed significant quantities of zinc and barium, as well as some silver and cobalt.

As a technique, NAA is more sensitive than SIMS, and so does not require a gettering layer to concentrate the impurities. This highlights a drawback of SIMS measurements, in that it can only detect gettered impurities, providing no information on how many are left in the bulk. By contrast, NAA detects the total impurity concentration, irrespective of its depth or chemical state in the silicon matrix. Consequently, it represents an excellent opportunity to examine changes in total metallic impurity content before and after gettering. NAA also has a significant advantage over DLTS in that unambiguous identification of impurities is often difficult in the latter. Further work in the area of NAA of mc-Si is planned.

4.6 Multicrystalline silicon PERC cells

The final section of this chapter discusses attempts to make high efficiency cells on low resistivity cast mc-Si produced by Eurosolare. The impetus for this work was the discovery of

relatively long lifetimes in $0.17\Omega\text{cm}$ material after an optimised gettering process, as discussed in detail in Chapter 2. The best wafers displayed bulk lifetimes of up to $22\mu\text{s}$ at an excess carrier concentration of $1 \times 10^{16}\text{cm}^{-3}$, however, high trap densities made lifetime measurements at one-sun illumination difficult. In order to use the lifetimes to calculate one-sun implied voltages, the lifetimes at high carrier densities were simply extrapolated to lower regions, noting that they appeared to be fairly injection-level independent. This procedure introduces some extra uncertainty, although the logarithmic nature of the relationship between the implied voltage and the carrier density at one-sun (in turn a linear function of the lifetime), keeps the uncertainty small (generally less than 5mV).

A lifetime of $22\mu\text{s}$ at one-sun in a $185\mu\text{m}$ thick cell with no antireflection coating ($f_{\text{abs}}=0.68$) gives an implied open circuit voltage of 679mV for $0.17\Omega\text{cm}$ material. Since this material is subject to strong thermal degradation effects, the key to maintaining a high lifetime, and hence obtaining a high voltage, is to minimise the thermal budget of the cell process. Fortunately, low resistivity ($<0.5\Omega\text{cm}$) wafers can be used to make Passivated Emitter and Rear Cells (PERC) [158,159], a cell design that held the single-crystal silicon efficiency record for several years before the advent of PERL cells. A potential advantage of the PERC process when applied to mc-Si is that it can achieve high efficiencies without the need for any rear boron or aluminium diffusions. Instead, ohmic contact is achieved by evaporating aluminium directly onto the base, through holes in a passivating oxide, at the rear. Therefore, the only high temperature steps required, after gettering, are an oxidation for rear passivation and an emitter diffusion.

4.6.1 Fabrication process

Prior to cell processing, the mc-Si wafers were gettered for 60 minutes at 900°C , in accordance with the optimum conditions found in Chapter 2. The heavy diffusion was then etched, and the wafers passivated with a standard light diffusion and *in situ* oxide plus forming gas anneal for lifetime measurement. This light diffusion was then removed also, and the cell process begun. Several $0.27\Omega\text{cm}$ single-crystal FZ wafers processed alongside the mc-Si samples. They served the purpose of defining the limitations on cell performance imposed by factors other than the bulk. The particular process used was as follows:

1. **Steam oxidation:** 850°C , 160 minutes. Oxide thickness $\sim 110\text{nm}$.
2. **Etch diffusion window** through oxide, $2 \times 2\text{cm}$.

3. **Emitter diffusion and oxidation:** 860°C, 25 minutes POCl₃ source, then *in situ* dry oxidation at 900°C for 20 minutes, followed by a 10 minute anneal in N₂. R_{sheet}=150Ω/□.
4. **Forming gas anneal (FGA):** 400°C, 40 minutes. τ measurement.
5. **Alneal:** evaporate 100nm Al on both sides, then FGA 400°C, 40 minutes, remove Al in hot orthophosphoric acid. τ measurement.
6. **Corona charge:** 3 minutes of charge deposition on each side. τ measurement.
7. **Open fingers on front and dots on rear:** dot diameter=0.3mm on 3mm triangular spacing.
8. **Evaporate metal:** Cr/Pd/Ag on front, Al on rear.
9. **‘Liftoff’ excess metal** in an ultrasonic bath, leaving metal in fingers and dots only.
10. **Evaporate Al** over rear oxide and dots.
11. **Electroplate fingers with Ag** up to a thickness of 28μm.
12. **FGA:** 400°C, 40 minutes. This step sinters the contacts, hydrogenates the front oxide, and alneals the rear oxide.
13. **Measure I-V curves.**

Note that the steam oxidation serves the dual purposes of rear passivation and front diffusion mask, hence the requirement for it to be quite thick. Although the cells fabricated here are planar, it would also be possible to use this same oxide as a texturing mask inside the cell area, prior to removing it from the window entirely for the diffusion. In such a way, so-called ‘tubs’[100] or ‘honeycomb’[101] texturing formed by anisotropic etching could be applied to reduce reflection loss in the cells.

Steps 4, 5 and 6 in the process above are included solely for lifetime monitoring. Each step provides successively more effective surface passivation, helping to reveal whether the wafers are surface or bulk limited, as discussed below. The effect of the corona charges lasts only for a few minutes, and does not impact on the final cell performance. The chosen geometry of the rear dots was found to provide the best results on FZ cells with various spacings and dot sizes. An AR coating was not deposited on these cells.

4.6.2 Results and discussion

Lifetime measurements and implied voltages for the best mc-Si and FZ cell precursors are given in Table 4.4. Note that the measurements at step 5 should correspond most closely

Process step	0.17 Ω cm mc-Si (185 μ m)		0.27 Ω cm FZ Si (280 μ m)	
	τ_{eff} (1-sun, μ s)	Imp. V_{OC} (1-sun, mV)	τ_{eff} (1-sun, μ s)	Imp. V_{OC} (1-sun, mV)
Before steam oxidation.	22	679	45	672
Step 4: oxid, diff & FGA.	4.3	637	27	659
Step 5: oxid, diff & alneal.	10	659	51	675
Step 6: oxid, diff & corona charged	11	661	87	689

Table 4.4. Measured effective lifetimes and corresponding implied open circuit voltages of mc-Si and FZ PERC cell precursors. The first row, labelled 'before steam oxidation', corresponds to light phosphorus, in situ thin oxide and FGA passivated samples, with the mc-Si sample being gettered previously.

with the final cells, since this step reflects most accurately the conditions of the surfaces in the completed devices.

For the FZ wafer, the effective lifetime before the initial steam oxide decreases from 45 to 27 μ s after step 4, due to the poorer surface passivation offered by the forming gas annealed steam oxide (at the rear surface) in comparison to the forming gas annealed light diffusion with thin dry oxide. The effective lifetime then recovers again to 51 μ s after an alneal at step 5. However, while the mc-Si sample also drops in lifetime after step 4, the drop is larger, and the subsequent recovery is considerably less. This reflects the fact that this sample has suffered from degradation of the bulk lifetime during the long steam oxidation step.

From step 5 to 6, with the application of corona charges, the FZ sample improved again, implying that at step 5 it was still limited by the surfaces to some extent. There are two important consequences of this increase. Firstly, it reveals that the corona charges significantly improve the surface passivation of the alnealed oxide. Secondly, since the measurements at step 5 should correspond most closely with the final cell performance, the FZ cell will ultimately be at least partly limited by surface recombination. In contrast, the mc-Si sample does not improve noticeably from step 5 to 6, despite the improvement in surface passivation. This implies that the mc-Si wafer is bulk limited at step 5, and hence will be bulk limited as a finished cell. These conclusions closely mirror those reached in section 4.2, where the mc-Si PERL cells were shown to be bulk dominated, as opposed to FZ PERL cells which are generally limited by a combination of bulk and surface effects.

The I-V curves of the finished devices, as measured in-house against independently calibrated devices, are shown in Figure 4.17. The V_{OC} of the FZ cell (670mV) is in reasonable agreement with that expected from the implied value from step 5 in Table 4.4 (675mV). The slight drop is most likely due to increased recombination under the contacts resulting from etching the oxide at those points. The difference between the implied voltage and that measured for the mc-Si cell (659 compared to 649mV) is somewhat larger. Some of the difference would be explained again by increased recombination under the contacts. The remainder may be due to uncertainty in extrapolating the effective lifetime from higher carrier densities down to the one-

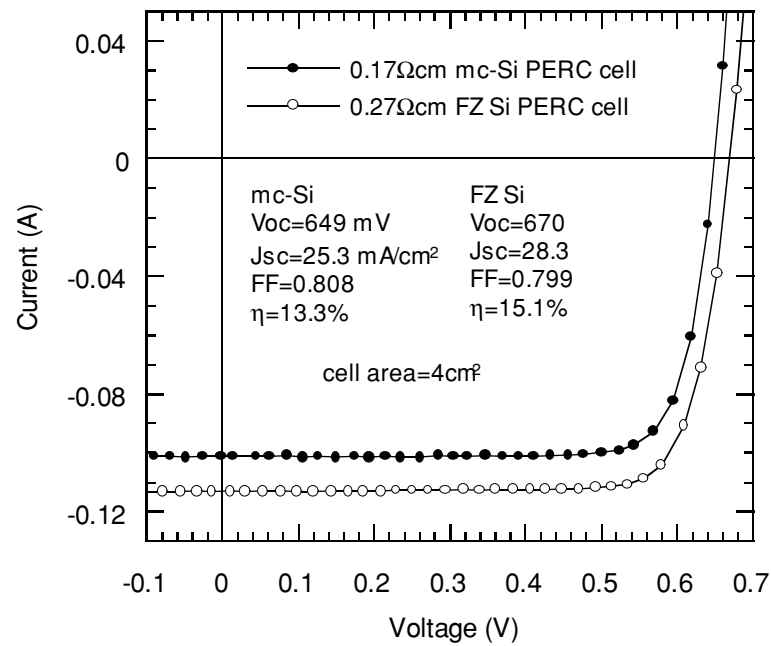


Figure 4.17. I-V curves for the best mc-Si and FZ PERC cells from Table 4.3. These cells had no anti-reflection coatings.

sun level, as is required to avoid trapping effects. Using the measured V_{OC} to ‘reverse calculate’ the global effective lifetime in the mc-Si substrate suggests a value of $7\mu\text{s}$ at one-sun open circuit conditions, as opposed to the extrapolated value of $10\mu\text{s}$ listed in Table 4.4. It is quite possible that this reduction continues towards maximum power conditions, meaning that the fill factor could be somewhat reduced in a similar way to the PERL cells in section 4.2.

The lower V_{OC} and J_{SC} of the mc-Si cell in comparison to the FZ cell essentially reflect the lower bulk lifetime. Unfortunately, this cell did not realise the potential voltage of the starting substrate due to thermal degradation during the steam oxidation. Obviously then, better results may be achieved by reducing or eliminating the oxidation step. Firstly, it could be reduced in duration by using a ‘mesa’ etch to isolate the junction, which would eliminate the need for a masking oxide at the front. A passivating oxide would still be required at the rear, but it could be substantially thinner than the 110nm oxide required here to mask the phosphorus at the front. A more attractive option is to use a low temperature passivation scheme, such as SiN, for the rear. This would entirely eliminate the need for an oxidation step.

Indeed, cells have recently been made by Mark Kerr[103] on the same low resistivity mc-Si material with SiN passivation on both the emitter and the rear. However, the process still involved a thick steam oxide as a diffusion mask. It is not surprising then, given that the cells presented here were found to be essentially bulk limited as a result of the steam oxidation, that the SiN cells yielded similar voltages of up to 655mV, compared with 649mV recorded here. The presence of an antireflection coating on the SiN cells accounts for the slight difference.

These conclusions are further corroborated by previous results on fully aluminium rear contacted $0.2\Omega\text{cm}$ gettered mc-Si cells made by Stocks[102], which had a best voltage of 659mV with ‘tubs’ texturing and a double-layer anti-reflection coating. The process used involved a number of long oxidations, meaning the bulk lifetime was again not at its greatest. The devices were long base cells (thickness of $380\mu\text{m}$), and hence were also bulk-dominated.

4.7 Summary

High efficiency PERL and PERC cells fabricated on cast mc-Si were found to be limited by bulk recombination at both open circuit and maximum power conditions, as opposed to FZ cells which are also affected by surface recombination, especially at maximum power. Furthermore, the injection-level dependence of the bulk centres in mc-Si has been shown to cause reduced fill factors in the PERL cells, and probably has similar effects on the PERC devices. Modelling of interstitial Fe bulk recombination centres revealed that their strong injection-level dependence can lead to even greater reductions in fill factor if they dominate cell behaviour.

By contrast, commercially produced screen-printed mc-Si cells were shown to be primarily limited by recombination in the heavily doped emitter region, which imposed a voltage cap of about 625mV. The bulk and Al BSF provide roughly equivalent limitations on the device performance, at around 640mV each. Taken together, these three recombination mechanisms create a global voltage cap of 605mV, slightly higher than observed in finished cells. The difference is due partly to shunting at the edges and also incomplete rear coverage of the Al BSF. However, degradation of the bulk lifetime during Al BSF firing may also be partly responsible.

Finally, SIMS of gettered impurities in Eurosolare cast mc-Si revealed the presence of significant quantities of Cr and Fe. Injection-level dependent lifetime analysis of these recombination centres subsequently showed that interstitial Cr fitted the measured lifetime curves, although only at massively reduced concentrations. However, its presence was subsequently placed in doubt by thermal annealing experiments, resulting in the final conclusion that these metals must reside almost entirely in precipitated form. This study also served the purpose of illustrating the powerful techniques that can be used when the energy levels and capture cross-sections of suspected impurities are well known. Unfortunately, this is not the case for the majority of metallic species, and other impurities, in silicon. These considerations lay the foundation for the next chapter, which presents a new technique for accurately determining such capture cross-sections.

CHAPTER 5

Injection-level Dependent Lifetime Spectroscopy (IDLs) of FeB Pairs in Silicon

5.1 Introduction

Metallic impurities in silicon are of great technological importance, and as such have been the subject of a large body of work since the very beginning of the microelectronics era, and in particular over the last twenty years[155,160]. The presence of these unintentional impurities has implications in many fields that involve the use of silicon, from integrated circuits, where they cause yield and performance problems[161], to photovoltaics, where they result in reduced conversion efficiencies[88,162]. There has been a significant amount of work devoted to characterising metallic impurities in silicon in order to better understand, and hopefully reduce, their impact on devices. Many different experimental techniques have been developed and applied to their study with these aims in mind.

Iron, a common impurity in silicon and one of the most widely studied, provides a good example of the general importance of metals in silicon[163]. In the microelectronics industry,

iron is the most common lifetime-killing contaminant, and has a tendency to form precipitates in active areas of a device[155,161]. As such it is responsible for increased leakage currents and reduced resistance to breakdown. The precipitates can also reduce yields, and as a result are currently under active research. Copper is also of concern due to its growing use in interconnections in integrated circuits. In addition, its presence in the wire saws used for wafering Czochralski and cast mc-Si ingots increases the chance of copper entering devices with negative effects[164]. Many other unintentional metal contaminants, such as chromium, nickel and gold, are often present in significant amounts in devices[160]. Non-metallic impurities, such as boron-oxygen complexes or oxygen precipitates in Czochralski silicon, are also often important lifetime-killing recombination centres[129]. Crystallographic defects such as dislocations, vacancies, silicon interstitials and grain boundaries are yet another source of states in the band gap. The latter are particularly important in mc-Si, and their interactions with impurities further complicates their study.

Consequently, the accurate electronic characterisation of these defects is of critical importance. According to Shockley-Read-Hall (SRH) recombination theory[17-19], there are four basic parameters that determine the extent to which a particular impurity affects the lifetime of a sample: the density of recombination centres N_{SRH} , the energy level E_{T} , and the electron and hole capture cross-sections σ_{n} and σ_{p} . The SRH lifetime is simply a linear function of the recombination centre density N_{SRH} . This parameter does not affect the injection-level dependence of the lifetime, and can be determined if the three other parameters are known and the SRH lifetime measured. It is the values of these three other parameters that determine the injection-level dependence, and the way this dependence changes with different dopant densities. These are the critical factors when attempting to discover unique properties of given defects that can allow them to be easily identified.

There are a number of techniques available that are used to measure the energy level and cross-sections of impurities in semiconductors. The most widely used is Deep Level Transient Spectroscopy (DLTS) and its many variants[45], and there exists a wealth of data in the literature on the energy levels of impurities and defects in silicon as measured by DLTS. However, broadly speaking, it is not such an accurate method for determining capture cross-sections. The fundamental reason for this is the need to extrapolate emission rate data to an axis, with any uncertainty in the intercept value causing an exponentially increasing uncertainty in the cross-section values[155]. Further problems arise from the fact that DLTS measurements necessarily scan a large temperature range, usually from 77K up to room temperature, often more. If the capture cross-sections have any significant temperature dependence in this range, the results can be distorted. There is also the potential for thermally-activated defect reactions that change the relative concentrations of impurities during the measurement, again causing ambiguous results.

Techniques for determining cross-sections based on room-temperature low-injection lifetime measurements also exist. These have the potential to be more accurate, but require the impurity to undergo thermally- or illumination-induced changes that allow discrimination between two different states of the defect. Zoth and Bergholz's study of interstitial Fe and FeB pairs provides a good example of this approach[53]. Clearly though, its application is limited.

In this chapter we examine a new technique for determining capture cross-sections, named Injection-level Dependent Lifetime Spectroscopy (IDLS), and apply it to the acceptor level of FeB pairs in silicon. The method is based on the analysis of the injection-level dependence of the recombination lifetime caused by a specific impurity. The concentration of the impurity must be known, which is possible by using ion-implantation and careful annealing, or by other techniques such as DLTS or Neutron Activation Analysis[45]. By fitting the standard Shockley-Read-Hall curves to the lifetime data, it is then possible to determine both the cross-sections and the energy level, although the technique is more sensitive to the cross-sections. If the energy-level is known from DLTS studies, which is often the case, then the accuracy of the cross-sections determined from IDLS is further improved. Consequently, the two techniques, DLTS and IDLS, are in fact complementary. A critical aspect of IDLS, as discussed below, is that samples with a large range of background dopant densities must be used to ensure accurate results.

A further benefit of IDLS is that the measurements are taken at room temperature, meaning any temperature dependence of the cross-sections or possible thermally-activated defect reactions are avoided. Most practical silicon devices such as solar cells and integrated circuits operate at or near room temperature, making the cross-sections determined by IDLS directly relevant.

Previous studies using IDLS have focussed on two current 'hot topics' in silicon devices: boron-oxygen complexes in p-type Czochralski-grown silicon[129], and analysis of interstitial iron and iron-boron pairs in p-type single-crystal silicon[165,166]. In the first case, boron-oxygen complexes, tentatively identified as BO_5 , play a critical role in reducing the efficiency of solar cells made with Czochralski silicon, and the IDLS technique was instrumental in determining their electronic properties. The second case, that of iron, is particularly relevant in that iron in silicon is well characterised by other studies, and thus provides a good reference for validating the IDLS method.

It should be mentioned that a related technique, called Temperature Dependent Lifetime Spectroscopy (TDLS), also exists[167-170]. It is based on the change in lifetime (usually under low-injection) over of few hundred degrees Kelvin, typically from room temperature up. TDLS only allows determination of the energy level, and is subject to the same defect reaction and temperature dependence problems as DLTS[167].

5.2 Theoretical Basis of Injection-level Dependent Lifetime Spectroscopy

Chapter 1 provides a general description of the SRH recombination theory. Since this theory forms the basis of the IDLS method, the relevant equations are repeated here. The injection-level dependence of the SRH lifetime $\tau_{SRH}(\Delta n)$ is itself a function of the dopant density N_A , defect energy level E_T and the capture cross-sections σ_n and σ_p , and for p -type Si is given by[17-19]:

$$\frac{1}{\tau_{SRH}} = \frac{N_A + \Delta n}{\tau_{p0}(n_1 + \Delta n) + \tau_{n0}(N_A + p_1 + \Delta n)} \quad (5.1)$$

Here, $\Delta n = \Delta p$ is the excess carrier density, in the absence of carrier trapping, and τ_{n0} and τ_{p0} are the fundamental electron and hole lifetimes, which are related to the recombination centre density, the thermal velocity[171] $v_{th} = 1.1 \times 10^7 \text{ cm s}^{-1}$, and the capture cross-sections via:

$$\tau_{n0} = \frac{1}{v_{th} \sigma_n N_{SRH}} \quad \tau_{p0} = \frac{1}{v_{th} \sigma_p N_{SRH}} \quad (5.2)$$

The electron and hole densities when the Fermi energy coincides with the recombination centre energy, n_1 and p_1 , are given by:

$$n_1 = N_C \exp\left(\frac{E_T - E_C}{kT}\right) \quad p_1 = N_V \exp\left(\frac{E_C - E_V - E_T}{kT}\right) \quad (5.3)$$

Values for the effective densities of states at the conduction and valence band edges and the energy gap at 25°C are taken as $N_C = 2.86 \times 10^{19} \text{ cm}^{-3}$, $N_V = 3.10 \times 10^{19} \text{ cm}^{-3}$, and $E_G = 1.124 \text{ eV}$ [130].

For carrier densities at which trapping effects are insignificant[17,104], and provided the recombination centre density is considerably less than the injected carrier density ($N_{SRH} \ll \Delta n$), then standard SRH theory is applicable[17], and $\Delta n = \Delta p$ is a reasonable simplifying assumption. If one or both of these conditions are not satisfied, then the excess carrier concentrations may become strongly unequal, resulting in distorted lifetime behaviour.

An important feature of Equation 5.1 is that it can be simplified under different conditions. It is common to distinguish between the low- ($\Delta n \ll N_A$) and high-injection ($\Delta n \gg N_A$) limits, but it is also possible to determine these limits for different defect energy levels. Table 5.1 lists these approximations, under low- and high-injection conditions, for five energy levels that have fundamentally different recombination properties, due to the placement of the energy

Description of defect state	Energy level $E_C - E_T$ (eV)	n_1 (cm^{-3})	p_1 (cm^{-3})	Low-injection $\tau_{\text{SRH}} (\Delta n \ll N_A)$	High-injection $\tau_{\text{SRH}} (\Delta n \gg N_A)$
Deep	0.55	1×10^{10}	6×10^9	τ_{n0}	$\tau_{n0} + \tau_{p0}$
Shallow – near CB	0.1	6×10^{17}	1×10^2	$\tau_{p0} n_1 / N_A$	$\tau_{p0} n_1 / \Delta n$
Shallow – near VB	1.024	1×10^2	6×10^{17}	$\tau_{n0} p_1 / N_A$	$\tau_{n0} p_1 / \Delta n$
Intermediate - CB	0.25	2×10^{15}	5×10^4	$\tau_{n0} + \tau_{p0} n_1 / N_A$	$\tau_{n0} + \tau_{p0}$
Intermediate - VB	0.874	4×10^4	2×10^{15}	$\tau_{n0} + \tau_{n0} p_1 / N_A$	$\tau_{n0} + \tau_{p0}$

TABLE 5.1. Approximations for the low- and high-injection SRH lifetimes τ_{SRH} for five qualitatively different types of defect state in the band gap for p-type silicon. Note that these limiting lifetimes are always independent of the dopant density for deep states. This may or may not be true for the other types of state, depending on the values of τ_{n0} and τ_{p0} , which are in turn determined by the capture cross-sections.

level in the band gap. The levels discussed are: deep (mid-gap), intermediate (0.25eV from each band edge), and shallow (0.1eV from each band edge). It should be noted that further divisions of the cases can be made for different inequalities between the capture cross-sections. These are discussed below but not shown in the table in order to preserve the important basic points.

A typical QSSPC injection-level dependent lifetime measurement will scan a range of Δn from around 1×10^{13} to $5 \times 10^{16} \text{ cm}^{-3}$, whilst N_A varies from 9×10^{13} to $7 \times 10^{16} \text{ cm}^{-3}$ for the IDLS study presented in this chapter. Note that for the ‘deep’ level, n_1 and p_1 are very small in comparison to both Δn and N_A . This is as expected, since a state near the middle of the gap implies a very low ‘dopant density’ if the Fermi level coincides with the defect level, or in other words, this situation is similar to intrinsic silicon, with $n_1, p_1 \approx n_i$. A direct consequence is that the low- and high-injection SRH lifetime limits **never** depend on either Δn or N_A . In fact they depend only on N_{SRH} and the cross-sections σ_n and σ_p , which determine τ_{n0} and τ_{p0} . Furthermore, in cases when $\sigma_p \gg \sigma_n$ and hence $\tau_{p0} \ll \tau_{n0}$, both the low- and high-injection lifetimes are simply given by τ_{n0} .

The situation is a little more complex for shallow levels. When near the conduction band, $n_1 \gg N_A$ and p_1 is insignificant, whilst when near the valence band, $p_1 \gg N_A$ and n_1 is insignificant. For these types of states, whether near the conduction or valence band, the low-injection lifetime **always** depends on the dopant density, irrespective of the capture cross-sections. Similarly, the high-injection lifetimes **always** depend on Δn . Obviously, this behaviour is qualitatively different from that of the deep levels.

For intermediate levels, neither deep nor shallow, the situation is different and more complex yet again. When near the conduction band, n_1 is of the order of N_A and p_1 is insignificant, whilst when near the valence band, p_1 is of the order of N_A and n_1 is insignificant.

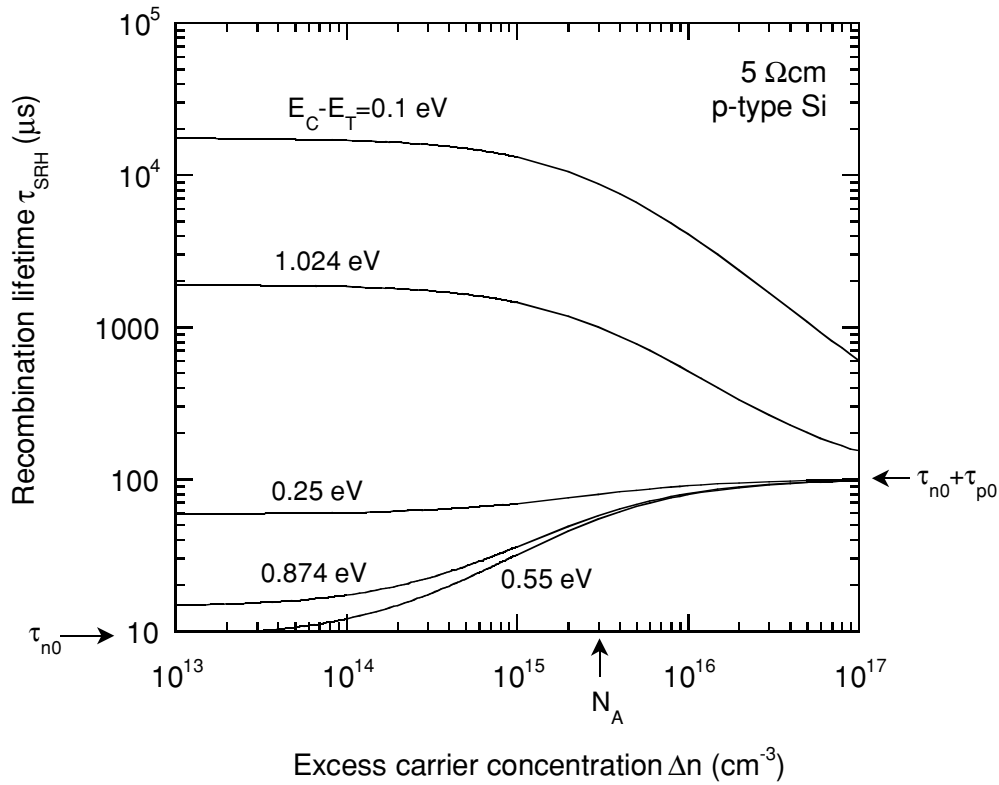


FIGURE 5.1. Injection-level dependent SRH lifetime curves for five different defect energy levels in 5 Ωcm p-type silicon. $N_{SRH}=1 \times 10^{12} \text{ cm}^{-3}$, $\sigma_n=1 \times 10^{-14} \text{ cm}^2$ and $\sigma_p=1 \times 10^{-15} \text{ cm}^2$.

The result is that the low-injection lifetimes *may* depend on the dopant density, depending on the cross-section values (i.e. the relative magnitudes of τ_{n0} and τ_{p0}). The high-injection lifetimes of intermediate levels follow the same pattern as deep levels, since $n_1, p_1 \ll \Delta n$.

A corollary of these general properties of the different levels, as revealed by Table 5.1, is that as the injection-level increases, the lifetime for deep levels *always increases or is constant*, while for shallow levels it *always decreases or is constant*, and for intermediate levels *may increase, decrease or remain constant*, depending on the values of the dopant density and cross-sections.

To further illustrate these important points, some injection-level dependent lifetime curves are depicted in Figures 5.1 and 5.2. The five energy level cases from Table 5.1 are plotted on each graph, with a density of recombination centres $N_{SRH}=1 \times 10^{12} \text{ cm}^{-3}$ and cross-sections $\sigma_n=1 \times 10^{-14} \text{ cm}^2$ $\sigma_p=1 \times 10^{-15} \text{ cm}^2$, resulting in $\tau_{n0}=9 \mu\text{s}$ and $\tau_{p0}=90 \mu\text{s}$. The only difference between the two figures is the p-type dopant density N_A , which is $3 \times 10^{15} \text{ cm}^{-3}$ (5 Ωcm) and $3 \times 10^{14} \text{ cm}^{-3}$ (50 Ωcm) for Figures. 5.1 and 5.2 respectively.

Firstly, notice that for the deep level the only change between the two resistivities is the horizontal shift of the mid-injection transition region by an order of magnitude, consistent with

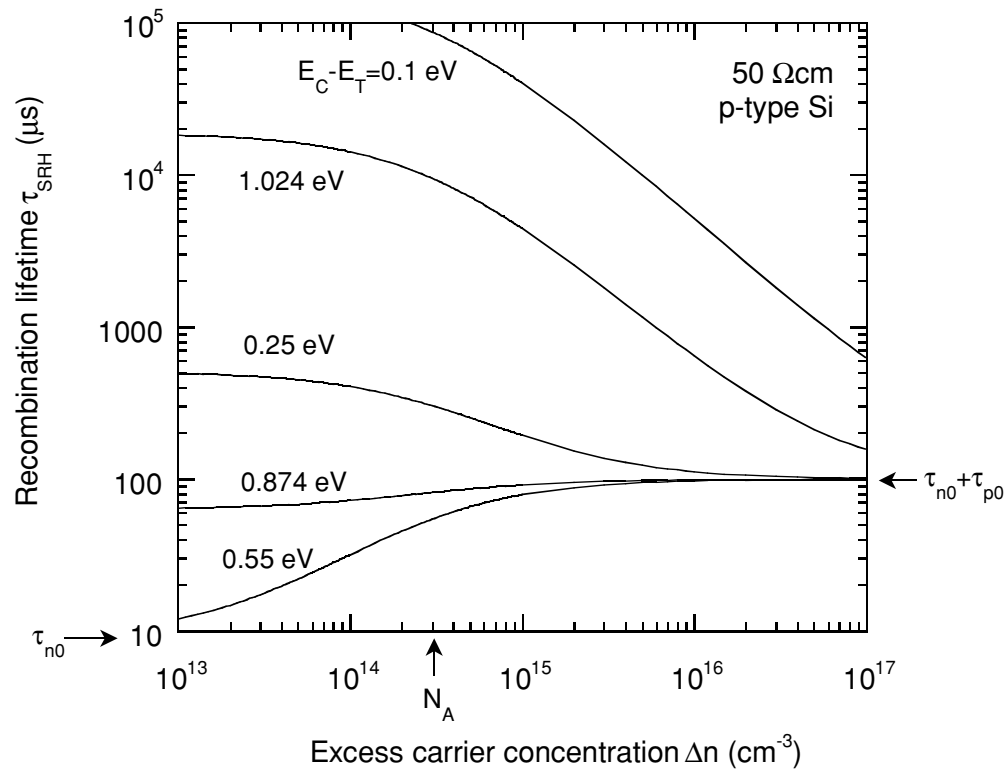


FIGURE 5.2. Injection-level dependent SRH lifetime curves for five different defect energy levels in 50Ωcm p-type silicon. $N_{SRH}=1 \times 10^{12} \text{ cm}^{-3}$, $\sigma_n=1 \times 10^{-14} \text{ cm}^{-2}$ and $\sigma_p=1 \times 10^{-15} \text{ cm}^{-2}$.

the order of magnitude change in dopant density. For the shallow levels, the high-injection region is the same in both cases, but differs at low-injection, as expected from Table 5.1.

For the intermediate defect levels the high-injection lifetime is the same as for the deep level, however the behaviour in the low-injection region is different. In the 50Ωcm case both levels reveal an increasing lifetime as the injection-level increases. For the 50Ωcm case, the dependence of the level at $E_C - E_T = 0.25 \text{ eV}$ changes direction whilst the other intermediate level retains an increasing lifetime. This change in direction is due to the dopant density becoming smaller than n_1 , and is an important property that is made use of in the following sections on IDLS studies of iron-boron pairs. Note that the reason for the level near the valence band not changing direction is the asymmetry between the cross-sections. This level would also undergo the change in dependence if the dopant density were reduced further still.

These fundamental differences between the behaviour of shallow, intermediate and deep levels under different injection conditions offers scope to distinguish between them using injection-level dependent lifetimes. In particular, the sensitive nature of these dependences on the cross-sections and the dopant density, allows accurate determination of the cross-sections when samples of widely different, but known, dopant densities are prepared. This is the underlying principle of the IDLS technique. Essentially the technique involves determining τ_{n0} and τ_{p0} by fitting SRH curves like those in Figures 5.1 and 5.2 to measured lifetime data. Then,

knowing the concentration of recombination centres from the implanted dose or by other techniques, it is straightforward to calculate the capture cross-sections. As mentioned above, IDLS can be used to determine energy levels also, but often these are already known from DLTS studies. Such prior knowledge further improves the accuracy of the cross-section calculations.

It is interesting to note that previous work by Hallen *et al.*[172] used energy levels and capture cross-sections derived from DLTS studies to calculate lifetime curves, in their case for proton-irradiated silicon. The technique of IDLS explored here is in fact the reverse: the use of injection-level dependent lifetime data to determine cross-sections and energy levels. For calculating cross-sections, this reverse process is in many cases inherently more accurate.

In the following parts of this chapter, IDLS is applied to iron, one of the most common impurities in silicon. Iron serves as a good initial case study for any new technique such as IDLS since it is probably the most accurately characterised and well understood metallic impurity in silicon, hence providing an opportunity to validate the technique. At room temperature, iron can occur in significant quantities in two distinct phases (apart from silicides or precipitates): either as interstitial iron (Fe_i), or as iron-boron (FeB) pairs that are bound together by Coulombic attraction. These two states have markedly different electronic properties and have been widely studied, although Fe_i is the more well known in terms of cross-sections. The IDLS studies presented here provide the most accurate determination to date of the cross-sections of the acceptor level of FeB pairs, and provides confirmation of the potential of the technique for characterising impurities in semiconductors in general.

5.3 IDLS studies of interstitial Fe and FeB pairs in silicon

5.3.1 Overview of Fe and FeB pairs in silicon

The recombination properties of FeB pairs in *p*-type silicon are of considerable interest in silicon device technology. The well established difference in the low-injection recombination strengths of Fe_i and FeB pairs can be exploited to make very sensitive measurements of the total iron concentration[53,173,174], provided the influence of other recombination centres can be discounted. While the fundamental recombination parameters of Fe_i , namely the defect energy level and the electron and hole capture cross-sections, are relatively well known[155], this is not the case for the acceptor level of FeB pairs. The energy level of the latter has been determined

by DLTS with reasonable accuracy, but measurement of the capture cross-sections has been uncertain, with estimates varying by up to two orders of magnitude[155].

There is strong evidence from various studies using DLTS, Hall effect and electron paramagnetic resonance (EPR) for the existence of two charge states of the FeB pair in silicon, as summarized recently by Istratov *et al.*[155]. One state occurs as a donor level at $E_V+0.1\text{eV}$, and the other as an acceptor level at $E_C-0.26(\pm 0.03)\text{eV}$. Brotherton *et al.*[175] argued that the acceptor level must be the dominant recombination centre of the two, due to the fact that it is deeper. Standard SRH recombination theory does not establish a mathematical link between energy levels and cross-sections. Therefore it is possible, within this theory, to attribute unphysically large cross-sections to a very shallow level, resulting in stronger recombination behavior than some deeper levels. However, considering that these recombination processes occur through multiple phonon emission, it seems physically reasonable to expect that shallow levels must have very small cross-sections for transitions to or from the furthest band edge, due to the prohibitively large number of phonons that are required simultaneously to carry off the energy difference. Consequently, the deeper acceptor level of FeB pairs should provide a much more efficient recombination channel than the donor level. Hayamizu *et al.*[168] showed that the acceptor level does indeed dominate recombination through FeB pairs at room temperature. They performed temperature dependent low-injection lifetime measurements using a microwave-detected photoconductance decay (PCD) method. Their data could only be adequately described by a relatively deep level around 0.29eV from either band edge, coinciding with previous DLTS measurements of the energy of the FeB acceptor level. Later temperature-dependent lifetime studies further confirmed their results[169,170].

Walz *et al.*[165] examined the injection-level dependence of the recombination lifetimes at room temperature of iron-diffused samples for a range of intermediate resistivities, and found that their data could be adequately explained by modelling the combined effect of the acceptor level and the level for interstitial iron. They were able to determine values for the capture cross-sections of the acceptor level by fitting SRH curves to the data for the different resistivities, using a technique which is essentially the same as IDLS. However, a crucial requirement of this technique is that samples with widely different dopant densities are used. The important feature of these different resistivities is that the injection-level dependence of the lifetime for a given defect is often markedly different, allowing accurate fitting of SRH curves with a consistent and unique pair of capture cross-sections. Walz *et al.*'s study was restricted to a resistivity range of 1 to $20\Omega\text{cm}$ due to constraints imposed by their lifetime measurement method (ELYMAT). This technique relies on surface passivation by HF, which is apparently only sufficient for this moderate resistivity range[176]. In this work, we study a larger range of resistivities, from 0.3 to $150\Omega\text{cm}$, made possible by use of the QSSPC lifetime technique. This corresponds to 25 times the dopant density range used by Walz *et al.*, a feature which turns out to be very important for

Recom. Centre	Energy Level (eV)	σ_n (cm ⁻²)	σ_p (cm ⁻²)	n_1 (cm ⁻³)	p_1 (cm ⁻³)	Low-inj. τ_{SRH}	High-inj. τ_{SRH}
Fe _i	E _V +0.38	5×10 ⁻¹⁴	7×10 ⁻¹⁷	6.9×10 ⁶	1.1×10 ¹³	τ_{n0}	τ_{p0}
FeB acceptor (this work)	E _C -0.23	3×10 ⁻¹⁴	2×10 ⁻¹⁵	3.6×10 ¹⁵	2.1×10 ⁴	$\tau_{p0}(n_1/N_A)+\tau_{n0}$	τ_{p0}
FeB acceptor (Walz <i>et al.</i>)	E _C -0.29	2.5×10 ⁻¹⁵	3×10 ⁻¹⁴	3.5×10 ¹⁴	2.2×10 ⁵	τ_{n0}^*	τ_{n0}

TABLE 5.2. Energy levels and capture cross-sections for Fe_i and the acceptor state of FeB pairs. Also shown are the SRH parameters n_1 and p_1 , and approximations for the SRH lifetimes under low- and high-injection conditions. These approximations reveal that the FeB pair as modelled by Walz *et al.* has effectively no injection-level dependence. The low-injection approximation(*) for their level is not strictly valid for the 150Ωcm case, but is only in error by around 20%. The parameters for Fe_i are taken from Istratov's review.

uniquely determining the cross-sections. Also, we explore a broader range of injection-levels for each resistivity, which is of further benefit in accurately calculating the cross-sections.

In addition to varying the dopant densities, the dissociation behavior of FeB pairs upon illumination[53] may be used to vary the recombination centre densities. By applying various levels of light-soaking to the samples before lifetime measurement, different relative populations of FeB pairs and Fe_i are obtained. In our experiments, the total iron concentration is known from the implantation dose, and so the sum of the modelled FeB and Fe_i centres can be forced to equal this value. In this way, a good fit can be achieved for each light-soaking condition and resistivity, with uniquely determined capture cross-sections.

At this stage it is useful to consider how the properties of Fe_i and FeB pairs compare with the five basic cases discussed above in Section 5.2. We do not discuss the shallow donor level, since it does not contribute significantly to recombination at room temperature, as mentioned above. Table 5.2 lists the energy levels and capture cross-sections for Fe_i and the acceptor level of FeB pairs. For interstitial iron, with an energy level close to the middle of the band-gap, both n_1 and p_1 are much less than N_A for all the resistivities used in this study, as shown in Table 5.2. Hence, the right hand side of Eq. 1 simplifies to $1/\tau_{n0}$ and $1/\tau_{p0}$ for low- and high-injection respectively, remembering that $\tau_{n0} \ll \tau_{p0}$ due to the values of the cross-sections. These limiting lifetime values are independent of the dopant density, a general feature of deep levels, irrespective of their capture cross-sections.

The acceptor state of FeB pairs is analogous to the intermediate level near the conduction band in Table 5.1. With an energy level of E_C-0.23eV, which was found to provide the best modelling results in this work, p_1 is still negligible, but $n_1 \approx 4 \times 10^{15} \text{ cm}^{-3}$. As a result, the low-injection lifetime depends strongly on the dopant density for the resistivities used in this study. The high-injection lifetime is once again given by τ_{p0} due to the fact that $\tau_{n0} \ll \tau_{p0}$. However, the

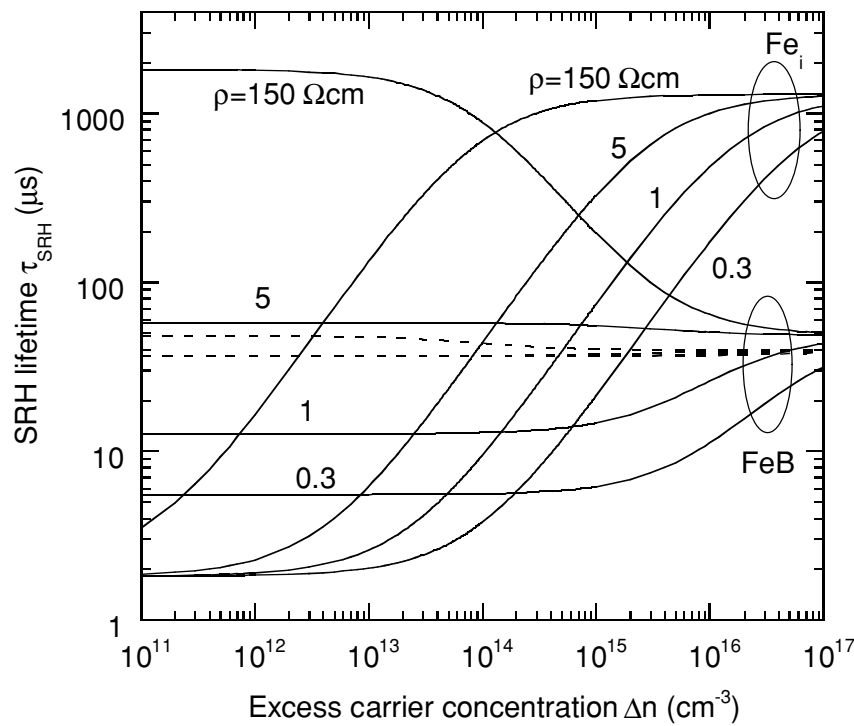


FIGURE 5.3. Shockley-Read-Hall injection-level dependent lifetime curves for different Fe-related recombination centres in p-type silicon of different resistivities. The density of centres has been taken as 10^{12} cm^{-3} . Curves for interstitial iron (Fe_i) and the acceptor level of FeB pairs are shown for resistivities of $\rho = 0.3, 1, 5$ and $150 \Omega \text{ cm}$. The values for the energy levels and capture cross-sections are given in Table 5.2, and for FeB pairs are those determined from this study. As a comparison, curves for the acceptor level of FeB using the energy level and cross-sections from Walz *et al.* are shown for each of the four resistivities as dashed lines. The lower dashed line represents the three lower resistivities, which coincide.

behavior of the FeB level can be entirely different if other recombination parameters are assumed. Table I also lists the energy levels and cross-sections reported by Walz *et al.*, and in this case, with a slightly deeper centre, $n_1 \approx 4 \times 10^{14} \text{ cm}^{-3}$. Considering this value, and their reversed asymmetry of the cross-sections, the resulting low- and high-injection lifetimes would both be approximately equal to τ_{n0} , indicating essentially no injection-level dependence.

Figure 5.3 illustrates the theoretical injection-level dependent lifetime curves for these three cases: interstitial iron, FeB pairs with the recombination parameters used in this work, and FeB pairs with those used by Walz. The curves, calculated for a bulk defect concentration of $1 \times 10^{12} \text{ cm}^{-3}$ for each of the four resistivities used in this study, reveal the distinct behavior of each level. Note in particular the lack of injection-level dependence of Walz's parameters for the FeB pair in comparison with those used in this study. However, as mentioned, Walz only measured samples in a small range of resistivities, from 1 to $20 \Omega \text{ cm}$, and over this narrow range the optimum parameters found in this current study also give a mild dependence with similar magnitudes (note the curve for the $5 \Omega \text{ cm}$ case). Hence, the parameters found in this work, and

those found by Walz, provide reasonable approximations to one another over the narrower dopant range, despite the large differences between the cross-section values. However, when data from a much larger dopant density range is examined, the cross-sections determined in this study must be used. These considerations reveal that it is essential to have data from a large range of resistivities to *uniquely* specify the cross-sections using IDLS.

On a general note, Figure 5.3 illustrates some interesting features of Fe_i/FeB pair recombination. Firstly, although the low-injection lifetime of the FeB pairs depends on the dopant density, these lifetimes are always significantly higher than those due to interstitial iron. Under high-injection conditions, however, the FeB pairs are the dominant centres. This leads to the lifetime curves for the dissociated and undissociated states for a single sample crossing over at some intermediate injection-level, which has been observed previously on several occasions[166,177]. This phenomenon initially highlighted the possibility of using injection-level dependent lifetimes to estimate the cross-sections.

5.3.2 Experimental methods

5.3.2.1 Sample preparation

Sample preparation is critical in an experiment aimed at investigating impurities in silicon. Care needs to be taken to ensure that the deliberately introduced impurities occur evenly throughout the bulk of the wafers, as this is essential for accurate injection-level dependent lifetime measurements. Also, the impurities to be studied should not be subject to significant gettering at the surfaces or damaged regions, nor undergo out-diffusion or precipitation in the bulk. In this study, avoiding loss of iron through these processes allows us to determine the bulk iron concentration, after annealing, from a knowledge of the implantation dose. This is important in modelling the lifetime data and allowing the accurate fitting of the SRH parameters.

Boron-doped *p*-type float zone (FZ) silicon samples of four resistivities (0.3, 1, 5 and 150Ωcm) were chosen for this study. The samples were initially etched and cleaned to remove any surface damage and contamination, and then implanted with 70keV ⁵⁶Fe to doses of $1 \times 10^{11} \text{cm}^{-2}$ and $1 \times 10^{12} \text{cm}^{-2}$. Annealing was then performed at 900°C for 1 hour, which is sufficiently long to distribute the iron uniformly throughout the wafers, taking into account the diffusivity of iron at this temperature[155] for wafers of 400μm thickness or less. Float zone silicon was chosen due to its low oxygen and crystallographic defect content, in order to avoid complicating defect reactions during the annealing stage[129]. The solubility limit of interstitial iron[155] at 900°C is about $5 \times 10^{13} \text{cm}^{-3}$, and so for a 300μm thick wafer implanted with a dose

of $1 \times 10^{12} \text{cm}^{-2}$, the resulting bulk concentration would be $3.3 \times 10^{13} \text{cm}^{-3}$. This is close to the solubility limit, but as revealed by the results below, does not create significant precipitation. For the $1 \times 10^{11} \text{cm}^{-2}$ doses, the solubility limit is comfortably avoided. Some samples were implanted with even higher doses ($1 \times 10^{13} \text{cm}^{-2}$), which did result in massive precipitation in the bulk and hence a loss of interstitial iron, as discussed in section 5.3.4.

During annealing, iron can also precipitate at the Si/SiO₂ interface[161]. To avoid this, the native oxide was removed immediately prior to annealing, and nitrogen gas was used during the anneal to avoid oxide growth. The samples were then cooled rapidly in air to ‘freeze’ the iron in the interstitial state. To minimise the possible loss of iron through out-diffusion, samples of the same implanted dose were annealed face-to-face, with the surfaces in contact. Out-diffusion through the rear of the samples should be insignificant due to the initially low surface concentrations there.

A low implantation energy of 70keV was used to minimise lattice damage, which can act as unwanted gettering sites during the anneal[178]. Such gettering action may result in non-uniform distributions, which can in turn distort the injection-level dependent lifetime measurements. Furthermore, any remaining lattice damage can directly affect the lifetime measurements and also hinder surface passivation. To avoid these potential problems, several microns of silicon were etched from the wafers after annealing to remove the implanted region. Lifetime measurements before and after this etch revealed no discernible change, indicating that residual damage and gettering in the implanted region was negligible. The etching only reduced the wafer thickness by about 3%, and hence had little impact on the total iron concentration present.

After annealing and etching, it is necessary to passivate the wafer surfaces to allow reliable bulk lifetime measurements. This was achieved by depositing films of stoichiometric plasma-enhanced chemical vapor deposited (PECVD) silicon nitride[55]. We chose this passivation method because it provides very low surface recombination velocities for a large range of resistivities, and also because the relatively low temperature and short time required for deposition (390°C for 10 minutes) avoid potential precipitation problems that can occur if higher temperature processes such as oxidation are used. Diffusions also had to be avoided because of their potential gettering effect, even if only slight. According to the results of Henley *et al.*[179], the SiN deposition should result in negligible precipitation for the lighter dose of $1 \times 10^{11} \text{cm}^{-2}$, and only a small proportion (about 10%) for the heavier dose of $1 \times 10^{12} \text{cm}^{-2}$. The effectiveness of the nitride films in passivating the surfaces was verified using control samples, as described below. As a general indication, this passivation allows lifetimes of above 1ms to be observed in high resistivity material.

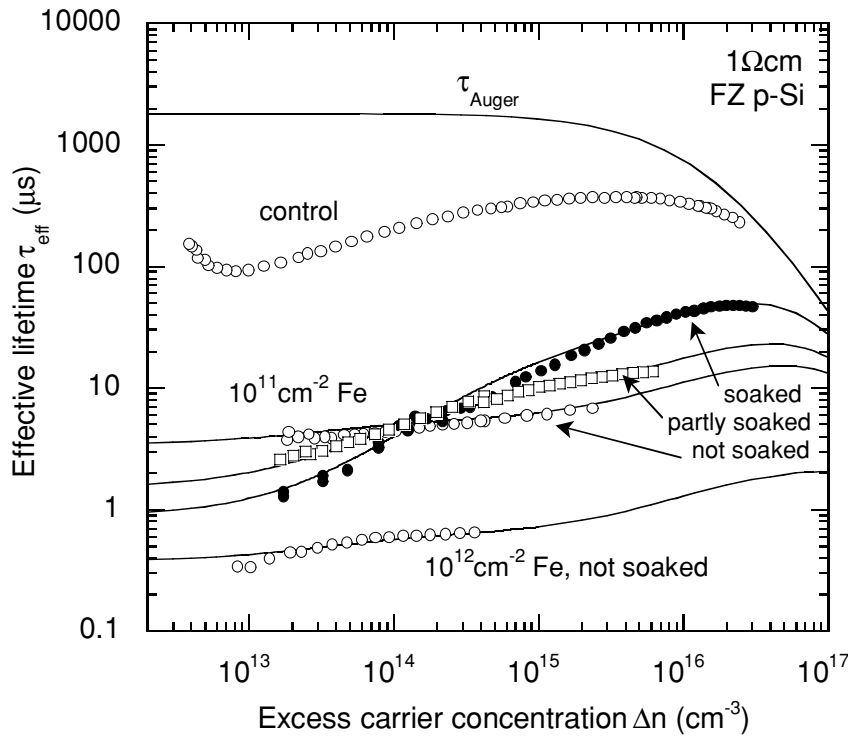


FIGURE 5.4. Lifetime measurements (symbols) and SRH fits (solid lines) for 1Ωcm samples implanted with iron doses of $1 \times 10^{11} \text{ cm}^{-2}$ and $1 \times 10^{12} \text{ cm}^{-2}$. For the $1 \times 10^{11} \text{ cm}^{-2}$ case, three curves corresponding to different light soaking levels are shown. The concentrations of Fe_i and FeB pairs used to generate the fits are given in Table 5.3, and the recombination parameters in Table 5.2. Also shown are the theoretical Auger limit and data from the non-implanted control sample.

5.3.2.2 Lifetime measurements

The quasi-steady-state photoconductance (QSSPC) technique[51], as discussed in detail in Chapter 1 was used to measure the injection-level dependence of the effective lifetimes of the iron-diffused samples. This method involves the use of a 2cm diameter coil which is inductively coupled to the test wafer. The implanted area of our samples was a square of 3cm×3cm, large enough to fully cover the measurement region. To ensure that the measured lifetimes reflect the recombination properties of the iron-related states only, and not surface effects or the pre-implanted lifetime of the FZ wafers, control samples were included. These were subjected to the same etching, cleaning, annealing and passivation treatments as the implanted samples.

Figure 5.4 shows injection-level dependent lifetime measurements of the 1Ωcm wafers. The fact that the effective lifetimes measured on the control samples were almost always an order of magnitude or more greater than the lifetimes of the iron implanted samples means that the measurements on the latter are not significantly affected by surface recombination, nor by the intrinsic bulk lifetime of the FZ wafers. It is in fact this constraint which places a lower limit

on the iron dose, as lighter doses would result in surface-affected lifetime measurements. If, however, the dose is too high, and the resultant lifetimes too low, the carrier profiles across the thickness of the samples will become strongly non-uniform (when measuring with white light), and the measured injection level dependence incorrect. It is possible to use an infra red filter to avoid this problem, but the low generation rates of the reduced photon flux do not allow sufficiently high carrier densities to be reached. Consequently, we are restricted to doses around $1 \times 10^{11} \text{ cm}^{-2}$ to $1 \times 10^{12} \text{ cm}^{-2}$ by considerations of surface recombination, non-uniform carrier profiles, and also by the solubility limit at the chosen annealing temperature.

One further point of interest with respect to photoconductance measurements in general is the observed behavior at very low carrier concentrations. Figure 5.4 shows that the lifetime abruptly increases below $1 \times 10^{13} \text{ cm}^{-3}$ for the control sample. This dependence is not related to SRH recombination through defects, but is a result of minority carrier trapping as discussed in Chapter 3. These trapping states, which trap and release electrons from the conduction band without directly contributing to recombination, may reside in the bulk or at the SiN/Si interface. In either case, they distort the recombination lifetime measurements in both the control and iron-diffused samples. This trap-affected data does not reflect the recombination lifetime, and must be discarded. This has been done for the iron-doped samples in Figure 5.4, and for all subsequent data plotted in this work, although other studies have sometimes failed to recognize this problem and erroneously considered the trap-affected data as SRH recombination lifetimes[180]. The onset of trapping is therefore an effective lower bound on the carrier densities for which reliable recombination lifetime data is available using photoconductance-based techniques. Surface photovoltage (SPV) methods are immune to trapping effects, but can only measure lifetimes under very low injection-level conditions and so are not appropriate for IDLS.

5.3.3 Modelling procedure

Lifetime measurements obtained by the QSSPC method, and by PCD methods also, represent effective lifetimes, meaning that they comprise components caused by various recombination mechanisms, as discussed in Chapter 1. It is essential therefore to be aware which mechanisms occur and what their relative contributions are in order to single out a particular mechanism for analysis. In many practical cases, more than one type of SRH centre may be present simultaneously, as is the case here for iron contaminated *p*-type Si which contains both FeB pairs and Fe_i. Also, the effects of Auger recombination are often important in heavily doped or highly excited silicon[23], and need to be considered here at the higher carrier concentrations. For reasons discussed below, contributions to the effective lifetime from the

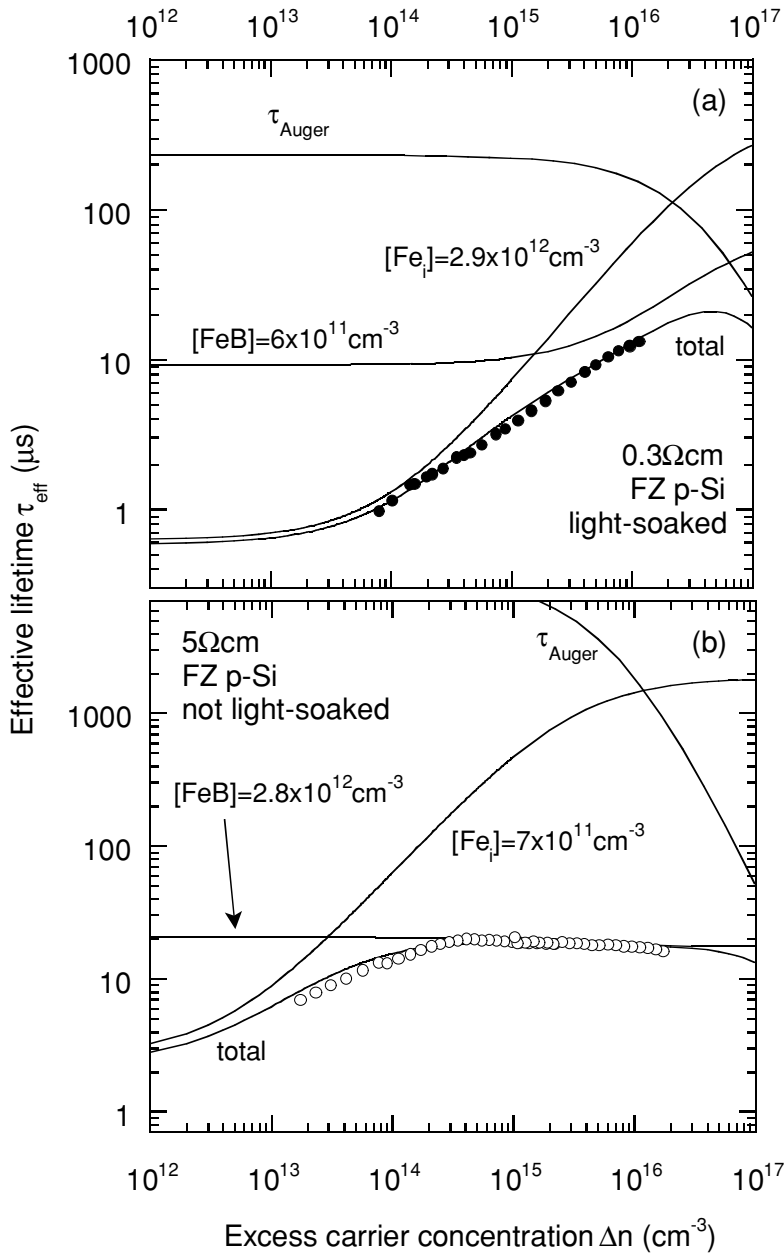


FIGURE 5.5. Examples of the fitting procedure for the effective lifetimes for: a) the 0.3Ωcm sample with light-soaking, and b) the 5Ωcm sample without light-soaking. The constituent curves for Fe_i , FeB pairs and Auger recombination are shown for each plot, and the concentrations of the recombination centres used for the fits are given in Table 5.3. In both cases the implanted dose was $1 \times 10^{11} \text{ cm}^{-2}$.

surfaces are not significant in the iron-diffused samples studied here, and radiative recombination is negligible in indirect semiconductors such as silicon. Therefore, the effective lifetime, comprising all of the important contributions, can be expressed as:

$$\frac{1}{\tau_{eff}} = \frac{1}{\tau_{SRH}^{Fe_i}} + \frac{1}{\tau_{SRH}^{FeB}} + \frac{1}{\tau_{Auger}} \quad (5.4)$$

Resist- ivity (Ωcm)	N_A (cm^{-3})	W (cm)	Fe implant dose (cm^{-2})	[Fe] (cm^{-3}) from dose	Light soaking	Modelled [Fe _i] (cm^{-3})	Modelled [FeB] (cm^{-3})	[Fe _i]+ [FeB]
0.3	6.6×10^{16}	0.0285	1.0×10^{11}	3.5×10^{12}	none	1.0×10^{12}	2.5×10^{12}	3.5×10^{12}
"	"	"	"	"	partial	2.0×10^{12}	1.5×10^{12}	"
"	"	"	"	"	full	2.9×10^{12}	0.6×10^{12}	"
1	1.7×10^{16}	0.0400	1.0×10^{11}	2.5×10^{12}	none	0.2×10^{12}	2.3×10^{12}	2.5×10^{12}
"	"	"	"	"	partial	1.1×10^{12}	1.4×10^{12}	"
"	"	"	"	"	full	2.0×10^{12}	0.5×10^{12}	"
"	"	"	1.0×10^{12}	2.5×10^{13}	none	0.2×10^{13}	2.0×10^{13}	2.2×10^{13}
5	3.0×10^{15}	0.029	1.0×10^{11}	3.5×10^{12}	none	0.7×10^{12}	2.8×10^{12}	3.5×10^{12}
"	"	"	"	"	full	3.2×10^{12}	0.3×10^{12}	"
150	9×10^{13}	0.035	1.0×10^{12}	2.9×10^{13}	none	0.5×10^{13}	2.0×10^{13}	2.5×10^{13}

TABLE 5.3. Modelled and implanted iron concentrations for the different resistivity samples under different light-soaking conditions. Note that the sum of the modelled Fe_i and FeB pair concentrations is always close to the total iron concentration expected from the implantation dose. Under strong light-soaking most of the iron is present as Fe_i, whereas without light-soaking FeB pairs dominate.

The Auger lifetime is calculated using a Coulomb-enhanced Auger recombination model[22,26] that is valid for all injection-levels and dopant densities, as described in Chapter 1. Values for the Auger coefficients C_n , C_p and C_a , as required in the Auger model, are taken from the literature[23,24].

The fitting procedure employed in this work essentially proceeds as follows. Curves such as those in Figure 5.3 are taken for interstitial iron and FeB pairs for the appropriate resistivity. These curves are combined according to Equation 5.4, with a term for Auger recombination included, and compared to the measured data. The concentrations of each centre are adjusted, and the shape of the FeB curve altered by changing the cross-sections, until a good fit is obtained for all the samples with a single set of cross-sections.

Two examples of the fitting process are given in Figure 5.5. In part (a) the light-soaked case for the $0.3\Omega\text{cm}$ sample is shown. Due to the light-soaking, the majority of the iron present in this sample occurs as interstitial iron. In part (b) data for the $5\Omega\text{cm}$ sample without light-soaking is shown, and is dominated by the presence of FeB pairs. Note that the dependence of the FeB pair curves is markedly different for the two resistivities, while the shape of the Fe_i curves are similar apart from being shifted due to the change in dopant density. It is an interesting coincidence that the linear combination of the FeB and Fe_i terms gives rise to a straight line in part (a) of the Figure.

For all samples, the sum of the modelled interstitial iron and FeB pair concentrations is forced to agree with that expected from the implantation dose. For parts (a) and (b) of Figure

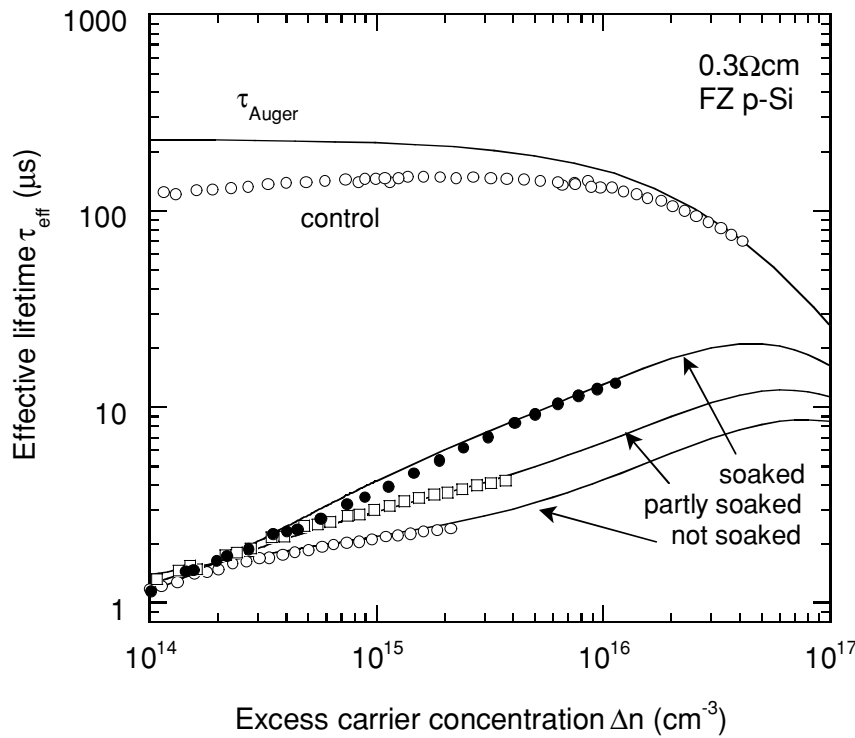


FIGURE 5.6. Lifetime measurements (symbols) and SRH fits (solid lines) for the 0.3 Ωcm sample implanted with an iron dose of $1 \times 10^{11} \text{ cm}^{-2}$. Three curves corresponding to different light soaking levels are shown. The concentrations of Fe_i and FeB pairs used to generate the fits are given in Table 5.3, and the recombination parameters in Table 5.2.

5.5, this sum equals $3.5 \times 10^{12} \text{ cm}^{-3}$, precisely that expected from an implant dose of $1 \times 10^{11} \text{ cm}^{-2}$ in a wafer of thickness 0.0285 cm. This process effectively determines the concentration of FeB pairs for any curve, leaving the two cross-sections of the FeB pairs as the only free parameters in the procedure. In principle, therefore, only two largely different resistivities are needed to obtain unique values of the cross-sections. However, the fact that these values also generate good results for the other resistivities used in this study, and also for the different concentrations of FeB pairs as brought about by light-soaking, provides greater confidence in the validity of the underlying method.

5.3.4 Results and discussion

Figure 5.4 depicts the results for the 1 Ωcm samples. The Auger lifetime represents an intrinsic upper limit in *p*-type silicon samples of this resistivity, which is approached by the control sample. Below these curves are data for two iron implanted samples, with doses of 1×10^{11} and $1 \times 10^{12} \text{ cm}^{-2}$. There are three curves for the lighter dose corresponding to different

light-soaking levels, and hence different relative populations of Fe_i and FeB pairs. The solid lines that pass through the data represent the SRH lifetimes as calculated using the appropriate recombination parameters for FeB and Fe_i as given in Table 5.2. Table 5.3 lists the concentrations of Fe_i and FeB pairs that were used to obtain the fits. The fact that these concentrations add to agree with that expected from the dose indicates that very little precipitation has occurred in the samples. This is further corroborated by the fact that a good fit for the heavier dose can be achieved by merely scaling up the concentrations by an order of magnitude (see Table 5.3), as should occur if precipitation is negligible. It is interesting to note that even in the fully light-soaked case, it is still necessary to include a small number of FeB pairs to describe the data well, indicating that either pair dissociation is not complete or that some re-pairing occurs between light-soaking and lifetime measurement.

Figures 5.6 and 5.7 show the results for the 0.3 and 5 Ωcm samples respectively, both implanted with a dose of $1 \times 10^{11} \text{cm}^{-2}$, under different light-soaking conditions. Once again, the sum of the modelled concentrations agrees well with that obtained from the dose. Note that the lifetimes of the control sample approach the Auger limit much more closely for the 0.3 Ωcm case, indicating either that these wafers are of better intrinsic quality or the surface passivation was superior. An important observation here is that the dependence of the two resistivities without light-soaking goes in opposite directions as the carrier density increases, as expected from Figure 5.3.

For the 150 Ωcm light-soaked case, the dependence becomes much more pronounced, as revealed by the data and fit in Figure 5.8. In this plot, the constituent SRH curves for the FeB pairs and Fe_i are also shown, similar to Figure 5.5. The strong dependence of the FeB curve is clear in this case, which contrasts with the weak dependence predicted by Walz's cross-sections. This comment also holds for the other extreme of dopant densities as shown in Figure 5.6 for the 0.3 Ωcm case, with the notable difference that the injection-level dependence goes in the opposite direction. The data in Figure 5.8 is for a sample that was implanted with a heavier dose of $1 \times 10^{12} \text{cm}^{-2}$. For this resistivity, the corresponding wafer with the lighter dose gave lifetime data that was too close to the control sample, meaning that surface recombination impacted on the measurements.

The fitting procedure revealed that, for low- and mid-injection behaviour, the more heavily doped samples are more sensitive to the electron capture cross-section, while the high resistivity samples are more strongly affected by the hole cross-section. This fortunate state of affairs allows both cross-sections to be determined accurately, and is consistent with the low-injection lifetime approximations in Table 5.2, which reveal that as N_A increases, the low-injection value is dominated by τ_{n0} . In fact, this will occur for any intermediate level, and is the

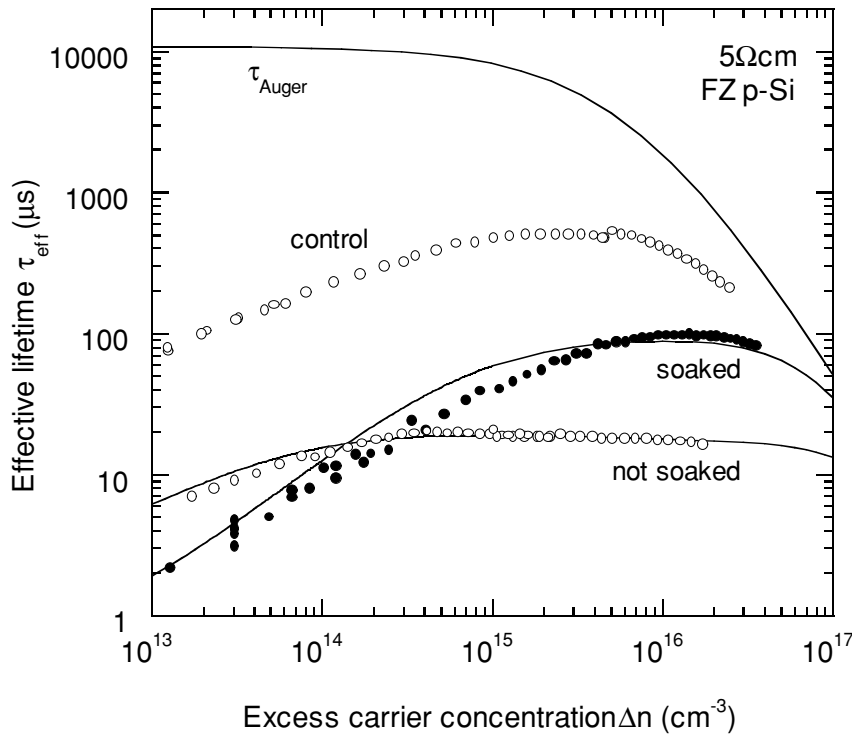


FIGURE 5.7. Lifetime measurements (symbols) and SRH fits (solid lines) for the 5Ωcm sample implanted with an iron dose of $1 \times 10^{11} \text{ cm}^{-2}$. Two curves corresponding to different light soaking levels are shown. The concentrations of Fe_i and FeB pairs used to generate the fits are given in Table 5.3, and the recombination parameters in Table 5.2.

basic reason for the need to use a large range of resistivities when dealing with any levels other than deep ones.

For all of the fits shown, the capture cross-sections used for the FeB pairs were $\sigma_n = 3 \times 10^{-14} \text{ cm}^2$ and $\sigma_p = 2 \times 10^{-15} \text{ cm}^2$. The best way to estimate the uncertainty in these values is by adjusting them and observing the effect on the fits. In conjunction with a typical uncertainty in the measured lifetimes of around 20%, and an uncertainty of about 5% in the dopant densities, it is possible to state that the cross-sections should reside in the ranges $\sigma_n = (3 \pm 2) \times 10^{-14} \text{ cm}^2$ and $\sigma_p = (2 \pm 1) \times 10^{-15} \text{ cm}^2$. The value of the energy level used was $E_c - 0.23 \text{ eV}$, which is somewhat different to that found in some other studies [165, 168, 175]. It is, nevertheless, within the uncertainty bounds reported by Istratov in his recent review of iron complexes in silicon [155]. It should be mentioned that our finding that $\sigma_n > \sigma_p$ is contradictory to the results of Walz, and also to expectations based on Coulombic effects due to the negative charge state of the acceptor level (FeB^-). However, cross-sections are not only determined by the charge state, but also by the energy level itself, hence it is possible that the proximity of the FeB acceptor level to the conduction band may negate the Coulombic repulsion for electrons.

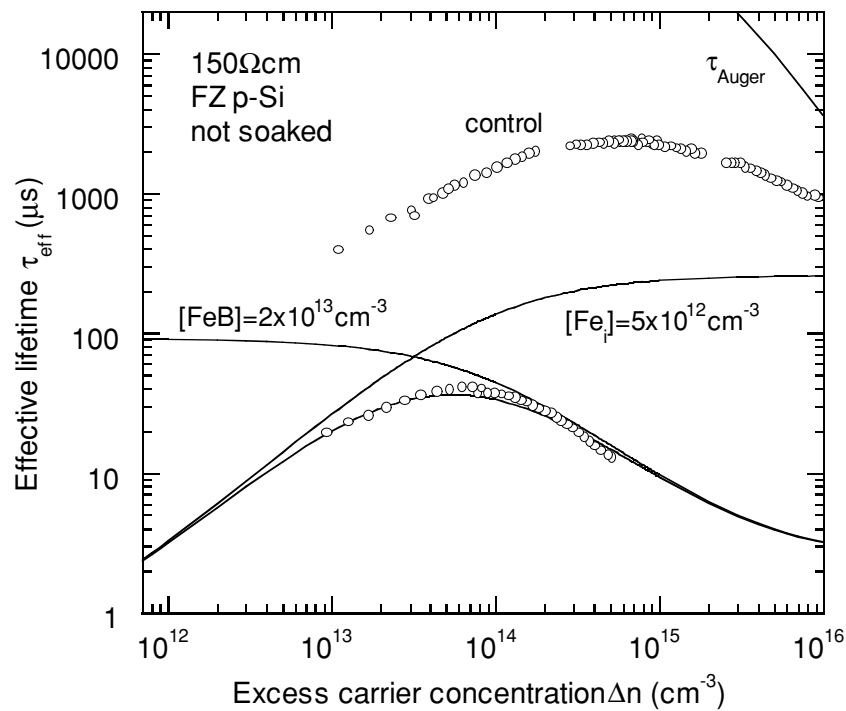


FIGURE 5.8. Lifetime measurements (symbols) and SRH fit (solid lines) for the 150Ωcm sample implanted with an iron dose of $1 \times 10^{12} \text{ cm}^{-2}$. The curve shown is for no light-soaking. The concentrations of Fe_i and FeB pairs used to generate the fit are given in Table 5.3, and the recombination parameters in Table 5.2.

Note that for both the heavier doses of $1 \times 10^{12} \text{ cm}^{-2}$ (in Figures 5.4 and 5.8), the sum of the modelled iron-related centres is a little less than expected, as shown in Table 5.3. This is possibly due to a small amount of precipitation, since these doses are close to the solubility limit for the 900°C anneal. In fact, the concentrations reported in Table 5.3 suggest that around 10% of the iron has precipitated, in accordance with the expectations from Henley's data[179], as discussed above.

Figure 5.9 illustrates the problems that can arise from severe precipitation as a result of inappropriate sample preparation. These high resistivity wafers ($>200 \Omega \text{ cm}$) were implanted with iron doses of $1 \times 10^{12} \text{ cm}^{-2}$ and $1 \times 10^{13} \text{ cm}^{-2}$ and annealed at 900°C. If all of the available iron was distributed uniformly throughout the bulk, these doses would correspond to bulk concentrations of $3.3 \times 10^{13} \text{ cm}^{-3}$ and $3.3 \times 10^{14} \text{ cm}^{-3}$ respectively. However, as mentioned, the solubility limit of interstitial iron at 900°C is around $5 \times 10^{13} \text{ cm}^{-3}$. Consequently, the more heavily implanted ($1 \times 10^{13} \text{ Fe cm}^{-2}$) sample will be subject to considerable loss of iron through precipitation, in fact about 85% will precipitate according to the solubility value. Figure 5.9 shows that this has indeed occurred, as evidenced by the small difference in the magnitudes of the recombination lifetimes for the two samples. If there had been no precipitation, doses which

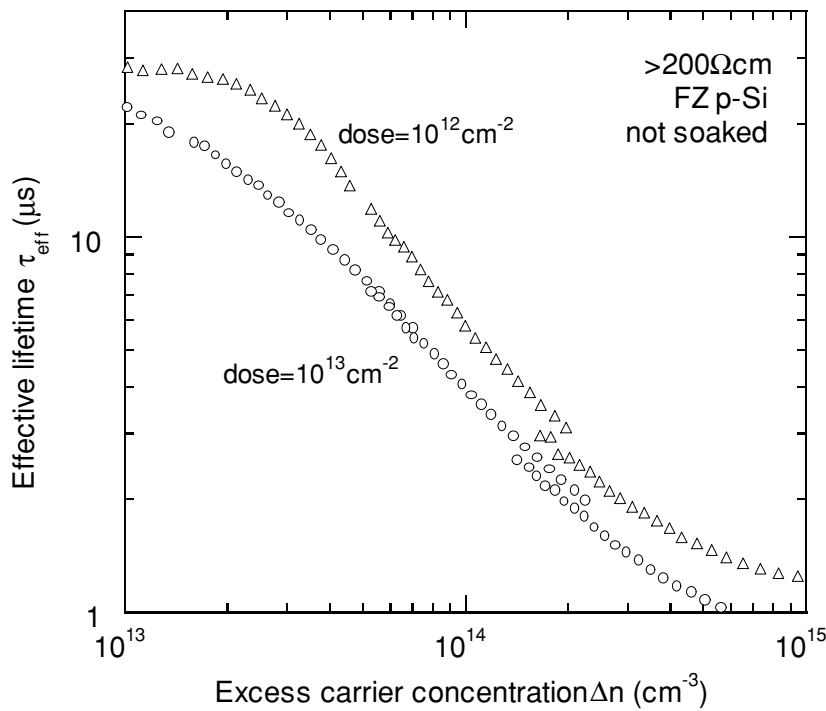


FIGURE 5.9. Lifetime measurements for high resistivity ($>200\Omega\text{cm}$) samples implanted with iron doses of $1\times 10^{12}\text{cm}^{-2}$ and $1\times 10^{13}\text{cm}^{-2}$. The small difference in recombination lifetimes reflects precipitation of iron during annealing.

differed by an order of magnitude should have resulted in lifetimes that differed by the same factor, as occurred for the two doses in Figure 5.4 (within 10%). However, the lifetimes for the two doses in Figure 5.9 differ by at most a factor of two (when compared at the same injection-level), implying that at least 80% of the iron has precipitated in the heavier dose ($1\times 10^{13}\text{cm}^{-2}$), in agreement with expectations from the solubility data.

Precipitation was one reason for leaving the data for the heavily implanted sample in Figure 5.9 out of the modelling exercise. However, both these wafers suffer from other problems and as a result both sets of data were excluded. For both samples, the recombination centre density is comparable to or greater than both the dopant density ($N_A < 6\times 10^{13}\text{cm}^{-3}$) and also the carrier densities at which the lifetime is to be measured. This implies that the excess carrier populations can become heavily unequal due to ‘trapping’ by the recombination centres, particularly if the capture cross-sections are largely unequal [17,139]. These effects can significantly distort the lifetime data, making standard SRH modelling inappropriate. Nevertheless, the general trend in Figure 5.9 agrees with the theoretical expectations indicated in Figure 5.3 for high resistivity samples, considering that the lifetime is shifted to much lower values due to the higher iron concentration in the sample in Figure 5.9.

Up to this point we have only considered FeB acceptors, and the shallower donor level has not been included in the modelling. But, curiously, it is also possible to obtain satisfactory

fits to all samples, with an energy level of $E_V+0.1\text{eV}$ and capture cross-sections of $\sigma_n=3\times10^{-13}\text{cm}^{-2}$ and $\sigma_p=3\times10^{-15}\text{cm}^{-2}$, plus the level for interstitial iron. This apparent weakness in the method, that is, its inability to identify the level causing the recombination, arises because of the indiscriminate treatment of the cross-sections and the energy levels in standard SRH statistics. It is necessary to invoke a physical argument, such as Brotherton[175] did, as discussed above, to decide which centre is dominant. The fact that neither the acceptor nor the donor FeB centre are deep means that the low-injection lifetime will vary with the dopant density. This is the important criterion for describing the changing injection-level dependence for the different resistivities as revealed by our data. However, although the method can not discriminate between these two levels, it is able to do so for the acceptor levels at $E_C-0.23$ and $E_C-0.29\text{eV}$, due to the $E_C-0.29\text{eV}$ state behaving more like a deep state.

In conclusion, by using a large range of dopant densities, the changing injection-level behavior of the acceptor level of FeB pairs allows accurate determination of the electron and hole capture cross-sections for this level at room temperature. The best fits across all samples were obtained with values of $E_C-0.23\text{eV}$ for the energy level, and $\sigma_n=3\times10^{-14}\text{cm}^{-2}$ and $\sigma_p=2\times10^{-15}\text{cm}^{-2}$ for the electron and hole capture cross-sections respectively. More generally, this work illustrates that with appropriate choices of implant dose, annealing temperature and time, and a good range of substrate resistivities, Injection-level Dependent Lifetime Spectroscopy (IDLS) offers an accurate alternative to DLTS techniques for determining capture cross-sections of defects in semiconductors, especially if the defect energy is known.

5.3.5 DLTS measurements

As mentioned, there have been numerous DLTS studies of FeB pairs in silicon, which have resulted in a range of energy values for the acceptor level of interest here. Brotherton *et al.*[175] reported the level at $E_C-0.29\text{eV}$, Lemke[181] found it to be at $E_C-0.23\text{eV}$, while Nakashima *et al.*[182] reported $E_C-0.29\text{eV}$. Other techniques have resulted in values of $E_C-0.25\text{eV}$ [183,184] (electron paramagnetic resonance), and $E_C-0.275\text{eV}$ [185,186] (Fourier transform infrared spectroscopy). The IDLS modelling presented here suggests an energy level of $E_C-0.23\text{eV}$. In an attempt to try to independently confirm the value of the energy level, diodes for DLTS measurements were fabricated on some of the iron-contaminated samples used in this study.

In *p*-type silicon, the standard majority carrier DLTS technique only probes the lower half of the band-gap, so it is necessary to use minority carrier injection to study the acceptor level of FeB pairs[175]. Consequently, a *p*-*n* junction diode is required, as opposed to the more easily fabricated Schottky diode for majority carrier DLTS. The *p*-*n* junction diode was formed

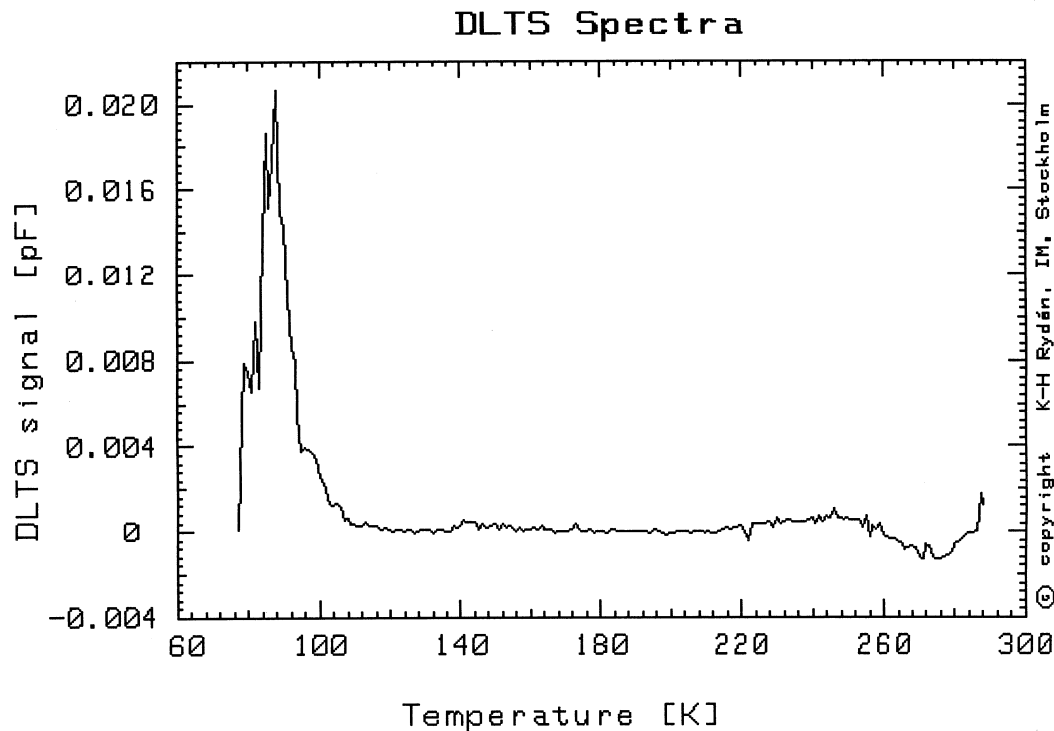


FIGURE 5.10. Minority carrier injection DLTS of a sample with a pre-diffusion iron concentration of $2.9 \times 10^{13} \text{ cm}^{-3}$ and dopant density of $9 \times 10^{13} \text{ cm}^{-3}$. FeB pairs would appear as a negative peak around 150K, but have been getterred by the diode diffusion. The positive peak below 100K is a measurement artifact.

by a phosphorus diffusion through a $0.3 \times 0.3 \text{ mm}$ window in a thick masking oxide, followed by Cr/Pd/Ag evaporated contacts on the diffusion and a Ga contact on the rear. The diffusion was performed at 900°C for 60 minutes, resulting in a sheet resistance of about $30 \Omega/\square$. Unfortunately, this diffusion had a strong gettering effect, and even for the sample with the highest iron concentration ($2.9 \times 10^{13} \text{ cm}^{-3}$) and lowest dopant density ($9 \times 10^{13} \text{ cm}^{-3}$), a combination which provides the most sensitive DLTS measurement, there was no discernible signal from the FeB pairs. Similarly, Schottky diodes fabricated to observe Fe_i in the lower half of the band-gap, revealed no trace of iron. For this dopant density, the sensitivity limit of DLTS should be at worst $1 \times 10^{12} \text{ cm}^{-3}$, indicating that the diffusion has reduced the iron concentration in the bulk significantly. Figure 5.10 shows the DLTS spectrum for the high-iron, low dopant density sample. FeB pairs, if present, would cause a hump around the 150K region [175], which clearly does not occur for this sample.

If future DLTS attempts were to be made, lighter phosphorus diffusions could be used, which should cause less gettering. Alternatively, ion-implanted phosphorus, followed by a short thermal electrical-activation step, could be used. Also, a higher initial concentration of iron in the sample could be achieved by annealing at higher temperatures at which the solubility limit

of iron is much higher. Of course, in such samples the lifetime would be extremely low, probably below the range that can be measured accurately using the QSSPC technique.

5.3.6 Ratio and difference of diffusion lengths

Zoth and Bergholz [53] found that samples dominated by Fe_i and FeB pairs could be identified by the ratio of the diffusion lengths L_1/L_0 , as measured by the Surface Photovoltage method (SPV), before (L_0) and after (L_1) thermal annealing at 210°C . Prior to annealing, the majority of the Fe is in the form of FeB pairs, whilst after annealing it is present as Fe_i . Due to constraints of the technique, SPV measurements are always performed under low-injection conditions. Since the low-injection lifetime of Fe_i is independent of the dopant density, while for FeB pairs it depends strongly on the dopant density, it follows that the ratio of the diffusion lengths is also a function of N_A . Indeed, Zoth and Bergholz found that this was true, and they reported the value of L_1/L_0 , to be about 0.5, 0.33 and 0.25 for dopant densities of 10^{16} , 10^{15} and $<5 \times 10^{14} \text{ cm}^{-3}$.

Using the energy level and cross section data from Table 5.2, and remembering that the diffusion length L_D is proportional to the square root of the lifetime, it is possible to calculate the diffusion length ratio L_1/L_0 as a function of the dopant density, under the assumption that the lifetime is dominated by iron-related centres. Figure 5.11 shows the results, with Zoth and Bergholz's SPV data included for comparison. The error bars for these experimental points are only estimates. Also shown are curves calculated using Walz *et al.*'s values for the energy level and cross-sections of FeB pairs.

An important consideration in calculating such curves is the proportion of the total iron concentration in the form of Fe_i or FeB pairs. Even after thermal annealing, not all FeB pairs dissociate, and some will re-pair during cooling down. Zoth and Bergholz estimated that for their samples, about 70% of the available iron was present as Fe_i after the thermal treatment. Similarly, not all the iron will re-pair after a finite period of time at room temperature. The re-pairing rate is dependent on the boron concentration[53,181], and there may be as much as 5% interstitial iron in higher resistivity samples even after long periods of resting in the dark. Our data in Table 5.3 shows that some samples without light-soaking had only 80-90% of the iron present as FeB pairs, although they were not rested for long periods of time, and so are not directly comparable to Zoth and Bergholz's samples in terms of relative populations. Further, SPV measurements are performed under very low injection, whereas the QSSPC measurements performed here are generally around mid-injection. These higher carrier concentrations can cause FeB pair splitting, resulting in more interstitial Fe in our non light-soaked measurements than in Zoth and Bergholz's.

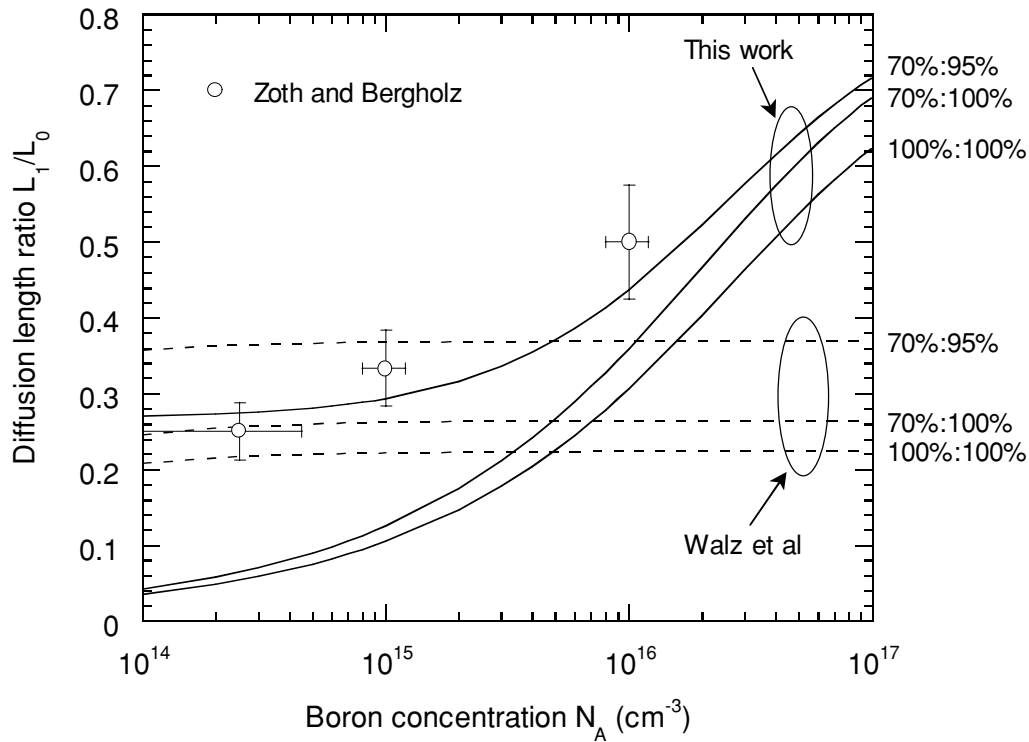


FIGURE 5.11. Diffusion length ratio (low-injection) after and before thermal annealing for iron-dominated p-type samples as a function of dopant density. Curves are shown for the energy level and cross-sections determined in this chapter, and also by Walz et al. Experimental data from Zoth and Bergholz is shown for comparison. Curves for different extents of dissociation (after anneal) and pairing (before) are labelled on the right.

To illustrate the effect of these variations, Figure 5.11 shows the curves calculated for three different conditions: 100% Fe_i after annealing and 100% FeB before (ideal state, shown as 100%:100%); 70% Fe_i after annealing and 100% FeB before (shown as 70%:100%); and 70% Fe_i after annealing and 95% FeB before (shown as 70%:95%). This final condition is probably a good approximation of the relative populations in Zoth and Bergholz's samples, and yields good agreement with their data when using the cross-sections and energy levels used in this work. The curves reveal the importance of careful sample treatment when dissociating FeB pairs, as slight changes in relative populations can impact heavily on the results. Note that the curves from Walz's parameters do not follow the trend of Zoth's data, and are essentially flat, reflecting the fact that the low-injection lifetime for Walz's FeB centre is independent of the dopant density, in contradiction to the experimental evidence presented here.

The curves in Figure 5.11 can be used to determine if a sample is dominated by iron. Zoth and Bergholz went on to show that in such cases, the absolute iron concentration can be determined by the following relation:

$$[Fe] = A \times \left(\frac{1}{L_1^2} - \frac{1}{L_0^2} \right) \quad (5.5)$$

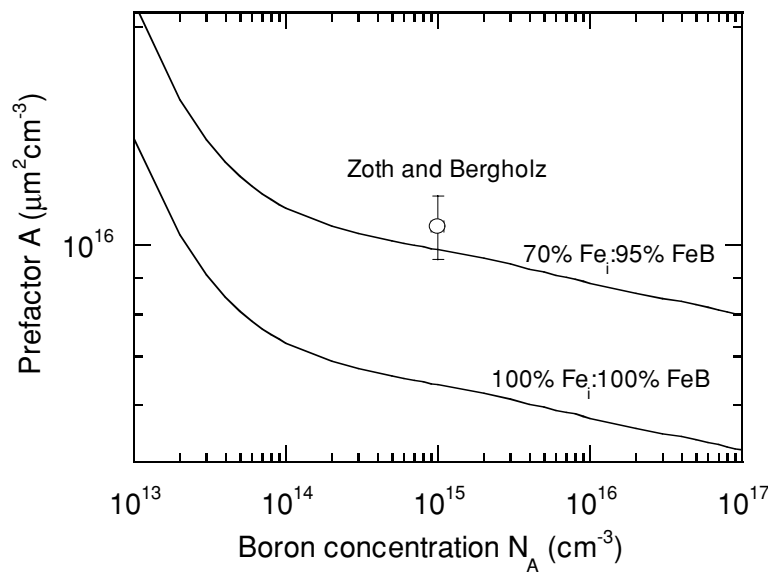


FIGURE 5.12. Pre-factor A for determining the absolute iron concentration in iron-dominated samples as a function of dopant density. Curves are shown for the energy level and cross-sections determined in this chapter for two different extents of dissociation and pairing. Experimental data from Zoth and Bergholz is shown for comparison.

The diffusion lengths must be in microns, and the computed iron concentration is in cm^{-3} . The pre-factor A was found by Zoth and Bergholz to be $1.06 \times 10^{14} \text{cm}^{-3}$ for samples with $N_A = 10^{15} \text{cm}^{-3}$. Using the cross-sections and energy level found in this chapter, it is possible to calculate this pre-factor for all resistivities. The result is shown in Figure 5.12, as well as Zoth and Bergholz's single data point. The 70% Fe_i after anneal:95% FeB before anneal curve falls within 10% of Zoth's data, and extends it to a large range of dopant densities.

The agreement between Zoth's data and the 70% Fe_i :95% FeB curves in Figure 5.11 and 5.12, which were generated with the electronic parameters of FeB pairs determined in this chapter using IDLS, provides greater confidence in the accuracy of this new technique. Furthermore, these curves allow unambiguous identification (Figure 5.11) and quantification (Figure 5.12) of iron dominated samples of any resistivity, and are a good example of the powerful diagnostic tools which can be developed when the cross-sections of an impurity are accurately known.

5.4 Other Potential Applications of IDLS

The technique of IDLS lends itself to studying other impurities in silicon that may be relevant for solar cell applications. Copper is one potential candidate, since it occurs in the wire

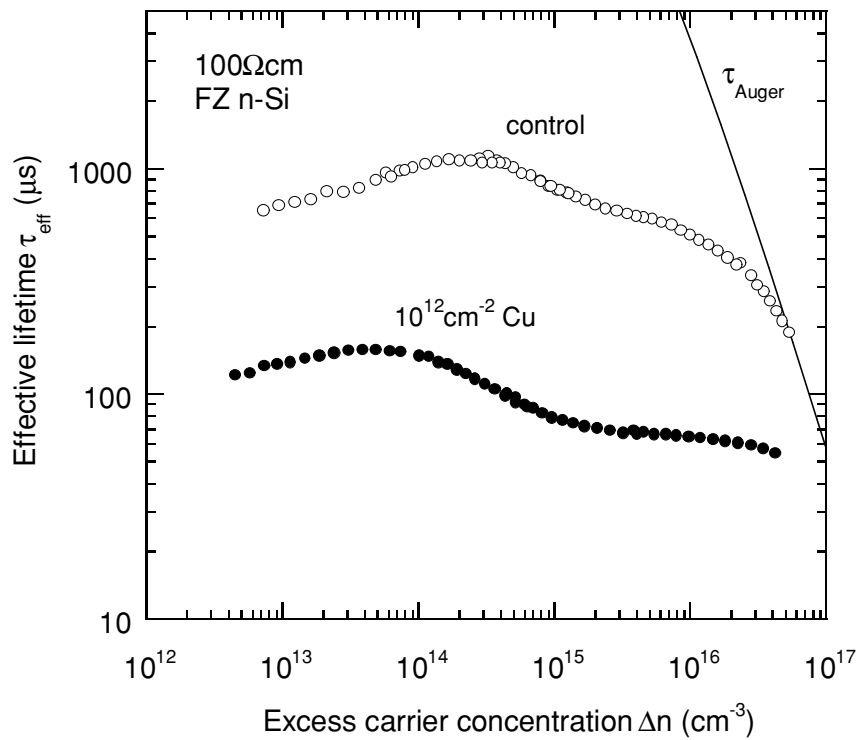


FIGURE 5.13. Lifetime measurements of Cu implanted and control 100Ωcm n-type samples.

saws used for wafering ingots, and also in microelectronic interconnects. Previous studies[164,187] have reported the presence of Cu-Cu pairs that dissociate upon illumination, resulting in a significantly degraded lifetime that does not seem to recover. IDLS offers the possibility of determining the cross-section of the Cu-Cu pairs and substitutional Cu, so that the change in low-injection lifetime upon illumination can be used to accurately determine the total Cu concentration. This would be analogous in many ways to the technique using the dissociation of FeB of Zoth and Bergholz[53].

Figure 5.13 shows QSSPC lifetime measurements of a Cu contaminated sample and a control sample. The two wafers were *n*-type 100Ωcm, one implanted with a Cu dose of $1 \times 10^{12} \text{ cm}^{-2}$, and both subsequently annealed, etched and passivated. Although the full SRH curves have not been fitted to this data, the hump-like nature of the curve reveals that at least two recombination centres, with opposing injection-level dependence, are present in the contaminated sample. It is possible that these two centres are Cu-Cu pairs and substitutional Cu. This is a promising area of study and further work is planned.

Another metal/dopant complex of interest is interstitial Cr and CrB pairs[134,156,176,188,189], which can only be dissociated by thermal annealing above 200°C. Also, considering the recently discovered boron-oxygen related defects in Czochralski silicon cells[129,190] and the resulting incentive to move towards Ga or Al doped Czochralski

wafers[148], IDLS offers an opportunity to accurately characterise FeGa, FeAl and other potentially important but relatively less studied metal/dopant systems[191].

Conclusions and Further Work

In general terms, this thesis has examined photoconductance-based lifetime measurements of mc-Si wafers, and applied them to studying the properties of recombination and trapping centres in this material. Such measurements have revealed themselves to be a very powerful tool in solar cell research, as the lifetime has a critical impact on all three cell performance parameters, namely the open circuit voltage, short circuit current and fill factor. Lifetime measurements allow accurate process monitoring to ensure parameters are within specification, and can be used to determine which aspects of a cell fabrication sequence place the greatest restrictions on the final cell performance. They also represent a unique prospect for characterising recombination centres in semiconductors in general. This is not surprising considering that the carrier lifetime is more sensitive to trace amounts of certain impurities than almost any other easily measured parameter.

The focus has been on bulk silicon, since it is the dominant solar cell material today. However, with the recent advent of flexible, fast and robust lifetime measuring techniques, it seems clear that lifetimes are set to play an increasingly important role as the photovoltaics industry continues to evolve. In particular, the current surge in research on thin-film materials has to date mostly focused on structural properties, as is natural when initially producing thin, small-grained layers. For high efficiencies however, even thin-film cells need a reasonable lifetime, and this is where part of the real challenge in producing cost-effective thin-film technologies lies. It seems likely then that lifetime measurement techniques and their interpretation will also play a critical role in allowing thin-films to fulfil their promise.

It is quite possible that these thin-films will display photoconductance properties similar in many ways to the mc-Si studied in this thesis. In particular, considering the correlation found between dislocations and trapping centres, and the likelihood of large dislocation densities in many thin-films, trapping effects could well occur in these new materials. Therefore, despite the specific focus on bulk mc-Si in this work, it is felt that many of the findings and methods used will be relevant in other parts of the photovoltaics field.

While it is important to consider long-term prospects, the immediate and direct applications of this work are mostly in mc-Si cells. Both bulk silicon in general, and mc-Si in particular, are likely to remain industrially relevant for some years to come, possibly many. However, the longevity of mc-Si technology will be partly determined by its ability to continually improve in cost per watt terms. This in turn depends on a better understanding of the electronic behaviour of mc-Si. The main contributions of this work to that improved

understanding are summarised below, including what appear to be the most compelling areas for future research.

Gettering and thermal degradation

Phosphorus gettering was found to increase the bulk lifetime of cast mc-Si wafers, except for those with very low mobile impurity densities or very high dislocation densities. It was shown that these two properties change dramatically from the bottom to the top of an ingot, and, as a direct consequence, so does the gettering effectiveness. It was also found that the particular details of these changes are not necessarily the same for ingots produced by different manufacturers. Further research on how these benefits could be incorporated easily into commercial cell processes could be very fruitful. In particular, the gettering action of the emitter diffusion could form part of future diffusion optimisations. In doing this, it would be important to consider the impact of subsequent thermal steps, such as BSF and front contact firing.

Another important property of cast mc-Si is that low resistivity wafers tend to suffer from thermal degradation of the bulk lifetime during high temperature steps. This will become an increasingly important issue if industry moves towards lower resistivities as substrates become thinner. One consequence of this phenomenon is that there is an optimum gettering time that becomes shorter as the resistivity decreases. Another is that minimising the overall thermal budget of a cell process is critical for low resistivity wafers. Using an optimised gettering regime and a low thermal budget process resulted in a PERC cell on 0.2 Ω cm mc-Si with an open circuit voltage of 649mV, without an anti-reflection coating.

The important question of what causes this thermal degradation has also been addressed in this work. Previous suggestions have been based on incomplete gettering due to the slow dissolution of precipitated metallic impurities. Modelling these processes showed that variable temperature gettering should result in more complete gettering, and hence minimise the thermal degradation effect. Such variable temperature gettering was attempted in this thesis, but did not result in more effective gettering. This result implies that either the precipitates are much more difficult to dissociate than is generally accepted, or that the thermal degradation is caused by some other process. Evidence of increased dislocation densities in thermally degraded wafers is presented as a possible alternative. Further studies on the physical cause of this phenomenon could examine the dissolution of precipitates with very high dissociation energies, possibly by deliberately introducing them in controlled samples. Transmission Electron Microscopy (TEM) could be useful in observing changes in precipitate size before and after thermal treatments. A concurrent study of any changes in the crystallographic quality would help to reveal the true cause of the thermal degradation effect.

Phosphorus gettering studies of Edge-defined Film-fed Growth (EFG) mc-Si have been presented. This material also improved after gettering, but not up to the same lifetime values of the cast mc-Si wafers. In agreement with previous work, the lifetime was found to improve further upon hydrogenation of bulk defects. In this work however, hydrogenation was achieved at lower temperatures than usual. A potentially important result arose from SIMS of gettered layers on EFG material, a technique by which the otherwise poor sensitivity of SIMS is magnified. These profiles revealed that significant quantities of Cu are removed by phosphorus diffusion. The results suggest that Cu contamination may be at least partly to blame for the generally low as-grown lifetimes in EFG material. It would be useful to confirm this with complementary studies, such as DLTS or Neutron Activation Analysis (NAA). If it were known that Cu was indeed causing low as-grown lifetimes, the source of the contamination in the casting process could be tracked down and eliminated, or at least reduced. Unfortunately, Cu and its complexes are not well characterised in terms of their electronic properties. Carefully prepared control samples in conjunction with the new technique of IDLS presented in Chapter 5 could be used to improve this state of affairs.

Trapping in mc-Si

Many researchers have observed unusual behaviour of the photoconductance at low to mid carrier densities in cast mc-Si samples. This had previously been vaguely ascribed to trapping effects, although little attempt was made to understand them more clearly. In this work, this anomalous injection-level dependence in modern mc-Si is coherently explained for the first time. This was achieved by adapting a minority carrier trapping model originally developed for single-crystal material in the 1950's, to allow direct comparison with QSSPC-measured lifetimes. The resulting model produced good agreement with experimental data, and revealed that such trapping effects often distort the recombination lifetime in the regions of interest for solar cell operation.

The trapping states are related to the presence of dislocations and also impurity-boron complexes. Dislocation-related traps are immune to gettering. The boron-impurity-related traps can be gettered, and can also be dissociated by low temperature annealing. Both types of trap do not directly affect cell performance, but they do hamper our ability to accurately measure the recombination lifetime. By comparison with both modelled and measured lifetime curves, an easily applied numerical method for correcting trap-affected data has been tested and found to improve the accuracy of the measurements considerably. Importantly, this improved data is often in the carrier density region of greatest interest. This correction technique could find applications in fast, contactless in-line process monitoring of mc-Si cell processes. Such

production monitoring techniques are becoming increasingly valued, but of course rely on data that is not corrupted by trapping effects.

As mentioned above, trapping effects are likely to occur in many of the emerging thin-film photovoltaic materials, both silicon and otherwise. They are sometimes present in single-crystal materials too. The results described in this thesis may be of value in these cases.

Recombination in mc-Si

Lifetime measurements were applied to the important question of determining the relative impact of various electronic loss mechanisms in mc-Si cells. Both high-efficiency devices produced in our laboratory and standard commercial mc-Si cells were examined in this way. High-efficiency PERL and PERC cells made with gettered mc-Si material were almost entirely limited by recombination in the base. A further discovery was that the injection-level dependence of these bulk lifetimes resulted in reduced fill factors. This injection-level dependence was relatively mild in these samples, but may be much greater if a wafer is dominated by deep levels with largely asymmetric capture cross-sections. Interstitial Fe is one such recombination centre, and modelling with PC-1D showed that it can degrade the fill factor quite significantly.

These conclusions regarding reduced fill factors do not only relate to high-efficiency mc-Si cells, but may also be relevant for commercial mc-Si devices. Single-crystal cells that are at least partly affected by bulk recombination, such as those made with Cz substrates, will also be subject to these effects.

In commercially produced mc-Si cells, the limiting mechanisms on the open circuit voltage were quite different to the high-efficiency devices. The strictest cap on the achievable open circuit voltage appeared to be imposed by recombination in the emitter. The post-diffusion bulk lifetime and rear surface passivation had less impact, and were comparable to each other in their effect limitation on the voltage. These results suggest that improving the electronic properties of the emitter is an important goal for lifting the performance of these cells. This is a difficult task, because it requires a less heavily-doped emitter, which is more difficult to contact with screen-printed fingers. Selective emitter processes coupled with passivation of the lightly-doped regions represents one approach to achieving these aims.

An important area for future work is to examine possible degradation of the bulk lifetime during thermal steps subsequent to emitter formation. The change in bulk lifetime during BSF and front contact firing, and possibly also ARC deposition, could be tracked during the cell process. This may reveal lifetime reductions that could be avoided by adjusting the process.

The physical identification of bulk recombination centres in mc-Si is another important

step towards improving mc-Si cell performance. SIMS profiles on gettered layers indicated that Fe and Cr occurred in large quantities in ungettered Eurosolare material. Further evidence, based on lifetime considerations and a lack of response to low temperature annealing, suggested that they exist almost entirely as precipitates. Preliminary NAA results confirmed the presence of these metals in BPSolar material also. NAA appears to be a useful tool for this type of experiment, although it has not been widely used for photovoltaic materials. It could be used, possibly in conjunction with TEM, to examine the important question of how such precipitated complexes respond to gettering. Powerful lifetime-based methods for detecting specific impurities could be developed, a task which would be made much easier if the energy levels and capture cross-sections were accurately known. This question was addressed by the final section of this thesis.

Injection-level dependent lifetime spectroscopy (IDLS)

IDLS is a new technique for determining the recombination parameters of impurities in silicon based on the injection-level dependence of the lifetime. As a test of its usefulness, it was applied to the case of FeB pairs in boron-doped silicon. By using samples with controlled impurity content, the method allowed the capture cross-sections, which are difficult to measure with traditional DLTS techniques, to be determined accurately. The results were found to be in agreement with previous work within the latter's regions of validity. The improved values of the cross-sections allowed Fe contamination monitoring techniques that had previously been valid for one resistivity only, to be extended to the entire range of likely cases. IDLS is especially sensitive when the levels are 'intermediate' in depth, since then the low- and high-injection lifetime limits depend strongly on the resistivity.

There are many other potential applications of this technique that could produce very useful results for the photovoltaic and microelectronics industries alike. In some cases they may lead to extremely sensitive methods for diagnosing impurity contamination, as mentioned above. Some specific applications would be to characterise the recombination properties of FeGa and FeAl pairs. These could become relevant if Cz silicon growth moves to Ga or Al as an alternative *p*-type dopant to avoid the recently documented boron-oxygen lifetime degradation effect. In that case, other metal-Ga pairs may warrant attention also. The presence of Cu in EFG material also suggests using IDLS to characterise Cu-related recombination centres.

There are some practical improvements that could be made to the IDLS technique as currently practised at the ANU. A more intense infrared light source would allow higher carrier concentrations to be reached in samples with high impurity concentrations (and therefore low

lifetimes). Such samples require infrared light to ensure reasonably uniform carrier profiles. For samples with relatively high impurity concentrations, it should also be remembered that the SRH theory might become invalid. The full continuity equation solutions outlined in Chapter 1 would then need to be used when analysing the lifetime data. Although these solutions are long, they are nonetheless easily computed.

The IDLS technique presented in this thesis provides one example of using lifetime measurements in solar cell research. Indeed, it seems obvious that the parameter which most directly determines the electronic properties of a solar cell should be the most worthwhile studying. Nevertheless, the complications of injection-level dependence, surface versus bulk effects, trapping, and other complexities, have often resulted in lifetimes being misused or even ignored. These difficulties, however, merely reflect the complex nature of real, imperfect semiconductor devices. When recognised as such, they can present opportunities for gaining greater insight into important electronic processes. The work in this thesis gives an indication of some of the powerful research applications that can arise from such detailed study of lifetime measurements.

List of Publications

Publications arising from the work in this thesis

Refereed journal papers

- [1] D. Macdonald and A. Cuevas, “*Comment on ‘Mechanisms for the anomalous dependence of carrier lifetime on injection level and photoconductance on light intensity’ [J. Appl. Phys. 89, 332 (2001)]*” accepted for publication in Journal of Applied Physics, 2001.
- [2] D. Macdonald, A. Cuevas and J. Wong-Leung, “*Capture cross-sections of the acceptor level of FeB pairs in p-type silicon by injection-level dependent lifetime measurements*” accepted for publication in Journal of Applied Physics. To be published 15th June 2001.
- [3] D. Macdonald, R. A. Sinton and A. Cuevas, “*On the use of a bias-light correction for trapping effects in photoconductance-based lifetime measurements in silicon*” Journal of Applied Physics, **89** (5), 2772-2778 (2001).
- [4] D. Macdonald and A. Cuevas, “*Understanding carrier trapping in multicrystalline silicon*” Solar Energy Materials and Solar Cells, **65** (4), 509-516 (2000).
- [5] D. Macdonald and A. Cuevas, “*Reduced fill factors in multicrystalline silicon solar cells due to injection-level dependent bulk recombination*” Progress in Photovoltaics, **8** (4), 363-375 (2000).
- [6] D. Macdonald and A. Cuevas, “*Trapping of minority carriers in multicrystalline silicon*” Applied Physics Letters, **74** (12), 1710-1712 (1999).
- [7] D. Macdonald, M. Kerr and A. Cuevas, “*Boron-related minority-carrier trapping centers in p-type silicon*” Applied Physics Letters, **75** (11), 1571-1573 (1999).
- [8] A. Cuevas, M. Stocks, D. Macdonald, M. Kerr and C. Samundsett, “*Recombination and trapping in multicrystalline silicon*” IEEE Transactions on Electron Devices, **46**, 2026-2034 (1999).
- [9] D. Macdonald, A. Cuevas and F. Ferrazza, “*Response to phosphorus gettering of different regions of cast multicrystalline silicon ingots*” Solid-State Electronics, **43**, 575-581 (1999).

Refereed papers presented at international conferences

- [10] D. Macdonald, A. Cuevas, M. Kerr, C. Samundsett, A. Sloan, A. Leo, M. Mrcarica, S. Winderbaum and S. Shea, “*Characterisation of a commercial silicon solar cell process*” Proc. of the 38th Annual Australian and New Zealand Solar Energy Society Conf., Brisbane, Australia, (2000).
- [11] D. Macdonald and A. Cuevas, “*The use of injection-level dependent lifetime measurements for determining solar cell parameters*” Proc. of the 38th Annual Australian and New Zealand Solar Energy Society Conf., Brisbane, Australia, (2000).
- [12] D. Macdonald and A. Cuevas, “*The trade-off between phosphorus gettering and thermal degradation in multicrystalline silicon*” Proc. of the 16th European Photovoltaic Solar Energy Conf., Glasgow, U.K., (2000).
- [13] A. Cuevas, D. Macdonald, M. Kerr, C. Samundsett, A. Sloan, S. Shea, A. Leo, M. Mrcarica and S. Winderbaum, “*Evidence of impurity gettering by industrial phosphorus diffusion*” Proc. of 28th IEEE Photovoltaics Specialists Conference, Anchorage, Alaska, (2000).
- [14] A. Cuevas and D. Macdonald, “*Origins of carrier trapping centres in p-type multicrystalline silicon*” Proc. 9th Workshop on the Role of Impurities and Defects in Silicon Device Processing, Colorado, (1999).
- [15] A. Cuevas, M. Stocks, D. Macdonald, M. Kerr and C. Samundsett, “*Multicrystalline silicon research at the Australian National University*” Proc. of World Renewable Energy Conference, Perth, Australia, (1999).
- [16] D. Macdonald and A. Cuevas, “*A study of minority carrier trapping in multicrystalline silicon*” Technical Digest of the 11th Photovoltaic Scientists and Engineers Conference, Sapporo, Japan, (1999).
- [17] D. Macdonald and A. Cuevas, “*Cross-contamination as a novel technique for studying impurities in multicrystalline silicon*” Proc. 2nd World Conf. on Photovoltaic Solar Energy Conversion, Vienna, Austria, (1998).
- [18] A. Cuevas and D. Macdonald, “*Lifetime studies of multicrystalline silicon*” Proc. 8th Workshop on the Role of Impurities and Defects in Silicon Device Processing, Colorado, 57 (1998).
- [19] A. Cuevas, M. Stocks, D. Macdonald and R. Sinton, “*Applications of the quasi-steady-state photoconductance technique*” Proc. 2nd World Conf. on Photovoltaic Solar Energy Conversion, Vienna, Austria, (1998).
- [20] D. Macdonald and A. Cuevas, “*Cross-contamination as a novel technique for studying impurities in multicrystalline silicon*” Proc. of the 8th Workshop on the Role of Impurities and Defects in Silicon Device Processing, Colorado, (1998).

Other related publications

Refereed journal papers

- [21] A. Cuevas, R. A. Sinton, M. Kerr and D. Macdonald, “*A contactless photoconductance technique to evaluate the quantum efficiency of solar cell emitters*” accepted for publication in Solar Energy Materials and Solar Cells, 2001.

Refereed papers presented at international conferences

- [22] A. Cuevas, M. Kerr, D. Macdonald and R. Sinton, “*Emitter quantum efficiency from contactless photoconductance measurements*” Proc. 28th IEEE Photovoltaic Specialists Conf., Anchorage, Alaska, (2000).
- [23] M. Stocks and D. Macdonald, “*Non-ideal resistive effects in silicon solar cells*” Proc. of the 16th European Photovoltaic Solar Energy Conf., Glasgow, U.K., (2000).

Bibliography

- [1] M. A. Green, 'Third generation photovoltaics: ultra-high conversion efficiency at low cost' *Prog. in Photovoltaics* **9** 123-135 (2001).
- [2] M. Schmela, 'PV in the fast lane: market survey on world cell production in 2000' *Photon International* 32-35 (March 2001).
- [3] M. A. Green, *Silicon Solar Cells: Advanced Principles and Practice*, Centre for Photovoltaic Devices and Systems, University of New South Wales, Sydney, Australia (1995).
- [4] R. Hulstrom, R. Bird and C. Riordan, 'Spectral solar irradiance data sets for selected terrestrial conditions' *Solar Cells* **15** 365-391 (1985).
- [5] T. Tiedje, E. Yablonovitch, G. D. Cody and B. G. Brooks, 'Limiting efficiency of silicon solar cells' *IEEE Trans. Elec. Dev.* **Ed-31** 711-716 (1984).
- [6] M. A. Green, 'Limits on the open-circuit voltage and efficiency of silicon solar cells imposed by intrinsic Auger processes' *IEEE Trans. Elec. Dev.* **Ed-31** 671-678 (1984).
- [7] A. G. Aberle, P. P. Altermatt, G. Heiser, S. J. Robinson, A. Wang, J. Zhao, U. Krumbein and M. A. Green, 'Limiting loss mechanisms in 23% efficient silicon solar cells' *J. Appl. Phys.* **77** 3491-3504 (1995).
- [8] J. H. Zhao, A. H. Wang and M. A. Green, '24.5% efficiency silicon PERT cells on MCZ substrates and 24.7% efficiency PERL cells on FZ substrates' *Prog. in Photovoltaics* **7** 471-474 (1999).
- [9] J. F. Nijs, J. Szlufcik, J. Poortmans, S. Sivoththaman and R. P. Mertens, 'Crystalline silicon solar cell technology for today and tomorrow' *Proc. 16th Euro. Photovoltaic Solar Energy Conf.* Glasgow, U.K. (2000).
- [10] P. A. Basore and D. A. Clugston, *PCID V5.3*, University of New South Wales, Sydney, Australia (1998).
- [11] W. Jooss, M. Spiegel, P. Fath, E. Bucher, S. Roberts and T. M. Bruton, 'Large area buried contact solar cells on multicrystalline silicon with mechanical surface texturisation and bulk passivation' *Proc. 16th Euro. Photovoltaic Solar Energy Conf.* Glasgow, U.K. 1169-1172 (2000).
- [12] F. Duerinckx, A. Noppe, P. Choulal, J. Szlufcik, J. Nijs and B. Habraken, 'Advanced industrial processes for large area screen printed multicrystalline silicon solar cells' *Proc. 16th Euro. Photovoltaic Solar Energy Conf.* Glasgow, U.K. 1301-1304 (2000).
- [13] S. DeWolf, P. Choulal, E. Vazsonyi, R. Einhaus, E. VanKerschaver, K. DeClercq and J. Szlufcik, 'Towards industrial application of isotropic texturing for multi-crystalline silicon solar cells' *Proc. 16th Euro. Photovoltaic Solar Energy Conf.* Glasgow, U.K. 1521-1523 (2000).

- [14] H. Dekkers, F. Duerinckx, J. Szlufcik and J. Nijs, 'Silicon surface texturing by reactive ion etching' *Proc. 16th Euro. Photovoltaic Solar Energy Conf.* Glasgow, U.K. 1532-1535 (2000).
- [15] A. R. Burgers, J. H. Bultman, C. Beneking, W. A. Nositschka, O. Voigt and H. Kurz, 'Silicon solar cells textured by reactive ion etching with natural lithography' *Proc. 16th Euro. Photovoltaic Solar Energy Conf.* Glasgow, U.K. 1427-1430 (2000).
- [16] D. K. Schroder, 'Carrier lifetimes in silicon' *IEEE Trans. Elec. Dev.* **44** 160-170 (1997).
- [17] J. S. Blakemore, *Semiconductor Statistics*, International Series of Monographs on Semiconductors, Vol. 3, Pergamon Press, Oxford (1962).
- [18] W. Shockley and W. T. Read, 'Statistics of the recombinations of holes and electrons' *Phys. Rev.* **87** 835-842 (1952).
- [19] R. N. Hall, 'Electron-hole recombination in germanium' *Phys. Rev.* **87** 387 (1952).
- [20] M. A. Green, *Solar cells*, The University of New South Wales, Kensington, NSW (1998).
- [21] H. Schlangenotto, H. Maeder and W. Gerlach, 'Temperature dependence of the radiative recombination coefficient in silicon' *Phys. Status Solidi A* **21** 357 (1974).
- [22] P. P. Altermatt, J. Schmidt, G. Heiser and A. G. Aberle, 'Assessment and parameterisation of Coulomb-enhanced Auger recombination coefficients in lowly injected silicon' *J. Appl. Phys.* **82** 4938-4944 (1997).
- [23] J. Dziewior and W. Schmid, 'Auger coefficients for highly doped and highly excited silicon' *Appl. Phys. Lett.* **31** 346-348 (1977).
- [24] R. A. Sinton and R. M. Swanson, 'Recombination in highly injected silicon' *IEEE Trans. Elec. Dev.* **34** 1380-1389 (1987).
- [25] A. Hangleiter and R. Hacker, 'Enhancement of band-to-band Auger recombination by electron-hole correlations' *Phys. Rev. Lett.* **65** 215-218 (1990).
- [26] S. W. Glunz, D. Biro, S. Rein and W. Warta, 'Field-effect passivation of the SiO₂-Si interface' *J. Appl. Phys.* **86** 683-691 (1999).
- [27] P. P. Altermatt, J. Schmidt, M. Kerr, G. Heiser and A. G. Aberle, 'Exciton-enhanced Auger recombination in crystalline silicon under intermediate and high injection conditions' *Proc. 16th Euro. Photovoltaic Solar Energy Conf.* Glasgow, U.K. 243-246 (2000).
- [28] A. G. Aberle, *Crystalline silicon solar cells: advanced surface passivation and analysis*, Centre for Photovoltaic Engineering, University of New South Wales, Sydney, Australia (1999).
- [29] A. B. Sproul, 'Dimensionless solution of the equation describing the effect of surface recombination on carrier decay in semiconductors' *J. Appl. Phys.* **76** 2851-2854 (1994).
- [30] A. Cuevas and R. A. Sinton, 'Prediction of the open-circuit voltage of solar cells from the steady-state photoconductance' *Prog. in Photovoltaics* **5** 79-90 (1997).
- [31] D. E. Kane and R. M. Swanson, 'Measurement of the emitter saturation current by a contactless photoconductivity decay method' *Proc. 18th IEEE Photovoltaic Specialists Conf.* Las Vegas 578-583 (1985).
- [32] A. Cuevas, 'The effect of emitter recombination on the effective lifetime of silicon wafers' *Sol. Energy Mater. Sol. Cells* **57** 277-290 (1999).
- [33] M. J. Kerr, J. Schmidt, A. Cuevas and J. Bultman, 'Surface recombination velocity of phosphorus-diffused silicon solar cell emitters passivated with plasma enhanced chemical

- vapor deposited silicon nitride and thermal silicon oxide' *J. Appl. Phys.* **89** 3821-3826 (2001).
- [34] R. R. King, R. A. Sinton and R. M. Swanson, 'Studies of diffused phosphorus emitters: saturation current, surface recombination velocity and quantum efficiency' *IEEE Trans. Elec. Dev.* **37** 365-371 (1990).
- [35] A. Cuevas, P. A. Basore, G. Giroult-Matlakowski and C. Dubois, 'Surface recombination velocity of highly doped *n*-type silicon' *J. Appl. Phys.* **80** 3370-3375 (1996).
- [36] A. B. Sproul and M. A. Green, 'Improved value for the silicon intrinsic carrier concentration from 275 to 375 K' *J. Appl. Phys.* **70** 846-854 (1991).
- [37] R. A. Sinton and A. Cuevas, 'A quasi-steady open-circuit voltage method for solar cell characterisation' *Proc. 16th Euro. Photovoltaic Solar Energy Conf.* Glasgow, U.K. 1152-1155 (2000).
- [38] C. T. Sah, R. N. Noyce and W. Shockley, 'Carrier generation and recombination in *P-N* junctions and *P-N* junction characteristics' *Proc. IRE* **45** 1228-1243 (1957).
- [39] S. C. Choo, 'Carrier generation-recombination in the space charge region of an asymmetrical *p-n* junction' *Solid-State Elec.* **11** 1069-1077 (1968).
- [40] K. McIntosh, P. P. Altermatt and G. Heiser, 'Depletion-region recombination in silicon solar cells: when does $m_{DR}=2$?' *Proc. 16th Euro. Photovoltaic Solar Energy Conf.* Glasgow, U.K. 251-254 (2000).
- [41] A. G. Aberle, S. J. Robinson, A. Wang, J. Zhao, S. R. Wenham and M. A. Green, 'High-efficiency silicon solar cells: fill factor limitations and non-ideal diode behaviour due to voltage-dependent rear surface recombination velocity' *Prog. in Photovoltaics* **1** 133-143 (1993).
- [42] A. Aberle, S. Glunz, A. Stephens and M. A. Green, 'High-efficiency silicon solar cells: Si-SiO₂ interface parameters and their impact on device performance' *Prog. in Photovoltaics* **2** 265-273 (1994).
- [43] S. J. Robinson, A. G. Aberle and M. A. Green, 'Recombination saturation effects in silicon solar cells' *IEEE Trans. Elec. Dev.* **41** 1556-1568 (1994).
- [44] J. Schmidt, A. Cuevas, S. Rein and S. Glunz, 'Impact of light-induced recombination centres on the current-voltage characteristic of Czochralski silicon solar cells' *Prog. in Photovoltaics* Accepted for publication (2001).
- [45] D. K. Schroder, *Semiconductor Material and Device Characterization*, John Wiley & Sons, New York (1990).
- [46] F. Dannhauser, 'Die abhangigkeit der tragerbeweglichkeit in silizium von der konzentration der freien ladungstrager - I' *Solid-State Elec.* **15** 1371-1375 (1972).
- [47] J. Krausse, 'Die abhangigkeit der tragerbeweglichkeit in silizium von der konzentration der freien ladungstrager - II' *Solid-State Elec.* **15** 1377-1381 (1972).
- [48] R. Brendel, 'Note on the interpretation of injection-level-dependent surface recombination velocities' *Appl. Phys. A* **60** 523-524 (1995).
- [49] A. W. Stephens and M. A. Green, 'Effectiveness of 0.08 molar iodine in ethanol solution as a means of chemical surface passivation for photoconductance decay measurements' *Sol. Energy Mater. Sol. Cells* **45** 255-265 (1997).

- [50] J. Schmidt, 'Measurement of differential and actual recombination parameters on crystalline silicon wafers' *IEEE Trans. Elec. Dev.* **46** 2018-2025 (1999).
- [51] R. A. Sinton and A. Cuevas, 'Contactless determination of current-voltage characteristics and minority-carrier lifetimes in semiconductors from quasi-steady-state photoconductance data' *Appl. Phys. Lett.* **69** 2510-2512 (1996).
- [52] H. Nagel, C. Berge and A. G. Aberle, 'Generalised analysis of quasi-steady-state and quasi-transient measurements of carrier lifetimes in silicon' *J. Appl. Phys.* **86** 6218-6221 (1999).
- [53] G. Zoth and W. Bergholz, 'A fast, preparation-free method to detect iron in silicon' *J. Appl. Phys.* **67** 6764-6771 (1990).
- [54] M. A. Green, 'Minority carrier lifetimes using compensated differential open circuit voltage decay' *Solid-State Elec.* **26** 1117-1122 (1983).
- [55] J. Schmidt and M. Kerr, 'Highest-quality surface passivation of low-resistivity p-type silicon using stoichiometric PECVD silicon nitride' *Sol. Energy Mater. Sol. Cells* **65** 585-591 (2001).
- [56] A. Rohatgi, V. Yelundur, J. Jeong, A. Ebong, D. Meier, A. M. Gabor and M. D. Rosenblum, 'Aluminium-enhanced PECVD SiN_x hydrogenation in silicon ribbons' *Proc. 16th Euro. Photovoltaic Solar Energy Conf.* Glasgow, U.K. 1120-1123 (2000).
- [57] O. F. Vyvenko, O. Kruger and M. Kittler, 'Cross-sectional electron-beam-induced current analysis of the passivation of extended defects in cast multicrystalline silicon by remote hydrogen plasma treatment' *Appl. Phys. Lett.* **76** 697-699 (2000).
- [58] E. Yablonovitch, D. L. Allara, C. C. Chang, T. Gmitter and T. B. Bright, 'Unusually low surface-recombination velocity on silicon and germanium substrates' *Phys. Rev. Lett.* **57** 249-252 (1986).
- [59] T. S. Horanyi, T. Pavelka and P. Tutto, 'In situ bulk lifetime measurement on silicon with a chemically passivated surface' *Applied Surface Science* **63** 306-311 (1993).
- [60] M. Schofthaler, R. Brendel, G. Langguth and J. Werner, 'High-quality surface passivation by corona-charged oxides for semiconductor surface characterization' *1st World Conference on Photovoltaic Solar Energy Conversion* Waikoloa, Hawaii 1509 (1994).
- [61] J. Schmidt and A. G. Aberle, 'Easy-to-use surface passivation technique for bulk carrier lifetime measurements on silicon wafers' *Prog. in Photovoltaics* **6** 259-263 (1998).
- [62] H. Hieslmair, S. McHugo and E. R. Weber, 'Aluminium backside segregation gettering' *Proc. 25th IEEE Photovoltaic Specialists Conf.* Washington D.C. 441-444 (1996).
- [63] J.-W. Jeong, M. D. Rosenblum, J. P. Kalejs and A. Rohatgi, 'Hydrogenation of defects in edge-defined film-fed grown aluminum-enhanced plasma enhanced chemical vapor deposited silicon nitride multicrystalline silicon' *J. Appl. Phys.* **87** 7551-7557 (2000).
- [64] M. Aoki, T. Itakura and N. Sasaki, 'Gettering of iron impurities in p/p+ epitaxial silicon wafers with heavily boron-doped substrates' *Appl. Phys. Lett.* **66** 2709-2711 (1995).
- [65] P. A. Stolk, J. L. Benton, D. J. Eaglesham, D. C. Jacobson, J.-Y. Cheng, J. M. Poate, S. M. Myers and T. E. Haynes, 'The mechanism of iron gettering in boron-doped silicon' *Appl. Phys. Lett.* **68** 51-53 (1996).
- [66] J. S. Kang and D. K. Schroder, 'Gettering in silicon' *J. Appl. Phys.* **65** 2974-2985 (1989).
- [67] S. M. Myers, M. Seibt and W. Schroter, 'Mechanisms of transition-metal gettering in silicon' *J. Appl. Phys.* **88** 3795-3819 (2000).

- [68] J. Wong-Leung, C. E. Ascheron, M. Petravic, R. G. Elliman and J. S. Williams, 'Gettering of copper to hydrogen-induced cavities in silicon' *Appl. Phys. Lett.* **66** 1231-1233 (1995).
- [69] N. Auriac, I. Perichaud and S. Martinuzzi, 'Gettering efficiency of He and H induced nanocavities in silicon wafers' *Proc. 16th Euro. Photovoltaic Solar Energy Conf.* Glasgow, U.K. 1234-1236 (2000).
- [70] A. Luque, A. Moehlecke, R. Lagos and C. delCanizo, 'Segregation model for Si gettering by Al' *Phys. Status Solidi A* **155** 43-49 (1996).
- [71] P. S. Plekhanov, R. Gafiteanu, U. M. Gosele and T. Y. Tan, 'Modeling of gettering of precipitated impurities from Si for carrier lifetime improvement in solar cell applications' *J. Appl. Phys.* **86** 2453-2458 (1999).
- [72] A. G. Shaikh, W. Schroter and W. Bergholz, 'Mechanism of phosphorus diffusion gettering of cobalt in silicon studied by Mossbauer spectroscopy' *J. Appl. Phys.* **58** 2519-2523 (1985).
- [73] E. O. Sveinbjornsson, O. Engstrom and U. Sodervall, 'Phosphorus diffusion gettering of gold in silicon' *Mater. Sci. Forum* **143-147** 1641-1646 (1994).
- [74] W. Schroter and R. Kuhnappel, 'Model describing phosphorus diffusion gettering of transition elements in silicon' *Appl. Phys. Lett.* **56** 2207-2209 (1990).
- [75] A. Ourmazd and W. Schroter, 'Phosphorus gettering and intrinsic gettering of nickel in silicon' *Appl. Phys. Lett.* **45** 781-783 (1984).
- [76] R. Falster, 'Platinum gettering in silicon by phosphorus' *Appl. Phys. Lett.* **46** 737-729 (1985).
- [77] W. K. Schubert and J. M. Gee, 'Phosphorus and aluminum gettering - investigation of synergistic effects in single-crystal and multicrystalline silicon' *Proc. 25th IEEE Photovoltaic Specialists Conf.* Washington D.C. 437-440 (1996).
- [78] W. Jooss, G. Hahn, P. Fath, G. Willeke and E. Bucher, 'Improvement of diffusion lengths in multicrystalline Si by P-Al co-gettering during solar cell processing' *Proc. 2nd World Conf. on Photovoltaic Solar Energy Conv.* Vienna, Austria (1998).
- [79] T. Y. Tan, R. Gafiteanu and U. M. Gosele, 'Toward understanding and modeling on impurity gettering in silicon' *Proc. 5th Workshop Role of Impurities and Defects in Silicon Devices* Boulder, Colorado 93-100 (1995).
- [80] Goetzberger and W. Shockley, 'Metal precipitates in silicon p-n junctions' *J. Appl. Phys.* **31** 1821-1824 (1960).
- [81] A. Cuevas, M. Stocks, S. Armand and M. Stuckings, 'High minority carrier lifetime in phosphorus-gettered multicrystalline silicon' *Appl. Phys. Lett.* **70** 1017-1019 (1997).
- [82] M. Ghosh, D. Yang, A. Lawrenz, S. Riedel and H. J. Moller, 'Investigation of minority carrier lifetime degradation in multicrystalline silicon ingots' *Proc. 14th Euro. Photovoltaic Solar Energy Conf.* Barcelona, Spain 724-727 (1997).
- [83] G. Goaer, D. Sarti, B. Paya, K. Mahfoud and J. C. Muller, 'Numerical thermal modelling, carbon and oxygen effects on polix multicrystalline silicon ingot' *Proc. 14th European Photovoltaic Solar Energy Conference* Barcelona, Spain 845-848 (1997).
- [84] A. Laugier, E. Borne, H. E. Omari, G. Goaer and D. Sarti, 'Transient thermal effects into a 155kg polix ingot' *Proc. 25th IEEE Photovoltaic Specialists Conf.* Washington 609-612 (1996).

- [85] F. Ferrazza, 'Growth and post growth processes of multicrystalline silicon for photovoltaic use', in *Polycrystalline Semiconductors IV*, Trans. Tech. Publ., (1995).
- [86] B. L. Sopori, L. Jastrzebski and T. Tan, 'A comparison of gettering in single- and multicrystalline silicon for solar cells' *Proc. 25th IEEE Photovoltaic Specialists Conf.* Washington 625-628 (1996).
- [87] M. Werner and E. Weber, 'Investigation of lifetime limiting microdefects in polycrystalline silicon for photovoltaic applications' *Proc. 24th IEEE Photovoltaic Specialists Conference Hawaii* 1611-1614 (1994).
- [88] S. A. McHugo, A. Thompson, I. Perichaud and S. Martinuzzi, 'Direct correlation of transition metal impurities and minority carrier recombination in multicrystalline silicon' *Appl. Phys. Lett.* **72** 3482-3484 (1998).
- [89] S. McHugo, J. Bailey, H. Hieslmair and E. Weber, 'Efficiency limiting defects in polycrystalline silicon' *Proc. 24th IEEE Photovoltaic Specialists Conference Hawaii* 1607-1610 (1994).
- [90] K. H. Yang, 'An etch for delineation of defects in silicon' *J. Electrochem. Soc.* **131** 1140-1145 (1984).
- [91] H. J. Moller, 'Multicrystalline silicon for solar cells' *Solid State Phenom.* **47-48** 127-142 (1996).
- [92] B. L. Sopori, W. Chen, J. Gee and K. Jones, 'On the performance limiting behavior of defect clusters in commercial silicon solar cells' *Proc. 2nd World Conf. on Photovoltaic Solar Energy Conv.* Vienna, Austria (1998).
- [93] S. McHugo, H. Hieslmair and E. Weber, 'Gettering of transition metals in multicrystalline silicon' *Mater. Sci. Forum* **196-201** 1979-1983 (1995).
- [94] I. Hanke, M. Apel and W. Schroter, 'Influence of annealing conditions of recombination properties and diffusion length in cast multicrystalline silicon for solar cells' *Proc. 14th Euro. Photovoltaic Solar Energy Conf.* Barcelona, Spain 735-738 (1997).
- [95] M. Mimura, S. Ishikawa and T. Saitoh, 'Effect of thermal annealing on minority-carrier lifetimes for multicrystalline silicon wafers' *Technical Digest of the 11th Photovoltaic Scientists and Engineers Conference Sapporo, Japan* 357-358 (1999).
- [96] S. A. McHugo, H. Hieslmair and E. R. Weber, 'Gettering of metallic impurities in photovoltaic silicon' *Appl. Phys. A: Mater. Sci. Process.* **64** 127-137 (1997).
- [97] M. Stocks, A. Blakers and A. Cuevas, 'Process monitoring of multicrystalline silicon solar cells using quasi-steady-state photoconductance measurements' *Proceedings of the 34th Annual Australian and New Zealand Solar Energy Society Conference Darwin, Australia* 31-38 (1996).
- [98] J. Zhao, A. Wang and M. A. Green, '24% efficient PERL structure silicon solar cells' *Proceedings of the 21st IEEE Photovoltaic Specialists Conference Orlando* 333-335 (1990).
- [99] J. Zhao and M. A. Green, 'Optimized antireflection coatings for high-efficiency silicon solar cells' *IEEE Trans. Elec. Dev.* **38** 1925-1934 (1991).
- [100] M. J. Stocks, A. J. Carr and A. W. Blakers, 'Texturing of polycrystalline silicon' *Sol. Energy Mater. Sol. Cells* **40** 33-42 (1996).

- [101] J. Zhao, A. Wang and M. A. Green, '19.8% efficient 'honeycomb' textured multicrystalline silicon solar cells' *Appl. Phys. Lett.* **73** 1991-1993 (1998).
- [102] M. J. Stocks, PhD thesis, 'High efficiency multicrystalline silicon solar cells', Australian National University, Canberra, Australia (1998).
- [103] M. Kerr, *PhD thesis*, The Australian National University, Canberra, Australia (in preparation).
- [104] D. Macdonald and A. Cuevas, 'Trapping of minority carriers in multicrystalline silicon' *Appl. Phys. Lett.* **74** 1710-1712 (1999).
- [105] A. Cuevas, M. Kerr, D. Macdonald, C. Samundsett and A. Sloan, 'Evidence of impurity gettering by industrial phosphorus diffusion' *Proc. 28th IEEE Photovoltaic Specialists Conf.* Anchorage, Alaska (2000).
- [106] D. Macdonald, A. Cuevas, M. Kerr, C. Samundsett, A. Sloan, A. Leo, M. Mrcarica, S. Winderbaum and S. Shea, 'Characterisation of a commercial silicon solar cell process' *Proc. 38th Annual Australian and New Zealand Solar Energy Society Conf.* Brisbane, Australia (2000).
- [107] A. Sloan, *Honours thesis*, The Australian National University, Canberra, Australia (2000).
- [108] M. J. McCann, K. R. Catchpole, A. W. Blakers and K. J. Weber, 'A review of thin film crystalline silicon for solar cell applications. Part 1: native substrates' *Sol. Energy Mater. Sol. Cells* **68** 135-171 (2001).
- [109] M. J. Kardauskus, M. D. Rosenblum, B. H. Mackintosh and J. P. Kalejs, 'The coming of age of a new PV wafer technology - some aspects of EFG polycrystalline silicon sheet manufacture' *Proc. 25th IEEE Photovoltaic Specialists Conf.* Washington (1996).
- [110] J. P. Kalejs and W. Schmidt, 'High productivity methods of preparation of EFG ribbon silicon wafers' *Proc. 2nd World Conf. on Photovoltaic Solar Energy Conv.* Vienna (1998).
- [111] S. K. Estreicher, J. L. Hastings and P. A. Fedders, 'Defect-induced dissociation of H₂ in silicon' *Phys. Rev. B* **57** R12663-R12665 (1998).
- [112] M. Stavola, 'Hydrogen diffusion and solubility in c-Si', in *Properties of Crystalline Silicon*, The Institution of Electrical Engineers, 511-521 (1999).
- [113] J. C. Tsai, 'Shallow phosphorus diffusion profiles in silicon' *Proc. IEEE* **57** 1499-1506 (1969).
- [114] R. B. Fair and J. C. C. Tsai, 'A quantitative model for the diffusion of phosphorus in silicon and the emitter dip effect' *J. Electrochem. Soc.* **124** 1107-1118 (1977).
- [115] G. Masetti, D. Nobili and S. Solmi, 'Profiles of phosphorus predeposited in silicon and carrier concentration in equilibrium with SiP precipitates', in *Semiconductor silicon 1977*, The Electrochemical Society, 648-657 (1977).
- [116] A. A. Istratov and E. R. Weber, 'Electrical properties and recombination activity of copper, nickel and cobalt in silicon' *Appl. Phys. A* **66** 123-136 (1998).
- [117] S. Naito and T. Nakashizu, *Mater. Res. Symp. Proc.* **262** 641 (1992).
- [118] R. A. Smith, *Semiconductors*, Cambridge University Press, Cambridge (1959).
- [119] J. A. Hornbeck and J. R. Haynes, 'Trapping of minority carriers in silicon. I. p-type silicon' *Phys. Rev.* **97** 311-321 (1955).

- [120] J. R. Haynes and J. A. Hornbeck, 'Temporary traps in silicon and germanium' *Phys. Rev.* **90** 152-153 (1953).
- [121] R. Lawrence, 'The temperature dependence of drift mobility in germanium' *Phys. Rev.* **89** 1295 (1953).
- [122] Gebbie, Nisenhoff and Fan, 'Photoconductivity and carrier traps in germanium' *Phys. Rev.* **91** 230 (1953).
- [123] J. R. Haynes and J. A. Hornbeck, 'Trapping of minority carriers in silicon. II. *n*-type silicon' *Phys. Rev.* **100** 606-615 (1955).
- [124] D. Navon and H. Y. Fan, 'Carrier traps in germanium at low temperatures' *Phys. Rev.* **91** 491 (1953).
- [125] H. Y. Fan, 'Effect of traps on carrier injection in semiconductors' *Phys. Rev.* **92** 1424-1428 (1953).
- [126] M. Stocks, A. Cuevas and A. Blakers, 'Process monitoring of multicrystalline silicon solar cells with quasi-steady state photoconductance measurements' *Proc. 26th IEEE Photovoltaic Specialists Conf. Anaheim, California* (1997).
- [127] R. K. Ahrenkiel and S. Johnston, 'Contactless measurement of recombination lifetime in photovoltaic materials' *Sol. Energy Mater. Sol. Cells* **55** 59-73 (1998).
- [128] R. K. Ahrenkiel, B. M. Keyes and D. L. Levi, 'Recombination processes in polycrystalline photovoltaic materials' *Proceedings 13th European Photovoltaic Solar Energy Conversion Conference Nice, France* 914-917 (1995).
- [129] J. Schmidt and A. Cuevas, 'Electronic properties of light-induced recombination centres in boron-doped Czochralski silicon' *J. Appl. Phys.* **86** 3175-3180 (1999).
- [130] M. A. Green, 'Intrinsic concentration, effective densities of states, and effective masses in silicon' *J. Appl. Phys.* **67** 2944-2954 (1990).
- [131] R. H. Glaenger and A. G. Jordan, 'The electrical properties of dislocations in silicon - I: the effects on carrier lifetime' *Solid-State Elec.* **12** 247-258 (1969).
- [132] K. D. Glinchuk, N. M. Litovchenko and V. A. Novikova, 'Trapping of carriers in plastically deformed silicon' *Sov. Phys. Solid State* **8** 777-778 (1966).
- [133] S. A. McHugo, A. C. Thompson, A. Mohammed, G. Lamble, I. Perichaud, S. Martinuzzi, M. Werner, M. Rinio, W. Koch, H. U. Hoefs and C. Haessler, 'Nanometer-scale metal precipitates in multicrystalline silicon solar cells' *J. Appl. Phys.* **89** 4282-4288 (2001).
- [134] K. Mishra, 'Identification of Cr in *p*-type silicon using the minority carrier lifetime measurement by the surface photovoltage method' *Appl. Phys. Lett.* **68** 3281-3283 (1996).
- [135] W. Bergholz, 'Pairing reactions of interstitial cobalt and shallow acceptors in silicon observed in Mossbauer spectroscopy' *Physica* **116B** 312-317 (1983).
- [136] R. A. Sinton, 'Possibilities for process-control monitoring of electronic material properties during solar-cell manufacture' *Proc. 9th Workshop Role of Impurities and Defects in Silicon Device Processing* Golden, Colorado 67-73 (1999).
- [137] O. Hahneiser and M. Kunst, 'Theoretical and experimental study of charge carrier kinetics in crystalline silicon' *J. Appl. Phys.* **85** 7741-7754 (1999).
- [138] O. Hahneiser, L. Elstner, S. v. Aichberger and M. Kunst, 'Charge carrier kinetics in crystalline silicon wafers' *Proc. 2nd World Conf. on Photovoltaic Solar Energy Conv.* Vienna, Austria 116-119 (1998).

- [139] S. Z. Karazhanov, 'Mechanisms for the anomalous dependence of carrier lifetime on injection level and photoconductance on light intensity' *J. Appl. Phys.* **89** 332-335 (2001).
- [140] A. Cuevas, M. Stocks, D. Macdonald, M. Kerr and C. Samundsett, 'Recombination and trapping in multicrystalline silicon' *IEEE Trans. Elec. Dev.* 2026-2034 (1999).
- [141] A. Rohatgi, S. Narashima, S. Kamra, P. Doshi, C. P. Khattak, K. Emery and H. Field, 'Record high 18.6% efficient solar cell on HEM multicrystalline material' *Proc. 25th IEEE Photovoltaic Specialists Conf.* Washington 1554 (1996).
- [142] M. Stocks and A. Cuevas, 'Surface recombination velocity of thermally oxidized multicrystalline silicon' *Proc. 2nd World Conf. on Photovoltaic Solar Energy Conv.* Vienna, Austria 1623 (1998).
- [143] M. Wolf, G. T. Noel and R. J. Stirn, 'Investigation of the double exponential in the current-voltage characteristics of silicon solar cells' *IEEE Trans. Elec. Dev.* **24** 419-428 (1977).
- [144] J.-P. Charles, G. Bordure, A. Khoury and P. Mialhe, 'Consistency of the double exponential model with the physical mechanisms of conduction for a solar cell under illumination' *J. Phys. D: Appl. Phys.* **18** 2261-2268 (1985).
- [145] R. Corkish and M. A. Green, 'Junction recombination current in abrupt junction diodes under forward bias' *J. Appl. Phys.* **80** 3083-3090 (1996).
- [146] H. J. Hovel, 'The effect of depletion region recombination currents on the efficiencies of Si and GaAs solar cells' *Proc. 10th IEEE Photovoltaic Specialists Conf.* 34-39 (1973).
- [147] M. J. Stocks, A. Cuevas and A. W. Blakers, 'Theoretical comparison of conventional and multilayer thin silicon solar cells' *Prog. in Photovoltaics* **4** 35-54 (1996).
- [148] T. Saitoh, H. Hashigami, S. Rein and S. Glunz, 'Overview of light degradation research on crystalline silicon solar cells' *Prog. in Photovoltaics* **8** 537-547 (2000).
- [149] R. H. Hopkins and A. Rohatgi, 'Impurity effects in silicon for high efficiency solar cells' *Journal of Crystal Growth* **75** 67-79 (1986).
- [150] H. Elgamel, 'High efficiency polycrystalline silicon solar cells using low temperature PECVD process' *IEEE Trans. Elec. Dev.* **45** 2131-2137 (1998).
- [151] J. H. Bultmann, R. Kinderman, J. Hoornstra and M. Koppes, 'Single step selective emitter using diffusion barriers' *Proc. 16th Euro. Photovoltaic Solar Energy Conf.* Glasgow, U.K. 1424-1426 (2000).
- [152] L. Debarge, J. C. Muller, B. Forget, D. Fournier and L. Frisson, 'Screen-printable paste and spin-on source applied to selective emitter formation in a single rapid thermal diffusion step' *Proc. 16th Euro. Photovoltaic Solar Energy Conf.* Glasgow, U.K. 1504-1507 (2000).
- [153] R. G. Wilson, F. A. Stevie and C. W. Magee, *Secondary Ion Mass Spectroscopy: A Practical Handbook for Depth Profiling and Bulk Impurity Analysis*, Wiley Interscience, (1989).
- [154] M. Petracic, personal communication.
- [155] A. A. Istratov, H. Hieslmair and E. R. Weber, 'Iron and its complexes in silicon' *Appl. Phys. A* **69** 13-44 (1999).
- [156] H. Conzelmann, K. Graff and E. R. Weber, 'Chromium and chromium-boron pairs in silicon' *Appl. Phys. A* **30** 169-175 (1983).

- [157] L. Jastrzebski, W. Henley, D. Schielein and J. Lagowski, 'Improvement of diffusion length in polycrystalline photovoltaic silicon by phosphorus and chlorine gettering' *J. Electrochem. Soc.* **142** 3869-3872 (1995).
- [158] A. W. Blakers, A. Wang, A. M. Milne, J. Zhao, X. Dai and M. A. Green, '22.6% efficient silicon solar cells' *Proc. 4th Photovoltaic Solar Energy Conf.* Sydney, Australia 111 (1989).
- [159] A. W. Blakers, J. Zhao, A. Wang, A. M. Milne, X. Dai and M. A. Green, '23% efficient silicon solar cell' *Proc. 14th European PVSEC* Freiburg, Germany 32 (1989).
- [160] E. R. Weber, 'Transition metals in silicon' *Appl. Phys. A* **30** 1-22 (1983).
- [161] J. Wong-Leung, D. J. Eaglesham, J. Sapjeta, D. C. Jacobson, J. M. Poate and J. S. Williams, 'The precipitation of Fe at the Si-SiO₂ interface' *J. Appl. Phys.* **83** 580-584 (1998).
- [162] J. R. Davis, A. Rohatgi, P. Rai-Choudhury, P. Blais, R. H. Hopkins and J. R. McCormick, 'Characterization of the effects of metallic impurities on silicon solar cell performance' *Proc. 13th IEEE Photovoltaic Specialists Conf.* Washington, DC 490-496 (1978).
- [163] A. A. Istratov, H. Hieslmair and E. R. Weber, 'Iron contamination in silicon technology' *Appl. Phys. A* **70** 489-534 (2000).
- [164] W. B. Henley, D. A. Ramappa and L. Jastrzebski, 'Detection of copper contamination in silicon by surface photovoltage diffusion length measurements' *Appl. Phys. Lett.* **74** 278-280 (1999).
- [165] D. Walz, J.-P. Poly and G. Kamarinos, 'On the recombination behaviour of iron in moderately boron-doped p-type silicon' *Appl. Phys. A* **62** 345-353 (1996).
- [166] R. Falster and G. Barionetti, 'The application of minority carrier lifetime techniques in modern CZ silicon', in *Recombination Lifetime Measurements in Silicon, ASTM STP 1340*, American Society for Testing and Materials, (1998).
- [167] S. Rein, T. Rehr, J. Isenberg, W. Warta and S. W. Glunz, 'Lifetime spectroscopy in silicon solar cells' *Proc. 16th Euro. Photovoltaic Solar Energy Conf.* Glasgow, U.K. 1476-1481 (2000).
- [168] Y. Hayamizu, T. Hamaguchi, S. Ushio and T. Abe, 'Temperature dependence of minority-carrier lifetime in iron-diffused p-type silicon wafers' *J. Appl. Phys.* **69** 3077-3081 (1991).
- [169] A. Kaniava, A. L. P. Rotondaro, J. Vanhellemont, U. Menczgar and E. Gaubas, 'Recombination activity of iron-related complexes in silicon studied by temperature dependent carrier lifetime measurements' *Appl. Phys. Lett.* **67** 3930-3932 (1995).
- [170] A. Kaniava, E. Gaubas, J. Vaitkus, J. Vanhellemont and A. L. P. Rotondaro, 'Recombination activity of iron related complexes in silicon' *Mat. Sci. and Tech.* **11** 670-674 (1995).
- [171] W. M. Bullis and H. R. Huff, 'Interpretation of carrier recombination lifetime and diffusion length measurements in silicon' *J. Electrochem. Soc.* **143** 1399-1405 (1996).
- [172] A. Hallen, N. Keskitalo, F. Masszi and V. Nagl, 'Lifetime in proton irradiated silicon' *J. Appl. Phys.* **79** 3906-3914 (1996).
- [173] J. Lagowski, P. Edelman, A. M. Kontkiewicz, O. Milic, W. Henley, M. Dexter, L. Jastrzebski and A. M. Hoff, 'Iron detection in the part per quadrillion range in silicon

- using surface photovoltage and photodissociation of iron-boron pairs' *Appl. Phys. Lett.* **63** 3043-3045 (1993).
- [174] K. Wunstel and P. Wagner, 'Interstitial iron and iron-acceptor pairs in silicon' *Appl. Phys. A* **27** 207-212 (1982).
- [175] S. D. Brotherton, P. Bradley and A. Gill, 'Iron and the iron-boron complex in silicon' *J. Appl. Phys.* **57** 1941-1943 (1985).
- [176] P. Eichinger, 'New developments of the ELYMAT technique', in *Recombination Lifetime Measurements in Silicon, ASTM STP 1340*, American Society for Testing and Materials, (1998).
- [177] G. Zoth, 'Aspects of silicon contamination control by lifetime', in *Recombination Lifetime Measurements in Silicon, ASTM STP 1340*, American Society for Testing and Materials, (1998).
- [178] J. Wong-Leung, J. S. Williams and E. Nygren, 'Gettering of Au to dislocations and cavities in silicon' *Appl. Phys. Lett.* **67** 416-418 (1995).
- [179] W. B. Henley and D. A. Ramappa, 'Iron precipitation in float zone grown silicon' *J. Appl. Phys.* **82** 589-594 (1997).
- [180] H. Hashizume, S. Sumie and Y. Nakai, 'Carrier lifetime measurements by microwave photoconductivity decay method', in *Recombination Lifetime Measurements in Silicon, ASTM STP 1340*, American Society for Testing and Materials, (1998).
- [181] H. Lemke, 'Dotierungseigenschaften von eisen in silizium' *Phys. Status Solidi A* **64** 215-224 (1981).
- [182] H. Nakashima and T. Sadoh, in *Defect Engineering in Semiconductor Growth, Processing and Device Technology*, Materials Research Society, 555 (1992).
- [183] W. Gehlhoff and U. Rehse, in *Defect Engineering in Semiconductor Growth, Processing and Device Technology*, Materials Research Society, 507 (1992).
- [184] W. Gehlhoff and K. Irmscher, *Solid State Phenom.* **32-33** 219 (1993).
- [185] S. Ghatnekar-Nilsson, M. Kleverman, P. Emanuelsson and H. G. Grimmeiss, 'Identification of the iron-boron line spectrum in silicon' *Semicond. Sci. Technol.* **8** 1857-1861 (1993).
- [186] S. Ghatnekar-Nilsson, M. Kleverman, P. Emanuelsson and H. G. Grimmeiss, 'Identification of the iron-boron line spectrum in silicon' *Mater. Sci. Forum* **143-7** 171-175 (1994).
- [187] I. Tarasov and S. Ostapenko, 'Light induced defect reactions in boron-doped silicon: Cu versus Fe' *Proc. 9th Workshop Role of Impurities and Defects in Silicon Device Processing* 207-210 (1998).
- [188] H. Conzelmann and J. Weber, 'Photoluminescence from chromium-boron pairs in silicon' *Physica* **116B** 291-296 (1983).
- [189] K. Kurita and T. Shingyouji, 'Identification and quantification of transition metal impurities in Czochralski silicon wafers using microwave photoconductive decay lifetime measurements' *Jpn. J. Appl. Phys.* **37** 5861-5865 (1998).
- [190] J. Schmidt, C. Berge and A. G. Aberle, 'Injection level dependence of the defect-related carrier lifetime in light-degraded boron-doped Czochralski silicon' *Appl. Phys. Lett.* **73** 2167-2169 (1998).

- [191] T. F. Ciszek, T. H. Wang, W. A. Doolittle and A. Rohatgi, 'Minority-carrier lifetime degradation in silicon co-doped with iron and gallium' *Proc. 26th IEEE Photovoltaic Specialists Conference* Anaheim, CA 59-62 (1997).